Theory and simulation of ultrafast autodetachment dynamics and nonradiative relaxation in molecules

Dissertation

zur Erlangung des naturwissenschaftlichen Doktorgrades der
Julius-Maximilians-Universität Würzburg

vorgelegt von
Kevin Issler
aus Lauda-Königshofen

Würzburg, November 2023

Eingereicht bei der Fakultät für Chemie und Pharmazie am

20. November 2023

_____

Gutachter der schriftlichen Arbeit

1. Gutachter: Prof. Dr. Roland Mitrić

2. Gutachter: Prof. Dr. Volker Engel

Prüfer des Promotionskolloquiums

1. Prüfer: Prof. Dr. Roland Mitrić

2. Prüfer: Prof. Dr. Volker Engel

3. Prüfer: Prof. Dr. Christoph Lambert

Datum des Promotionskolloquiums

18. März 2024

_____

Doktorurkunde ausgehändigt am

_____

Danksagung

Zunächst möchte ich Prof. Dr. Roland Mitrić danken, zum einen für die Möglichkeit meine Promotion in seiner Arbeitsgruppe durchzuführen, vor allem jedoch für seinen Umgang mit jedem einzelnen seiner Gruppenmitglieder. Die vergangenen Jahre waren zum Teil sehr schwierige, sowohl wissenschaftlich-thematisch, als auch persönlich, und doch hatte ich zu jedem Zeitpunkt das Gefühl, mir würde nichts als Vertrauen und Unterstützung entgegengebracht. Die Kraft und das Selbstbewusstsein welche ich daraus ziehen konnte waren sicherlich ein bedeutender Faktor im schlussendlichen Gelingen dieser Arbeit. Meinen allerherzlichsten Dank dafür!

Ein besonderer Dank gilt Dr. Jens Petersen für seine intensive und engagierte Betreuung mit aus meiner Sicht genau der richtigen Mischung aus Motivation, Humor, Verständnis und Beharrlichkeit, die dazu geführt hat nicht den Faden zu verlieren und letztlich am Ziel anzukommen. Auch kann ich sagen, dass es mich stolz macht in Jens über die Jahre einen guten Freund gefunden zu haben.

Vielen Dank auch den gesamten Arbeitsgruppen Mitrić und Röhr, insbesondere Michael Wenzel, der mir zunächst als Bürokollege (später ein paar Räume weiter weg, aber dennoch) vor allem durch seine Hilfsbereitschaft ans Herz gewachsen ist und über die Jahre für mich zu einer Art Anlaufstelle für alle möglichen (hauptsächlich programmiertechnischen) Fragen geworden ist.

Weiterer Dank gilt der Zeichnerin des Logos des HORTENSIA-Programmpakets, Maiti Laserna de Himpsl, sowie den fleißigen Korrekteuren dieser Arbeit, Maximilian Gutwein, Violetta Himpsl und Dr. Jens Petersen.

Zu guter Letzt möchte ich meiner Frau Teresa und meiner Omi Hannelore danken für ihre selbstlose Liebe und bedingungslose emotionale Unterstützung, sowie der ganzen Familie Himpsl, die mich wie selbstverständlich bei sich aufgenommen hat und mir immer das Gefühl gibt, eine Heimat gefunden zu haben.

Contents

Chapter 1

Introduction

An important aspect of the characteristic properties of molecules is their behavior during and after exposure to radiation, which includes structural changes, emission of light or the ejection of electrons. As a result, emission properties may be altered or chemical reactions such as isomerization or bond-breaking induced.[1] These light-induced processes can generally compete with each other on ultra-fast timescales in the femto- and picosecond regime and the molecular relaxation dynamics is therefore a topic of utmost relevance in modern natural sciences.[2] Although experimental data is the basis upon which all of the characterization of molecules is rested, spectroscopic methods only provide indirect access to molecular observables and the results need to (and often cannot with certainty) be interpreted. Hence, theoretical methods need to be employed which are able to describe the occurring processes on a molecular level. For this reason, significant advances have been made over the years in the development of static quantum-chemical methods describing molecular systems, from ground state, vibrational and ionization energies to excited states and properties such as transition moments,[3,4] as well as nonadiabatic dynamics simulations[5–8] accounting for the coupled motion of electrons and nuclei.

Especially in the case of molecular anions however, being usually characterized by small binding energies[9], even the static description is theoretically complicated, since the weak binding in anions generally leads to significantly more diffuse distributions of the "extra" electron around the molecular core as opposed to the neutral case.[10] Many of these anionic systems support experimentally observable resonances, that is, metastable states with respect to electron loss, that deactivate on femto- to microsecond timescales.[11–13] In principle there are three possible deactivation pathways a metastable anion can go through[14]: Assuming a lower-lying, stable state exists, the first is radiative decay, which does not chemically alter the molecular system, in contrast to the other two possibilities. Furthermore there is dissociative electron attachment, in which the unbound anion decomposes into two stable fragments. For example this is observed prominently in DNA bases[15,16], DNA strand breaks[17,18] through radiation and DNA photolesion repair[19]. The last deactivation option is autodetachment, meaning the ejection of an electron after a finite lifetime. This process was first observed on the metastable ex-

cited state of C_2^- in 1968 [20,21] and has been a growing research field ever since. The autodetachment phenomenon can be used in the accurate determination of anionic properties [22–24] and characteristics of isomerization reactions [25,26], to name a few examples. While in many cases autodetachment is happening due to an unstable electron configuration, some molecules possess bound electronic states with such low binding energies that even vibrational excitation suffices to overcome the detachment threshold, therefore resulting in vibration-induced autodetachment. It was observed that autodetachment can be highly mode-specific [27–29] and therefore the redistribution of vibrational energy and the ensuing geometric changes in molecules are of great interest in the dynamics of molecular anions. [30,31] Although experimentally well-observed, there is still a need for theoretical methods in the description of the process of vibrational autodetachment in a time-resolved manner. The task of deriving an efficient, accurate methodology for the simulation of autodetachment dynamics is tackled in this thesis.

On the other hand are electron detachment experiments not only important for metastable resonances, but photodetachment is also an established tool in the understanding of bound-state dynamics [32] and the combination with theoretical simulations is a standard, for example in ultrafast time-resolved photoelectron spectroscopy experiments. [33] These joint theoretical-experimental studies are also able to resolve conformational changes in molecules which can greatly alter their chemical characteristics such as radiative deactivation.

Of great relevance at the moment, for example, are so-called charge transfer processes, in which after photoexcitation electron density is redistributed in a way that is significantly different from the ground state, with a charge separation between positively and negatively charged sites. [34] Materials which are able to support such charge-transfer processes are widely used as semiconductors, [35] for example in solar cells [36,37] and OLEDs [38,39]. A special case is the intramolecular charge transfer (ICT), in which donor and acceptor are within the same molecule. [34] In the case of ICT a prominent example for the importance of accurate theoretical models is the alteration of emission properties in the 4-(dimethylamino)benzonitrile (4-DMABN), which was the first detected molecule that shows two distinct fluorescence bands with solvent-dependent intensity distributions. [40,41] Theoretical models suggested both an energetic minimum in the first excited state close to the ground state equilibrium geometry as well as fast transition to a charge-transfer state at a twisted geometry energetically separated by a solvent-dependent activation barrier. [42] The occurrence of dual fluorescence is highly molecule specific in that even the replacement of the nitrile group in 4-DMABN with an isoelectronic ethyne group is sufficient to prevent this phenomenon, [43] which calls for theoretical approaches to the understanding of these intricate observations. In this case, the theoretical simulation of molecular dynamics is able to disentangle the experimental time-resolved signals in the photoelectron spectrum and draw conclusions on the emission behavior. [43]

With respect to the two topics introduced above (autodetachment after

vibrational or vibronic excitation and photodetachment after electronic excitation), this cumulative thesis presents theoretical contributions to the understanding of ultrafast molecular processes during electron detachment, consisting of four publications in scientific journals. All investigations were carried out in the framework of the surface-hopping methodology, in which dynamic processes are simulated in a quantum-classical manner, with the nuclear motion described as an ensemble of classical trajectories propagated in the field of the quantum-mechanically obtained potential energy surfaces. Since a variety of different aspects of electron detachment dynamics is approached in this work, it is useful to first give a quick overview of the overall structure of the thesis:

In chapter 2 the theoretical foundation is laid for the understanding of the following chapters. The surface-hopping methodology (section 2.1) as well as the employed quantum-chemical methods (section 2.2) are explained briefly and aspects are addressed that are skipped over in the theory sections of the subsequent publications. Moreover a discussion of molecular anions and its characteristic electronic properties (section 2.3) is given together with a look on computational peculiarities concerning anions, which also necessarily includes the consideration of resonance states as well as spectroscopic techniques.

Chapter 3 discusses the theory behind the newly developed methodology for the theoretical description of vibration-induced autodetachment processes. A formulation is developed in which the electronic detachment event is described by nonadiabatic couplings to the discretized continuum states comprised of orthogonalized plane waves. The arising coupling terms are derived, which yields formulae that are solved in the framework of the surface-hopping methodology. The theory is validated by comparison of the obtained theoretical data with experimental findings on the vinylidene anion molecule, thereby extending the understanding of the vinylidene-acetylene isomerization process.

The publication in chapter 4 should be viewed complementary to chapter 3: Whereas in the aforementioned chapter the theoretical ideas are presented, this publication focuses on computational implementation within the HORTENSIA program package. The underlying algorithms are discussed in more detail and necessary approximations as well as general performance with respect to computation time and resource usage are assessed. Furthermore another example molecule is studied, the 2-cyanopyrrolide anion, to show the implemented extension of the methodology to electronically excited states.

While in chapters 3 and 4 the focus is on molecules in which a single bound state plays the central role, the nitropropane anion presented in chapter 5 features an interplay between the ground and the dipole-bound excited state. The simulation reproduces existing electron kinetic energy distributions to an adequate degree and further analysis of geometric data allowed for the validation of experimentally predicted autodetachment pathways. The coupling between the excited dipole-bound state to the initially populated ground state is revealed to be of great importance in the autodetachment efficiency, with its transient population effectively acting as a mediator of electron ejection on an

ultrafast timescale.

In chapter 6 the ultrafast dynamics of the 4-(dimethylamino)benzethyne molecule after electronic excitation is investigated. The joint theoretical and experimental study revealed an ultrafast geometric change by partial twisting of the dimethylamino group with respect to the molecular plane, leading to vanishing electron intensity on the timescale of $\sim$100 fs in the experimental time-resolved photoelectron spectrum.

These publications are followed by an overall discussion and conclusion in chapter 7, after which a brief summary of this thesis is given in chapters 8 and 9 in English and German, respectively.

Finally it has to be noted that the publications used for this cumulative dissertation (chapters 3-6) are reproduced from their original journal publications word by word. Changes were made only to achieve a uniform formatting and citation throughout the thesis. Therefore it also has to be stressed that the citation numbering in this work differs from the ones in the reproduced publications.

Chapter 2

Theoretical Methodology

In the following the theoretical foundations necessary for the method development presented in this thesis will be discussed.

2.1 Molecular dynamics simulations

The complete evolution of a molecular system, consisting of an arrangement of nuclei and electrons, in time and space is given by its wavefunction $\Phi(\mathbf{r}, \mathbf{q}, t)$ ($\mathbf{r}$ denotes the vector of all electronic coordinates, $\mathbf{q}$ the vector of all nuclear coordinates and t time), which needs to satisfy the time-dependent Schrödinger equation[44]

$$i\hbar \frac{\mathrm{d}}{\mathrm{d}t}\Phi(\mathbf{r}, \mathbf{q}, t) = \hat{H}\Phi(\mathbf{r}, \mathbf{q}, t) = (\hat{T} + \hat{V})\Phi(\mathbf{r}, \mathbf{q}, t), \qquad (2.1)$$

containing the Hamiltonian operator $\hat{H}$ comprised of the operators for the kinetic and potential energy, $\hat{T}$ and $\hat{V}$, respectively. Separating the Hamiltonian $\hat{H}$ in equation 2.1 with regards to nuclear (n) and electronic (e) contributions yields

$$\hat{H} = \hat{T}_n + \hat{T}_e + \hat{V}_{ee} + \hat{V}_{nn} + \hat{V}_{en} = \hat{T}_n + \hat{H}_{el}, \qquad (2.2)$$

where $\hat{H}_{el}$ is called the electronic Hamiltonian. The terms $\hat{V}_{ij}$ signify the Coulomb potentials between all pairs of involved particles. Since equation 2.1 is not analytically solvable in most cases because of the correlation of all electrons and nuclei, it is necessary to introduce an approximation that, at least partly, simplifies the search for a(n approximate) solution to the Schrödinger equation for the considered molecular system. The so-called Born-Oppenheimer approximation[45] proposes a separation ansatz based on the argument that the masses of nuclei and electrons are magnitudes apart and therefore the velocities of nuclei significantly smaller in comparison to those of the electrons. Within this approximation one regards nuclear and electronic degrees of freedom as separable and for the electron system the nuclear kinetic energy as negligible, i.e. the nuclear coordinates to be fixed. This leads to the stationary eigenvalue equation called the electronic Schrödinger equation

$$\hat{H}_{el}\psi_i(\mathbf{r}; \mathbf{q}) = (\hat{T}_e + \hat{V})\psi_i(\mathbf{r}; \mathbf{q}) = E_{el,i}(\mathbf{q})\psi_i(\mathbf{r}; \mathbf{q}). \qquad (2.3)$$

The complete orthonormal set of eigenfunctions to the electronic Hamiltonian $\hat{H}_{el}$ are called the adiabatic eigenstates $\{\psi_i\}$, which only parametrically depend on the nuclear coordinates $\mathbf{q}$ (indicated by a semicolon).[2] Hence, since all $\{\psi_i\}$ form a complete basis of the system space, the total wavefunction $\Psi(\mathbf{r}, \mathbf{q}, t)$ can be constructed as a linear combination of these states,

$$\Psi(\mathbf{r}, \mathbf{q}, t) = \sum_i \chi_i(\mathbf{q}, t)\psi_i(\mathbf{r}; \mathbf{q}), \qquad (2.4)$$

where $\{\chi_i(\mathbf{q}, t)\}$ are called the nuclear wavefunctions. Substitution of equation 2.4 into 2.1, subsequent multiplication from the left with ψ_j^* and integration over the electronic coordinates leads to

$$i\hbar\dot{\chi}_j = (\hat{T}_n + E_{el,j}(\mathbf{q}))\chi_j$$
$$- \sum_i \sum_I \frac{\hbar^2}{2M_I}\Big(2\langle\psi_j|\nabla_I|\psi_i\rangle \cdot \nabla_I\chi_i + \langle\psi_j|\nabla_I^2|\psi_i\rangle\,\chi_i\Big), \qquad (2.5)$$

the time-dependent nuclear Schrödinger equation. Here it was inserted that $\hat{T}_n = -\frac{\hbar^2}{2M_I}\sum_I \nabla_I^2$, with the mass M_I and the gradient ∇_I with respect to nuclear coordinates for a nucleus I. The last term on the right includes the so-called nonadiabatic coupling terms of first and second order arising from the mutual dependence of electronic and nuclear motion, and the complete neglect of these terms is called the Born-Oppenheimer approximation with the expression

$$i\hbar\dot{\chi}_j = (\hat{T}_n + E_{el,j}(\mathbf{q}))\chi_j. \qquad (2.6)$$

One can see that the eigenvalues of the electronic Schrödinger equation, dependent on the nuclear configuration $\mathbf{q}$, appear as the potential energies in the nuclear Schrödinger equation, hence the name potential energy surface.[2]

2.1.1   Classical nuclear dynamics

There are several approaches to finding a solution for the time evolution of the nuclear wavefunction. One possibility is the explicit numerical integration of the time-dependent nuclear Schrödinger equation, where operators and wavefunctions are represented on a spatial grid and time integration is performed in discrete steps.[46–48] These strictly quantum-dynamical methods are, however, only applicable for a very small number of nuclear degrees of freedom, since the size of the grid on which one numerically propagates the wavefunctions scales exponentially with the nuclear coordinates.[46] An entirely different approach that opens the possibility to describe far bigger molecular systems is to assume the nuclei as classical and formally replacing the nuclear wavefunction as $\chi_j(\mathbf{q}, t) \to c_j(t)\delta(\mathbf{q} - \mathbf{q}'(t))$, meaning that the nuclear wavefunction is substituted with moving point charges bearing an electronic probability amplitude.

One possibility of this classical nuclear motion ansatz which is used in all the work presented in the following chapters is based on such a quantum-classical approach to molecular dynamics. This means that at a specific instant of time for a set configuration of nuclear point charges at coordinates $\mathbf{q}$ the (quantum-mechanical) electronic potential energy $E_{el}(\mathbf{q})$ along with its gradient $\nabla_{\mathbf{q}}$ with respect to all nuclear degrees of freedom is evaluated. The force acting on the nuclei is then given as the gradient of the potential energy surface according to Newton's equations of motion,

$$\mathbf{M}\ddot{\mathbf{q}} = \mathbf{F} = -\nabla_{\mathbf{q}}E_{el}(\mathbf{q}), \tag{2.7}$$

with the diagonal matrix of the nuclear masses $\mathbf{M}$. Subsequent integration of these equations then leads to classical trajectories of point masses, $\mathbf{q}(t)$, moving along quantum-chemically evaluated potential energy surfaces.[2]

Since $\nabla_{\mathbf{q}}E_{el}(\mathbf{q})$ is calculated on the fly along the trajectory, equation 2.7 needs to be solved numerically at each time step. This can be done using a Taylor expansion of $\mathbf{q}(t + \Delta t)$ around $\mathbf{q}(t)$ in a procedure called the Velocity-Verlet algorithm[49]:

$$\mathbf{q}(t + \Delta t) = \mathbf{q}(t) + \dot{\mathbf{q}}(t)\Delta t + \frac{1}{2}\ddot{\mathbf{q}}(t)\Delta t^2. \tag{2.8}$$

At the new nuclear geometries it is possible to evaluate a new potential energy gradient $\nabla_{\mathbf{q}}E_{el}(\mathbf{q}(t + \Delta t))$, resulting in the new accelerations $\ddot{\mathbf{q}}(t + \Delta t)$. From this, velocities at the new time step are generated according to

$$\dot{\mathbf{q}}(t + \Delta t) = \dot{\mathbf{q}}(t) + \frac{1}{2}(\dot{\mathbf{q}}(t) + \dot{\mathbf{q}}(t + \Delta t))\Delta t. \tag{2.9}$$

This algorithm is straightforward in that only the previous nuclear geometries and velocities need to be known to propagate a trajectory in time. In addition this means that initial conditions for these quantities need to be found that realistically model the molecular starting state.

One widely used method for the generation of initial conditions is sampling of a phase space distribution function, of which the Wigner function[50] is the most commonly used. It is given by

$$\rho_W(\mathbf{q}, \mathbf{p}) = (\pi\hbar)^{-N} \int \langle \mathbf{q} - \mathbf{y}|\hat{\rho}|\mathbf{q} + \mathbf{y}\rangle \, e^{2i\mathbf{p}\cdot\mathbf{y}} \, d\mathbf{y} \tag{2.10}$$

$$= (\pi\hbar)^{-N} \int \chi^*(\mathbf{q} + \mathbf{y})\chi(\mathbf{q} - \mathbf{y})e^{2i\mathbf{p}\cdot\mathbf{y}} \, d\mathbf{y}, \tag{2.11}$$

where $\mathbf{q}$ and $\mathbf{p}$ are normal coordinates and momenta, respectively, of dimension N. The transition from equation 2.10 to 2.11 is only correct for pure states, which is assumed here. The Wigner function is defined so that

$$\int \rho_W(\mathbf{q}, \mathbf{p}) \, d\mathbf{p} = |\Psi(\mathbf{q})|^2 \quad \text{and} \quad \int \rho_W(\mathbf{q}, \mathbf{p}) \, d\mathbf{q} = |\Psi(\mathbf{p})|^2, \tag{2.12}$$

meaning that by integration over either spatial coordinates or momenta, the probability density in the respective other space is obtained. Therefore the most common case now is to sample phase space points from the Wigner function of a harmonic oscillator for each normal mode, which for a canonical (thermal) ensemble takes the form[51]

$$\rho_W(\mathbf{q}, \mathbf{p}) = \frac{1}{(\pi\hbar)^N} \prod_{i=1}^{N} \alpha_i(T) \exp\left(-\frac{\alpha_i(T)}{\hbar\omega_i}(p_i^2 + \omega_i^2 q_i^2)\right) \qquad (2.13)$$

with

$$\alpha_i(T) = \tanh\frac{\hbar\omega_i}{2k_B T}. \qquad (2.14)$$

For $T \to 0$, it follows that $\alpha_i \to 1$ and the expression reduces to the ground state of the oscillator corresponding to an average energy value of $\hbar\omega/2$. This distribution was used in the generation of initial conditions for the 4-DMABE dynamics in chapter 6. In the remaining publications another, more general distribution function was used, specifically

$$\rho_{vib}(\mathbf{q}, \mathbf{p}) = \prod_{i=1}^{N} \rho_v^{(i)}(q_i, p_i) = \prod_{i=1}^{N} |\chi_v^{(i)}(q_i)|^2 |\tilde{\chi}_v^{(i)}(p_i)|^2, \qquad (2.15)$$

where $\chi_v^{(i)}(q_i)$ and $\tilde{\chi}_v^{(i)}(p_i)$ are the harmonic oscillator wavefunctions of the normal mode ν_i in position and momentum space, respectively. Here υ is the vibrational quantum number of each normal mode, which was chosen to be 1 for specific excited vibrations and 0 otherwise in chapters 3 to 5. Hence this allows for the generation of initial conditions including vibrationally excited states. In the special case of all υ being 0, equation 2.15 reduces again to the Wigner distribution with all $\alpha_i = 1$.

Using the described Velocity-Verlet algorithm, one now propagates classical trajectories on a single electronic potential energy surface, which can be sufficient, for example if one wants to investigate ground state dynamics. However more often than not the interest lies in the transition to other electronic states, especially in the field of photochemistry. Hence it is necessary to incorporate more than a single electronic state into the theoretical description of dynamic processes.

2.1.2 Surface-hopping dynamics

Since to each adiabatic electronic state there corresponds a distinct potential energy surface, the classical nuclear dynamics is naturally strongly dependent on which electronic state is occupied and therefore what force the nuclei experience. Broadly speaking, in the field of experimental physical chemistry the fundamental investigation method of molecular systems relies on inducing state transitions through radiation. This has to be taken into account theoretically as well. One method to include multiple electronic states into the

molecular dynamics simulation is the surface-hopping methodology introduced by Tully[52]. Building upon the quantum-classical molecular dynamics discussed before, it allows for transitions between adiabatic electronic states according to the fewest-switches algorithm, which is based on the following: Considering the time-dependent electronic Schrödinger equation

$$\hat{H}_{el} \ket{\Psi} = i\hbar \frac{\mathrm{d}}{\mathrm{d}t} \ket{\Psi} \tag{2.16}$$

and with the requirement that some trajectory $\mathbf{q}(t)$ exists that describes the nuclear motion in time, an ansatz for the solution of the above equation is an expansion in terms of the eigenfunctions of the electronic Hamiltonian $\hat{H}_{el}$ along the nuclear trajectory as

$$\Psi(\mathbf{r}; \mathbf{q}(t), t) = \sum_i c_i(t) \psi_i(\mathbf{r}; \mathbf{q}(t)), \tag{2.17}$$

with the state expansion coefficients $c_i(t)$. This ansatz can be substituted into equation 2.16, yielding

$$\hat{H}_{el} \sum_i c_i \ket{\psi_i} = i\hbar \sum_i \left[\dot{c}_i \ket{\psi_i} + c_i \ket{\dot{\psi}_i} \right]. \tag{2.18}$$

From here on the Dirac notation is used in this section to facilitate readability and comprehensibility. Rearranging the result and multiplying on the left by $\bra{\psi_j}$ results in

$$i\hbar \sum_i \dot{c}_i \braket{\psi_j | \psi_i} = \sum_i c_i \left[\braket{\psi_j | \hat{H}_{el} | \psi_i} - i\hbar \braket{\psi_j | \dot{\psi}_i} \right]$$

$$\dot{c}_j = - \sum_i c_i \left[\frac{i}{\hbar} H_{ji} + D_{ji} \right], \tag{2.19}$$

so a differential equation for the electronic state coefficients. Using the chain rule, the nonadiabatic coupling terms D_{ji} can be expressed as

$$D_{ji} = \braket{\psi_j | \dot{\psi}_i} = \dot{\mathbf{q}} \cdot \braket{\psi_j | \nabla_{\mathbf{q}} \psi_i} = \dot{\mathbf{q}} \cdot \mathbf{d}_{ji}. \tag{2.20}$$

The equations derived so far all silently assumed the operator $\hat{H}_{el}$ to have adiabatic eigenstates $\ket{\psi_i}$ with discrete eigenvalues $E_{el,i}$. This implies these solutions to be the bound electronic states of the system, which is often sufficient in the study of excited state dynamics. However, since the main focus of this thesis is on electron detachment processes, the states above the detachment threshold which form a continuous spectrum,

$$\ket{\tilde{\Psi}} = \sum_n \int \mathrm{d}^3\mathbf{k} \, \tilde{c}_n(\mathbf{k}, t) \ket{\tilde{\psi}_n(\mathbf{k})}, \tag{2.21}$$

also have to be considered. As an integration variable the wave vector $\mathbf{k}$ of the unbound electron is introduced here already, since in the following chapters

these continuum states will be constructed as a combination of a free single-electron wavefunction and molecular "core systems" n (in the usual case of anions, the core systems are the neutral molecules' bound electronic states), the details of which will be explained extensively later. The individual states are chosen to satisfy

$$\hat{H}_{el} |\tilde{\psi}_n(\mathbf{k})\rangle = E_{el,n}(\mathbf{k}) |\tilde{\psi}_n(\mathbf{k})\rangle ,$$
$$\langle \tilde{\psi}_n(\mathbf{k})|\tilde{\psi}_{n'}(\mathbf{k}')\rangle = \delta_{nn'}\delta(\mathbf{k} - \mathbf{k}'), \qquad (2.22)$$

leading to the full expansion

$$|\Psi\rangle = \sum_i c_i(t) |\psi_i\rangle + \sum_n \int \mathrm{d}^3\mathbf{k}\ \tilde{c}_n(\mathbf{k}, t) |\tilde{\psi}_n(\mathbf{k})\rangle \qquad (2.23)$$

of the electronic wavefunction in the basis of the discrete and continuous adiabatic eigenstates of the electronic Hamiltonian.[2] To make the inclusion of these continuum states in the dynamics simulations computationally feasible, an approximative approach was pursued in this thesis which discretizes the $\mathbf{k}$ space according to

$$\int \mathrm{d}^3\mathbf{k}\ \tilde{c}_n(\mathbf{k}, t) |\tilde{\psi}_n(\mathbf{k})\rangle \approx \sum_l \Delta V_k\ \tilde{c}_n(\mathbf{k}_l, t) |\tilde{\psi}_n(\mathbf{k}_l)\rangle$$
$$= \sum_l \left[(\Delta V_k)^{\frac{1}{2}}\ \tilde{c}_n(\mathbf{k}_l, t) \right] \left[(\Delta V_k)^{\frac{1}{2}} |\tilde{\psi}_n(\mathbf{k}_l)\rangle \right]$$
$$= \sum_l c_n(\mathbf{k}_l, t) |\psi_n(\mathbf{k}_l)\rangle , \qquad (2.24)$$

with the approximative volume element ΔV_k. The expressions in equations 2.23 and 2.24 substituted into equation 2.16 then eventually yield the Schrödinger equation for the electronic degrees of freedom in the basis of the bound and discretized continuum states, analogous to equation 2.19.

It should be noted here that in the case of adiabatic eigenstates, the matrix $\mathbf{H}$ (comprised of the elements H_{ji} as defined in equation 2.19) is diagonal, containing the eigenenergies of the electronic states. For the most part this will not be the case in the following chapters, since for computational feasibility approximations will have to be made for the electronic discretized continuum states that result in wavefunctions which are no exact eigenfunctions of $\hat{H}_{el}$. The justification for this will be discussed in the following chapter.

When now starting a dynamics simulation in an electronic state of interest, j, one sets the expansion coefficients to $c_i(t = 0) = \delta_{ij}$ and propagates the nuclear degrees of freedom on the potential energy surface $E_{el,j}$. Alongside, one evaluates $\mathbf{c}(t + \Delta t)$ by integration of the electronic Schrödinger equation 2.19, for which the electronic wavefunctions ψ_i have to be calculated. Now knowing how to obtain the time evolution of $\mathbf{c}$, it has to be determined when and how to "hop" on another potential energy surface, i.e. switch the electronic state. This is done stochastically by calculating a hopping probability from

the presently occupied state to every other state and deciding which event occurs by generating a random number between 0 and 1 at every time step. The hopping probabilities from state i to j are obtained from electronic state populations $\rho_{ii} = |c_i|^2$ as the product of the depopulation probability of i,

$$P_{depop,i} = -\Theta(-\dot{\rho}_{ii})\frac{\dot{\rho}_{ii}}{\rho_{ii}}\Delta t, \tag{2.25}$$

and the population probability of j,

$$P_{pop,j} = \Theta(\dot{\rho}_{jj})\frac{\dot{\rho}_{jj}}{\sum_k \Theta(\dot{\rho}_{kk})\dot{\rho}_{kk}}, \tag{2.26}$$

subsequently leading to

$$P_{i \to j} = P_{depop,i}P_{pop,j} \tag{2.27}$$

$$= \Theta(-\dot{\rho}_{ii})\Theta(\dot{\rho}_{jj})\frac{-\dot{\rho}_{ii}\dot{\rho}_{jj}}{\sum_k \Theta(\dot{\rho}_{kk})\dot{\rho}_{kk}\rho_{ii}}\Delta t, \tag{2.28}$$

with the Heaviside function Θ, which is unity for positive arguments and zero otherwise. It follows that hopping probabilities are only non-zero if the state population of i is decreasing and that of j is increasing.[53] The occurring derivatives $\dot{\rho}_{ii}$ are obtained by a finite difference approximation from the populations of two subsequent time steps

$$\dot{\rho}_{ii}(t + \Delta t) \approx \frac{\rho_{ii}(t + \Delta t) - \rho_{ii}(t)}{\Delta t}. \tag{2.29}$$

In the case of a successful hopping event, the kinetic energy of the nuclei is rescaled so that the total energy of the molecular system is constant and the trajectory is then propagated in the field of the electronic state j which is now occupied.

It is noteworthy that by also explicitly including an arbitrary laser field in the electron dynamics, it is possible to simulate the complete molecular dynamics from photoexcitation to relaxation.[54] However, this was not done in the presented work and will therefore not be discussed further.

Having presented the basic concept of quantum-classical dynamics, there is a problem yet to be discussed: in Newton's equations of motion (equation 2.7) describing the nuclear trajectories in the presented surface-hopping approach, the gradient of the electronic potential energy surface of a particular electronic state is needed. Furthermore, in equation 2.19 couplings and electronic energies are required. As described before, in principle one "only" has to solve the electronic Schrödinger equation 2.3 for the adiabatic eigenstates of the molecule, from which the gradient as well as the coupling terms could be computed. However solving equation 2.3 is not possible to achieve analytically for all but the simplest of systems because of electron correlation. Hence methodologies have to be employed which permit the approximative solution to the electronic eigenstates, a few of which relevant for this thesis shall be presented in the following.

2.2   Electronic structure calculations

In this thesis, two different quantum-chemical methods were employed in the dynamics simulations, namely (time-dependent) density functional theory (TD-DFT) in chapters 3-5 and the algebraic-diagrammatic construction scheme through second order (ADC(2)) method in chapter 6. Since both these methods, the DFT approach at least in the here-employed Kohn-Sham ansatz, are based on or related to the Hartree-Fock method and a significant amount of integrals in the methodology of chapter 3 are derived from the ideas of Hartree-Fock, it is useful to give an overview over this method first.

2.2.1   The Hartree-Fock method

One of the fundamental principles of quantum mechanics is the Pauli exclusion principle, which states that two electrons in a quantum system cannot occupy the same quantum state.[55] From this it directly follows that an N-electron wavefunction $\Psi(\mathbf{x}_1, ..., \mathbf{x}_N)$ (with the electron spin coordinates $\mathbf{x}_i = (\mathbf{r}_i, \omega)$) describing a quantum-mechanical system needs to be antisymmetric with respect to interchange of electronic coordinates, i.e.

$$\Psi(\mathbf{x}_1, ..., \mathbf{x}_i, ..., \mathbf{x}_j, ..., \mathbf{x}_N) = -\Psi(\mathbf{x}_1, ..., \mathbf{x}_j, ..., \mathbf{x}_i, ..., \mathbf{x}_N). \qquad (2.30)$$

Since naturally determinants satisfy this principle, it leads to the wavefunction ansatz of so-called Slater determinants defined as

$$\Psi(\mathbf{x}) \approx \Phi(\mathbf{x}) = \frac{1}{\sqrt{N!}} \begin{vmatrix} \chi_1(\mathbf{x}_1) & \cdots & \chi_N(\mathbf{x}_1) \\ \vdots & \ddots & \vdots \\ \chi_1(\mathbf{x}_N) & \cdots & \chi_N(\mathbf{x}_N) \end{vmatrix} = |\chi_1 \chi_2 \cdots \chi_{N-1} \chi_N\rangle. \qquad (2.31)$$

The term on the right simply defines a short-hand notation. The functions $\{\chi_i\}$ are one-electron wavefunctions, also called molecular orbitals (MOs), which can be separated into spatial and spin components,

$$\chi_i(\mathbf{x}_j) = \begin{cases} \psi_i(\mathbf{r}_j)\alpha(\omega) \\ \psi_i(\mathbf{r}_j)\beta(\omega), \end{cases} \qquad (2.32)$$

and that are eigenfunctions of an electronic Hamiltonian describing a system of non-interacting electrons, i.e. with electron-electron repulsion terms neglected.[3]

There is a set of rules that arise in the mathematics involving Slater determinants, commonly referred to as the Slater-Condon rules. The first rule concerns the scalar product of two Slater determinants, showing that

$$\langle \chi_1 \chi_2 \cdots \chi_i \cdots \chi_{N-1} \chi_N | \chi_1 \chi_2 \cdots \chi_j \cdots \chi_{N-1} \chi_N \rangle = \delta_{ij}, \qquad (2.33)$$

given an orthonormal MO basis $\{\chi_i\}$, i.e. the determinants constructed from this basis are also orthonormal themselves. Moreover, since the Hamiltonian is a linear operator in that the arising terms can generally be expressed

as one-electron operators $\hat{O}_1 = \sum_i \hat{o}_1(i)$ and two-electron operators $\hat{O}_2 = \sum_i \sum_{j>i} \hat{o}_2(i,j) = \frac{1}{2} \sum_{i,j} \hat{o}_2(i,j)$ it follows that

$$\langle \Phi | \hat{O}_1 | \Phi \rangle = \langle \chi_1 ... \chi_i ... \chi_N | \hat{O}_1 | \chi_1 ... \chi_i ... \chi_N \rangle = \sum_k^N \langle \chi_k | \hat{o}_1 | \chi_k \rangle$$

$$\langle \Phi_i^r | \hat{O}_1 | \Phi \rangle = \langle \chi_1 ... \chi_r ... \chi_N | \hat{O}_1 | \chi_1 ... \chi_i ... \chi_N \rangle = \langle \chi_r | \hat{o}_1 | \chi_i \rangle$$

(2.34)

in the one-electron case. In the two-electron case it leads to

$$\langle \Phi | \hat{O}_2 | \Phi \rangle = \langle \chi_1 ... \chi_i \chi_j ... \chi_N | \hat{O}_2 | \chi_1 ... \chi_i \chi_j ... \chi_N \rangle$$
$$= \frac{1}{2} \sum_m \sum_n \langle \chi_m \chi_n | \hat{o}_2 | \chi_m \chi_n \rangle - \langle \chi_m \chi_n | \hat{o}_2 | \chi_n \chi_m \rangle$$

$$\langle \Phi_i^r | \hat{O}_2 | \Phi \rangle = \langle \chi_1 ... \chi_r \chi_j ... \chi_N | \hat{O}_2 | \chi_1 ... \chi_i \chi_j ... \chi_N \rangle$$
$$= \sum_m \langle \chi_m \chi_r | \hat{o}_2 | \chi_m \chi_i \rangle - \langle \chi_m \chi_r | \hat{o}_2 | \chi_i \chi_m \rangle$$

(2.35)

$$\langle \Phi_{ij}^{rs} | \hat{O}_2 | \Phi \rangle = \langle \chi_1 ... \chi_r \chi_s ... \chi_N | \hat{O}_2 | \chi_1 ... \chi_i \chi_j ... \chi_N \rangle$$
$$= \langle \chi_r \chi_s | \hat{o}_2 | \chi_i \chi_j \rangle - \langle \chi_r \chi_s | \hat{o}_2 | \chi_j \chi_i \rangle .$$

In the above expressions $|\Phi_i^r\rangle$ denotes a determinant where χ_i is replaced with a virtual orbital χ_r as compared to $|\Phi\rangle$. Accordingly $|\Phi_{ij}^{rs}\rangle$ differs by two orbitals χ_r and χ_s from $|\Phi\rangle$. Besides, any more differences in two Slater determinants than in the considered cases (0, 1, or 2 orbitals different) yield zero.[56]

Having established some calculation rules, the central idea of the Hartree-Fock theory is then that an optimal Slater determinant needs to be constructed, that is, the one which minimizes the eigenvalue of the time-independent Schrödinger equation 2.3, the electronic energy E, according to the variational principle. Therefore E is a functional of the molecular spin orbitals ($E = E[\{\chi_i\}]$), which are altered in the variation process, while still remaining orthonormality. In the following it is useful to divide the Hamiltonian in a part dependent on two electronic coordinates each, i.e. electron-electron repulsion, and the remaining terms only dependent on a single electron coordinate, denoted by $\hat{h}$ in the following. It then follows[3] that the optimal orbitals satisfy

$$\epsilon_i |\chi_i(\mathbf{x}_1)\rangle = \hat{f}(\mathbf{x}_1) |\chi_i(\mathbf{x}_1)\rangle = \left[\hat{h}(\mathbf{x}_1) + \sum_j \hat{J}_j(\mathbf{x}_1) - \hat{K}_j(\mathbf{x}_1) \right] |\chi_i(\mathbf{x}_1)\rangle , \quad (2.36)$$

with the one-electron operator $\hat{h} = -\frac{1}{2}\nabla_i^2 - \sum_I \frac{Z_I}{r_{iI}}$, that is, the kinetic energy and electron-nuclear interaction, and the so-called Coulomb and exchange operators $\hat{J}$ and $\hat{K}$, respectively, whose action on $|\chi_i\rangle$ is defined as

$$\hat{J}_j(\mathbf{x}_1) |\chi_i(\mathbf{x}_1)\rangle = \langle \chi_j(\mathbf{x}_2) | r_{12}^{-1} | \chi_i(\mathbf{x}_1) \chi_j(\mathbf{x}_2) \rangle_{\mathbf{x}_2} \quad (2.37)$$

$$\hat{K}_j(\mathbf{x}_1) |\chi_i(\mathbf{x}_1)\rangle = \langle \chi_j(\mathbf{x}_2) | r_{12}^{-1} | \chi_j(\mathbf{x}_1) \chi_i(\mathbf{x}_2) \rangle_{\mathbf{x}_2} . \quad (2.38)$$

Equation 2.36 is an eigenvalue equation of the Fock operator $\hat{f}(\mathbf{x}_i)$ and ϵ_i is called the orbital energy.[3] The term $\sum_j \hat{J}_j(\mathbf{x}_1) - \sum_j \hat{K}_j(\mathbf{x}_1)$ is also called the

effective Hartree-Fock potential. It treats the interaction of an electron with all other electrons in an averaged way (which is the main cause of error in comparison to the exact solution of the Schrödinger equation). The difference between the system's exact energy and the energy obtained with the Hartree-Fock ansatz is commonly referred to as the electron correlation energy, whose minimization is the goal of the so-called post-Hartree-Fock methods.[3]

The Fock operator itself is dependent on the solutions for $\{|\chi_i\rangle\}$, hence one usually calls the equation a pseudo-eigenvalue problem, which directly leads to fact that one has to find the solutions iteratively. In general one gets an infinite number of eigenfunctions $|\chi_i\rangle$ in the construction of the total wavefunction, of which one only considers a finite amount, namely the energetically lowest, occupied N.

Here it is useful to introduce a notation convention: when multiplying the two-electron terms from the left with $\langle\chi_i(\mathbf{x}_1)|$, this gives electron repulsion integrals which can be abbreviated as

$$\langle\chi_i(\mathbf{x}_1)\chi_j(\mathbf{x}_2)|r_{12}^{-1}|\chi_k(\mathbf{x}_1)\chi_l(\mathbf{x}_2)\rangle = \langle ij|kl\rangle \tag{2.39}$$

$$\langle ij|kl\rangle - \langle ij|lk\rangle = \langle ij||kl\rangle\,, \tag{2.40}$$

from which follows that the ground state energy can be written as

$$E_0 = \langle\Phi_0|\hat{H}_{el}|\Phi_0\rangle = \sum_i^N \langle i|\hat{h}|i\rangle + \frac{1}{2}\sum_i^N\sum_j^N \langle ij||ij\rangle\,. \tag{2.41}$$

Now focusing on spin, substitution of equation 2.32 into equation 2.36 and multiplication by $\langle\alpha(\omega)|$ yields

$$\langle\alpha(\omega)|\hat{f}(\mathbf{x}_1)|\alpha(\omega)\rangle\,|\phi_i(\mathbf{r}_1)\rangle = \epsilon_i\,|\phi_i(\mathbf{r}_1)\rangle$$

$$\hat{f}^\alpha(\mathbf{r}_1)\,|\phi_i(\mathbf{r}_1)\rangle = \epsilon_i\,|\phi_i(\mathbf{r}_1)\rangle\,. \tag{2.42}$$

The operator $\hat{f}^\alpha(\mathbf{r}_1)$ contains same-spin terms as well as opposite-spin Coulomb interaction:

$$\hat{f}^\alpha(\mathbf{r}_1) = \hat{h}(\mathbf{r}_1) + \sum_i^{N_\alpha}\left[J_i^\alpha(\mathbf{r}_1) - K_i^\alpha(\mathbf{r}_1)\right] + \sum_i^{N_\beta} J_i^\beta(\mathbf{r}_1). \tag{2.43}$$

Multiplying equation 2.36 with $\langle\beta|$ and subsequent evaluation yields the analogous formula for β spin.

It is not known how to solve equations 2.42 and the analogous equations for β without further assumptions or approximations. Hence introduction of a set of basis functions for which an analytical expression is known is necessary. In practice this most commonly leads to a linear expansion of the MOs into a (finite) set of well-defined atomic basis functions $|\phi_m\rangle$, so

$$|\chi_i^\alpha(\mathbf{x}_1)\rangle = |\alpha(\omega)\rangle \sum_m c_{mi}^\alpha\,|\phi_m(\mathbf{r}_1)\rangle\,, \tag{2.44}$$

$$|\chi_i^\beta(\mathbf{x}_1)\rangle = |\beta(\omega)\rangle \sum_m c_{mi}^\beta\,|\phi_m(\mathbf{r}_1)\rangle\,. \tag{2.45}$$

For α orbitals, substitution of equation 2.44 in equation 2.42 and multiplication with $\langle\phi_n|$ from the left results in

$$\sum_m c_{mi}^\alpha \langle\phi_n(\mathbf{r}_1)|\hat{f}^\alpha(\mathbf{r}_1)|\phi_m(\mathbf{r}_1)\rangle = \epsilon_i^\alpha \sum_m c_{mi}^\alpha \langle\phi_n(\mathbf{r}_1)|\phi_m(\mathbf{r}_1)\rangle$$

$$\sum_m F_{nm}^\alpha c_{mi}^\alpha = \epsilon_i^\alpha \sum_m S_{nm} c_{mi}^\alpha. \tag{2.46}$$

This can also be expressed in matrix form and, together with the analogous formula for β spin, yields the Pople-Nesbet equations[3]

$$\mathbf{F}^\alpha \mathbf{C}^\alpha = \mathbf{S}\mathbf{C}^\alpha \boldsymbol{\epsilon}^\alpha$$
$$\mathbf{F}^\beta \mathbf{C}^\beta = \mathbf{S}\mathbf{C}^\beta \boldsymbol{\epsilon}^\beta. \tag{2.47}$$

Here $\mathbf{F}$ denotes the Fock matrix and $\mathbf{S}$ the overlap matrix between the AO basis functions. A special case, called restricted Hartree-Fock, arises for $\langle\alpha|\chi_i^\alpha\rangle = \langle\beta|\chi_i^\beta\rangle$ and typically occurs for closed-shell systems, where pairs of α and β electrons populate the spatial MOs. Thereby equations 2.47 reduce to the Roothaan-Hall equations for the $N/2$ spatial orbitals. This is the assumed case in the remainder of this chapter.

As implied before, it is possible to construct determinants consisting of others than the energetically lowest N spin orbitals, which are normally denoted with respect to the ground state determinant, e.g. $|\Phi_i^r\rangle$ is called singly-excited, $|\Phi_{ij}^{rs}\rangle$ is called doubly-excited, and so on. Since all spin-orbitals are eigenfunctions of the Fock operator, so are all Slater determinants constructed from them. An important note for the methodology in upcoming chapters is the fact that a singly-excited determinant generated in this way is not an eigenfunction of $\hat{S}^2$, i.e. this does not result in a spin eigenstate. However a singlet eigenstate for example can be constructed from this determinant via symmetry-adapted linear combination with the corresponding determinant of opposite spin MOs:

$$|^1\Phi_i^r\rangle = \frac{1}{\sqrt{2}}\Big(|\chi_1^2\chi_2^2\cdots\chi_i^\alpha\chi_r^\beta\rangle + |\chi_1^2\chi_2^2\cdots\chi_i^\beta\chi_r^\alpha\rangle\Big) = \frac{1}{\sqrt{2}}\Big(|\Phi_i^r\rangle + |\overline{\Phi_i^r}\rangle\Big), \quad (2.48)$$

the result being called the configuration state function (CSF).[57] Although not particularly relevant in the context of ground state Hartree-Fock, excited determinants are important in the construction of post-Hartree-Fock methods such as configuration interaction (CI) based approaches, coupled cluster theory, Møller-Plesset perturbation theory and excited-state methods and should therefore be kept in mind in the following.

In solving the Hartree-Fock equations, only an approximative solution $|\Phi_0\rangle$ for the ground state electronic wavefunction can be found. On the other hand, $|\Phi_0\rangle$ is an exact solution to the Hartree-Fock Hamiltonian[3]:

$$\langle\Phi_0|\hat{H}_0|\Phi_0\rangle = \langle\Phi_0|\sum_i^N \hat{f}(\mathbf{x}_i)|\Phi_0\rangle = \sum_i^N \epsilon_i = E_0^{(0)}. \tag{2.49}$$

Note here that $E_0^{(0)} \neq E_0$, i.e. the sum of orbital energies ϵ_i, is not the Hartree-Fock ground state energy. Rather, the eigenvalue of the Hartree-Fock Hamiltonian, $E_0^{(0)}$, can be interpreted as the zeroth order energy of an unperturbed Hamiltonian $\hat{H}_0$ as a starting point in the post-Hartree-Fock method called Møller-Plesset perturbation theory, which is described in the following.

2.2.2   Møller-Plesset perturbation theory

The general problem of quantum chemistry, again, is that no exact solutions $|\Psi_i\rangle$ to the Schrödinger equation can be found. However, in the last paragraph it was shown that exact solutions $|\Phi_i\rangle$ can be found for an approximative Hartree-Fock Hamiltonian $\hat{H}_0$. If one is now to construct the exact electronic Hamiltonian as the sum of this approximative ansatz (the unperturbed system represented by $\hat{H}_0$) and a correction term, called the perturbation $\hat{V}$,

$$\hat{H}_{el} = \hat{H}_0 + \hat{V}, \tag{2.50}$$

it follows that

$$\hat{V} = \sum_i \sum_{j>i} \frac{1}{r_{ij}} - \sum_i \sum_j \hat{J}_{ij} - \hat{K}_{ij} \tag{2.51}$$

is the discrepancy between the exact and Hartree-Fock Hamiltonian, so the difference between exact electron-electron interaction and the effective Hartree-Fock potential.[3] To connect the unperturbed and perturbed system, a parameter λ is introduced,

$$\hat{H}_{el} = \hat{H}_0 + \lambda\hat{V}, \tag{2.52}$$

so that $\lambda = 0$ results in the Hartree-Fock case and $\lambda = 1$ in the exact Hamiltonian, now causing $\hat{H}_{el}$ and therefore $|\Psi_i\rangle$ and $E_{el,i}$ to depend on λ. One could assume that if the perturbation is small, the eigenfunctions of $\hat{H}_0$ are reasonable approximations to the eigenfunctions of $\hat{H}_{el}$, $|\Psi_i\rangle$, that reproduce the exact eigenvalues $E_{el,i}$ reasonably well. In this case it is possible to expand the eigenfunctions and eigenvalues of $\hat{H}_{el}$ around $\lambda = 0$ in a power series as

$$|\Psi_i\rangle = |\Psi_i\rangle\big|_{\lambda=0} + \frac{\partial|\Psi_i\rangle}{\partial\lambda}\bigg|_{\lambda=0}\lambda + \frac{\partial^2|\Psi_i\rangle}{\partial\lambda^2}\bigg|_{\lambda=0}\frac{\lambda^2}{2!} + ...$$
$$= |\Phi_i^{(0)}\rangle + \lambda|\Phi_i^{(1)}\rangle + \lambda^2|\Phi_i^{(2)}\rangle + ... \tag{2.53}$$
$$E_{el,i} = E_{el,i}\big|_{\lambda=0} + \frac{\partial E_{el,i}}{\partial\lambda}\bigg|_{\lambda=0}\lambda + \frac{\partial^2 E_{el,i}}{\partial\lambda^2}\bigg|_{\lambda=0}\frac{\lambda^2}{2!} + ...$$
$$= E_i^{(0)} + \lambda E_i^{(1)} + \lambda^2 E_i^{(2)} + ... \;. \tag{2.54}$$

The superscript numbers in brackets denote the orders in λ, zeroth order being the Hartree-Fock solutions. Since the resulting higher-order terms are not known, the central idea is to express those terms in quantities that can be evaluated through Hartree-Fock. If the eigenfunction of H_{el} is chosen to be normalized with respect to the Hartree-Fock wavefunction, so $\langle\Psi_i|\Phi_i^{(0)}\rangle = 1$,

called intermediate normalization, it immediately follows that all higher order wavefunctions in equation 2.53 are orthogonal to $|\Phi_i^{(0)}\rangle$.[57]

By inserting equations 2.52, 2.53 and 2.54 into the electronic Schrödinger equation 2.3, one is able to separate the result by orders of λ. Multiplying each equation from the left with $\langle\Phi_j^{(0)}|$ and using $\langle\Phi_j^{(0)}|\Phi_i^{(0)}\rangle = \delta_{ji}$ then yields in particular for the terms up to second order:

$$\langle\Phi_j^{(0)}|\hat{H}_0|\Phi_i^{(0)}\rangle = E_i^{(0)}\delta_{ji} \tag{2.55}$$

$$\langle\Phi_j^{(0)}|\hat{V}|\Phi_i^{(0)}\rangle = E_i^{(1)}\delta_{ji} + (E_i^{(0)} - E_j^{(0)})\langle\Phi_j^{(0)}|\Phi_i^{(1)}\rangle \tag{2.56}$$

$$\langle\Phi_j^{(0)}|\hat{V}|\Phi_i^{(1)}\rangle = E_i^{(2)}\delta_{ji} + E_i^{(1)}\langle\Phi_j^{(0)}|\Phi_i^{(1)}\rangle + $$
$$(E_i^{(0)} - E_j^{(0)})\langle\Phi_j^{(0)}|\Phi_i^{(2)}\rangle. \tag{2.57}$$

For $j = i$, this results in the n'th order energies

$$E_i^{(0)} = \langle\Phi_i^{(0)}|\hat{H}_0|\Phi_i^{(0)}\rangle \tag{2.58}$$

$$E_i^{(1)} = \langle\Phi_i^{(0)}|\hat{V}|\Phi_i^{(0)}\rangle \tag{2.59}$$

$$E_i^{(2)} = \langle\Phi_i^{(0)}|\hat{V}|\Phi_i^{(1)}\rangle. \tag{2.60}$$

Remembering Hartree-Fock theory, the zeroth order energy is just the sum of the occupied orbital energies, while including the first order yields the electronic energy of the Slater determinant, showing that the first contribution beyond Hartree-Fock is the second order energy term.

The n'th order wavefunctions can be derived from equations 2.55 to 2.57 (and the following orders), if one considers that the eigenfunctions of $\hat{H}_0$ form a complete basis into which the higher order wavefunctions can be expanded:

$$|\Phi_i^{(n)}\rangle = \sum_j a_{ij}^{(n)} |\Phi_j^{(0)}\rangle \text{ with } a_{ij}^{(n)} = \langle\Phi_j^{(0)}|\Phi_i^{(n)}\rangle. \tag{2.61}$$

For the first order, using equation 2.56, it follows that

$$a_{ij}^{(1)} = \frac{\langle\Phi_j^{(0)}|\hat{V}|\Phi_i^{(0)}\rangle}{E_i^{(0)} - E_j^{(0)}} \tag{2.62}$$

for the expansion coefficients, allowing one to construct $|\Phi_i^{(1)}\rangle$, with which one is able to compute the energy up to second order. For every order n, the corresponding energy $E_i^{(n)}$ can be evaluated analogously from a lower-order wavefunction, which in turn can always be expanded into the eigenfunctions of the Hartree-Fock Hamiltonian.[3]

One variant of the second-order Møller-Plesset perturbation theory (MP2), which is the only order actually employed in this thesis, that is commonly used, is the spin-component scaled MP2 (SCS-MP2) method. Considering the Slater-Condon rules and Brillouin's theorem[58] (which states that matrix elements of the electronic Hamiltonian between a ground and singly-excited Slater determinant is zero, i.e. $\langle\Phi|\hat{H}_{el}|\Phi_i^r\rangle = 0$), the only non-zero coefficients

for the construction of the MP2 wavefunction in equation 2.62 are between the Hartree-Fock ground state and doubly-excited determinants. In general the one-particle basis set correlation energy, i.e. the difference between exact electronic and Hartree-Fock energy ($E_c = E_{\text{exact}}$ - E_{HF}), can therefore be expressed by expansion into the doubly-excited determinants and moreover, separated into parallel ('triplet') and antiparallel ('singlet') spin components, i.e. $E_c = E_S + E_T$ with

$$
\begin{aligned}
E_S &= \sum_{a\bar{b}r\bar{s}} a_{a\bar{b}}^{r\bar{s}} \langle a\bar{b}|r\bar{s}\rangle \\
E_T &= \frac{1}{2}\left[\sum_{abrs}(a_{ab}^{rs} - a_{ab}^{sr}) \langle ab|rs\rangle + \sum_{\bar{a}\bar{b}\bar{r}\bar{s}}(a_{\bar{a}\bar{b}}^{\bar{r}\bar{s}} - a_{\bar{a}\bar{b}}^{\bar{s}\bar{r}}) \langle \bar{a}\bar{b}|\bar{r}\bar{s}\rangle \right],
\end{aligned}
\tag{2.63}
$$

where a missing bar over AO indices denotes α spin and barred indices β spin.[59] Within MP2 the coefficients a are simply the ones derived in equation 2.62, since in this case $\langle\Phi_j^{(0)}|$ are the doubly-excited Slater determinants and therefore

$$
a_{ij}^{(1)} = a_{ab}^{rs} = \frac{\langle ab|rs\rangle}{\epsilon_a + \epsilon_b - \epsilon_r - \epsilon_s}.
\tag{2.64}
$$

In the SCS-MP2 variant, the singlet and triplet energy components are now scaled separately using semi-empirical factors, so that

$$
E_c \approx E_{c,\text{SCS-MP2}} = p_S E_S + p_T E_T
\tag{2.65}
$$

with $p_S = 6/5$ and $p_T = 1/3$.[59] Another variant of this approach is the so called spin-opposite scaled MP2 (SOS-MP2), where $p_S = 1.3$ and $p_T = 0.0$, so complete neglect of parallel-spin integrals for improved computational performance at a small cost of chemical accuracy compared to SCS-MP2.[60] These scaled MP2 methods can be justified qualitatively as follows: In reality, Coulomb interaction always leads to the repulsion of two electrons irrespective of spin, i.e. the probabilities of finding electron one in a volume element $d\mathbf{x}_1$ and electron two in $d\mathbf{x}_2$ are not independent of one another. This is not the case in the Hartree-Fock wavefunction for electrons in opposite-spin MOs, which are therefore uncorrelated at this level of theory.[3] For same-spin MOs the exchange term leads to mutually dependent spatial probabilities, yielding the so-called Fermi hole, where the probability of finding two electrons at the same point in space is zero. The unbalanced description of same- and opposite-spin electron correlation in the Hartree-Fock wavefunction, which is in turn carried over to MP2, is now aimed to be reduced by semi-empirically weighting the respective two-electron integrals in the aforementioned way.[61]

Since a strong focus of this thesis lies on photodynamic processes, electronically excited states need to be considered in the theoretical approaches. Based on Møller-Plesset perturbation theory, there exists an excited-state approach called the algebraic-diagrammatic construction method, which was utilized in chapter 6 and therefore will be presented in the following paragraph.

2.2.3 The algebraic-diagrammatic construction method

The method known as the algebraic diagrammatic construction scheme of n'th order (ADC(n)) is an excited-states method based on Møller-Plesset perturbation theory and was originally derived from many-body Green's functions / propagators in the frame of diagrammatic perturbation theory.[62] Fourier transformation of the polarization propagator leads to its spectral representation, in which excitation energies were found as poles. Transition moments were accessible using this approach as well.[62] However, since no discrete expression of excited state wavefunctions was yielded, most excited state properties could not be evaluated. In recent years another derivation of the methodology arose, called the intermediate state representation (ISR)[63], which overcomes these limitations. It is the default implementation in commercial quantum chemistry program packages and shall therefore be presented here.

Beginning from the electronic Schrödinger equation for an excited state $|\Psi_n\rangle$ and denoting its excitation energy from the electronic ground state as $\omega_n = E_n - E_0$, the following equation holds:

$$(\hat{H}_{el} - E_0)\,|\Psi_n\rangle = \omega_n\,|\Psi_n\rangle. \tag{2.66}$$

The total electronic wavefunctions of the excited states are normally not known, so, as already mentioned in the past paragraphs, they can be written as a linear combination of a complete set of orthonormal basis functions in the respective Hilbert space which are more accessible either computationally or analytically,

$$|\Psi_n\rangle = \sum_i y_{ni}\,|\tilde{\psi}_i\rangle, \tag{2.67}$$

where $|\tilde{\psi}_i\rangle$ are called the intermediate states. One should note that in general these need not be eigenstates of the electronic Hamiltonian. This results in a Hermitian matrix representation of the electronic Hamiltonian,

$$\tilde{H}_{ij} = \langle\tilde{\psi}_i|\hat{H}|\tilde{\psi}_j\rangle, \tag{2.68}$$

which leads to the eigenvalue equation

$$(\tilde{\mathbf{H}} - E_0\mathbb{1})\mathbf{Y} = \mathbf{Y}\boldsymbol{\Omega}$$
$$\mathbf{MY} = \mathbf{Y}\boldsymbol{\Omega}, \ \mathbf{Y}^\dagger\mathbf{Y} = \mathbb{1}, \tag{2.69}$$

with the diagonal matrix $\boldsymbol{\Omega}$ containing the excitation energies $\omega_n = E_n - E_0$ and the matrix of eigenvectors $\mathbf{Y}$ in the basis of the intermediate states.[56]

The intermediate states can be generated through a set of excitation operators

$$\{\hat{C}_i\} = \{\hat{c}_a^\dagger\hat{c}_r, \hat{c}_a^\dagger\hat{c}_b^\dagger\hat{c}_r\hat{c}_s, ...\}, \tag{2.70}$$

as a combination of annihilation and creation operators as defined in the realm of second quantization, so accordingly the first given terms correspond to single excitations of a state from orbital a to r, the second term to double excitation

from a, b to r, s, and so on. In direct analogy to the CI expansion in the case of a ground state Hartree-Fock wavefunction (although in the CI case orthogonal), action of these operators on the MPn ground state wavefunction then yields the non-orthogonal, so-called correlated excited states

$$|\psi_i^0\rangle = \hat{C}_i \,|\Psi_0\rangle \,, \tag{2.71}$$

from which subsequently the intermediate states are constructed using Gram-Schmidt orthogonalization.[64] The matrix $\mathbf{M}$, which also needs to be expanded in perturbation orders analogously to the ground state wavefunction and energy,

$$\mathbf{M} = \mathbf{M}^{(0)} + \mathbf{M}^{(1)} + \mathbf{M}^{(2)} + ... \,, \tag{2.72}$$

can then be evaluated and solution of equation 2.69 thus yields the excitation energies $\mathbf{\Omega}$.

Moreover, one is often also interested in transition moments, which are given by

$$\mathbf{t}_n = \langle \Psi_n | \hat{D} | \Psi_0 \rangle \,, \tag{2.73}$$

with the operator $\hat{D}$ representing the quantity of interest (usually the dipole operator, thus yielding transition dipole moments). Now, since explicit expressions for excited state wavefunctions are available, transition moments can be calculated with eigenvectors $\mathbf{y}_n$ of $\mathbf{Y}$

$$\mathbf{t}_{nm} = \langle \Psi_n | \hat{D} | \Psi_m \rangle = \sum_i \sum_j y_{ni} y_{mj} \langle \tilde{\psi}_i | \hat{D} | \tilde{\psi}_j \rangle \,, \tag{2.74}$$

or in matrix notation

$$\mathbf{T} = \mathbf{Y}^\dagger \tilde{\mathbf{F}} \mathbf{Y}, \tag{2.75}$$

with $\mathbf{F}$ denoting the matrix of transition moments between all intermediate states (and the ground state). In the case of the dipole operator for example, one can directly calculate the transition dipole moments (for $n \neq m$) and the static dipole moments of all states (for $n = m$). Moreover, if in equation 2.70 the operators are considered to act on spin orbitals and the reference wavefunction $|\Psi_0\rangle$ is an unrestricted MPn ground state, this directly yields unrestricted ADC(n) equations.[65]

In the description of the 4-(dimethylamino)benzethyne molecule presented in chapter 6 the ADC(2) method, which is obtained by using the MP2 ground state wavefunction as $|\Psi_0\rangle$ in equation 2.71, was used in its SCS variant. This is obtained by replacement of the first-order amplitudes in the construction of the ground state MP2 wavefunction with SCS-MP2 analogues derived from the spin-component scaled approach (cf. equations 2.62 and 2.65),[66] or alternatively in analogy to SCS-CC2 as developed by Hättig *et al.*[67]

2.2.4   Density-functional theory

Most modern quantum-chemical methods have their roots in the Hartree-Fock approach. The main issue with this is that to describe the electronic system

completely, the electronic wavefunction is dependent on $3N$ spatial and N spin coordinates, i.e. $|\Psi\rangle = |\Psi(\mathbf{x}_1, \mathbf{x}_2, ... \mathbf{x}_N)\rangle\rangle$, which makes even approximative solutions computationally expensive. However, there is another ansatz that does not, or at least did not in the beginning, use wavefunctions as the fundamental quantity. Since its foundation is the electron density of a system, it is called density functional theory (DFT).

Ground state density functional theory

The electron density of a system is given by[68]

$$\rho(\mathbf{r}) = N \int ... \int d\omega\, d\mathbf{x}_2\, d\mathbf{x}_3... d\mathbf{x}_N |\Psi(\mathbf{x}, \mathbf{x}_2, \mathbf{x}_3, ..., \mathbf{x}_N)|^2. \qquad (2.76)$$

To understand how this expression is useful in the description of a molecular system, one has to start again from the electronic Schrödinger equation 2.3, but inserting an arbitrary trial wavefunction $|\Psi_{trial}\rangle$. Multiplication with $\langle\Psi_{trial}|$ from the left results in

$$E_{el} = \frac{\langle\Psi_{trial}|\hat{H}_{el}|\Psi_{trial}\rangle}{\langle\Psi_{trial}|\Psi_{trial}\rangle}, \qquad (2.77)$$

showing that $E_{el} = E_{el}[\Psi_{trial}]$, so the energy is a functional of the wavefunction. If $|\Psi_{trial}\rangle$ is expanded into the orthonormal eigenstates of $\hat{H}_{el}$ (see equation 2.4), the above equation yields

$$E_{el}[\Psi_{trial}(\mathbf{q})] = \frac{\sum_i |\chi_i(\mathbf{q})|^2 E_{el,i}(\mathbf{q})}{\sum_i |\chi_i(\mathbf{q})|^2}, \qquad (2.78)$$

which directly suggests that there is a lower boundary for the energy of this system ($E_{el}[\Psi_{trial}] \geq E_{el,0}$).[68] When considering equation 2.2, it is also evident that if the number of electrons N is given, the electronic Hamiltonian, excluding nuclear-nuclear repulsion, is universally defined by N for arbitrary molecular systems. One can therefore also conclude that the energy is a functional of the number of electrons and the electron-nuclear repulsion ($E = E[N, V_{ne}]$), which is why the latter is commonly referred to as the external potential $v(\mathbf{r}_i)$ in DFT.[68]

In 1964 Hohenberg and Kohn[69] were able to prove that the ground state electron density in fact uniquely defines the number of electrons and, apart from an additive constant, the external potential, which in turn define the energy and the wavefunction of the system. Moreover they were able to show that there exists a unique ground state density corresponding to the ground state wavefunction, which therefore minimizes the electronic energy of the system. These two principles form the so-called Hohenberg-Kohn theorem. They theoretically reduced the problem of finding a $4N$-parameter wavefunction to a quantity only dependent on three spatial coordinates, although it is not known how to construct either an electron density without knowledge of a wavefunction first, nor is it known how the energy is calculated from the electron density.[57]

To solve the issue, Kohn and Sham[70] proposed the ansatz to equate the real ground state electron density of a molecule, ρ_0, to that of a fictitious one ρ_s for a system of non-interacting electrons moving in an external potential $v_s(\mathbf{r})$, thereby choosing $v_s(\mathbf{r})$ in a way that $\rho_0 = \rho_s$ (also all quantities relating to the non-interacting system are denoted with a subscript s in the following). In the non-interacting case, the Hamiltonian is a linear operator comprised of a sum of the one-electron Kohn-Sham Hamiltonians

$$\hat{H}_s = \sum_i^N \left[-\frac{1}{2}\nabla_i^2 + v_s(\mathbf{r}_i) \right] = \sum_i^N \hat{h}_i^{KS}. \tag{2.79}$$

Analogous to the one-electron Fock operator in Hartree-Fock theory, eigenfunctions to the one-electron operators $\hat{h}_i^{KS}$ are Slater determinants of the so-called Kohn-Sham spin orbitals $\chi_i^{KS}(\mathbf{x}_j) = \sigma(\omega_j)\psi_i^{KS}(\mathbf{r}_j)$ so that

$$\hat{h}_1^{KS}\psi_i(\mathbf{r}_1) = \epsilon_i\psi_i(\mathbf{r}_1), \tag{2.80}$$

which are again constructed to be orthonormal. It then follows that the electron probability density of such a Slater determinant is

$$\rho_s = \rho_0 = \sum_i^N |\psi_i^{KS}|^2. \tag{2.81}$$

One solves for the Kohn-Sham MOs using the variational principle, but since the electron density is directly dependent on the MOs through equation 2.81, one can vary the orbitals directly instead with the restriction of orthonormality. It can be shown that the respective Kohn-Sham MOs need to satisfy the so-called Kohn-Sham equation

$$\left[-\frac{1}{2}\nabla_{\mathbf{r}_1}^2 - \sum_I \frac{Z_I}{r_{1I}} + \int d\mathbf{r}_2 \frac{\rho(\mathbf{r}_2)}{r_{12}} + \frac{\delta E_{xc}[\rho(\mathbf{r}_1)]}{\delta\rho(\mathbf{r}_1)} \right] \psi_i^{KS}(\mathbf{r}_1) = \epsilon_i^{KS}\psi_i^{KS}(\mathbf{r}_1), \tag{2.82}$$

which by comparison with equations 2.79 and 2.80 in turn also gives a definition for v_s and $\hat{h}_i^{KS}$, respectively.[68] In the last term of the operator one finds the so-called exchange-correlation functional

$$\begin{aligned} E_{xc}[\rho] &= \Delta T[\rho] + \Delta V_{ee}[\rho] \\ &= T[\rho] - T_s[\rho] + V_{ee}[\rho] - \frac{1}{2}\iint d\mathbf{r}_1\,d\mathbf{r}_2 \frac{\rho(\mathbf{r}_1)\rho(\mathbf{r}_2)}{r_{12}}, \end{aligned} \tag{2.83}$$

which contains the differences in the electronic kinetic energy and electron-electron interaction terms between the interacting and non-interacting system. Furthermore, comparison with the Hartree-Fock equation 2.36 shows the direct analogy between the Fock and Kohn-Sham operators, with the difference that the exchange term in Hartree-Fock is replaced with the potential $v_{xc} = \frac{\delta E_{xc}[\rho(\mathbf{r}_1)]}{\delta\rho(\mathbf{r}_1)}$ including exchange and electron correlation treatment.[68]

Subsequently one then finds for the total energy functional that

$$E_0[\rho_0] = T_s[\rho_0] + \int d\mathbf{r}\rho_0(\mathbf{r})v(\mathbf{r}) + \iint d\mathbf{r}_1\,d\mathbf{r}_2 \frac{1}{2}\frac{\rho_0(\mathbf{r}_1)\rho_0(\mathbf{r}_2)}{r_{12}} + E_{xc}[\rho_0]$$

$$= -\frac{1}{2}\sum_i^N \langle\psi_i^{KS}|\nabla^2_{\mathbf{r}_1}|\psi_i^{KS}\rangle - \sum_I Z_I\int d\mathbf{r}_1\frac{\rho_0(\mathbf{r}_1)}{r_{1I}}$$

$$+ \frac{1}{2}\iint d\mathbf{r}_1\,d\mathbf{r}_2\frac{\rho_0(\mathbf{r}_1)\rho_0(\mathbf{r}_2)}{r_{12}} + E_{xc}[\rho_0], \tag{2.84}$$

meaning that the energy of the real molecular system can be expressed as a sum of the non-interacting system's energy and the difference between the two, contained within the exchange-correlation functional, the only quantity in equation 2.84 that is not known.[57] Its approximation is the key of modern DFT method development and since there is no way to analytically derive expressions for the mathematical form of E_{xc}, DFT is not systematically improvable in the sense of CI or perturbation theory. However there are different methods of obtaining exchange correlation functionals, namely the local-density approximation (LDA) suggested by Kohn and Sham[70], which assumes slowly varying electron densities with respect to $\mathbf{r}$ (which, when considering open-shell systems, can be expanded to the local-spin-density approximation (LSDA)), generalized gradient approximations (GGA) which also includes the density gradients (and second derivatives for meta-GGA) to allow for greater variations in electron density, and so-called hybrid functionals, which are a combination of GGA and Hartree-Fock exchange terms.[57] The latter, including for example (CAM)-B3LYP, ωB97XD and PBE0, are arguably the most widely used functionals in modern quantum chemistry.

DFT calculations are carried out in a similar fashion to Hartree-Fock calculations in that one first guesses an electron density, from which the exchange-correlation potential is calculated in some way. One then solves equation 2.82 for the Kohn-Sham MOs, which yields a new electron density with equation 2.81, i.e. the DFT method is iterative. The Kohn-Sham orbitals are again built as linear combinations of (atomic orbital) basis sets, a discussion of which will be given more in depth in subsection 2.3.4.

Here it also has to be noted that although the Kohn-Sham orbitals are technically just arbitrary functions whose sole purpose is to construct a Slater determinant of a fictitious, non-interacting system, they are still successfully used in the discussion of molecular properties, since in reality they are usually reasonably close to the molecular orbitals in Hartree-Fock theory.[57] Some literature even suggests that Hartree-Fock orbitals, which are technically also unphysical since they represent eigenfunctions of a system of electrons in potentials of averaged electron-electron interaction far away from reality, are less suited for qualitative analysis of properties than their Kohn-Sham analogs.[71,72]

Density-functional theory for excited states

Up to this point, the formulation of DFT only concerns the ground state of a molecular system. However in photochemistry electronically excited states obviously play a fundamental role, be it in dyes, fluorescence phenomena, charge-transfer processes, etc. Naturally, the theoretical descriptions in DFT also need to be extended to account for electronic excitation, resulting in a method known as time-dependent density functional theory (TD-DFT).

The basis of all types of TD-DFT formulations is rooted in the work of Runge and Gross[73], who, in an analogous fashion to Hohenberg and Kohn, were able to prove that in a system obeying the time-dependent Schrödinger equation, the time-dependent electron density $\rho(\mathbf{r}, t)$ and the initial wavefunction $\Psi(t_0)$ fully determine the external potential and therefore the time evolution of the system up to an additive function of time. Furthermore they again introduced a Kohn-Sham formulation, that is, a Slater determinant ansatz of MOs in a non-interacting electron system producing the same electron density as the interacting system, which is calculated according to equation 2.81.

The starting point is the time-dependent Schrödinger equation with a Hamiltonian comprised of a time-independent part as known from ground state DFT, $\hat{H}_0(\mathbf{r})$, and a time-dependent perturbation, $\hat{V}(\mathbf{r}, t) = \sum_i^N v(\mathbf{r}_i, t)$, yielding in total $\hat{H}(\mathbf{r}, t) = \hat{H}_0(\mathbf{r}) + \hat{V}(\mathbf{r}, t)$. It can be shown that from a time-dependent analogue to the variational principle the time-dependent Kohn-Sham equations for the MOs of the non-interacting system can be derived, which read

$$i\frac{\partial}{\partial t}\psi_i^{KS}(\mathbf{r}, t) = \hat{h}^{KS}(\mathbf{r}, t)\psi_i^{KS}(\mathbf{r}, t), \tag{2.85}$$

with

$$\hat{h}^{KS}(\mathbf{r}, t) = -\frac{1}{2}\nabla_{\mathbf{r}}^2 + v(\mathbf{r}, t) + \int \mathrm{d}\mathbf{r}' \frac{\rho(\mathbf{r}', t)}{|\mathbf{r} - \mathbf{r}'|} + \frac{\delta A_{xc}}{\delta\rho(\mathbf{r}, t)}. \tag{2.86}$$

Here, the action integral in the frame of the Kohn-Sham formalism,

$$\begin{aligned} A[\rho] &= \int_{t_0}^{t_1} \mathrm{d}t \left\langle \Psi[\rho](\mathbf{r}, t) \left| i\frac{\partial}{\partial t} - \hat{H}(\mathbf{r}, t) \right| \Psi[\rho](\mathbf{r}, t) \right\rangle \\ &= \int_{t_0}^{t_1} \mathrm{d}t \left\langle \Psi[\rho](\mathbf{r}, t) \left| i\frac{\partial}{\partial t} - \hat{T}(\mathbf{r}, t) \right| \Psi[\rho](\mathbf{r}, t) \right\rangle - A_{xc}[\rho] \\ &\quad - \int_{t_0}^{t_1} \int \mathrm{d}\mathbf{r}\,\mathrm{d}t\rho(\mathbf{r}, t)v(\mathbf{r}, t) - \frac{1}{2}\int_{t_0}^{t_1} \iint \mathrm{d}\mathbf{r}\,\mathrm{d}\mathbf{r}'\,\mathrm{d}t\frac{\rho(\mathbf{r}, t)\rho(\mathbf{r}', t)}{|\mathbf{r} - \mathbf{r}'|}, \end{aligned} \tag{2.87}$$

is introduced, of which the functional derivative of the so-called exchange-correlation part with respect to the electron density, A_{xc}, is needed.[4] Analogous to E_{xc} in ground state DFT, A_{xc} contains all terms that are not known and has to be approximated, with the difference that A_{xc} is now time-dependent. Runge and Gross first suggested a local approximation in time called the adiabatic approximation of TD-DFT,[73] which is now widely in use and enables the use of the standard ground state DFT functionals for A_{xc}.

Assuming the perturbations $v(\mathbf{r}, t)$ to be weak, the orbitals will change only slightly with time. Therefore usually only first-order terms of time-dependent perturbation theory are considered, leading subsequently to the Casida equations[74], a non-hermitian eigenvalue problem yielding the excitation energies and transition amplitudes as eigenvalues and eigenvectors:

$$
\begin{bmatrix} \mathbf{A} & \mathbf{B} \\ \mathbf{B}^* & \mathbf{A}^* \end{bmatrix} \begin{bmatrix} \mathbf{X} \\ \mathbf{Y} \end{bmatrix} = \omega \begin{bmatrix} 1 & 0 \\ 0 & -1 \end{bmatrix} \begin{bmatrix} \mathbf{X} \\ \mathbf{Y} \end{bmatrix} \tag{2.88}
$$

in the Kohn-Sham molecular orbital basis with the matrices

$$
A_{ia,jb} = \delta_{ij}\delta_{ab}(\epsilon_a - \epsilon_i) + \langle ij|ab\rangle + \langle ij|f_{xc}|ab\rangle \tag{2.89}
$$
$$
B_{ia,jb} = \langle ib|aj\rangle + \langle ib|f_{xc}|aj\rangle . \tag{2.90}
$$

This approximative approach is called linear-response TD-DFT.[4] In the adiabatic approximation, the operator f_{xc} in the last term in equations 2.89 and 2.90 is given as the second functional derivative of the exchange-correlation energy (cf. equation 2.83), so

$$
\langle ij|f_{xc}|ab\rangle = \iint \mathrm{d}\mathbf{r}\,\mathrm{d}\mathbf{r}'\psi_i^*(\mathbf{r})\psi_j^*(\mathbf{r}')\frac{\delta^2 E_{xc}}{\delta\rho(\mathbf{r})\delta\rho(\mathbf{r}')}\psi_a(\mathbf{r})\psi_b(\mathbf{r}'). \tag{2.91}
$$

It can be noted here that replacing the Kohn-Sham orbitals in this formalism with Hartree-Fock orbitals and replacing the term in equation 2.91 with the Hartree-Fock exchange terms directly yields the working equations of time-dependent Hartree-Fock theory (analogous to equation 2.88). Since the elements of $\mathbf{B}$ are usually small, a widely used approximation is to set $\mathbf{B} = 0$, the so-called Tamm-Dancoff approximation, in which case the left matrix in equation 2.88 becomes block-diagonal.[75] In the corresponding case in TD-HF this approach is called configuration interaction with singles (CIS).

2.2.5 Scattering theory

An electron detachment process generally results in an ejected electron and a molecule with an $N - 1$ electron system. In the paragraphs before, various quantum-chemical methods were presented for the characterization of bound molecular systems, but since the main focus of this thesis is on detachment phenomena, it is necessary to consider both products of the process, i.e. also the description of the ejected electron. From an electron's perspective, detachment can be viewed as a scattering process on a potential created by the molecule core that it is leaving behind.

In a sense, the easiest example of electron scattering is the case of an electron free of any interaction, that is, an unscattered electron with a wavefunction that satisfies a special case of the time-independent Schrödinger equation 2.3, the Helmholtz equation

$$
\nabla_i^2 |\psi\rangle = -k^2 |\psi\rangle . \tag{2.92}
$$

Solutions to this equation are the so-called plane waves of the form

$$\psi(\mathbf{k}, \mathbf{r}) = e^{i\mathbf{k}\cdot\mathbf{r}} \tag{2.93}$$

with eigenvalues

$$E_k = \frac{\hbar^2 k^2}{2m} \tag{2.94}$$

to the system's Hamiltonian.[76]

Although an unrealistic scenario (since no real system is completely without interaction of any kind), one could argue that this can still be a valid approximation of electronic behavior for example in the region far away from a neutral molecule, where no Coulomb interaction is present.

If one does not neglect the scattering center, one can construct solutions of the form

$$\psi(\mathbf{k}, r, \theta, \phi) \approx N \left(e^{ikz} + f(\theta, \phi)\frac{e^{i\mathbf{k}\cdot\mathbf{r}}}{r} \right), \tag{2.95}$$

with the scattering amplitude f and the scattering angles θ and ϕ. This represents the sum of an incoming plane wave and the outgoing, scattered particle function, which is represented by a spherical wave modulated by the angle-dependent scattering amplitude.[77] The square of the absolute value of f subsequently defines the angle-dependent differential cross section, which is usually the quantity of interest in scattering experiments.[76] Traditionally there are two approaches to solving such problems that both rely on solutions to the time-independent Schrödinger equation at distances far away from the scattering center: partial wave analysis and the Born approximation.

The basis of the first method, the partial wave analysis, is the fact that the Laplace operator in spherical coordinates can be expressed through the squared angular momentum operator, $\hat{L}^2$,

$$\nabla^2 = \frac{\partial^2}{\partial r^2} + \frac{2}{r}\frac{\partial}{\partial r} - \frac{\hat{L}^2}{\hbar^2 r^2}, \tag{2.96}$$

whose solutions, the spherical harmonics, can be readily used in a separation ansatz, $\psi(r, \theta, \phi) = R_l(r)Y_{lm}(\theta, \phi)$, if the potential is spherically symmetric, i.e. $V(\mathbf{r}) = V(r)$. The resulting radial equation

$$\left[\frac{1}{r}\frac{\partial^2}{\partial r^2}r - \frac{l(l+1)}{r^2} - \frac{2m}{\hbar^2}(V(r) - E) \right] R_l = 0 \tag{2.97}$$

is the fundamental equation which has to be solved in this approach. In the case where the potential V asymptotically approaches zero faster than r^{-2}, that is, the second term in the above equation, the asymptotic solutions for R_l can be constructed as a linear combination of spherical Bessel and Neumann functions:

spherical Bessel functions: $\qquad j_l(r) = (-r)^l \left(\frac{1}{r}\frac{d}{dr} \right)^l \frac{\sin r}{r} \qquad (2.98)$

spherical Neumann function: $\qquad n_l(r) = -(-r)^l \left(\frac{1}{r}\frac{d}{dr} \right)^l \frac{\cos r}{r}, \qquad (2.99)$

where $h_l = j_l + in_l \sim R_l$ are known as the spherical Hankel functions.[76] This prerequisite is in principle fulfilled for anions with an electron far away from the molecular core (on the supposition that the molecule is not dipole-bound, the meaning of which will be discussed later in subsection 2.3.3). It should be noted that the above formulation is equivalent to a description using plane waves.

In the Born approximation on the other hand, one starts by rewriting the Schrödinger equation as an inhomogeneous analogue to the Helmholtz equation,

$$\nabla^2\psi + k^2\psi = \frac{2m}{\hbar^2}V(\mathbf{r})\psi = Q(\mathbf{r}), \tag{2.100}$$

and shows that the solution is comprised of a sum of the general solution to the homogeneous Helmholtz equation and a particular solution to the inhomogeneous equation, which are both Green's functions to the equation above. This results in the Lippmann-Schwinger equation

$$\psi = \psi_0 - \frac{m}{2\pi\hbar^2}\int d\mathbf{r}'\frac{e^{ik|\mathbf{r}-\mathbf{r}'|}}{|\mathbf{r}-\mathbf{r}'|}V(\mathbf{r}')\psi(\mathbf{r}')$$

$$\approx \psi_0 - \frac{m}{2\pi\hbar^2}\frac{e^{ikr}}{r}\int d\mathbf{r}'e^{i\mathbf{k}\cdot\mathbf{r}'}V(\mathbf{r}')\psi(\mathbf{r}'). \tag{2.101}$$

In the Born approximation for the wavefunction in the integral one utilizes $\psi(\mathbf{r}') \approx \psi_0(\mathbf{r}') = e^{i\mathbf{k}'\cdot\mathbf{r}'}$, resulting in a scattering amplitude (see equation 2.95) of

$$f_{\mathrm{Born}}(\theta, \phi) = -\frac{m}{2\pi\hbar^2}\int d\mathbf{r}'e^{i(\mathbf{k}-\mathbf{k}')\cdot\mathbf{r}'}V(\mathbf{r}'). \tag{2.102}$$

It also has to be noted that this result only holds true in the case of elastic scattering. In the general case of inelastic scattering, the initial and final state of the scattering center, i.e. the molecule (with an electronic wavefunction φ), also needs to be considered. This results in terms of the form $\langle\varphi_f, \psi_f|V|\varphi_i, \psi_i\rangle$ in the scattering amplitude, which now requires a full description of the molecular system.

All approaches so far neglected the complex structure of molecules with all electrons and nuclei interacting with the scattered electron. Therefore, up to this point only solutions for the electronic wavefunction far away from the scattering center were yielded, which nevertheless suggests plane waves as a legitimate starting point in the approximation of the scattered electron's wavefunction. If one is interested in molecular dynamics however and tries to describe electron detachment through nonadiabatic transitions as described before, these wavefunctions at large distances are not sufficient, since the actual functions are important for the evaluation of all coupling terms in equation 2.19. Hence, another ansatz needs to be considered, namely, approximating the wavefunctions of a free electron by including, to an extent, dependence on the molecular electronic structure. For this one again starts with solutions to the unscattered electron wavefunctions, i.e. plane waves, as in equation 2.93. The wavefunctions can then be approximated by orthogonalizing the free states

with respect to occupied molecular orbitals (as done firstly for the calculation of photodetachment cross sections[78–80]), so

$$\tilde{\psi}(\mathbf{k}_i) = (2\pi)^{-3/2} \mathcal{N}_{ortho} \left(e^{i\mathbf{k}_i \cdot \mathbf{r}} - \sum_m^{\text{occ}} \langle \phi_m | e^{i\mathbf{k}_i \cdot \mathbf{r}} \rangle \phi_m \right)$$

$$= \mathcal{N}_{ortho} \left(\psi(\mathbf{k}_i) - \sum_m^{\text{occ}} \langle \phi_m | \psi(\mathbf{k}_i) \rangle \phi_m \right), \qquad (2.103)$$

where the normalization constant is given as

$$\mathcal{N}_{ortho} = \left(1 - \sum_m^{\text{occ}} \big| \langle \phi_m | \psi(\mathbf{k}_i) \rangle \big|^2 \right)^{-1/2}. \qquad (2.104)$$

The factor of $(2\pi)^{-3/2}$ is the normalization constant of the plane wave in a spatial box of length $L = 2\pi/\Delta k$, such that orthonormality between the discretized continuum functions is given (see equation 2.22). This serves two purposes: firstly, it incorporates a dependence of the (approximate) scattering functions on the molecular system where the electron density of the neutral core is high and the plane wave ansatz therefore qualitatively wrong.[80] And secondly, it yields (augmented) plane waves that are orthogonal to the bound state orbitals of the molecular core system. Although this suggests orthogonalization to the neutral core MOs, in the methodology presented in chapter 3 the plane waves are chosen to be orthogonal to the occupied anionic MOs. This is done based on the assumption that anionic and neutral orbitals are very similar in a Koopmans'-like argument,[80] the main reason for this being the simplification of arising integrals, that is the computational saving of time, within the developed methodology.

With the basics of the theory and methods behind all upcoming simulations presented, it is now necessary to also take a closer look at the systems that will be described, namely, molecular anions.

2.3   Molecular anions

The addition of an extra electron to a neutral molecule produces a bound molecular anion, if the resulting system is stable with respect to electron-loss. These systems are often characterized by small detachment energies and diffuse distributions of the extra charge around the neutral molecular "core", since the electron only experiences charge-multipole interactions (as opposed to a Coulomb potential in the case of a cationic core) at large separations from the molecule. These weakly-bound anions, "weakly" in this case referring to the usual observation that the AEAs are significantly lower than the IEs in the neutral molecule[81], are therefore prone to electron detachment (or other reaction pathways such as dissociation of fragments after bond-break) by addition of sufficient energy to overcome the ionization potential barrier, for example with the kinetic energy of the captured electron or by radiation.[10]

In the case of formation of a metastable state, one then observes a deactivation of this system on a finite timescale. Therefore, to understand the ultrafast dynamics of such metastable anions, one first has to take a closer look at what so-called resonances are and what different types thereof can occur.

2.3.1 Types of resonances

In the most general sense, resonances in the field of scattering theory are states that are metastable with respect to some kind of dissociation of the form $AB^* \to A + B$, the star indicating that the state is metastable. In this thesis one can restrict oneself to anions and therefore the cases of

$$(AB^-)^* \to A + B^-. \tag{2.105}$$

One can firstly differentiate between different dissociation products B^-. If B^- is an atom or molecular fragment, $(AB^-)^*$ is called a heavy-particle resonance. They play a role for example in predissociation or dissociative electron attachment phenomena and are experimentally observable with (time-resolved) mass spectrometry. In the case where B^- is an electron, one calls $(AB^-)^*$ an electronic resonance and the relaxation process is autodetachment, yielding the molecular core A after some time, usually in the range from femto- to microseconds.[11–13]

Furthermore a resonance can be formed two different ways when focusing on the neutral core: Firstly by addition of an electron to a molecular core in its electronic ground state, called a 'single-particle resonance'. If the anion in its electronic, vibrational and rotational ground state is a bound molecule, resonances can then be observed by vibrational or rotational excitation. One example would be the vinylidene anion[25,26,82], whose vibration-induced autodetachment dynamics are discussed in chapter 3. The second possibility of resonance generation is by attaching an extra electron to a molecule and in that process exciting the neutral core (or generating a bound anionic molecule in its ground state and subsequently exciting the system above the ionization threshold), thus creating an electronically excited anion, which is called a 'core-' or 'target-excited resonance'.[10,83] An example for this would be the 2-cyanopyrrolide anion[84,85] discussed in chapter 4.

A third (and for this thesis arguably the most important) distinction can be made with respect to the combined potential energy of the fragments, i.e. the dissociation potential: In a so-called 'shape resonance' the energy lies above the dissociation potential and the state is trapped by a potential energy barrier. An example is shown in Figure 2.1a), in which after dissociation the excess energy of the system, E_{kin}, is redistributed to the kinetic energy of the fragments. The deactivation pathway, in this case, is tunneling through the barrier and the lifetime of such states is determined mainly by the tunneling probability dependent on the height and width of the barrier.[86] If the resonance energy lies below the dissociation potential of the occupied state but above the dissociation potential of a lower-lying state, a 'Feshbach resonance' is present.
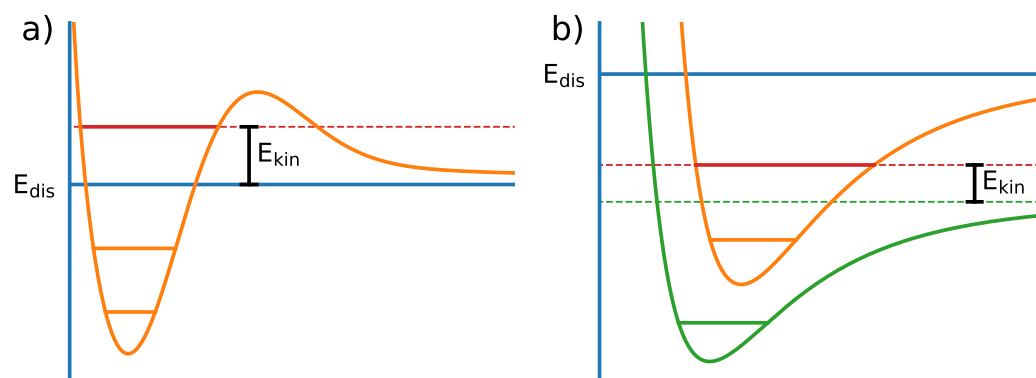
Figure 2.1: a) Schematic depiction of a shape resonance (red). The state is unstable with respect to dissociation, but trapped behind a repulsive potential energy barrier. The system deactivates by tunneling through the barrier. b) Schematic depiction of an excited Feshbach resonance (red). The orange and green lines represent two different potential energy curves of electronic states. The current system is stable with respect to dissociation, but couples to the lower-lying state and eventually deactivates by state transition with a kinetic energy of the fragments of E_{kin} as depicted.

An exemplary schematic depiction of an electronic Feshbach resonance is given in Figure 2.1b), in which two potential energy curves are shown as a function of the molecule-electron distance. In this case the system is able to deactivate by coupling of the resonance state to the lower-lying green electronic state, resulting in ejection of an electron with the kinetic energy E_{kin}. The lifetime of this state is determined by the coupling strength to the lower-lying state.[86] Shape and Feshbach resonances can have lifetimes of the same magnitude and can therefore be competing phenomena in deactivation, especially on ultrafast timescales. However generally speaking, Feshbach resonances tend to be decaying slower.[10] Also noteworthy is that the character of a resonance can change as a result of solvation effects, for example from shape to Feshbach character in polar solvents, resulting in a drastically increased lifetime.[87]

These different types of resonances are naturally not mutually exclusive in a specific molecule, resulting in multiple simultaneously accessible deactivation pathways for example autodetachment and dissociative electron attachment in DNA strand breaks.[17,18]

2.3.2   Experimental characterization of molecules

Although experiments were not part of the author's work in this thesis, theoretical simulations are generally validated by their agreement with experimental data. Hereof, it also follows that to develop new theoretical methods and be able to interpret the yielded results reliably, it is necessary to also understand the associated experiments. Therefore, a short overview of the most important experimental methods related to the theoretical methodology in this thesis as well as a historical summary of the discovery of molecular anions shall be given in this paragraph.

Before being able to characterize molecular gas-phase anions, one has to produce them first. This bears some difficulties arising from the small electron attachment energies, often prohibiting direct electron collision which produces electronically excited or vibrationally hot products, as the excess energy could be enough to ionize the molecule again.[9] Therefore possible other generation methods include fragmentation from a dissociative electron attachment process of more complex metastable anions, where the yield is diminished by autodetachment of the parent anion, gas-phase chemical reactions, collision of neutral species with highly excited atoms or molecules with detachment energies matching the electron affinity of the neutral, and so-called spray techniques.[9] The last method, in which a desired anion contained in a stabilizing liquid solution is sprayed in the gas phase under high voltage[88], was used, for example, in the experimental study of the 2-cyanopyrrolide anion[84] which has been theoretically investigated in chapter 4.

One of the defining characteristics of a molecular anion is the adiabatic detachment energy (ADE) or alternatively the adiabatic electron affinity (AEA) of the corresponding neutral system, i.e. the energy difference between the neutral and anionic molecule in both their electronic, vibrational and rotational ground state. One has to be careful with the nomenclature here: although in this case the AEA is the released energy upon addition of an electron to the neutral molecule and ADE the energy one has to put into the anionic system to extract an electron, the energy of both processes are often simply referred to as "the AEA" in this field of research. For clarity it should further be noted that all mentioned quantities (ADE/AEA) are only semantically different, the actual values are equal and defined as positive if the considered molecule is stable with respect to electron detachment. Another important characteristic is the vertical detachment energy (VDE). It describes the potential energy difference between neutral and anionic system at the same nuclear geometry. For a non-specific, more general detachment energy, the abbreviation DE will be used from now on.

For a bound molecule stable with respect to electron loss, the AEA is positive, otherwise negative. Consequently the knowledge of a molecule's AEA is of great concern for the stability of molecular anions. For bound anions a possible way to obtain accurate electron affinities is through photodetachment experiments.[89,90] The basic idea thereof is the removal of an electron through radiation:

$$A^- + h\nu \rightarrow A + e^-. \tag{2.106}$$

In principle there exist two possibilities to investigate electron affinities,[91] namely threshold photodetachment, among this especially zero-electron kinetic energy (ZEKE) spectroscopy, and photoelectron spectroscopy (PES), which should be described briefly, since these methods are used to gain all experimental data that have been simulated using the theoretical approaches presented in this thesis.

The first method records the reaction yield of equation 2.106 as a function of the tunable photon energy. This is in direct analogy to the photoelectric

effect and the work function of solid state surfaces, from which this method is derived. A signal is then detected either by capturing of photoelectrons/neutral molecule species or the decrease in anion concentration, and one therefore finds the DE directly at the threshold laser energy. Especially popular, since it allows for even higher-resolved data, is ZEKE spectroscopy, in which a weak current is applied in the reaction chamber at the detachment threshold after an amount of time to separate the produced electrons by kinetic energy, only counting those with an initial EKE of zero.[92] The resolution of such experiments is in general far higher than for PES,[93] on the other hand tunable laser setups have to be used. This leads not only to technical inconveniences, also the intensity of measured signals can change with the photon energy, complicating the analysis.[32]

The latter method of photoelectron spectroscopy is not only one of the leading techniques in the characterization of molecular anions, but in general throughout the whole field of molecular physics. Accordingly it is also the main source of experimental data in all studies presented in chapters 3 to 6, which is why it should be discussed in a bit more detail in the following. In PES radiation of specific photon energies higher than the ADE is used and ejected electrons are measured as a function of particle kinetic energy (in the following chapters this quantity is referred to as "electron kinetic energy" or EKE). One can then draw conclusions on the DE (or in the special case of starting molecules in their ground state: ADE) considering conservation of the total energy of the system including the ejected electrons:

$$\text{DE} = h\nu - \text{EKE} = h\nu - \frac{m_e}{2}\dot{\mathbf{r}}_e^2. \tag{2.107}$$

Although rather limited in resolution compared to threshold photodetachment spectroscopy, there is a major advantage: Since the whole range of photoelectrons is detected energy-resolved, PES is able to provide information about the electronic structure of the ionized molecule as well.[94] This includes not only electronic state differentiation, but also vibrational analysis of the starting molecule as well as the ionized species, allowing for conclusions on the molecular geometries. Moreover, angular-resolved detection of photoelectrons provides direct information about the electron detachment continuum wavefunctions and photodynamics in contrast to the aforementioned threshold photodetachment spectrum.[32] By combining all of the above methodology with ultrashort laser pulses, one is able to not only resolve energetically (and angularly), but also in the time domain with a resolution of down to a few femtoseconds. On these timescales molecular vibrations as well as nonadiabatic electronic relaxation processes take place. Particularly the possibility to track nuclear rearrangement to produce different isomers, especially after prior photoexcitation, should be noted. Application of this so-called (femtosecond) time-resolved photoelectron spectroscopy (TRPES) directly reveals ultrafast dynamic relaxation processes in molecules experimentally. These findings can then be built upon using theoretical approaches to connect this data with dynamical processes at the molecular level. Together with surface-hopping

simulations, femtosecond pump-probe TRPES experiments after initial excitation into an excited electronic state are the basis of the combined theoretical-experimental approach presented in chapter 6.

Sometimes one finds a combination of both methodologies, meaning experiments where the laser photon energy is tunable in a desired energy range and one still detects the photoelectrons energy-resolved. This leads to 2D data, in which one finds specific ionization transitions along a diagonal in the spectrum, i.e. with an EKE linearly increasing with photon energy. This combines all the advantages of both described methods (but also the disadvantages such as reduced resolution), but facilitates interpretation of experimental data. Summation of the signal over the EKE range of 0 to $\sim$50-100 meV yields the so-called slow photoelectron spectrum with improved signal-to-noise ratios when compared with threshold photodetachment spectroscopy.[32]

It is no surprise that the first interest in molecular anions arose mainly from the desire to determine electron affinities of neutral systems, but on the other hand also because of their role in a variety of chemical gas-phase reactions.[95] Their generally diffuse electron densities lead to strong interaction with the molecular surrounding (for example in solution or solid state) and therefore easily available reaction pathways, enabling the observation of their immediate vicinity by probing anions,[9,81] an example of which are the completely different photoelectron spectra found in the uracil anion upon differing experimental preparations.[96,97] The earliest detected molecular anion was found in 1968 by Herzberg and Lagerqvist[20], who assumed characteristic features in their emission spectrum to be the C_2^- anion, which was later confirmed by Lineberger *et al.*[21] in one of the very early uses of resonance-enhanced multiphoton ionization (REMPI) spectroscopy, which at the time was still restricted by the problems in the generation of higher-energy photons at the necessary intensities.[98] Other early examples are the OH^-/OD^- and the O_2^- molecules[99,100], and small hydrocarbons such as the CH^- and CH_2^- molecules[101,102], the latter of which being able to establish spectroscopy on molecular anions in the determination of singlet-triplet energy splitting of corresponding neutral molecules. In 1983 Lineberger *et al.*[103] first measured the AEA of vinylidene to be 0.47 eV, which induced a variety of experimental studies on the vinylidene anion[25,82,104]. Because of the excellent availability of data on this molecule, it eventually served as the first working example for the developed autodetachment dynamics methodology[26] presented in this thesis.

2.3.3 Valence-bound and dipole-bound anions

To differentiate between the characteristics of anionic bound states, it is useful to first take a look at the general electric potential created by an arbitrary electrostatic charge density $\rho(\mathbf{r})$ given in atomic units as

$$V(\mathbf{r}) = \int d^3\mathbf{r}' \frac{\rho(\mathbf{r}')}{|\mathbf{r} - \mathbf{r}'|}. \tag{2.108}$$

For positions $\mathbf{r}$ sufficiently far from regions of large charge density the term $|\mathbf{r} - \mathbf{r}'|^{-1}$ can be expressed through a Taylor expansion around $\mathbf{r}' = 0$,

$$\frac{1}{|\mathbf{r} - \mathbf{r}'|} = \frac{1}{r} + \frac{\mathbf{r}' \cdot \mathbf{r}}{r^3} + \frac{3(\mathbf{r}' \cdot \mathbf{r})^2 - r'^2 r^2}{2r^5} + \dots . \tag{2.109}$$

This result and the definitions

$$\text{total electric charge:} \qquad q = \int \mathrm{d}^3\mathbf{r}'\rho(\mathbf{r}') \tag{2.110}$$

$$\text{dipole moment:} \qquad \boldsymbol{\mu} = \int \mathrm{d}^3\mathbf{r}'\rho(\mathbf{r}')\mathbf{r}' \tag{2.111}$$

$$\text{quadrupole moment:} \qquad Q_{ij} = \int \mathrm{d}^3\mathbf{r}'\rho(\mathbf{r}')(3r_i'r_j' - r'^2\delta_{ij}) \tag{2.112}$$

substituted into equation 2.108 then yield

$$V(\mathbf{r}) = \frac{q}{r} + \frac{\mathbf{r} \cdot \boldsymbol{\mu}}{r^3} + \frac{1}{2}\sum_{i,j} Q_{ij}\frac{r_i r_j}{r^5} + \dots , \tag{2.113}$$

the so-called multipole expansion of the electrostatic potential.[105] Due to the increasing power in r for each subsequent term, in turn leading to faster convergence to zero, the long-range effect of the potential on a charged particle is mainly dominated by the first non-zero term of the expansion.

In the case of anions, when viewing the molecular system as an electron in the field of the neutral molecular core, the first term in equation 2.113 disappears, since $q = 0$, leaving higher multipole potentials responsible for long-range binding effects. Solving the Schrödinger equation for an electron in the field of a point dipole results in an infinite number of bound states for dipole moments that are greater than 1.625 D[106,107] without considering any electronic molecular structure. It can be shown that in the case of a finite dipole, this critical value does not change.[108] Further critical dipole moments are found much higher (9.6375 D, 19.101 D, ...), and the spatial shape of the dipole-bound electronic wavefunctions can be associated with the solutions of H_2^+ and the order of the respective critical moment (1.625 D $\rightarrow \sigma$, 9.6375 D $\rightarrow \pi$, ...).[108] Later it was found by Garrett[109] that in the field of a rotating finite dipole the number of bound states reduce to only a handful, even only one, depending on the considered system. Also the critical dipole moment was found to depend strongly on the system's moment of inertia and charge separation, i.e. there is no set critical value at which electron binding can be expected. Generally, the first critical moment is often observed to be around 2.4 D.[108]

Of course only considering multipole potentials is not a valid approach in the case of real molecular anions anymore due to valence-type contributions arising from direct, strong interaction of the extra electron with the molecule's other individual electrons and nuclei. Nevertheless it can still be useful to distinguish electronic states by their main contribution leading to electron binding, that is, multipole-bound and valence-bound anions, valence-bound generally meaning electron distributions that are more confined in space around

the molecular core,[10] recognizing that the last remark is in itself a vague distinction. The main difference lies in how localized the electron density of the extra electron is and in its actual spatial shape. Commonly valence states are recognized by their resemblance to typical orbitals in neutral molecules, e.g. σ- or π-type distributions, albeit more diffuse due to the missing long-range Coulomb interaction, and rather large VDEs. Multipole-bound states on the other hand usually resemble very diffuse electron densities and shapes analogous to Rydberg states in neutral molecules and are characterized by small VDEs, resulting from the limited influence of the extra electron on the nuclear geometry, i.e. anion and neutral have almost the same equilibrium geometry. Consequently one would also expect the binding energy of an electron to shrink for higher multipoles. A good example for the breaking of this rule is the $(BeO)_2^-$ anion, classified as quadrupole-bound, with a VDE of 1.1 eV[110], well above the usual values of below hundreds of meV.

Experimentally, photoelectron spectroscopy can help in the differentiation between valence and multipole-bound character: Since the equilibrium geometry of the neutral species and the multipole-bound anion are virtually the same, one can expect similar vibrational wavefunctions and therefore a strong $0 \rightarrow 0$ peak in the photoelectron spectrum. In contrast to this in the case of valence states one expects a more pronounced vibrational progression with the brightest peak most likely not being the $0 \rightarrow 0$ transition. This can be observed nicely in the uracil anion, which possesses both a valence- and dipole-bound state and shows two very different photoelectron spectra depending on the preparation of the system.[96,97]

There is a variety of molecules that possess both valence and dipole-bound states, and interaction between the two types can lead to interesting behavior. In the nitropropane molecule for example it was shown that electron capturing can be achieved by population of the dipole-bound state, which can subsequently stabilize the resulting anion by coupling to the valence ground state.[108,111] The inverse effect, the mediation of autodetachment of vibrationally excited nitropropane by transient population of a dipole-bound state can be seen in the work presented in chapter 5.

2.3.4 Computational challenges of molecular anions

As is always the case in computational chemistry, in practice the accuracy of the description of molecular anions is limited by the temporal effort of the computations, especially if, as already implied in subsection 2.1.2, two quantum-chemical calculations (for the anion and neutral molecule) have to be carried out per nuclear dynamics time step. As a consequence, one has to carefully choose the level of theory for an acceptable accuracy-efficiency compromise, which normally involves two aspects: the actual quantum-chemistry method and the atomic basis set, from which molecular orbitals are constructed.

Considering quantum chemistry methods, one has to be aware that since electronic energies (AEAs, excitation energies, etc...) are rather small in anions and relative errors therefore larger, electron correlation cannot be neglected

(i.e. Hartree-Fock is unusable), nor should it be described poorly. This effectively leaves post-Hartree-Fock methods such as MPn, (MR-)CI, MCSCF and coupled cluster theory, or DFT.[9] In principle post-Hartree-Fock methods should yield the most reliable and accurate results, since they are systematically improvable in that they give exact solutions to the electronic Schrödinger equation in their respective method limit. In practice it is highly debatable if this limit is even remotely reached in the current state of approximations. Furthermore the enormous computational effort of these methods makes them very impractical in quantum-classical dynamics simulations. This is the reason why in this thesis most results were obtained using the DFT method, which of course bears its own difficulties. As described before in subsection 2.2.4, no expression is known for the exchange-correlation functional and plenty of different functionals have been developed that try to approximate it. Unfortunately with most functionals the Kohn-Sham orbitals of anions show incorrect behavior for large distances away from the molecule, as they contain terms that arise from the improper cancellation of self-interaction in the electron-electron interaction (third term in the operator of equation 2.82).[9] To understand this, one needs to consider the operator in equation 2.82: The first term is the electron's kinetic energy operator, the remaining three define the potential energy, consisting of electron-nuclear attraction, electron-electron repulsion and the exchange-correlation potential containing all corrections from the non-interacting electron gas to the real molecule. In the asymptotic case of very large r away from the molecule, one can show that in the exact case $v_{xc} \sim -r^{-1}$ and therefore for large r

$$v_{KS}(r) = -\frac{Z - N + 1}{r}, \qquad (2.114)$$

where Z denotes the sum of all atomic numbers. This means that for anions, where the number of electrons is $N = Z + 1$, $v_{KS}(r) \to 0$. The problem now arises from the fact that in DFT the electron-electron repulsion term describes the interaction of an electron with the total electron density (including the very electron itself) instead of the density of an $N - 1$ electron system, which is called the self-interaction error. In the approximative case, most functionals rely on local derivations of the potential v_{xc}, which fail to fully cancel this error and fall off exponentially, therefore leading to $v_{KS}(r) \to r^{-1}$ for an anion, that is, a repulsive potential for large separations using standard approximative functionals.[10] One could argue that this phenomenon could not be too big of a problem in the case of valence-bound anions with compact electronic structure, but it should lead to systematically wrong description for diffuse dipole-bound states. It is evident that the problem of self interaction has to be tackled one way or another to yield useful results. The most prominent solution is the use of long-range corrected functionals. These functionals split the two-electron operator into a long-range and short-range part, mostly according to

$$\frac{1}{r_{12}} = \underbrace{\frac{1 - \mathrm{erf}(-\mu r_{12})}{r_{12}}}_{\text{short-range}} + \underbrace{\frac{\mathrm{erf}(-\mu r_{12})}{r_{12}}}_{\text{long-range}}, \qquad (2.115)$$

where μ denotes a tunable, so-called range separation parameter.[10] Considering exchange-correlation functionals that are separable into their respective exchange and correlation part, the long-range part is normally considered with exact Hartree-Fock exchange terms, since they provide correct behavior for large r and do not rely on local approximations, and the short-range part is used in a combination of Hartree-Fock and GGA exchange, so

$$E_{xc}^{LC} = E_c + c_{HF}E_{x,HF}^{SR} + (1 - c_{HF})E_{x,GGA}^{SR} + E_{x,HF}^{LR} \qquad (2.116)$$

where SR and LR denote quantities that include the short- and long-range terms of equation 2.115, respectively, and c_{HF} is the proportion of Hartree-Fock exchange in the total short-range exchange term. This means that the resulting functionals are hybrid functionals with correct long-range performance.[10] Examples of such are ωB97XD, CAM-B3LYP or LC-ωPBE, which were used in all the publications of chapters 3-5.

The second leverage point are atomic basis sets. In the general valence case, bases need to be able to both describe the varying extent of anionic and neutral systems sufficiently well, while also allowing for the inclusion of electron correlation effects. This is done by inclusion of additional diffuse as well as polarization functions, that is, basis functions of higher l quantum number. Since (spatially) wide-spread electron densities are to be expected in multipole-bound states, the used basis sets need to reflect this characteristic by employing extra-diffuse basis functions.[9] Usually these are build by extension of standard basis sets, generating new function exponents through a geometric progression based on the most diffuse function of the underlying "default" basis, α_0, so

$$\alpha_n = \frac{\alpha_0}{c^n}, \quad n = 0, 1, 2, ... \qquad (2.117)$$

with c usually in the range of 3-5.[10] As described before, a finite dipole with a dipole moment smaller than 9.6375 D only supports s-type bound states, so the dipole-bound states of a molecular anion with a not too large dipole moment can also be expected to possess s-type character. It follows that s-type basis functions should in principle be sufficient to accurately describe the electronic distribution, however also in this case polarization functions can be necessary to account for electron correlation or errors arising in the actual spatial centering of the additional functions. Although from an intuitive point of view the extra electron binds more to the positive end of the molecular dipole and the basis functions should therefore be centered there, either on the closest atom or a ghost center[112], it can be shown that the actual positioning of additional extra-diffuse functions barely has any effect on the shape of the electronic distribution and therefore on the energies within quantum-chemical calculations of small anions (small in comparison to the extent of the diffuse MO).[10] In their study on several molecules up to 5 atoms, Morgan and Fortenberry even state that "the placement of the additional functions [...] should be a nonconsideration", as long as the center of the functions is reasonably within the extent of the molecule.[113]

Chapter 3

Quantum-classical dynamics of vibration-induced autoionization in molecules

Abstract

We present a novel method for the simulation of the vibration-induced autoionization dynamics in molecular anions in the framework of the quantum-classical surface hopping approach. Classical trajectories starting from quantum initial conditions are propagated on a quantum-mechanical potential energy surface while allowing for autoionization through transitions into discretized continuum states. These transitions are induced by the couplings between the electronic states of the bound anionic system and the electron-detached system composed of the neutral molecule and the free electron. A discretization scheme for the detached system is introduced and a set of formulae is derived which enables the approximate calculation of couplings between the bound and free-electron states.

We demonstrate our method on the example of the anion of vinylidene, a high-energy isomer of acetylene, for which detailed experimental data is available. Our results provide information on the time scale of the autoionization process and give an insight into the energetic and angular distribution of the

ejected electrons as well as into the associated changes of the molecular geom-
etry. We identify the formation of structures with reduced C-C bond lengths
and T-like conformations through bending of the CH_2 group with respect to
the C-C axis and point out the role of autoionization as a driving process for
the isomerization to acetylene.

3.1   Introduction

Molecular anions are often characterized by small electron binding energies,
and it is not uncommon that the additional electron(s) are not strictly bound
at all, the anionic molecular system thus being in a metastable or "quasi-
bound" state that after a finite lifetime decays by ejecting an electron in a
process termed autoionization.[9,10] This seemingly quite exotic process is in
fact relevant in a variety of areas. Notably, the capture of slow electrons
by biological molecules such as nucleobases may populate metastable states
that decay by autoionization, accompanied by chemical transformations of the
molecule.[15,16,114,115] In DNA, electron attachment and subsequent autoioniza-
tion can occur both at nucleobases and the phosphate-deoxyribose backbone,
causing single and, through consecutive reaction of fragments, double strand
breaks.[17,18,115] Since the electrons can, e.g., be produced by primary ioniza-
tion due to nuclear radiation, this makes autoionization processes a key step
in the radiation damage of biological systems. Furthermore, low-energy elec-
tron generation via intermolecular coulombic decay, first discovered in noble
gas clusters[116] and liquid water[117], occurs in biology at the $FADH^-$ cofactor
where it enables the mechanism of photolesion repair in DNA by photolyases.[19]
Autoionization is also an important part of the manifold generation and dissi-
pation mechanisms in solvent clusters with excess electrons,[118,119] which in turn
play a significant role in processes such as nucleation and aerosol formation in
the upper atmosphere[120] or in the formation of solvated electrons in living
organisms upon UV irradiation of riboflavin and its derivatives.[121] Moreover,
the formation of anions that can undergo autoionization is also an important
mechanism in the creation of complex molecules in interstellar space.[122]

The metastable states or resonances from which autoionization takes place
can be classified as rotational, vibrational, or electronic. While for the latter,
electronic excitation is responsible for reaching the ionization continuum, in the
two former cases it is an excess of nuclear rotational or vibrational energy that
brings the system above the ionization threshold. The autoionization process
itself can then be viewed as a nonadiabatic transition (internal conversion)
between the initial rotationally or vibrationally excited N-electron molecule
and the final system of $N-1$-electron molecule and free electron, where the $N-$
1-electron molecule bears a reduced internal energy. Vibrational autoionization
has been identified over the last decades in a variety of molecules, ranging from
small anionic diatomics,[123,124] Rydberg-excited states of neutral molecules[30] to
dipole- or quadrupole-bound states of polyatomic anions[27,28,31,84,114,125–130] and
has been utilized to measure highly resolved photodetachment spectra. In

some cases, vibrational autoionization from valence states has been observed as well.[25,104,131] Real-time access to the dynamics of such processes could be recently gained via pump-probe experiments.[29,130,132]

Theoretical considerations of vibrational autoionization have been originally outlined by Berry[133] and later formulated for anions by Simons, who established propensity rules for such transitions for model cases[134] and computed autoionization rates for several small molecules using time-independent[135] as well as time-dependent pictures.[136] Going beyond the calculation of rates and fully simulating the real-time dynamics of such processes for complex molecules is highly desirable, but a completely quantum mechanical treatment, including the full dimensional nuclear motion and the description of electron scattering states, is computationally prohibitive. However, given the great success of mixed quantum-classical approaches to describe the bound-state nonadiabatic dynamics[5–7,54,137–139] as well as time-resolved spectroscopic observables[33,140,141] of a large variety of molecules, it suggests itself to consider such an ansatz as well for vibration-induced autoionization. Recently, the dynamics of electronically metastable anion states has been addressed by combining classical trajectory simulations with quantum mechanically calculated ionization probabilities based on the width of the electronic resonance.[142,143] In the present work, we will introduce a novel methodology for the dynamics of vibrationally metastable anions which is based on Tully's trajectory surface hopping,[52] treating the nuclear motion classically, while retaining the quantum mechanical description of the electronic system. The energy exchange between the electronic and nuclear subsystems will be described by nonadiabatic transitions between the bound and continuum electronic states, accompanied by an associated change of the classical vibrational energy of the molecule.

After presenting the theory we will illustrate our method on the example of the vinylidene anion, $C_2H_2^-$. *Neutral* vinylidene is a high-energy isomer of the well-known acetylene molecule, HCCH, to which it readily isomerizes.[144–146] As an anion, however, vinylidene is stable on the time scale of seconds,[147] while the acetylene anion is electronically unbound.[146,148] Vinylidene anions can be produced in the gas phase e.g. by injection of electrons in a precursor gas mixture containing ethylene and N_2O, where the reaction proceeds via intermediately formed O^-.[104] Using photodetachment and photoelectron spectroscopy techniques, the vinylidene anion has been utilized to gain information about the electronic and vibrational states of neutral vinylidene.[103,146,149] In this way, it could be established that neutral vinylidene represents a local minimum on the C_2H_2 potential energy surface with several clearly assignable vibrational states, while with higher vibrational energy, the distinction between the vinylidene and acetylene isomers gets lost. Therefore, as shown by quantum dynamics simulations, isomerization to acetylene readily occurs on a sub-picosecond time scale upon vibrational excitation, while for the vibrational ground state much larger lifetimes of several hundred picoseconds can be expected.[150–152] In fact, experiments employing Coulomb explosion imaging provided even more evidence for the presence of vinylidene on the much

longer time scale of several microseconds after its initial generation.[153] With the help of classical molecular dynamics simulations, it could be shown that this finding is due to frequent forth- and back-formation of vinylidene after initial isomerization provided the vibrational energy is sufficient to overcome the isomerization barrier.[154]

With regard to the ionization process itself, photoelectron spectroscopy studies have enabled the determination of vinylidene's adiabatic electron affinity (AEA), with the current most precise value being 0.4866(8) eV (3935 cm^{-1}).[82] Employing vibrational predissociation spectroscopy of Ar-tagged vinylidene anions, the vibrational structure of the anionic ground state has been investigated, revealing prominent spectral features around 2600 and 4000 cm^{-1}.[104] As the latter value lies above the AEA, it is also visible as a resonance in photodetachment spectroscopy, indicating that the respective vibrational states couple to the ionization continuum. Interestingly, also the lower-energy band around 2600 cm^{-1} appears prominently in photodetachment, although under the experimental conditions used in Ref.[104] one-photon ionization is dominant and thus direct detachment should be improbable. This finding could be attributed to the presence of molecules that are initially occupying excited vibrational states due to thermal energy and are further photoexcited above the AEA, followed by vibrational autoionization. The photoelectron spectra resulting from such detachment processes allow for conclusions on the vibrational structure of the neutral species as well as on the initially populated anion vibrational states. In addition, recent experiments employing slow electron velocity imaging (SEVI) photoelectron spectroscopy provided highly resolved spectra (<10 cm^{-1}) that allowed one to disentangle further structures in the photoelectron spectra obtained from the vibrational resonances just above the ionization threshold.[25] Specifically, two types of spectral features were found: (i) peaks with electron kinetic energies shifting proportionally to the incident photon energy, as is expected from a direct photodetachment process, and (ii) peaks of constant electron kinetic energy over a range of photon energies, covering a region up to 100 cm^{-1}. This finding can be explained by intermediate excitation of rovibrational states of the anion that are resonant to the photon energy that decay via autoionization to the neutral species. In this process the rotational quantum numbers remain unchanged, hence the occurrence of constant-energy photoelectrons. These findings provided direct evidence for vibration-induced autoionization processes following the excitation of anion vibrational states above the ionization threshold. What has remained undisclosed until now, however, are their time scales. The present paper aims to shed light on this dynamical process by simulating directly the autoionization dynamics in full dimensionality.

Our paper is organized as follows: In section 3.2 the theoretical methodology will be presented and in section 3.3 the computational details are given. This is followed by the results and discussion provided in section 3.4. Finally, conclusion and outlook are given in section 3.5.

3.2 Theoretical Approach

In the frame of the Born-Oppenheimer approximation, a vibrational resonance can be described by a product of a vibrational and an electronic wavefunction, $\chi_{vib}(\varepsilon)\Phi_{el}^N(E)$, with vibrational energy ε and electronic energy E, where the total energy $E + \varepsilon$ exceeds the ionization threshold while the electronic portion is still below it. The autoionization process can then be viewed as the internal conversion to an isoenergetic state $\chi_{vib}(\varepsilon')\Phi_{el}^N(E')$ in which part of the vibrational energy has been transformed into electronic energy, leading to an electronic state with increased energy E' that is unbound with respect to single-electron loss and can be described as an antisymmetrized product of an $N - 1$ electron bound state and a free electron continuum state with wave vector $\mathbf{k}$, $\Phi_{el}^N(E') = \mathcal{A}(\Phi_{el}^{N-1}\psi(\mathbf{k}))$.

Since we aim to establish a method that is applicable for complex molecules, instead of a fully quantum mechanical description of the autoionization dynamics a mixed quantum-classical picture is desirable, in which only the quantum nature of the electronic part is retained while the nuclear motion is described classically. For nonadiabatic processes between bound electronic states, the surface hopping method[52] has proven to be a very versatile approach. In this framework, the nuclear degrees of freedom are propagated classically by solving Newton's equations of motion,

$$M\ddot{\mathbf{R}} = -\nabla_{\mathbf{R}} E_i(\mathbf{R}), \tag{3.1}$$

for an ensemble of initial conditions, thereby giving rise to nuclear trajectories $\mathbf{R}(t)$ moving on an electronic potential energy surface $E_i(\mathbf{R})$. The quantity M denotes a diagonal matrix containing the nuclear masses. In parallel, along each trajectory an electronic time-dependent Schrödinger equation is solved, which most generally reads

$$i\hbar\frac{d}{dt}\Psi(\mathbf{r}, t; \mathbf{R}[t]) = \hat{H}_{el}\Psi(\mathbf{r}, t; \mathbf{R}[t]), \tag{3.2}$$

with $\hat{H}_{el}$ being the electronic Hamiltonian of the system. The electronic wavefunction can be expanded with respect to a set of orthogonal basis states as

$$\Psi(\mathbf{r}, t; \mathbf{R}[t]) = \sum_i c_i(t)\Phi_i(\mathbf{r}; \mathbf{R}[t]), \tag{3.3}$$

leading to the following set of coupled differential equations for the coefficients c_i:

$$i\hbar\dot{c}_i(t) = \sum_j [H_{ij}(\mathbf{R}[t]) - i\hbar D_{ij}(\mathbf{R}[t])]\, c_j(t), \tag{3.4}$$

where $H_{ij} = \langle\Phi_i|\hat{H}_{el}|\Phi_j\rangle$ denotes the matrix elements of the electronic Hamiltonian. The D_{ij} represent the nonadiabatic couplings that arise from the

parametric dependence of the wavefunction on the nuclear trajectory and can be written as

$$D_{ij} = \langle \Phi_i | \dot{\Phi}_j \rangle = \dot{\mathbf{R}} \cdot \langle \Phi_i | \nabla_R | \Phi_j \rangle \tag{3.5}$$

where the last expression makes clear the dependence on the nuclear velocities $\dot{\mathbf{R}}$. Thus, the coupling between electronic states is mediated by the nuclear motion. The time-dependent coefficients $c_i(t)$ are employed in the surface hopping approach to devise probabilities for each nuclear trajectory to switch its electronic state, and the time-dependent properties of the nonadiabatically evolving system are obtained by averaging the quantities of interest over the entire ensemble that typically contains up to hundreds of trajectories.

In the following, we will develop a surface-hopping methodology for the description of molecular autoionization dynamics. For a system that can be ionized, the expansion of the electronic state given in equation 3.3 has to be extended by the set of continuum eigenstates:

$$\Psi\big(\mathbf{r}, \mathbf{R}[t], t\big) = \sum_m c_m(t) \Phi_m\big(\mathbf{r}, \mathbf{R}[t]\big)$$
$$+ \sum_n \int d^3\mathbf{k}\, \tilde{c}_n(\mathbf{k}, t) \tilde{\Phi}_n(\mathbf{k}, \mathbf{r}, \mathbf{R}[t]), \tag{3.6}$$

where the first sum includes the N-electron bound states of the molecule, while the second sum and integral encompass the set of singly ionized states characterized by the discrete quantum number n of the bound $N-1$-electron system and the continuously varying wavevector $\mathbf{k}$ of the free electron. Bound and continuum eigenstates are mutually orthogonal in the sense

$$\langle \Phi_m | \Phi_{m'} \rangle = \delta_{mm'} \qquad \text{(bound-bound)} \tag{3.7}$$

$$\langle \Phi_m | \tilde{\Phi}_n(\mathbf{k}) \rangle = 0 \qquad \text{(bound-continuum)} \tag{3.8}$$

$$\langle \tilde{\Phi}_n(\mathbf{k}) | \tilde{\Phi}_{n'}(\mathbf{k}') \rangle = \delta_{nn'} \delta(\mathbf{k} - \mathbf{k}'). \qquad \text{(continuum-continuum)} \tag{3.9}$$

In the following, we will specifically consider the ionization of a negatively charged molecule, thus our N-electron system is an anion (a), the $N-1$-electron system is neutral (n). In order to simulate the dynamics of the autoionization process on similar grounds as bound state nonadiabatic dynamics, several approximations have to be introduced.

3.2.1 Discretized continuum approximation for ionized states

We discretize the set of continuum states as

$$\int d^3\mathbf{k}\, \tilde{c}_n(\mathbf{k}, t) \tilde{\Phi}_n(\mathbf{k}, \mathbf{r}, \mathbf{R}[t]) \tag{3.10}$$

$$\approx \sum_i (\Delta V_k)^{\frac{1}{2}} \tilde{c}_n(\mathbf{k}_i, t)(\Delta V_k)^{\frac{1}{2}} \tilde{\Phi}_n(\mathbf{k}_i, \mathbf{r}, \mathbf{R}[t]) \tag{3.11}$$

$$\approx \sum_i c_n(\mathbf{k}_i, t) \Phi_n(\mathbf{k}_i, \mathbf{r}, \mathbf{R}[t]) \tag{3.12}$$
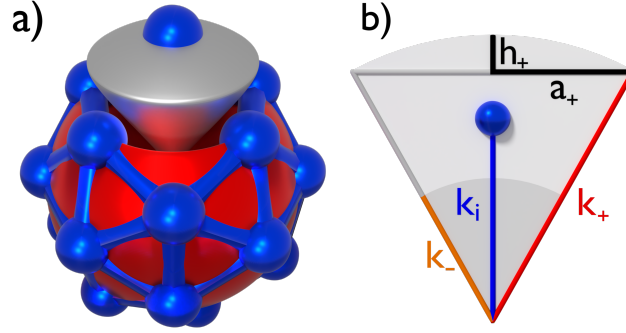
Figure 3.1: (a) Snub cube arrangement of 24 points on a spherical surface. A selected spherical sector (grey) is slightly lifted for illustrative purposes. (b) Cut through the spherical sector with assignment of several k-space distances discussed in the text.

where ΔV_k is the approximate volume element in k-space, and the continuum and discretized versions of coefficients and wave functions are related according to $c_n(\mathbf{k}_i, t) = (\Delta V_k)^{\frac{1}{2}} \tilde{c}_n(\mathbf{k}_i, t)$ and $\Phi_n = (\Delta V_k)^{\frac{1}{2}} \tilde{\Phi}_n$.

For the discretization of k-space, different approaches can be employed. Most simply, the Cartesian components of the k-vector can be discretized evenly, leading to the approximation of the volume element in k-space as

$$d^3\mathbf{k} \approx \Delta V_k = \Delta k_x \Delta k_y \Delta k_z. \tag{3.13}$$

While being conceptually straightforward (especially if the same spacing is used for all three spatial directions), this approximation may be considered not optimal if one aims at analyzing the free electrons in terms of directions and kinetic energies (the latter depending on the length of the k-vector). Therefore, we employed an alternative discretization scheme where the absolute values of the k-vectors were discretized such that a given energy region was evenly covered. For each energy value, the orientations of the k-vector were discretized by distributing points approximately uniformly on the corresponding spherical surface. This is equivalent to the well-known Thomson problem of finding the optimal placement of electrical charges on a sphere so as to minimize their repulsion energy. For the case of 24 points, the optimal distribution is exactly known and results in a snub cube as depicted in Figure 3.1a. For an arbitrary number of surface points, the optimal distribution can be approximately determined using, e.g., the Fibonacci sphere algorithm.[155] To determine the volume element covered by each point $\mathbf{k}_i$, we consider the volume difference of two spherical sectors with k-space radii k_+ and k_- (cf. Figure 3.1b) corresponding to the energies $E_\pm = E(\mathbf{k}_i) \pm \frac{\Delta E}{2}$, where ΔE is the fixed discretization width for the energies, such that

$$k_\pm = \sqrt{k_i^2 \pm \frac{m_e \Delta E}{\hbar^2}} \tag{3.14}$$

and hence

$$d^3\mathbf{k} \approx \Delta V_k = V_+ - V_- = \frac{2\pi}{3}(k_+^2 h_+ - k_-^2 h_-) \tag{3.15}$$

The height $h_\pm$ of the spherical cap can be expressed using the cap radius $a_\pm$ and the sphere radius $k_\pm$:

$$h_\pm = k_\pm - \sqrt{k_\pm^2 - a_\pm^2}, \tag{3.16}$$

leading to

$$\Delta V_k = \frac{2\pi}{3}\left(k_+^2\left(k_+ - \sqrt{k_+^2 - a_+^2}\right) - k_-^2\left(k_- - \sqrt{k_-^2 - a_-^2}\right)\right) \tag{3.17}$$

The cap radius $a_\pm$ is linearly dependent on the k-space radius $k_\pm$, $a_\pm = \tilde{a}k_\pm$, with $\tilde{a}$ being independent of the radius, which results in

$$\Delta V_k = \frac{2\pi}{3}\left(1 - \sqrt{1 - \tilde{a}^2}\right)\left(k_+^3 - k_-^3\right) = c\left(k_+^3 - k_-^3\right). \tag{3.18}$$

The diameter $2a_\pm$ of the spherical cap is taken as the average distance between a specific point on the sphere and the six points surrounding it. For the snub cube, this corresponds to a universal $\tilde{a}$ value of ≈ 0.39779. The sum of spherical cap surfaces obtained in this way results in a surface area deviating from the actual spherical surface by less than 3 % for the Fibonacci algorithm and only 1 % for a snub cube, and in a sphere volume of similar accuracy, therefore justifying the approximation.

As a next step, the discretized continuum state expansion obtained this way is inserted into the time-dependent Schrödinger equation 3.2 to derive the equations of motion for the electronic degrees of freedom, as detailed below.

3.2.2   Time-dependent Schrödinger equation in the discretized continuum approximation

After insertion into the time-dependent Schrödinger equation 3.2, the discretized continuum state expansion is projected on the electronic basis states, resulting in a set of coupled equations of motion for the bound and continuum state coefficients completely analogous to equation 3.4. In the expressions below, m, m' denote the bound electronic states of the anion, n, n' the bound electronic states of the neutral molecule, and i is the index counting the discretized scattering states of the detached electron:

$$\text{(bound)} \qquad i\hbar\dot{c}_m(t) = \sum_{m',\text{anion}}\left[H_{mm'}(\mathbf{R}[t]) - i\hbar D_{mm'}(\mathbf{R}[t])\right]c_{m'}(t)$$

$$+ \sum_{n',\text{neutral}}\sum_{i,\text{free}}\left[H_{mn'}(\mathbf{k}_i, \mathbf{R}[t])\right.$$

$$\left. - i\hbar D_{mn'}(\mathbf{k}_i, \mathbf{R}[t])\right]c_{n'}(\mathbf{k}_i, t) \tag{3.19}$$

$$\text{(continuum)} \qquad i\hbar\dot{c}_n(\mathbf{k}_i, t) = \sum_{m',\text{anion}}\left[H_{nm'}(\mathbf{k}_i, \mathbf{R}[t])\right.$$

$$\left. - i\hbar D_{nm'}(\mathbf{k}_i, \mathbf{R}[t])\right]c_{m'}(t) \tag{3.20}$$

with the diabatic and nonadiabatic couplings between two bound anion states,

$$H_{mm'} = \langle \Phi_m | \hat{H} | \Phi_{m'} \rangle \tag{3.21}$$

$$D_{mm'} = \langle \Phi_m | \dot{\Phi}_{m'} \rangle, \tag{3.22}$$

and between a bound and a discretized continuum state,

$$H_{nm'}(\mathbf{k}_i) = (\Delta V_k)^{\frac{1}{2}} \langle \tilde{\Phi}_n(\mathbf{k}_i) | \hat{H} | \Phi_{m'} \rangle \tag{3.23}$$

$$D_{nm'}(\mathbf{k}_i) = \langle \Phi_n(\mathbf{k}_i) | \dot{\Phi}_{m'} \rangle = (\Delta V_k)^{\frac{1}{2}} \langle \tilde{\Phi}_n(\mathbf{k}_i) | \dot{\Phi}_{m'} \rangle. \tag{3.24}$$

The coupling among the discretized continuum states has been neglected in the above equations.

3.2.3 Plane-wave approximation for continuum states

As we treat the electron detachment from anions, the continuum states $\tilde{\Phi}_n(\mathbf{k}_i)$ correspond to an antisymmetrized linear combination of a bound state of the neutral molecule and a molecular scattering state of the free electron,

$$\tilde{\Phi}_n(\mathbf{k}_i) = \mathcal{A} \left(\Phi_n^{(\mathrm{n})} \cdot \psi(\mathbf{k}_i) \right) \tag{3.25}$$

The simplest approximation to the scattering continuum, with asymptotic wave vector $\mathbf{k}_i$, is provided in such a case by using plane waves,

$$\psi(\mathbf{k}_i) \approx \mathcal{N} \mathrm{e}^{i\mathbf{k}_i \cdot \mathbf{r}}. \tag{3.26}$$

We set $\mathcal{N} = (2\pi)^{-3/2}$ such that for $\tilde{\Phi}_n(\mathbf{k}_i)$ the normalization condition 3.9 is fulfilled. For the *discretized* state $\Phi_n(\mathbf{k}_i)$, this corresponds to normalization within a spatial box of length $L = \frac{2\pi}{\Delta k}$, such that $\langle \Phi_n(\mathbf{k}_i) | \Phi_{n'}(\mathbf{k}_j) \rangle_{\mathrm{box}} = \delta_{nn'} \delta_{ij}$. The free electron state obtained this way bears no dependence on the molecular structure, which is a strong simplification. In order to include this dependence at least to a certain extent, we consider plane waves orthogonalized with respect to the occupied molecular orbitals (MOs) $\phi_m(\mathbf{r}, \mathbf{R}[t])$ of the anion,

$$\tilde{\psi}(\mathbf{k}_i) = (2\pi)^{-3/2} \left(\mathrm{e}^{i\mathbf{k}_i \cdot \mathbf{r}} - \sum_m^{\mathrm{occ}} \langle \phi_m | \mathrm{e}^{i\mathbf{k}_i \cdot \mathbf{r}} \rangle \phi_m \right) \tag{3.27}$$

$$= \psi(\mathbf{k}_i) - \sum_m^{\mathrm{occ}} \langle \phi_m | \psi(\mathbf{k}_i) \rangle \phi_m, \tag{3.28}$$

as has been also frequently done in the past for the calculation of photoionization cross sections.[78–80] The energy of such a discretized continuum state can be approximated as

$$E_n(\mathbf{k}_i) = E_n^{(\mathrm{n})} + \frac{k_i^2}{2m_e} \tag{3.29}$$

with $E_n^{(\mathrm{n})}$ as the electronic energy of the neutral molecule and $\frac{k_i^2}{2m_e}$ as the asymptotic kinetic energy of the free electron.

Employing this orthogonalized plane wave approximation, the matrix elements for the electronic couplings between the bound and continuum states can now be constructed as will be outlined in Sec. 3.2.4.

3.2.4   Electronic coupling

The molecular electronic wavefunctions employed in our approach are based on separate quantum chemical calculations for the anionic and the neutral molecule. Therefore, they are approximations to the bound eigenfunctions of the N- or $N-1$-electron Hamiltonian, respectively, and thus the bound-state N- or $N-1$-electron Hamiltonian matrices are considered diagonal. However, the N-electron continuum states are not determined self-consistently but constructed from the MOs of the neutral molecule and an orthogonalized plane wave approximating the free electron. Therefore, the Hamiltonian matrix elements between N-electron continuum and bound states are non-zero, i.e., a diabatic coupling appears due to the use of approximate continuum state wavefunctions. Additionally, dynamical nonadiabatic couplings due to the change of the electronic wavefunctions with the nuclear geometry occur as well in the time-dependent Schrödinger equation, in complete analogy to the case of bound-state dynamics. Below, we outline our approach to calculate these couplings in an approximate way.

Diabatic coupling

In the following, we consider ionization transitions between the electronic ground states of both the anionic and the neutral species. As a shorthand notation, we label by Φ_0 the electronic ground state of the anion, and by Φ_i the discretized continuum state where the neutral molecular core is also in the ground state and the free electron has wave vector $\mathbf{k}_i$. Thus, we can write the diabatic matrix element between these states as

$$H_{00}(\mathbf{k}_i) \equiv \langle \Phi_i | \hat{H} | \Phi_0 \rangle \equiv (\Delta V_k)^{\frac{1}{2}} V_{i0}^{\mathrm{dia}}(\mathbf{k}_i). \qquad (3.30)$$

We assume the two ground-state wavefunctions Φ_0 and Φ_i to be represented by single Slater determinants. For the bound anionic system, these are as usual constructed from the occupied anion molecular orbitals (MOs) ϕ_p. For the ionized system, the Slater determinant is formed from the orthogonalized plane wave $\tilde{\psi}(\mathbf{k}_i)$ and the occupied neutral MOs χ_n. The two wavefunctions are thus constructed by two mutually non-orthogonal sets of MOs. The derivation of matrix elements between such wavefunctions has been performed first by Löwdin.[156] Along these lines, we show in Appendix 3.6.1 that expansion with respect to the MOs leads to the following expression for the diabatic coupling:

$$\begin{aligned}
V_{i0}^{\mathrm{dia}}(\mathbf{k}_i) = &\sum_p \langle \tilde{\psi} | \hat{h} | \phi_p \rangle (-1)^{p+1} \det \mathbf{S}_{i,p} \\
&+ \sum_n \langle \tilde{\psi} \chi_n | \hat{v} | \sum_{q,p<q} (\phi_p \phi_q - \phi_q \phi_p) \rangle \\
&\times (-1)^{n+p+q-1} \det \mathbf{S}_{in,pq}, \qquad (3.31)
\end{aligned}$$

where $\hat{h}$ and $\hat{v}$ denote the usual one- and two-electron parts of the electronic Hamiltonian, $\det \mathbf{S}_{i,p}$ is the minor determinant obtained from the overlap ma-

trix

$$
\mathbf{S} = \begin{pmatrix}
\langle \tilde{\psi} | \phi_1 \rangle & \dots & \langle \tilde{\psi} | \phi_p \rangle & \dots & \langle \tilde{\psi} | \phi_N \rangle \\
\langle \chi_1 | \phi_1 \rangle & \dots & \langle \chi_1 | \phi_p \rangle & \dots & \langle \chi_1 | \phi_N \rangle \\
\dots & \dots & \dots & \dots & \dots \\
\langle \chi_n | \phi_1 \rangle & \dots & \langle \chi_n | \phi_p \rangle & \dots & \langle \chi_n | \phi_N \rangle \\
\dots & \dots & \dots & \dots & \dots \\
\langle \chi_{N-1} | \phi_1 \rangle & \dots & \langle \chi_{N-1} | \phi_p \rangle & \dots & \langle \chi_{N-1} | \phi_N \rangle
\end{pmatrix}, \tag{3.32}
$$

between bound- and continuum state orbitals by deleting the row of the plane wave $\tilde{\psi}(\mathbf{k}_i)$ and the column of the anion MO ϕ_p, while $\det \mathbf{S}_{in,pq}$ denotes the minor determinant obtained by deleting the rows of the plane wave and the neutral MO χ_n as well as the columns of the anion MOs ϕ_p and ϕ_q.

By expanding the neutral molecule's MOs with respect to the occupied and virtual anion MOs it can be shown that the one-electron contributions and those two-electron contributions associated with the occupied anion MOs vanish, as detailed in Appendix 3.6.1. Therefore, the final MO form of the diabatic coupling only includes electron-electron interactions between the plane wave and the virtual anion MOs on the one hand and the occupied anion MOs on the other hand:

$$
V_{i0}^{\mathrm{dia}}(\mathbf{k}_i) = \sum_{n}^{\mathrm{occ}} \sum_{u}^{\mathrm{virt}} \langle \chi_n | \phi_u \rangle \langle \tilde{\psi} \phi_u | \hat{v} | \sum_{q,p<q}^{\mathrm{occ}} (\phi_p \phi_q - \phi_q \phi_p) \rangle
$$
$$
\times (-1)^{n+p+q-1} \det \mathbf{S}_{in,pq}, \tag{3.33}
$$

where $\langle \chi_n | \phi_u \rangle$ denotes the overlap integral between an occupied neutral and a virtual anion MO. Inserting the definition of the orthogonalized plane waves and expansion of the MOs with respect to the atomic orbital (AO) basis, as described in detail in Appendix 3.6.2, finally leads to working equations for the diabatic coupling that involve overlap and electron-electron repulsion integrals between basis functions and/or plane waves:

$$
V_{i0}^{\mathrm{dia}}(\mathbf{k}_i) = \sum_{\lambda \mu \nu} \left[A_{\lambda \mu \nu} \left(\langle \mathbf{k}_i \lambda || \mu \nu \rangle - \sum_{\sigma} B_{\sigma} \langle \sigma \lambda || \mu \nu \rangle \right) + \right.
$$
$$
\left. \bar{A}_{\lambda \mu \nu} \left(\langle \mathbf{k}_i \lambda | \mu \nu \rangle - \sum_{\sigma} B_{\sigma} \langle \sigma \lambda | \mu \nu \rangle \right) \right] \tag{3.34}
$$

where the Greek indices denote AO basis functions and $\langle ab || cd \rangle = \langle ab | cd \rangle - \langle ab | dc \rangle$ is an antisymmetrized electron-electron repulsion integral. The prefactors $A_{\lambda \mu \nu}$, $\bar{A}_{\lambda \mu \nu}$ and B_{σ} are computed from AO expansion coefficients and overlap integrals as detailed in Appendix B, equations 3.78-3.80. As the appropriate basis functions for molecular calculations we employ Cartesian Gaussian functions of the form

$$
\varphi_\nu(\mathbf{r}) = \prod_{j=x,y,z} (r_j - A_{\nu,j})^{n_{\nu,j}} \, \mathrm{e}^{-\alpha_\nu (\mathbf{r} - \mathbf{A}_\nu)^2}, \tag{3.35}
$$

where $\mathbf{A}_\nu$ denotes the center of the Gaussian (usually an atomic position), and the $n_{\nu,j}$ are angular momentum quantum numbers.

The calculation of the diabatic coupling according to equation 3.34 thus involves four types of integrals:

Overlap integrals between MOs   These can be reduced to overlaps between Gaussian basis functions which are analytically calculated according to Ref.[157]

Overlap integrals between a Gaussian and a plane wave   These correspond to inverse Fourier transforms of the basis functions and are analytically calculated as

$$\langle \mathbf{k}|\nu\rangle = \frac{1}{(2\pi)^{3/2}} \int d^3\mathbf{r}\, e^{-i\mathbf{k}\cdot\mathbf{r}}\varphi_\nu(\mathbf{r}) \tag{3.36}$$

$$= \left(\frac{1}{2\alpha_\nu}\right)^{\frac{3}{2}} e^{-i\mathbf{k}\cdot\mathbf{A}_\nu - \frac{k^2}{4\alpha_\nu}}$$

$$\times \prod_{j=x,y,z} \left(\frac{-i}{2\sqrt{\alpha_\nu}}\right)^{n_{\nu,j}} H_{n_{\nu,j}}\left(\frac{k_j}{2\sqrt{\alpha_\nu}}\right), \tag{3.37}$$

where the $H_{n_{\nu,j}}$ are the Hermite polynomials of order $n_{\nu,j}$.

Electron-electron repulsion integrals between Gaussian basis functions   For these integrals, efficient analytical expressions have been derived in the literature and used in quantum chemical programs. In the present contribution, we employ the Rys quadrature method[158,159] as implemented in the `libcint`[160] library.

Electron-electron repulsion integrals between a plane wave and Gaussian basis functions   Analytical formulae for these integrals have been reported,[161,162] but are not commonly available in molecular quantum chemistry codes. As an efficient alternative, we instead employ approximate formulae based on the observation that, for most of the Gaussian functions in our basis set, the plane waves under consideration do not strongly change within the width of the Gaussian. Therefore, in the integral $\langle \mathbf{k}_i\lambda|\mu\nu\rangle$ it is reasonable to replace the plane wave by the first terms of its Taylor expansion around the center $\mathbf{R}_\mu$ of the Gaussian $\varphi_\mu(\mathbf{r}_1)$ according to

$$e^{-i\mathbf{k}_i\cdot\mathbf{r}_1} \approx e^{-i\mathbf{k}_i\cdot\mathbf{R}_\mu}\left[1 - i\mathbf{k}_i\cdot(\mathbf{r}_1 - \mathbf{R}_\mu)\right] \tag{3.38}$$

In this way, the integrals reduce to common Gaussian three-center two-electron integrals, which are also used as implemented in `libcint`. Systematic tests of the approximation are summarized in Table 3.1. We find good accuracy for small values of the plane wave energy, with discrepancies increasing with growing energies. Up to 0.5 eV, which represents the range most relevant for the present study, the errors are still moderate.

Table 3.1: Average values (in E_H) and errors (in %) of hybrid Gaussian-plane wave electron repulsion integrals $\langle \mathbf{k}_i \lambda | \mu\nu \rangle$ for vinylidene employing the d-aug-cc-pVDZ basis set. The molecular structure has been optimized at the DFT/ωB97XD/d-aug-cc-pVDZ level. I_{ex} denotes the exact integral, I_{ap} the approximate value according to equation 3.38. For each plane wave energy E, the average has been taken over all distinct integrals provided by the basis set as well as over 24 different k-vectors corresponding to the direction vectors of the vertices of a snub cube.

E/eV	$\langle |I_{ex}| \rangle$	$\frac{\langle |I_{ex}-I_{ap}| \rangle}{\langle |I_{ex}| \rangle}$	$\left\langle \frac{|I_{ex}-I_{ap}|}{|I_{ex}|} \right\rangle^{[a]}$
0.0015	0.249	$1 \cdot 10^{-3}$	13.0
0.1	0.276	$9 \cdot 10^{-2}$	19.7
0.5	0.275	0.5	31.3

[a] Average computed for all integrals with $|I_{ex}| > 10^{-16} \, E_H$.

Nonadiabatic coupling

The molecular wavefunctions Φ_0 and Φ_i of the bound anion and the continuum state are not strictly diabatic but still bear a dependence on the nuclear geometry. Therefore, in addition to the diabatic coupling, there is also residual nonadiabatic coupling

$$D_{i0}(\mathbf{k}_i) = \langle \Phi_i(t)| \frac{d}{dt} \Phi_0(t) \rangle \tag{3.39}$$

present, which we calculate employing a finite-difference approximation for the time derivative similar to the procedure presented in Ref.[163]:

$$D_{i0} \approx \frac{1}{2\Delta t} \Big(\langle \Phi_i(t)|\Phi_0(\tau) \rangle - \langle \Phi_i(\tau)|\Phi_0(t) \rangle \Big)$$

with $\tau \equiv t + \Delta t$. The quantity $\langle \Phi_i(t)|\Phi_0(\tau) \rangle$ reduces to a one-electron integral of the form

$$(\sqrt{N})^{-1} \langle \tilde{\psi}(\mathbf{k}_i, t)|\psi^D(t, \tau) \rangle, \tag{3.40}$$

involving the function

$$\psi^D(t, \tau) = \sqrt{N} \langle \Phi_0^{N-1}(t)|\Phi_0^N(\tau) \rangle_{1...N-1}. \tag{3.41}$$

which can be regarded as an analog to a molecular Dyson orbital, but with the N- and $N-1$-electron wavefunctions taken at different time steps, i.e., different molecular geometries. Inserting the definition of the orthogonalized plane wave $\tilde{\psi}(\mathbf{k}_i, t)$, equation 3.28, into expression 3.40 leads to

$$\langle \Phi_i(t)|\Phi_0(\tau) \rangle = (\sqrt{N})^{-1} \big[\langle \psi(\mathbf{k}_i)|\psi^D(t, \tau) \rangle$$
$$- \sum_n \langle \psi(\mathbf{k}_i)|\phi_n(t) \rangle \langle \phi_n(t)|\psi^D(t, \tau) \rangle \big]. \tag{3.42}$$

For the nonadiabatic couplings, this gives rise to the final expression

$$D_{i0}(\mathbf{k}_i) = \frac{(\Delta V_k)^{\frac{1}{2}}}{2\sqrt{N}\Delta t} \Big[\big\langle \psi(\mathbf{k}_i)|\psi^D(t,\tau)\big\rangle - \sum_n \big\langle \psi(\mathbf{k}_i)|\phi_n(t)\big\rangle$$

$$\times \big\langle \phi_n(t)|\psi^D(t,\tau)\big\rangle - \big\langle \psi(\mathbf{k}_i)|\psi^D(\tau,t)\big\rangle$$

$$+ \sum_n \big\langle \psi(\mathbf{k}_i)|\phi_n(\tau)\big\rangle \, \big\langle \phi_n(\tau)|\psi^D(\tau,t)\big\rangle \Big] \qquad (3.43)$$

The Dyson orbitals ψ^D are constructed following the procedure outlined by Humeniuk et al.,[140] which eventually leads to their representation as linear combinations of atomic basis functions,

$$\psi^D(t,\tau) = \sum_\nu c_\nu^D(t,\tau)\varphi_\nu(\tau), \qquad (3.44)$$

where the coefficients c_ν^D are computed from overlap integrals between the basis functions of the N- and $N-1$-electron systems at the respective time steps.

The integrals in equation 3.43 involving plane waves $\psi(\mathbf{k}_i)$, which correspond to inverse Fourier transforms of the respective Dyson or anion molecular orbitals, can thus be reduced to integrals of the type given in equation 3.37, e.g.,

$$\big\langle \psi(\mathbf{k}_i)|\psi^D(t,\tau)\big\rangle = \sum_\nu c_\nu^D \big\langle \mathbf{k}_i|\nu\big\rangle, \qquad (3.45)$$

while the overlap integrals $\langle \phi_n|\psi^D\rangle$ between anion MOs and Dyson orbitals reduce to overlaps between Gaussian basis functions.

3.2.5   Quantum-classical surface hopping dynamics

Having established the equations of motion for the nuclear and electronic degrees of freedom, equation 3.1 and equations 3.19/3.20, as well as the necessary energies and couplings, the coupled electron-nuclear dynamics can be described using the surface hopping methodology. Solving equations 3.19/3.20 along the nuclear trajectories provides us with the time-dependent electronic state coefficients $c_i(t)$. These are employed in a stochastic process to decide if a switch from the anionic state in which the trajectories are propagated to any of the states of the discretized ionization continuum occurs. Specifically, in every nuclear time step a hopping probability is calculated which depends on the electronic state populations $\rho_{ii} = |c_i|^2$ according to

$$P_{i\to j} = -\frac{\dot{\rho}_{ii}}{\rho_{ii}}\frac{\dot{\rho}_{jj}}{\sum_k \dot{\rho}_{kk}}\Delta t, \qquad (3.46)$$

for $\dot{\rho}_{ii} < 0$ (decrease of initial state population) and $\dot{\rho}_{jj} > 0$ (increase of final state population).[53,164] The sum over k in the denominator extends over all

possible final states with a growing population. For all other cases, the hopping probability is set to zero.

As a result of the hopping procedure, we are provided with the instant of time in which the autoionization takes place, as well as with the specific kinetic energy and k-vector of the generated free electron.

To ensure the energy conservation of the system, a hop is performed only if the total energy of a given trajectory (the anion's electronic energy $E_i^{(\mathrm{a})}$ plus kinetic energy $T^{(\mathrm{a})}$) is at least equal to the final state electronic energy (potential energy $E_j^{(\mathrm{n})}$ of the neutral molecule plus kinetic energy $E_{\mathrm{el}}(\mathbf{k}_i)$ of the free electron), and the kinetic energy of the neutral molecule, $T^{(\mathrm{n})}$ is rescaled accordingly such that

$$T^{(\mathrm{n})} = E_i^{(\mathrm{a})} + T^{(\mathrm{a})} - E_j^{(\mathrm{n})} - E_{\mathrm{el}}(\mathbf{k}_i). \tag{3.47}$$

Finally, from the hopping times of the individual trajectories a time-dependent anion population is generated by averaging over the full ensemble of trajectories.

3.2.6 Approximate description of adiabatic ionization

While the main focus of the present work lies on the description of vibration-induced autoionization, which is a nonadiabatic process, the possibility of a purely electronic mechanism without the exchange of energy between the electronic and nuclear degrees of freedom needs to be considered as well. Such mechanism, which we term *adiabatic* in the following, implies that during the course of a trajectory the electron detachment energy may become negative as a result of gradual changes of the nuclear geometry, i.e. the system gets unstable with respect to electron loss. In this situation, one of the system's electrons will form a free wavepacket which will rapidly spread in space, giving rise to a decreasing electron density near the cationic core. In order to obtain an approximate measure of the time scale of this ionization process, we have employed the following procedure for several sample trajectories: For each occurence of a negative VDE in the given trajectory, we take the HOMO of the last step where the electron was still bound (t_{initial}) and consider it as the initial free electron wavepacket. The latter is then propagated freely, and the expectation value of $\hat{r}^2$ (electronic spatial extent) as a function of time is calculated as a measure of the wavepacket spreading as detailed in Appendix 3.6.3. To relate this quantity in a simple way to a gradual population loss due to ionization, we consider the following model: The actual wavepacket is replaced by a $1s$-like spherically symmetric electron distribution giving rise to the same value of $\langle \hat{r}^2 \rangle$. At t_{initial}, for this distribution the radius of a sphere containing 99% of the probability is calculated. Subsequently, for each time step the integrated probability within the sphere is computed for the broadening distribution. As a result, a population decay curve is obtained, from which a half-life is determined. The average half-life obtained in these calculations is then employed in the actual simulations of the trajectory ensemble as a time constant to model an exponential population decay due to adiabatic ionization.

3.3   Computational Details

The electronic structure of vinylidene was described using density functional theory (DFT). Although the molecule is in principle small enough to afford the use of more accurate ab initio methods, our goal of simulating the dynamics over long time durations in the picosecond regime, as well as the potential applicability of our method to larger molecules, requires the use of a computationally efficient method. In order to serve this purpose in the optimal way, various combinations of the long-range-corrected functionals ωB97XD[166], LC-ωPBE[167] and CAM-B3LYP[168] and the basis sets 6-311++G**[169,170], (d)aug-cc-pVDZ[171–173] and (d)aug-cc-pVTZ[171–173] were employed to calculate the geometries, energetics and harmonic normal modes of both the anion and the neutral molecule within the Gaussian 09 program package[174]. The detailed results are presented in Table 3.2 together with data obtained with CCSD[175,176]/(d-)aug-cc-pVDZ[171–173] and experimental and CCSD(T) data from the literature.[104,146,165] Inspection of Table 3.2 makes clear that among the DFT functionals, ωB97XD provides the best agreement to the experimental and higher-level theoretical data. In an attempt to balance computational cost and the capability of the employed method to properly describe the spatially diffuse electron distribution of the vinylidene anion, we chose to combine ωB97XD with the d-aug-cc-VDZ basis set[173] for use in the trajectory calculations. The initial conditions for all dynamics simulations have been obtained by sampling a quantum phase space distribution. Since the autoionization takes place after vibrational excitation of the molecule, we determined the initial conditions from harmonic normal mode displacements according to the distribution function $P_v^\nu(Q_\nu, P_\nu) = |\chi_v^\nu(Q_\nu)|^2 |\tilde{\chi}_v^\nu(P_\nu)|^2$, where $\chi_v^\nu(Q_\nu)$ and $\tilde{\chi}_v^\nu(P_\nu)$ are the harmonic oscillator wavefunctions of normal coordinate ν in position and momentum space, respectively. We set $v = 1$ for selected normal modes according to the experimental findings, and $v = 0$ otherwise. Specifically, we considered the situation where both a single quantum of the C-C stretching (ν_2) and of the antisymmetric C-H stretching mode (ν_5) are excited, corresponding to the most intense autoionization resonance K observed by DeVine *et al*[25,82], and propagated 100 trajectories for a total simulation time of 3 ps using the d-aug-cc-pVDZ basis set.

The propagation of the nuclei was performed by numerically solving Newton's equations of motion using the velocity Verlet algorithm[49] with a time step of 0.2 fs. By solving the time-dependent Schrödinger equation in the manifold of the electronic ground state of the vinylidene anion and a large number of discretized continuum states corresponding to the neutral ground state and the detached electron (as detailed below) the electronic degrees of freedom were propagated using Adams's method as implemented in the `ode` class of Python's `scipy.integrate` module[177] with a time step of $2 \cdot 10^{-3}$ fs. For the description of the continuum states, an evenly spaced grid of kinetic energies between 0.0 and 1.5 eV was employed. For each kinetic energy, the spatial orientations were chosen to evenly cover a spherical surface according to the Fibonacci sphere distribution. The quality of different discretization schemes

Table 3.2: Comparison of adiabatic electron affinities (AEA), structural parameters and vibrational wavenumbers of vinylidene. The normal modes are denoted as: ν_1: symmetric C-H stretch, ν_2: C-C stretch, ν_3: CH$_2$ scissoring, ν_4: out-of-plane bending, ν_5: antisymmetric C-H stretch, ν_6: CH$_2$ rocking. Normal mode wavenumbers in parentheses are harmonic, the remaining ones anharmonic.

	AEA / eV	r_{CC} / Å	r_{CH} / Å	α_{HCC}	ν_1	ν_2	ν_3	ν_4	ν_5	ν_6
					vib. modes / cm^{-1}					
ωB97XD										
6-311++G**	0.5760	1.337	1.108	123.6	2632	1485	1316	768	2580	869
aug-cc-pVDZ	0.5830	1.341	1.111	123.5	2622	1470	1294	734	2574	847
d-aug-cc-pVDZ	0.5865	1.341	1.111	123.5	2621	1470	1292	732	2571	844
					(2866)	(1531)	(1339)	(775)	(2839)	(874)
d-aug-cc-pVTZ	0.5434	1.332	1.105	123.6	2628	1488	1309	767	2571	861
CAM-B3LYP										
6-311++G**	0.6350	1.333	1.107	123.6	2686	1496	1325	780	2626	875
d-aug-cc-pVDZ	0.6463	1.341	1.112	123.5	2694	1497	1304	777	2647	865
LC-ωPBE										
6-311++G**	0.6931	1.333	1.105	123.4	2759	1525	1329	797	2739	883
d-aug-cc-pVDZ	0.6992	1.341	1.110	123.4	2767	1541	1312	797	2774	880
CCSD										
aug-cc-pVDZ	0.3911	1.364	1.117	123.5	(2894)	(1513)	(1341)	(784)	(2877)	(888)
d-aug-cc-pVDZ	0.3961	1.364	1.117	123.5	(2892)	(1512)	(1340)	(777)	(2875)	(885)
CCSD(T)										
aug-cc-pVDZ[a]		1.3668	1.1187	123.53	2667	1462	1289	748	2621	846
Experiment										
	0.4866[b]				2663[c]	1485[d]	1305[d]		2606[c]	

[a] Ref.165 , [b] Ref.82 , [c] Ref.104 , [d] Ref.146

Table 3.3: Discretization parameters used for a sample trajectory. The boxed "x" indicates the choice of parameters used for the ensemble of trajectories.

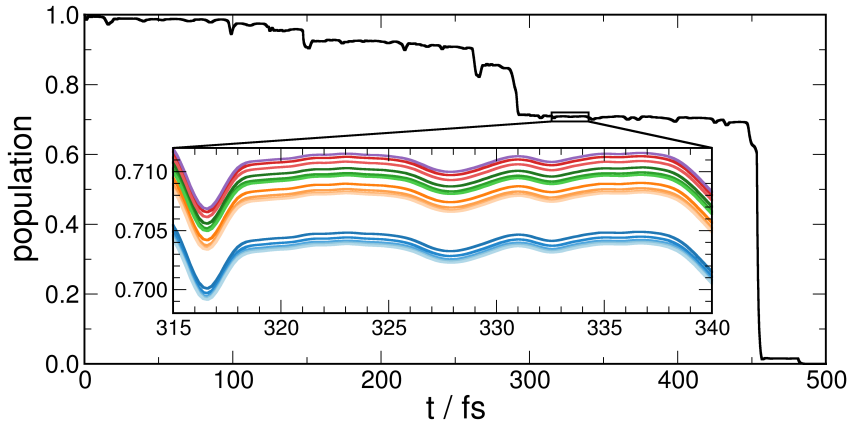| Different	Orientations per energy				
energies	24	48	96	192	384
500	x	x	x	x	x
1000	x	x	x̲	x	
2000	x	x	x		
4000	x	x			
8000	x				

Figure 3.2:   Anion populations for a sample trajectory run with different numbers of discretized continuum states according to Table 3.3. The colors represent the discretization scheme as follows: Blue, orange, green, red, and violet correspond to 24, 48, 96, 192, and 384 orientations, while the number of energies in each group increases from darker to lighter colors.

was assessed by running a sample trajectory with identical initial conditions for various total numbers of kinetic energies and orientations, as summarized in Table 3.3. The outcome in terms of anion populations are shown in Figure 3.2 and make clear that generally, very similar results are obtained for the tested parameters. The largest population difference is less than 1 % between the settings employing the most vs. the least number of plane waves. Besides the settings with 24 orientations, which stand a bit off (blue curves in Figure 3.2), the population differences for the other cases are even smaller, around 0.4 %. As a compromise between a reasonable number of plane waves and computational efficiency, we finally chose a total of 1000 energies and 96 orientations per energy, thus a number of 96000 k-vectors, for the simulation of the complete trajectory ensemble. This corresponds to the middle green curve in Figure 3.2.

Employing the respective discretization scheme the system of coupled equations 3.19 and 3.20 was set up, the diabatic and non-adiabatic couplings were evaluated and the state coefficients calculated. The hopping probabilities were determined in each nuclear time step from the rate of change of the electronic populations according to equation 3.46.
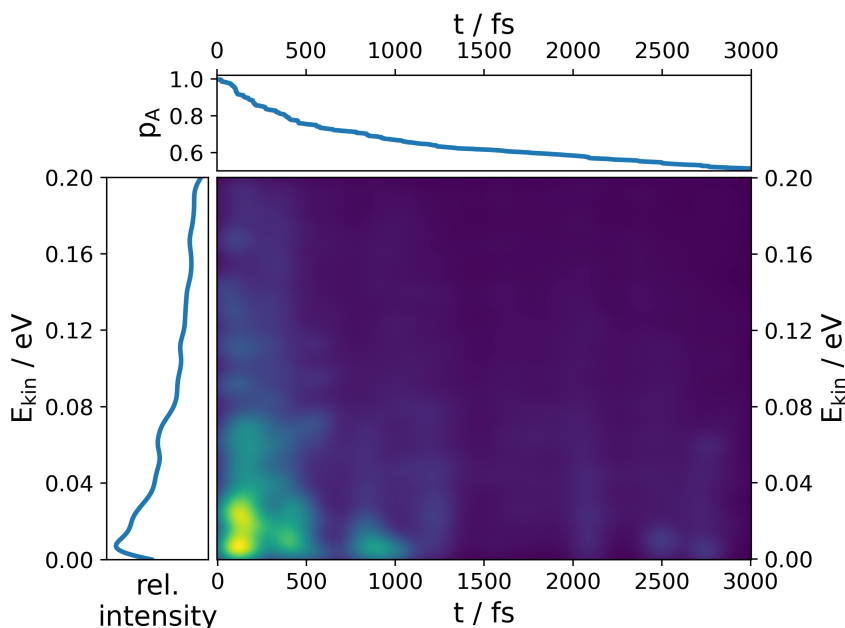
Figure 3.3: Autoionization of vinylidene anions for excitation of the C-C stretching and the antisymmetric C-H stretching vibration ($2_1 5_1$) using the d-aug-cc-pVDZ basis set. Upper panel: Time-dependent anion population. Left panel: Time-integrated electron kinetic energy distribution. Middle panel: Time-resolved kinetic energy spectrum.

Since our interest is focused on the course of the ionization process rather than on the fate of the resulting neutral species, we do not propagate the trajectories in the neutral state once a hop has occurred. This in turn allows us to employ a modification of the surface hopping scheme to improve the hopping statistics: Each trajectory is propagated in the anionic state over the full simulation time, and initially, a "trajectory population" of 1000 is assigned to it. In each nuclear time step, hopping is attempted as many times as given by the actual trajectory population, which is then reduced according to the number of successful hops. This procedure is actually equivalent to propagating each set of initial conditions 1000 times. If desired, sequel trajectories in the neutral state could be run nonetheless in order to study the dynamics after the ionization has taken place.

3.4 Results and Discussion

Experimentally, autoionization of vinylidene can be induced by infrared excitation of specific normal modes featuring energies above the electron detachment threshold.[25,104] For vibrationally cold molecules, this applies notably to combinations of the C-C stretching and the C-H stretching vibrations, which are visible as pronounced resonances in the photodetachment spectrum.[25] In our dynamics simulations, we model this situation by sampling initial normal coordinates and momenta from a phase space distribution function accounting for the vibrational excitation as described in the Computational Section. The

coupled electron-nuclear dynamics is then simulated employing equation 3.1 for the nuclei and equations 3.19 and 3.20 for the electronic degrees of freedom.

In the following, we consider excitation of the modes ν_2 (C-C stretch) and ν_5 (antisymmetric C-H stretch), which corresponds to the photodetachment peak K in Ref.[25] and is henceforth abbreviated as $2_1 5_1$. The simulation gives rise to autoionization events producing free electrons of specific kinetic energies which can be arranged in a two-dimensional time-resolved kinetic energy spectrum as presented in Figure 3.3. The plot shows the highest intensity in the time range below 500 fs with energies mostly between 0.0-0.04 eV and a maximum at 0.01 eV. For later times the intensity is weaker and remains maximal around 0.01 eV with almost no intensity above 0.02 eV. Integration over the energies yields the total time-dependent ionization intensity, corresponding to the anion population shown in the upper part of Figure 3.3, which exhibits a decrease by 50 % within 3 ps. The time-integrated energy distribution of the ejected electrons presented in the left part of Figure 3.3 exhibits a maximum around 0.01 eV.

These results can be confronted with the experimental data from Ref.[25], where electrons with a constant kinetic energy of about 115 cm^{-1} (0.0143 eV) were reported to result from excitation of the $2_1 5_1$ peak in the photodetachment spectrum. Our kinetic energies are in very good agreement with the experimental data, although more broadly dispersed. This can be expected due to the classical description of the vibrational motion, where no discrete vibrational energy level structure is included in our simulations. Nonetheless, our approach provides for the first time data on the expected time scales of the autoionization (which is discussed in more detail below) and allows us to analyse the underlying dynamical mechanism.

For this purpose, in the first place we investigate how the molecular structures have changed at the time of the ionization transitions compared to the initial conditions. These changes can be visualized by the distribution of structural parameters (bond lengths, angles) for the whole ensemble of trajectories, as presented in Figure 3.4 for the bond lengths and in Figure 3.5 for several angles. With regard to bond lengths, ionization preferably takes place for shorter values of the C-C bond (Figure 3.4a). This is consistent with the finding that the equilibrium C-C bond length is shorter in neutral vinylidene (anion: 1.34 Å, neutral: 1.30 Å), and this situation is even more pronounced in actetylene (1.21 Å), whose anion is not bound at all (values obtained using DFT, ωB97XD/d-aug-cc-pVDZ). For the C-H bonds there is a tendency avoiding very large and, to a lesser extent, very small values, thus approaching the value for the equilibrium structure (cf. Figure 3.4b and c). For the angles (Figure 3.5), there is a clear increase of the larger C-C-H angle (α), and a decrease of the smaller one (β), while the H-C-H angle (γ) only marginally increases. This can be conceived as the whole CH$_2$ group bending with respect to the C-C bond axis, leading to a T-shaped structure.

The correlation between the two parameters most distinctly deviating from the initial values, the C-C distance and the C-C-H angle β, is illustrated more
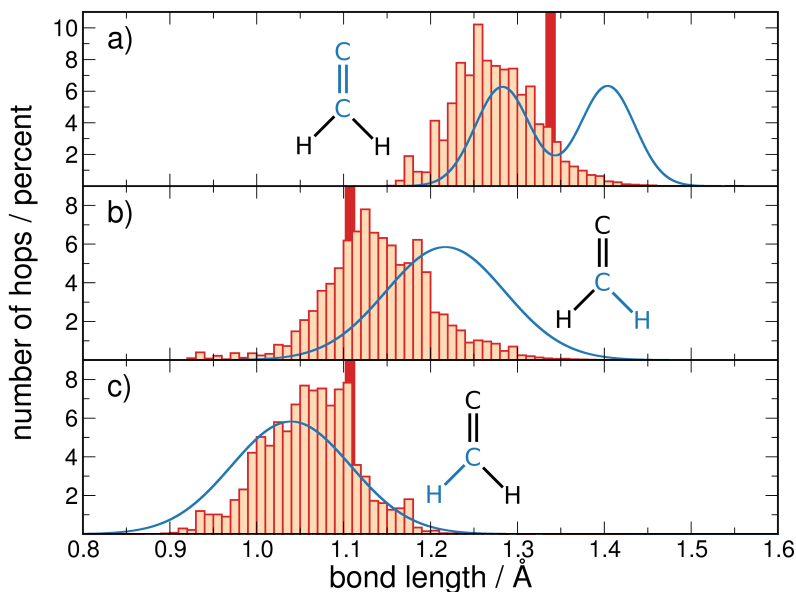
Figure 3.4: Distribution of bond lengths at the transition to the ionized state (orange bars) and at $t = 0$ (blue curve). The values for the minimum energy structure are given as thick red bars. (a) C-C bond, (b) the longer of the two C-H bonds, (c) the shorter of the two C-H bonds. Notice, that the blue curves do not maximize at the equilibrium values due to the use of vibrationally excited initial conditions.
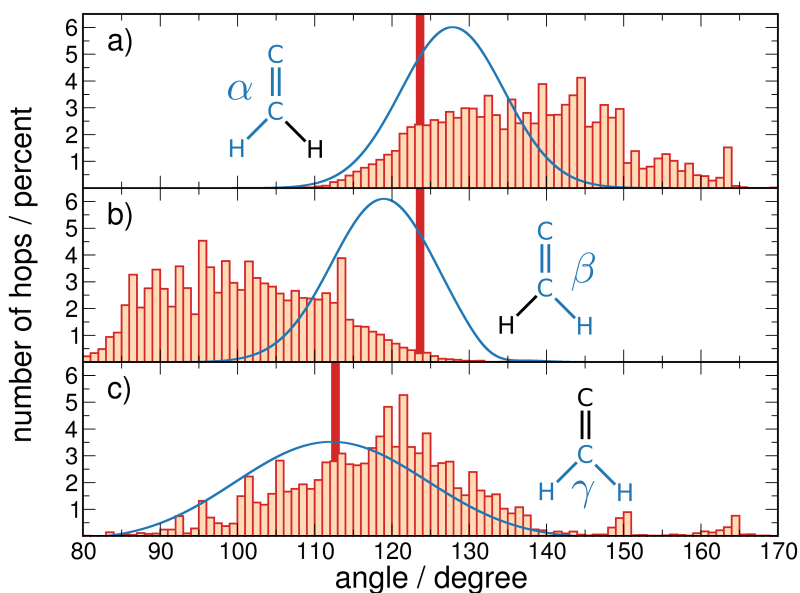

Figure 3.5: Distribution of bond angles at the transition to the ionized state (orange bars) and at $t = 0$ (blue curve). The values for the minimum energy structure are given as thick red bars. (a) larger C-C-H angle, (b) smaller C-C-H angle, (c) H-C-H angle.
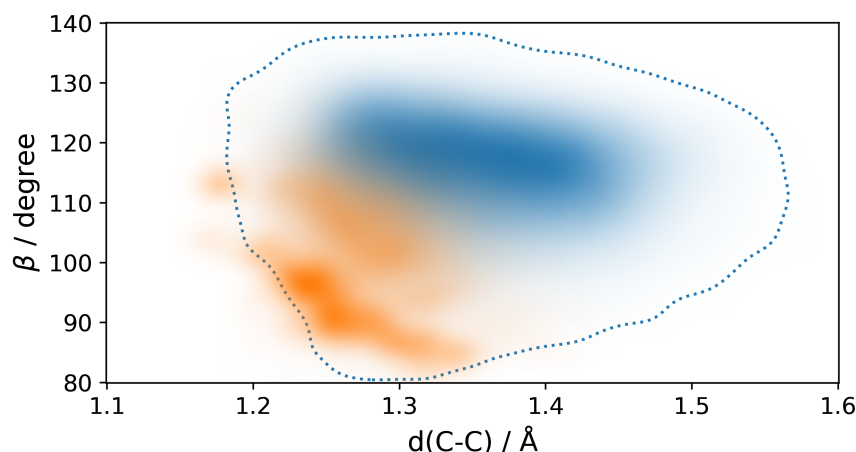
Figure 3.6: Correlation of C-C distance and the smaller C-C-H bond angle β, shown both at the ionization events (orange) and at all instants of time during the dynamics (blue). More intense color indicates more occurrences of the respective bond length/angle combination. The blue dotted curve represents a contour line with 1 % of the maximum value of the blue distribution.

explicitly in Figure 3.6, where the blue area marks the full range of values reached throughout the dynamics simulation while the red area indicates the distribution at the ionization events. The data shows that ionization occurs preferably at geometries with shortened C-C bonds and decreased C-C-H angle. This implies the formation of structures approaching a T-shaped geometry with short C-C bonds, which is known to be the first step in the isomerization from vinylidene to linear acetylene.[154] Since anionic acetylene is unstable with respect to electron loss, it is clear that such a process will be accompanied by autoionization.

Furthermore, the angular distribution of ejected electrons can be analysed from our simulation data. In Figure 3.7, this has been accomplished in the form of a Mollweide projection,[178] which is an equal-area, pseudocylindrical map projection of a sphere onto a plane. Each point on the plane corresponds to a direction characterized by the polar and azimuthal angle, θ and φ. In the Figure, regions of high electron intensity are marked by bright yellow color, regions of low intensity by dark color. A distinct anisotropy can be observed with electrons primarily ejected at φ values around 90º and 270º, i.e., within the molecular plane. Also for θ, an anisotropy is discernible, with preferred values around 45º and 150º. This distribution is paralleled by a Dyson orbital calculated for an "average ionization" structure, which has been obtained by averaging all structures at which ionization transitions occurred (see Figure 3.7b). The corresponding electron distribution is similar to a d-type orbital situated in the molecular plane. Electron ejection preferentially takes place in the directions of the orbital lobes within the molecular plane, while relatively few electrons leave perpendicular to this plane.

Having established some structural features promoting autoionization, the question remains at which time scales these are exhibited and how they influence the energetics and couplings governing the ionization efficiency. To this
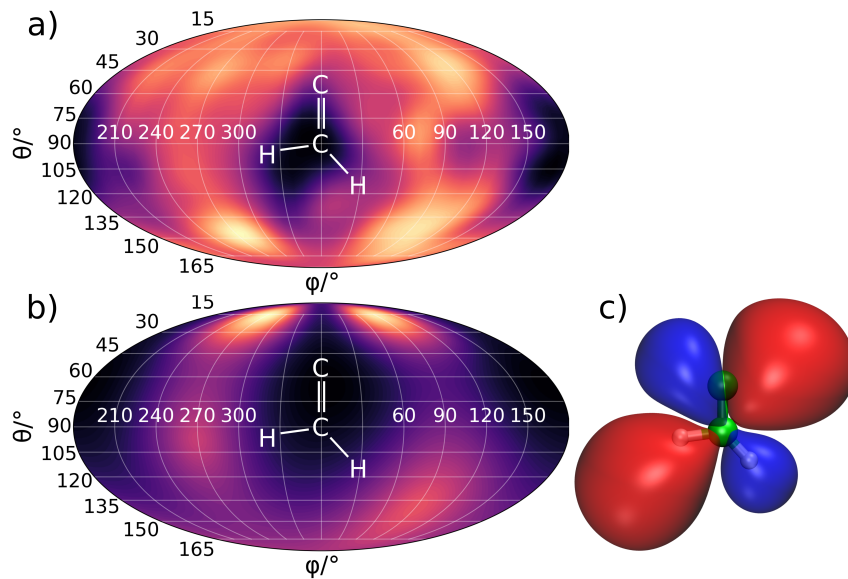
Figure 3.7: (a) Mollweide projection of the angular distribution of ejected electrons summed over all energies. The bright yellow regions indicate large, the dark ones low electron intensity. Overall, the darkest areas feature about 2/3 of the intensity of the brightest ones; (b) Probability density of the Dyson orbital for a mean "ionization geometry" obtained by averaging all structures at which ionization transitions occurred. The electron distribution has been integrated up to 10 Å from the center of mass of the molecule. (c) Surface plot of the Dyson orbital obtained with a cutoff value of 0.01; the molecular plane represents the yz-plane, to which the direction given by $(\theta, \varphi) = (90°, 0°)$ is perpendicular.

end, we analyse in the following the temporal evolution of two sample trajectories in terms of geometric changes and electronic couplings. The trajectories have been chosen such that one exhibits a moderate, the other a strong ionization efficiency. For the moderately efficient trajectory presented in Figure 3.8, the dynamics is characterized by small-amplitude nuclear vibrations without significant structural deformations. Ionization events, which are manifest by a dropping anionic population (cf. Figure 3.8a), preferably occur at small C-C distances and low VDEs, as indicated by the grey bars at 80 and 1340 fs. In these particular regions, the coupling (which is presented as a running average for better comprehensibility) between the bound and ionized states exhibits broad maxima, exceeding the average coupling present at other times. One can also see an overall increased coupling strength with larger times, leading to a gradual increase in population loss for this trajectory. The final anionic population reaches about 40 %.

For the strongly ionizing trajectory illustrated in Figure 3.9, the situation is different insofar as large-amplitude nuclear motion takes place. Specifically, the C-H bonds exhibit intense vibrations from 300 fs onwards, until ultimately at 1200 fs a geometry is adopted in which one of the hydrogens migrates from one carbon atom to the other, giving rise to an acetylene-like structure. Since anionic acetylene is electronically unstable, this means that the system should now be actually composed of a neutral acetylene molecule and a free electron. Ionization is achieved efficiently by an "adiabatic" electronic mechanism in this
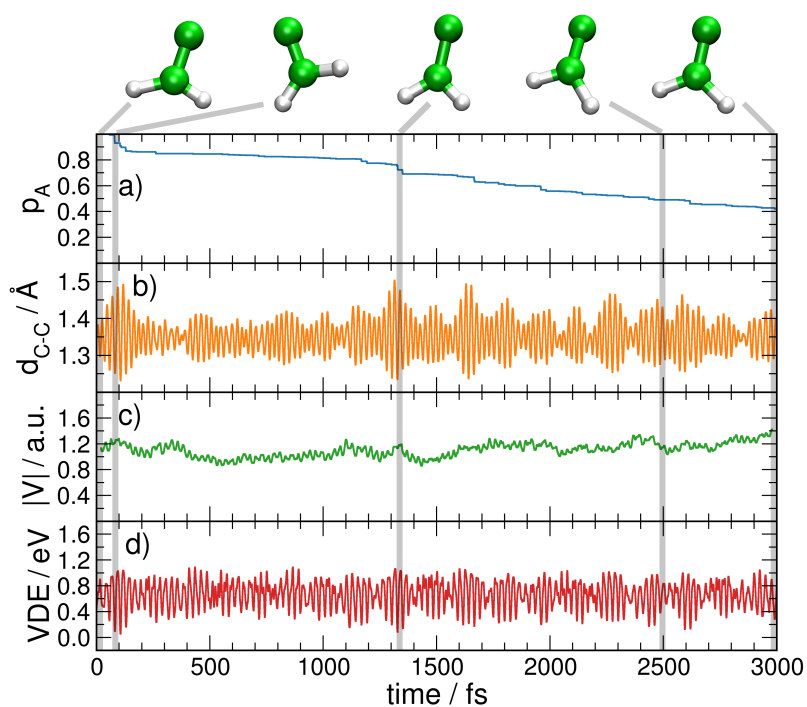
Figure 3.8:   Analysis of a moderately ionizing trajectory. (a) anion population, (b) C-C bond length, (c) average coupling into the ionization continuum, (d) vertical detachment energy (VDE).
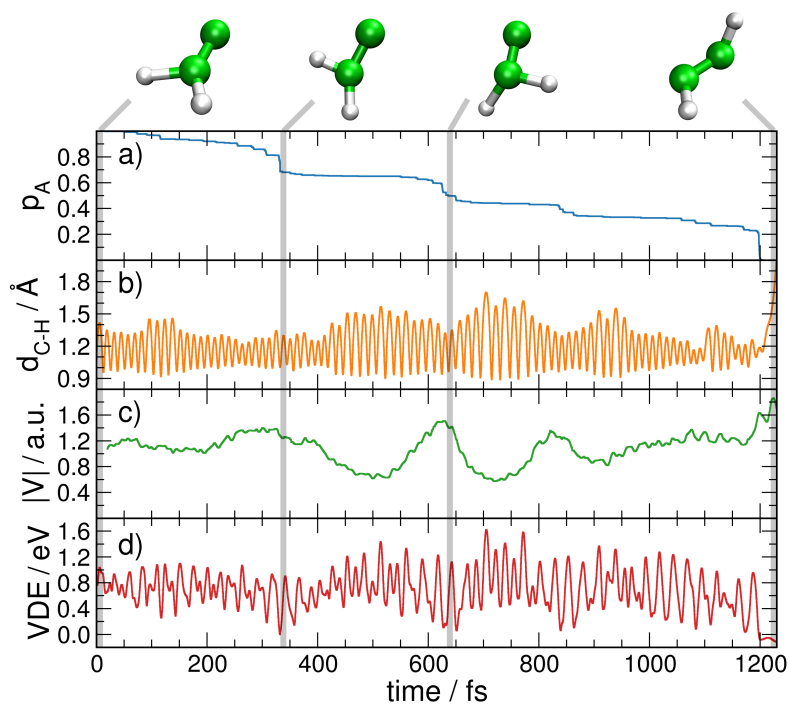

Figure 3.9:   Analysis of a strongly ionizing trajectory. (a) anion population, (b) C-H bond length, (c) average coupling into the ionization continuum, (d) vertical detachment energy (VDE).
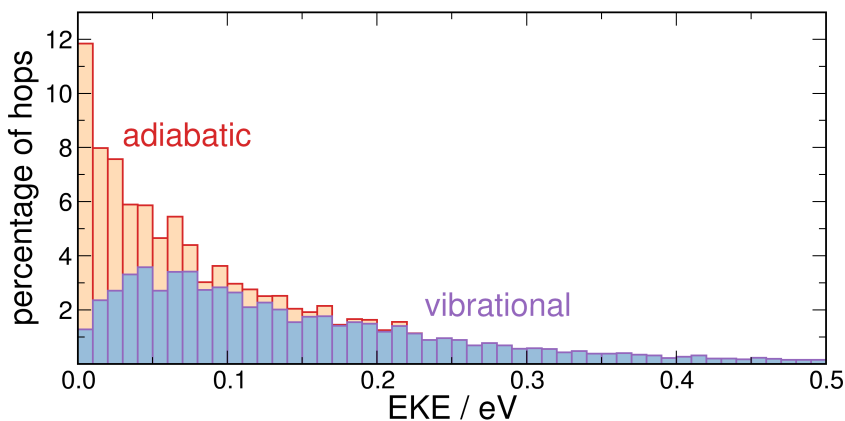
Figure 3.10: Stacked column chart showing the kinetic energy distribution in terms of hopping events pertaining to the vibrational (positive VDE, blue bars) and adiabatic (negative VDE, orange bars) ionization mechanisms.

case, i.e. the continuous change in nuclear configuration gradually lowers the VDE until a negative value is reached. The use of a doubly-augmented Gaussian basis set allows for an approximate modelling of this process, although the ultimately the localized nature of the basis set prevents a full description of an electron moving away from the molecule. Instead, an artificial rebound of the electron would be observed for sufficiently long simulation times. What should happen in reality, though, is a fast dispersion of the unbound electron wavefunction, leaving behind neutral acetylene. To grasp an approximate time scale of this ionization mechanism, we have modelled the wavepacket dispersion according to the procedure described in Section 3.2.6, which results in a very fast decay of the anionic population once a negative VDE occurs. Having reached zero population, the respective trajectories are aborted (e.g., at 1200 fs for the trajectory shown in Figure 3.9. It should be noted in these cases two different autoionization mechanisms are observed: On the one hand the nonadiabatic vibration-induced autoionization, which is induced by the electronic couplings discussed in Section 3.2.4 and is accompanied by energy redistribution between the electronic and nuclear degrees of freedom, and on the other hand the aforementioned purely electronic adiabatic mechanism which is active as soon as molecular geometries with a negative VDE are reached (at, e.g., around 330 fs, 630 fs and 1200 fs in Figure 3.9). In this situation, the electron configuration itself becomes unstable, and the excess electron can move away without the need of energy gain from the nuclear system. This mechanism occurs in 25 of 100 trajectories and is responsible for 35 % of all ionization events in the present simulation. The time scale of free electron dispersion is around 1 fs on average. The decomposition of the kinetic energy spectrum with respect to the two mechanisms is illustrated in Figure 3.10, showing that the adiabatic mechanism preferably results in low energy electrons.

The presence of two autoionization mechanisms together with the fact that individual trajectories may ionize on different time scales necessitates a more comprehensive analysis of the temporal characteristics of the ionization pro-
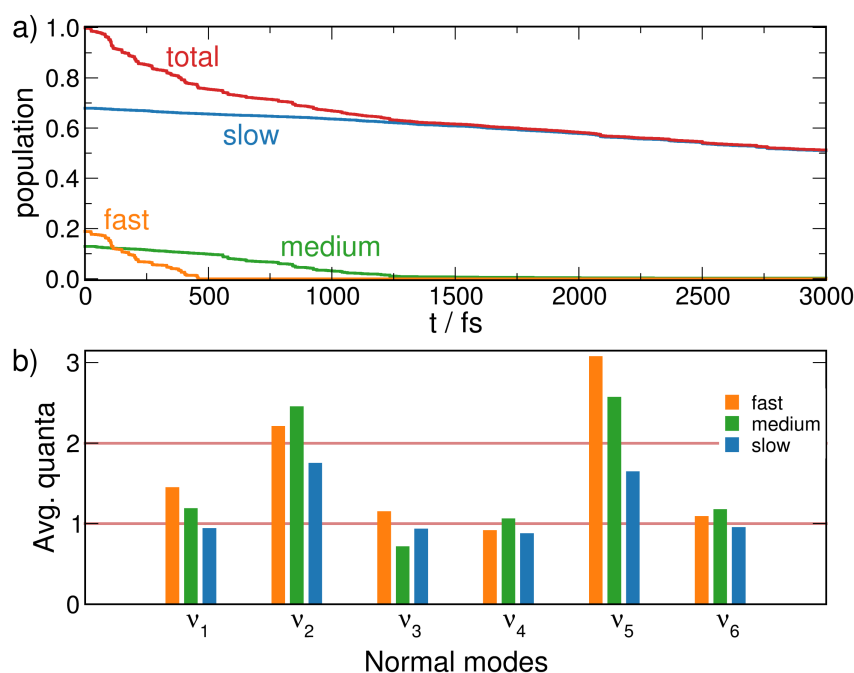
Figure 3.11: (a) Decomposition of the total anion population (red) according to the speed of ionization of the underlying trajectories. Fast trajectories (orange) lose 50% of their population within 500 fs, medium ones (green) within 1500 fs and slow ones (blue) need more than 1500 fs. (b) Group-averaged energy distribution of the initial conditions in terms of normal mode vibrational quanta.

cess. To this end, the population curve from Figure 3.3 is replotted in Figure 3.11a (red curve). Inspection of this curve already hints at different underlying time scales, as within the first 500 fs the it decreases more steeply than afterwards.

This finding can be made more quantitative by arranging the trajectories into groups according to the speed of the ionization process. Specifically, we define three groups by asking when the individual trajectory population has decreased below 50 %: For the fast group, this occurs within the first 500 fs of the dynamics, for the medium group between 500 and 1500 fs, and for the slow group at times beyond 1500 fs. The resulting decomposition of the anionic populations is presented in Figure 3.11a, proving that the initial drop of the total population (red curve) within the first 500 fs is indeed due to only a small fraction of trajectories (orange curve). Besides another part that ionizes in an intermediate time range (green curve), the largest subgroup consists of trajectories ionizing only slowly within the simulation time (blue curve).

With regard to adiabatic ionization, we find that it is exhibited mostly by trajectories of the fast group (64%), while the medium and slow groups only amount 24 and 12 %, respectively. Within the groups, the mechanism occurs in a large majority of the fast trajectories (84%), while it is much rarer in the medium (46%) and slow (4%) groups.

To explain the different behavior of the three groups, we analysed the initial energy distribution of the trajectories in terms of averaged harmonic normal

mode quantum numbers as shown in Figure 3.11b. The general appearance of the plotted average quanta per normal mode and trajectory group reflects the fact that the employed initial conditions feature vibrational excitation (i.e. 2 quanta) in modes 2 and 5, while for the others the vibrational ground state was populated (1 quantum). Overall, for the two excited modes 2 and 5 as well as for mode 1, the slow group clearly exhibits the lowest average quantum numbers. For mode 5, the differences are most pronounced, with the fast group being excited on average by about 3 quanta, while for the slow group an average quantum number well below two is observed. However, for the other excited mode (2), differences between the groups are smaller, and the highest average quantum number is observed for the "medium" group, although both the medium and fast groups exhibit average quantum numbers above two. Generally, higher initial quantum numbers correlate with faster ionization, and for mode 2 (C-C bond stretching), this can be directly linked to the fact that for elongated C-C bonds the VDE is reduced. Even stronger reduction of the VDE would be expected for motion towards T-shaped or acetylene-like structures, as promoted by the CH_2 rocking mode (mode 6). This mode is not directly excited at the beginning, but seems to be sufficiently strongly coupled to modes 5 and 1 (antisymmetric and symmetric C-H stretch) such that excitation of the latter also contributes to faster ionization time scales.

3.5 Conclusion

We have presented a generally applicable method for the simulation of vibration-induced autoionization dynamics in molecules. Our approach is based on the mixed quantum-classical surface hopping scheme where the nuclei are propagated classically while the electronic degrees of freedom are treated quantum mechanically. The electronic states considered include (i) the bound states of the molecular anion, which are described using quantum chemical methods employing sufficiently diffuse basis sets, and (ii) the ionized system composed of the neutral molecular core (also treated by standard quantum chemical methods) and the free electron, which is approximated by orthogonalized plane waves. The ionization continuum is discretized and represented by a large set of individual discrete box-normalized states. The electronic couplings necessary to describe the transitions between the bound and ionized molecular states consist of two contributions: (i) the nonadiabatic couplings due to the change of the anion and neutral electronic wavefunctions as a function of the nuclear coordinates, and (ii) a diabatic coupling between anionic and neutral states which results from the fact that the ionized-state wavefunction is not obtained self-consistently, but is constructed from individually computed neutral molecular and free electron wavefunctions. In addition to the ionization mechanism mediated by these couplings, we also include in our treatment a purely electronic effect which occurs when due to the nuclear motion the anionic wavefunction "adiabatically" becomes unbound without direct coupling to the nuclear degrees of freedom.

We have illustrated our approach by simulating the autoionization dynamics of the vinylidene anion following vibrational excitation. Our results provide for the first time an estimate for the time scale of this process which has been previously studied experimentally[25] and allow us to link the ionization efficiency to specific geometrical deformations of the molecules as well as to the choice of initial conditions in terms of vibrational excitation. Our methodology can be straightforwardly applied to more complex molecules, providing a means to assess the autoionization dynamics for cases well beyond the reach of full quantum wavepacket based simulations.

Acknowledgments

Author declarations

Conflict of interest

The authors have no conflicts to disclose.

Author contributions

Kevin Issler: Data curation (lead); Formal analysis (equal); Investigation (lead); Methodology (equal); Software (lead); Visualization (lead); Writing - original draft (equal).
Roland Mitrić: Conceptualization (equal); Funding acquisition (lead); Methodology (supporting); Project administration (lead); Resources (lead); Supervision (equal); Writing - review & editing (equal).
Jens Petersen: Conceptualization (equal); Formal analysis (equal); Methodology (lead); Software (supporting); Supervision (equal); Visualization (supporting); Writing - original draft (equal), Writing - review & editing (equal).

Data availability

The data that support the findings of this study are available from the corresponding author upon reasonable request.

3.6 Appendix

3.6.1 Derivation of diabatic coupling

In the following, the diabatic coupling elements between a bound anion ground state, $|\Phi_0\rangle$, and a singly-ionized continuum state, $|\Phi_i(\mathbf{k}_i)\rangle$, which are both approximated by a single Slater determinant will be derived. The two determinants read:

$$|\Phi_0\rangle = \frac{1}{\sqrt{N!}} \begin{vmatrix} \phi_1(1) & ... & \phi_N(1) \\ ... & ... & ... \\ \phi_1(N) & ... & \phi_N(N) \end{vmatrix} \tag{3.48}$$

$$|\Phi_i(\mathbf{k}_i)\rangle = \frac{1}{\sqrt{N!}} \begin{vmatrix} \tilde{\psi}(\mathbf{k}_i,1) & \chi_1(1) & ... & \chi_{N-1}(1) \\ ... & ... & ... & ... \\ \tilde{\psi}(\mathbf{k}_i,N) & \chi_1(N) & ... & \chi_{N-1}(N) \end{vmatrix}, \tag{3.49}$$

where ϕ_i denotes anion MOs, χ_i neutral MOs, and $\tilde{\psi}(\mathbf{k}_i)$ is the orthogonalized plane wave describing the free electron. For later convenience, we also define the overlap matrix between the two sets of orbitals:

$$\mathbf{S} = \begin{pmatrix} \langle\tilde{\psi}|\phi_1\rangle & ... & \langle\tilde{\psi}|\phi_N\rangle \\ \langle\chi_1|\phi_1\rangle & ... & \langle\chi_1|\phi_N\rangle \\ ... & ... & ... \\ \langle\chi_{N-1}|\phi_1\rangle & ... & \langle\chi_{N-1}|\phi_N\rangle \end{pmatrix}. \tag{3.50}$$

The diabatic coupling can then be written as

$$\begin{aligned} V_{i0}^{\mathrm{dia}}(\mathbf{k}_i) &= \langle\Phi_i(\mathbf{k}_i)|\hat{H}|\Phi_0\rangle \\ &= \sum_{a=1}^{N}\langle\Phi_i(\mathbf{k}_i)|\hat{h}(a)|\Phi_0\rangle + \sum_{a=1}^{N}\sum_{b=a}^{N}\langle\Phi_i(\mathbf{k}_i)|\hat{v}(a,b)|\Phi_0\rangle \\ &\equiv V^{\mathrm{dia},1} + V^{\mathrm{dia},2}, \end{aligned} \tag{3.51}$$

where $\hat{h}(a) = -\frac{1}{2}\nabla_a^2 + v_{\mathrm{ne}}(a) + v_{\mathrm{nn}}(a)$ denotes the one-electron part of the Hamiltonian pertaining to electron a and comprises the kinetic energy as well as the potential energies of the electron-nuclear (v_{ne}) and the internuclear interactions (v_{nn}). The potential energy operator for the interaction between electrons a and b is denoted as $\hat{v}(a,b)$. In the last row of equation 3.51 the coupling has been formally decomposed into one- and two-electron contributions. For the one-electron part, it can be shown that the matrix element reduces to a form only involving the plane wave $\tilde{\psi}$ and the Dyson orbital $\psi^D = \sqrt{N}\langle\Phi_0^{N-1}|\Phi_0^N\rangle$ for the ionization transition:

$$V^{\mathrm{dia},1} = \langle\tilde{\psi}|\hat{h}(1)|\sum_p (-1)^{p+1}\det\mathbf{S}_{i,p}|\phi_p\rangle \tag{3.52}$$

$$= \langle\tilde{\psi}|\hat{h}|\psi^D\rangle. \tag{3.53}$$

Before turning to the two-electron part, for brevity we introduce a short-hand notation for the electron-electron interaction integrals,

$$\langle \tilde{\psi}(\mathbf{k}_i)(1)\chi_n(2)|\hat{v}(1,2)|\phi_p(1)\phi_q(2)\rangle \equiv \langle \tilde{\mathbf{k}}_i n|pq\rangle, \tag{3.54}$$

and further, for their antisymmetrized versions,

$$\langle \tilde{\mathbf{k}}_i n|pq\rangle - \langle \tilde{\mathbf{k}}_i n|qp\rangle \equiv \langle \tilde{\mathbf{k}}_i n||pq\rangle. \tag{3.55}$$

The two-electron part can be reduced to integrals involving up to four different MOs:

$$V^{\mathrm{dia},2} = \sum_n \sum_{q,p<q} \langle \tilde{\mathbf{k}}_i n||pq\rangle \cdot (-1)^s \det \mathbf{S}_{in,pq}, \tag{3.56}$$

with $s = n + p + q - 1$ and $\det \mathbf{S}_{in,pq}$ as the minor determinant of matrix $\mathbf{S}$ where the rows i and n as well as the columns p and q have been deleted. In order to further simplify this expression, we expand the neutral MOs χ_n with respect to the anionic ones, ϕ_u, which leads to

$$V^{\mathrm{dia},2} = \sum_n^{\mathrm{occ}} \sum_u^{\mathrm{all}} \langle \chi_n|\phi_u\rangle \sum_{q,p<q}^{\mathrm{occ}} \langle \tilde{\mathbf{k}}_i u||pq\rangle (-1)^s \det \mathbf{S}_{in,pq} \tag{3.57}$$

$$= \sum_u^{\mathrm{all}} \sum_{q,p<q}^{\mathrm{occ}} \langle \tilde{\mathbf{k}}_i u||pq\rangle \sum_n^{\mathrm{occ}} S_{nu}(-1)^s \det \mathbf{S}_{in,pq} \tag{3.58}$$

If ϕ_u is an occupied orbital, the last sum in equation 3.58 can be further simplified:

$$\sum_n^{\mathrm{occ}} S_{nu} \cdot (-1)^{n+p+q-1} \det \mathbf{S}_{in,pq} \tag{3.59}$$

$$= \begin{cases} (-1)^q \det \mathbf{S}_{i,q} & u = p \\ (-1)^{p-1} \det \mathbf{S}_{i,p} & u = q \\ 0 & u \neq p, q \end{cases} \tag{3.60}$$

With this, the two-electron part of the coupling can be decomposed into an occupied and a virtual part as

$$V^{\mathrm{dia},2}_{\mathrm{occ}} = \sum_{q,p<q}^{\mathrm{occ}} \Big(\langle \tilde{\mathbf{k}}_i p||pq\rangle (-1)^q \det \mathbf{S}_{i,q}$$
$$+ \langle \tilde{\mathbf{k}}_i q||pq\rangle (-1)^{p-1} \det \mathbf{S}_{i,p} \Big) \tag{3.61}$$

$$V^{\mathrm{dia},2}_{\mathrm{virt}} = \sum_u^{\mathrm{virt}} \sum_{q,p<q}^{\mathrm{occ}} \langle \tilde{\mathbf{k}}_i u||pq\rangle \sum_n^{\mathrm{occ}} S_{nu} \cdot (-1)^s \det \mathbf{S}_{in,pq} \tag{3.62}$$

The occupied part can be reformulated by setting $\sum_{q,p<q} \to \frac{1}{2}\sum_{pq}$ and interchanging the indices p and q in the first summand, giving rise to

$$
V_{\text{occ}}^{\text{dia},2} = \frac{1}{2}\sum_{pq}^{\text{occ}} \Big(\langle \tilde{\mathbf{k}}_i q || qp \rangle (-1)^p \det \mathbf{S}_{i,p}
$$

$$
+ \langle \tilde{\mathbf{k}}_i q || pq \rangle (-1)^{p-1} \det \mathbf{S}_{i,p} \Big) \tag{3.63}
$$

$$
= \sum_{pq}^{\text{occ}} \langle \tilde{\mathbf{k}}_i q || pq \rangle (-1)^{p+1} \det \mathbf{S}_{i,p} \tag{3.64}
$$

$$
= \sum_{p}^{\text{occ}} \langle \tilde{\mathbf{k}}_i | \sum_{q}^{\text{occ}} (\hat{J}_q - \hat{K}_q) | \phi_p \rangle (-1)^{p+1} \det \mathbf{S}_{i,p} \tag{3.65}
$$

Together with the one-electron part we get

$$
V^{\text{dia},1} + V_{\text{occ}}^{\text{dia},2} = \sum_{p}^{\text{occ}} \langle \tilde{\mathbf{k}}_i | \hat{h} + \sum_{q}^{\text{occ}} (\hat{J}_q - \hat{K}_q) | \phi_p \rangle (-1)^{p+1} \det \mathbf{S}_{i,p} \tag{3.66}
$$

$$
= \sum_{p}^{\text{occ}} \langle \tilde{\mathbf{k}}_i | \hat{f} | \phi_p \rangle (-1)^{p+1} \det \mathbf{S}_{i,p}, \tag{3.67}
$$

where $\hat{f}$ denotes the Fock operator. If the ϕ_p are Hartree-Fock orbitals, $\hat{f}|\phi_p\rangle = \varepsilon_p|\phi_p\rangle$ and the complete expression $V^{\text{dia},1} + V_{\text{occ}}^{\text{dia},2}$ becomes identically zero due to the orthogonality between the free electron wavefunction $\tilde{\psi}(\mathbf{k}_i)$ and the MOs ϕ_p. In our case, by contrast, the ϕ_p are Kohn-Sham orbitals. This means that we approximate the wavefunction of the system by the Kohn-Sham reference determinant, which is similar to the use of a CIS-like wavefunction expansion for excited states in TDDFT as proposed by Casida.[74] In our simulations, we find the Kohn-Sham orbitals to be very close to the Hartree-Fock orbitals obtained using the same basis set, thus the following relation still holds approximately:

$$
V^{\text{dia},1} + V_{\text{occ}}^{\text{dia},2} \approx 0. \tag{3.68}
$$

Therefore, the expression for the diabatic coupling in the MO basis, as also given in equation 3.33 of the main text, reads

$$
V_{i0}^{\text{dia}}(\mathbf{k}_i) = \sum_{u}^{\text{virt}} \sum_{q,p<q}^{\text{occ}} \langle \tilde{\mathbf{k}}_i u || pq \rangle \sum_{n}^{\text{occ}} S_{nu} (-1)^s \det \mathbf{S}_{in,pq}. \tag{3.69}
$$

If the N-electron system is a spin doublet anion and the electron ejected in the ionization process has α spin, the p sum in the above formula becomes restricted to α orbitals only. In addition if q represents a β orbital all exchange

terms in the electron-electron repulsion integrals are also zero. Inserting subsequently the expression for the orthogonalized plane wave,

$$\langle \tilde{\mathbf{k}}_i | = \langle \mathbf{k}_i | - \sum_r^{\text{occ},\alpha} \langle \mathbf{k}_i | r \rangle \langle r |, \tag{3.70}$$

with r denoting occupied anion orbitals, yields

$$V_{i0}^{\text{dia}}(\mathbf{k}_i) = \sum_p^{\text{occ},\alpha} \left[\sum_n^{\text{occ},\alpha} \sum_{q>p}^{\text{occ},\alpha} (-1)^s \det \mathbf{S}_{in,pq} \text{K} \right.$$
$$\left. + \sum_{\bar{n}}^{\text{occ},\beta} \sum_{\bar{q}}^{\text{occ},\beta} (-1)^{\bar{s}} \det \mathbf{S}_{i\bar{n},p\bar{q}} \bar{\text{K}} \right] \tag{3.71}$$

with

$$\text{K} = \sum_u^{\text{virt},\alpha} S_{nu} \left(\langle \mathbf{k}_i u || pq \rangle - \sum_r^{\text{occ},\alpha} \langle \mathbf{k}_i | r \rangle \langle ru || pq \rangle \right) \tag{3.72}$$

$$\bar{\text{K}} = \sum_{\bar{u}}^{\text{virt},\beta} S_{\bar{n}\bar{u}} \left(\langle \mathbf{k}_i \bar{u} | p\bar{q} \rangle - \sum_r^{\text{occ},\alpha} \langle \mathbf{k}_i | r \rangle \langle r\bar{u} | p\bar{q} \rangle \right) \tag{3.73}$$

where $\langle \mathbf{k}_i |$ is the pure plane wave of wavevector $\mathbf{k}_i$.

A final technical simplification can be achieved by noticing that there are usually many more virtual than occupied orbitals. Therefore, we use the expansion of the neutral MOs $\langle n |$ with respect to the anionic ones, $\langle u |$, to set

$$\sum_u^{\text{virt}} S_{nu} \langle u | = \langle n | - \sum_u^{\text{occ}} S_{nu} \langle u |, \tag{3.74}$$

thus avoiding the summation over all virtual anion MOs:

$$\text{K} = \langle \mathbf{k}_i n || pq \rangle - \sum_r^{\text{occ},\alpha} \langle \mathbf{k}_i | r \rangle \langle rn || pq \rangle -$$
$$\sum_u^{\text{occ},\alpha} S_{nu} \left(\langle \mathbf{k}_i u || pq \rangle - \sum_r^{\text{occ},\alpha} \langle \mathbf{k}_i | r \rangle \langle ru || pq \rangle \right) \tag{3.75}$$

$$\bar{\text{K}} = \langle \mathbf{k}_i \bar{n} | p\bar{q} \rangle - \sum_r^{\text{occ},\alpha} \langle \mathbf{k}_i | r \rangle \langle r\bar{n} | p\bar{q} \rangle -$$
$$\sum_{\bar{u}}^{\text{occ},\beta} S_{\bar{n}\bar{u}} \left(\langle \mathbf{k}_i \bar{u} | p\bar{q} \rangle - \sum_r^{\text{occ},\alpha} \langle \mathbf{k}_i | r \rangle \langle r\bar{u} | p\bar{q} \rangle \right) \tag{3.76}$$

3.6.2 Calculation of diabatic coupling in terms of basis functions

For the actual computation of the diabatic coupling, the MOs appearing in the electron-electron repulsion integrals in equation 3.71 are further expanded with respect to the AO basis, giving rise to

$$V_{i0}^{\mathrm{dia}}(\mathbf{k}_i) = \sum_n^{\mathrm{occ},\alpha} \sum_p^{\mathrm{occ},\alpha} \sum_{q>p}^{\mathrm{occ},\alpha} (-1)^s \det \mathbf{S}_{in,pq} \sum_{\lambda\mu\nu} \left(c_\lambda^{(n)} - \sum_u^{\mathrm{occ},\alpha} c_\lambda^{(u)} S_{nu} \right) c_\mu^{(p)} c_\nu^{(q)}$$

$$\times \left[\langle \mathbf{k}_i \lambda || \mu\nu \rangle - \sum_r^{\mathrm{occ},\alpha} \sum_{\rho\sigma} c_\rho^{(r)} c_\sigma^{(r)} \langle \mathbf{k}_i | \rho \rangle \, \langle \sigma\lambda || \mu\nu \rangle \right]$$

$$+ \sum_{\bar{n}}^{\mathrm{occ},\beta} \sum_p^{\mathrm{occ},\alpha} \sum_{\bar{q}}^{\mathrm{occ},\beta} (-1)^{\bar{s}} \det \mathbf{S}_{i\bar{n},p\bar{q}} \sum_{\lambda\mu\nu} \left(c_\lambda^{(\bar{n})} - \sum_{\bar{u}}^{\mathrm{occ},\beta} c_\lambda^{(\bar{u})} S_{\bar{n}\bar{u}} \right) c_\mu^{(p)} c_\nu^{(\bar{q})}$$

$$\times \left[\langle \mathbf{k}_i \lambda | \mu\nu \rangle - \sum_r^{\mathrm{occ},\alpha} \sum_{\rho\sigma} c_\rho^{(r)} c_\sigma^{(r)} \langle \mathbf{k}_i | \rho \rangle \, \langle \sigma\lambda | \mu\nu \rangle \right]$$

$$\tag{3.77}$$

where the Greek indices indicate Gaussian-type atomic basis functions.

Reordering the summations with respect to MO and AO indices, and defining

$$A_{\lambda\mu\nu} = \sum_n^{\mathrm{occ},\alpha} \sum_{q,p<q}^{\mathrm{occ},\alpha} (-1)^s \det \mathbf{S}_{in,pq}$$

$$\times \left(c_\lambda^{(n)} - \sum_u^{\mathrm{occ},\alpha} c_\lambda^{(u)} S_{nu} \right) c_\mu^{(p)} c_\nu^{(q)} \tag{3.78}$$

$$\bar{A}_{\lambda\mu\nu} = \sum_{\bar{n}}^{\mathrm{occ},\beta} \sum_p^{\mathrm{occ},\alpha} \sum_{\bar{q}}^{\mathrm{occ},\beta} (-1)^{\bar{s}} \det \mathbf{S}_{i\bar{n},p\bar{q}}$$

$$\times \left(c_\lambda^{(\bar{n})} - \sum_{\bar{u}}^{\mathrm{occ},\beta} c_\lambda^{(\bar{u})} S_{\bar{n}\bar{u}} \right) c_\mu^{(p)} c_\nu^{(\bar{q})} \tag{3.79}$$

$$B_\sigma = \sum_r^{\mathrm{occ},\alpha} \sum_\rho c_\sigma^{(r)} c_\rho^{(r)} \langle \mathbf{k}_i | \rho \rangle \tag{3.80}$$

leads to the working equation

$$V_{i0}^{\mathrm{dia}}(\mathbf{k}_i) = \sum_{\lambda\mu\nu} \left(\left[\langle \mathbf{k}_i \lambda | \mu\nu \rangle - \sum_\sigma B_\sigma \langle \sigma\lambda | \mu\nu \rangle \right] \left(A_{\lambda\mu\nu} + \bar{A}_{\lambda\mu\nu} \right) \right.$$

$$\left. - \left[\langle \mathbf{k}_i \lambda | \nu\mu \rangle - \sum_\sigma B_\sigma \langle \sigma\lambda | \nu\mu \rangle \right] A_{\lambda\mu\nu} \right). \tag{3.81}$$

3.6.3 Spreading of a freely propagated LCAO-wavepacket

For the approximate description of adiabatic ionization processes as discussed in subsection 3.2.6, we consider the HOMO $\phi(\mathbf{r})$ of anionic vinylidene as the

initial free-electron wavepacket and compute its $\hat{\mathbf{r}}^2$ expectation value during free propagation,

$$\langle\hat{\mathbf{r}}^2\rangle(t) = \langle\phi(\mathbf{r},t)|\hat{\mathbf{r}}^2|\phi(\mathbf{r},t)\rangle = \sum_{\mu\nu} c_\mu c_\nu \langle\varphi_\mu(\mathbf{r},t)|\hat{\mathbf{r}}^2|\varphi_\nu(\mathbf{r},t)\rangle, \qquad (3.82)$$

where $\varphi_{\mu,\nu}$ denote the time-propagated Gaussian atomic basis functions. Employing the free propagator $K(\mathbf{r},\mathbf{r}',t,0) = \langle\mathbf{r}|\exp(-i\hat{\mathbf{p}}^2 t/2m_e\hbar)|\mathbf{r}'\rangle$ these can be calculated as

$$\varphi_\mu(\mathbf{r},t) = \int d^3\mathbf{r}\, K(\mathbf{r},\mathbf{r}',t,0)\varphi_\mu(\mathbf{r},0). \qquad (3.83)$$

For Cartesian basis functions of s, p and d type at the center $\mathbf{A}$, with the angular momentum quantum numbers l, m and n for the three spatial dimensions, the following analytic expressions are obtained:

$$\varphi_\mu(\mathbf{r},t) = N_{lmn} e^{-\frac{3i\pi}{2}} (1+i\beta t)^{-(l+m+n+\frac{3}{2})} e^{-\frac{\alpha}{1+i\beta t}\mathbf{r}^2}$$
$$\times\, (x-A_x)^l(y-A_y)^m(z-A_z)^n \qquad (3.84)$$

if l, m, n assume values of 0 or 1 and

$$\varphi_\mu(\mathbf{r},t) = N_{lmn} e^{-\frac{3i\pi}{2}} e^{-\frac{\alpha}{1+i\beta t}\mathbf{r}^2}\left[-\frac{i\beta t}{2\alpha}(1+i\beta t)^{-\frac{5}{2}}\right.$$
$$\left. -\,(1+i\beta t)^{-\frac{7}{2}}(x-A_x)^l(y-A_y)^m(z-A_z)^n\right] \qquad (3.85)$$

if one of the numbers l, m, n equals 2 and the others are zero. In the above expressions, α denotes the basis function exponent and $\beta = \frac{2\hbar\alpha}{m_e}$. The basic AO integrals occuring in equation 3.82 can be calculated with common algorithms such as the McMurchie-Davidson scheme.[179]

Chapter 4

HORTENSIA, a program package for the simulation of nonadiabatic autoionization dynamics in molecules

Abstract

We present a program package for the simulation of ultrafast vibration-induced autoionization dynamics in molecular anions in the manifold of the adiabatic anionic states and the discretized ionization continuum. This program, called HORTENSIA (*Ho*pping *r*eal-time *tr*ajectories for *e*lectron-ejection by *n*onadiabatic *s*elf-*i*onization in *a*nions), is based on the nonadiabatic surface-hopping methodology, wherein nuclei are propagated as an ensemble along classical trajectories in the quantum-mechanical potential created by the electonic density of the molecular system. The electronic Schrödinger equation is numerically integrated along the trajectory, providing the time evolution of electronic state coefficients, from which switching probabilities into discrete electronic states are determined. In the case of a discretized continuum state, this hopping event is interpreted as the ejection on an electron. The derived diabatic and nonadiabatic couplings in the time-dependent electronic Schrödinger equation are calculated from anionic and neutral wavefunctions obtained from

quantum chemical calculations with commercially available program packages interfaced with our program.

Based on this methodology, we demonstrate the simulation of autoionization electron kinetic energy spectra that are both time- and angle-resolved. In addition, the program yields data that can be interpreted easily with respect to geometric characteristics such as bonding distances and angles, which facilitates the detection of molecular configurations important for the autoionization process.

Furthermore, several useful extensions beyond the dynamics simulation are included, namely tools for the generation of initial conditions (based on phase space distribution sampling) and input files as well as for the evaluation of output files, all of this both through console commands and a graphical user interface.

4.1   Introduction

After generation of a temporary molecular anion through electron attachment, there are three possible competing relaxation mechanisms.[14] These are a) radiative deactivation, assuming that there is a lower-lying anion state that is stable with respect to ionization, b) dissociative electron attachment, in which the captured electron induces geometric change in the molecule resulting in fragmentation into more stable products, a neutral and an anionic subsystem. And lastly, c) autoionization, in which after a finite period of time the metastable state decays via electron ejection. The process of dissociative electron attachment is observed for example in DNA, where capture of low-energy electrons leads to single and double strand breaks[17,18], or in a variety of substances in nanoscale thin films[180]. Prominent examples for autoionization include excited dipole- and quadrupole-bound anions with binding energies slightly below the ionization threshold[27,84,126,128], intermolecular Coulombic decay at the $FADH^-$ cofactor involved in DNA-photolesion repair[19] and autoionization induced by vibrational excitation in organic molecules[25,28,31,82,127,129]. Generally the finite lifetime of a metastable state with respect to autoionization can vary strongly from only a few femtoseconds[11,12] up to milliseconds[11,13]. Recently, several experiments have provided insights into the dynamics of such processes in dipole- and quadrupole-bound organic anions on a (sub-)picosecond timescale.[28,29,127,131,132,181]

Although the process of autoionization is well-known and -observed experimentally by a multitude of methods, as can be seen in the references given above, the theoretical description of autoionizing systems is challenging[10], especially if one is interested in the mechanistic details of the intricate ultrafast relaxation dynamics. Autoionization processes can follow different general mechanisms, depending on how energy is redistributed among the system's degrees of freedom. Besides a purely electronic variant, where already the electronic energy of the system lies above the ionization threshold and electron ejection may proceed via tunneling, there is also the possibility of a nonadi-

abatic mechanism in which rotational or vibrational energy of the nuclei is transformed into the kinetic energy of the ejected electron.

In the following, we focus on the case of vibrational autoionization. This process can thus be viewed as a nonadiabatic transition between a vibrationally excited bound N-electron system and continuum electronic states consisting of an N-1 electron molecular core and a free electron. Early theoretical treatments have focused on the computation of ionization rates[86,133,136] as well as on establishing propensity rules for the ionization transitions[134]. While a full dynamical treatment of vibrational autoionization is highly desirable, an entirely quantum-dynamical approach is computationally prohibitive. As an alternative, a mixed quantum-classical ansatz can be considered, further motivated by the success of this type of methodology in the description of bound-state nonadiabatic processes and the simulation of time-resolved spectroscopic signals.[5,7,33,139,140] Although to date there have been several implementations of mixed quantum-classical dynamics simulations for bound-state problems made publicly available[182–184], no program addressing the simulation of vibration-induced autoionization processes has been published so far.

Therefore, in this work we present the program package implementing our approach to describe vibrational autoionization through quantum-classical dynamics in the framework of the surface-hopping methodology in the manifold of bound and continuum electronic states as described recently[26]. Therein, nuclear motion is considered classically, while the electronic system is treated quantum-mechanically. Nonadiabatic transitions between electronic states accompanied by change of the classical vibrational energy of the molecule describe the energy exchange between the two subsystems. With this program package and the underlying methodology, one is able to gain insight into the geometric and electronic evolution in the course of the autoionization process as well as to calculate the time-, energy- and angle-distribution of the generated free electrons, which serve as experimental observables for monitoring autoionization dynamics.

We illustrate our program on the example of the 2-cyanopyrrolide anion, which bears a dipole-bound excited state slightly below the electron detachment threshold while the vibrationally excited states are metastable and decay via autoionization.[84]

In the following section a brief theoretical description of the method is given. In section 4.3 an overview of the actual implementation is provided. The subsequent section 4.4 details performance-related issues, namely quality of approximations in the theory and runtime and memory optimization within the program, as well as a dynamics simulation example for the 2-cyanopyrrolide anion. Finally in section 4.5 a conclusion and outlook are given.

4.2 Theory

Our methodological framework is based on the surface-hopping procedure as proposed by Tully[52], in which the coupled electron-nuclear dynamics of molec-

ular systems is approached in a quantum-classical fashion. Specifically, the nuclei are propagated classically according to Newton's equations of motion,

$$M\ddot{\mathbf{R}}(t) = \mathbf{F}_i(\mathbf{R}[t]) \equiv -\nabla_{\mathbf{R}}E_i(\mathbf{R}[t]), \tag{4.1}$$

where the force $\mathbf{F}_i(\mathbf{R}[t])$ is obtained as the negative gradient of the electronic potential energy surface (PES) $E_i(\mathbf{R}[t])$. In the above equation, M denotes a diagonal matrix containing the nuclear masses. For an ensemble of initial conditions, this leads to trajectories $\mathbf{R}(t)$ moving on the given PES. Simultaneously, the electronic time-dependent Schrödinger equation

$$i\hbar\dot{\Psi}(\mathbf{r};\mathbf{R}[t]) = \hat{H}_{el}\Psi(\mathbf{r};\mathbf{R}[t]), \tag{4.2}$$

with the electronic Hamiltonian $\hat{H}_{el}$ is solved. The electronic wavefunction can be expanded into a set of orthonormal basis states, which in the case of autoionization includes bound states $\Phi_{m'}$ (denoted with a primed index) as well as continuum states $\tilde{\Phi}_{m''}$ (denoted with a double-primed index):

$$\Psi\big(\mathbf{r},\mathbf{R}[t],t\big) = \sum_{m'} c_{m'}(t)\Phi_{m'}\big(\mathbf{r},\mathbf{R}[t]\big) +$$
$$\sum_{m''}\int d^3\mathbf{k}\; \tilde{c}_{m''}(\mathbf{k},t)\tilde{\Phi}_{m''}(\mathbf{k},\mathbf{r},\mathbf{R}[t]), \tag{4.3}$$

where $\mathbf{k}$ denotes the continuously varying wave vector of the free electron, while m'' is the quantum number of the remaining neutral state. We assume the wavefunctions $\Phi_{m'}$ and $\tilde{\Phi}_{m''}$ to be single Slater determinants (ground state) or an expansion of singly excited Slater determinants (excited state).

4.2.1 Discretized continuum states

In the frame of the presented methodology we discretize the continuum states, leading to

$$\int d^3\mathbf{k}\; \tilde{c}_{m''}(\mathbf{k},t)\tilde{\Phi}_{m''}(\mathbf{k},\mathbf{r},\mathbf{R}[t])$$
$$\approx \sum_i (\Delta\mathcal{V}_k)^{\frac{1}{2}}\tilde{c}_{m''}(\mathbf{k}_i,t)(\Delta\mathcal{V}_k)^{\frac{1}{2}}\tilde{\Phi}_{m''}(\mathbf{k}_i,\mathbf{r},\mathbf{R}[t])$$
$$\approx \sum_i c_{m''}(\mathbf{k}_i,t)\Phi_{m''}(\mathbf{k}_i,\mathbf{r},\mathbf{R}[t]), \tag{4.4}$$

where $\Delta\mathcal{V}_k$ denotes the volume element in k-space and the discretized and continuum state expansion coefficients are related according to $c_{m''}(\mathbf{k}_i,t) = (\Delta\mathcal{V}_k)^{\frac{1}{2}}\tilde{c}_{m''}(\mathbf{k}_i,t)$. The actual determination of the wave vectors and the implementation of the discretization procedure are explained in detail in the next chapter.

Insertion of equation 4.3 into the time-dependent Schrödinger equation 4.2, multiplication from the left by an eigenstate $\langle\Phi_n|$ and evaluation of the arising

terms leads to a set of coupled differential equations for the electronic state coefficients c_n:

$$\dot{c}_n(t) = \sum_j \left[-\frac{i}{\hbar} H_{nm}(\mathbf{R}[t]) - D_{nm}(\mathbf{R}[t]) \right] c_m(t), \qquad (4.5)$$

with the matrix elements of the electronic Hamiltonian $H_{nm} = \langle \Phi_n | H_{el} | \Phi_m \rangle$ and the nonadiabatic couplings $D_{nm} = \langle \Phi_n | \dot{\Phi}_m \rangle = \dot{\mathbf{R}} \cdot \langle \Phi_n | \nabla_R | \Phi_m \rangle$. These can be divided into separate expressions for the bound and continuum states, resulting in the diabatic and nonadiabatic couplings between two bound anion states,

$$H_{n'm'} = \langle \Phi_{n'} | \hat{H} | \Phi_{m'} \rangle \qquad (4.6)$$

$$D_{n'm'} = \langle \Phi_{n'} | \dot{\Phi}_{m'} \rangle , \qquad (4.7)$$

and between a bound and a discretized continuum state,

$$H_{n''m'}(\mathbf{k}_i) = (\Delta \mathcal{V}_k)^{\frac{1}{2}} \langle \tilde{\Phi}_{n''}(\mathbf{k}_i) | \hat{H} | \Phi_{m'} \rangle \qquad (4.8)$$

$$D_{n''m'}(\mathbf{k}_i) = \langle \Phi_{n''}(\mathbf{k}_i) | \dot{\Phi}_{m'} \rangle = (\Delta \mathcal{V}_k)^{\frac{1}{2}} \langle \tilde{\Phi}_{n''}(\mathbf{k}_i) | \dot{\Phi}_{m'} \rangle . \qquad (4.9)$$

In the above equations, the approximation to neglect the coupling terms between the continuum states has been introduced. The discretized continuum states consist of an antisymmetrized product of a bound $N-1$ electron neutral state and a molecular scattering state of the free electron

$$\tilde{\Phi}_{n''}(\mathbf{k}_i) = \mathcal{A} \left(\Phi_{n''}^{(\mathrm{n})} \cdot \psi(\mathbf{k}_i) \right) . \qquad (4.10)$$

The simplest approximation to the free electron states in the presence of a neutral molecular core are plane waves

$$\psi(\mathbf{k}_i) \approx \mathcal{N} \mathrm{e}^{i \mathbf{k}_i \cdot \mathbf{r}} \qquad (4.11)$$

with a normalization constant $\mathcal{N} = (2\pi)^{-3/2}$ to satisfy the orthonormality demanded in equation 4.3. Since this function would be completely independent on the electronic and nuclear configuration of the molecular core, which is a strong simplification, the plane waves are orthogonalized with respect to the anion's molecular orbitals (MOs) ϕ_m to include (at least to a certain degree) dependence on the molecular structure according to

$$\tilde{\psi}(\mathbf{k}_i) = (2\pi)^{-3/2} \mathcal{N}_{ortho} \left(\mathrm{e}^{i \mathbf{k}_i \cdot \mathbf{r}} - \sum_m^{\mathrm{occ}} \langle \phi_m | \mathrm{e}^{i \mathbf{k}_i \cdot \mathbf{r}} \rangle \phi_m \right)$$

$$= \mathcal{N}_{ortho} \left(\psi(\mathbf{k}_i) - \sum_m^{\mathrm{occ}} \langle \phi_m | \psi(\mathbf{k}_i) \rangle \phi_m \right), \qquad (4.12)$$

with the normalization constant

$$\mathcal{N}_{ortho} = \left(1 - \sum_m^{\mathrm{occ}} \left| \langle \phi_m | \psi(\mathbf{k}_i) \rangle \right|^2 \right)^{-1/2} \qquad (4.13)$$

arising from the orthogonalization.

Notably, the summation over m includes the occupied MOs in all 'relevant' Slater determinants of all considered electronic states, that is, we considered all determinants which are needed to sufficiently represent the ground state and full CIS wavefunction of the excited state. Beginning from the highest contribution to a wavefunction, determinants are included until a specific percentage or a user-adjusted maximum number of configurations per electronic state is reached (95 % / 10 configurations in the case of vinylidene[26]). Considering for now the special case where only the anion's ground state is included, the used MOs are simply the energetically lowest ones up to the highest-occupied molecular orbital (HOMO).

The overlap integral between a plane wave and an MO present in equation 4.13, $\langle \phi_m | \psi(\mathbf{k}_i) \rangle$, can be computed analytically by expanding the MO into the Gaussian atomic orbital (AO) basis, with the integral involving a single AO $|\nu\rangle$ given by

$$
\begin{aligned}
\langle \nu | \psi(\mathbf{k}) \rangle &= (2\pi)^{-3/2} \int d^3\mathbf{r}\, e^{i\mathbf{k}\cdot\mathbf{r}} \varphi_\nu(\mathbf{r}) \\
&= (2\alpha_\nu)^{-3/2} \exp\left(i\mathbf{k} \cdot \mathbf{A}_\nu - \frac{k^2}{4\alpha_\nu} \right) \\
&\quad \times \prod_{j=x,y,z} (-i\sqrt{4\alpha_\nu})^{-n_{\nu,j}} H_{n_{\nu,j}}\left(\frac{k_j}{\sqrt{4\alpha_\nu}} \right),
\end{aligned} \tag{4.14}
$$

where the $H_{n_{\nu,j}}$ are the Hermite polynomials of order $n_{\nu,j}$.

4.2.2 Electronic coupling terms

There are anionic systems, for example the vinylidene anion[26], that do not support a bound excited state, in which case the consideration of only the ground state and the continuum in the process of autoionization is sufficient. Besides that, for example in molecules exhibiting dipole-bound excited states[84,108,185], several bound anionic states and the interaction among them are relevant as well. Nonetheless, to keep the formalism concise, if not noted otherwise we discuss in the following the electronic coupling terms for the special case of both anion and neutral molecule being in their respective electronic ground states, which in turn are represented by a single Slater determinant. The generalization to excited states and/or multideterminantal wavefunctions is straightforward.[185] We denote the bound anionic ground state wavefunction by $|\Phi_0\rangle$ and the continuum wavefunctions by $|\Phi_i\rangle$, the latter being constructed as an antisymmetrized product of the neutral ground state and a free electron state function with wave vector $\mathbf{k}_i$, similar to equation 4.10.

Diabatic couplings

In the case of two adiabatic bound anion states, the coupling matrix elements $H_{n'm'}$ given in equation 4.6 yield zero for all $n' \neq m'$ since these states are orthonormal eigenstates of the electronic Hamiltonian.

On the other hand, since in our methodology the bound and continuum state wavefunctions are constructed using separate quantum-chemical calculations for the anion and neutral, and the free electron wavefunction is taken as a plane wave, the continuum state functions are crude approximations to the actual adiabatic eigenfunctions of the electronic Hamiltonian for the N-electron system and therefore, diabatic couplings between the bound and continuum electronic states arise.

As elaborated in detail in Ref.[26], according to equation 4.8 and defining $V_{i0}^{\text{dia}}(\mathbf{k}_i)$ as

$$H_{i0}(\mathbf{k}_i) \equiv \langle \Phi_i | \hat{H} | \Phi_0 \rangle \equiv (\Delta \mathcal{V}_k)^{\frac{1}{2}} V_{i0}^{\text{dia}}(\mathbf{k}_i), \qquad (4.15)$$

the diabatic coupling between a bound and a continuum state can be written in terms of the AO basis as

$$V_{i0}^{\text{dia}}(\mathbf{k}_i) = \sum_{\lambda\mu\nu} \left[A_{\lambda\mu\nu} \left(\langle \mathbf{k}_i \lambda || \mu\nu \rangle - \sum_{\sigma} B_\sigma \langle \sigma\lambda || \mu\nu \rangle \right) + \right.$$
$$\left. \bar{A}_{\lambda\mu\nu} \left(\langle \mathbf{k}_i \lambda | \mu\nu \rangle - \sum_{\sigma} B_\sigma \langle \sigma\lambda | \mu\nu \rangle \right) \right]. \qquad (4.16)$$

In this formula the Greek letters denote the AO basis functions, $\langle \mathbf{k}_i \lambda | \mu\nu \rangle$ is an electron-electron repulsion integral and $\langle \mathbf{k}_i \lambda || \mu\nu \rangle = \langle \mathbf{k}_i \lambda | \mu\nu \rangle - \langle \mathbf{k}_i \lambda | \nu\mu \rangle$ its antisymmetrized variant. The prefactors $A_{\lambda\mu\nu}$, $\bar{A}_{\lambda\mu\nu}$ and B_σ comprise AO expansion coefficients and overlap integrals and are defined as follows (assuming that the extra electron of the anion has α spin):

$$A_{\lambda\mu\nu} = \sum_{n}^{\text{occ},\alpha} \sum_{q,p<q}^{\text{occ},\alpha} (-1)^{n+p+q-1} \det \mathbf{S}_{in,pq}$$
$$\times \left(c_\lambda^{(n)} - \sum_{u}^{\text{occ},\alpha} c_\lambda^{(u)} S_{nu} \right) c_\mu^{(p)} c_\nu^{(q)} \qquad (4.17)$$

$$\bar{A}_{\lambda\mu\nu} = \sum_{\bar{n}}^{\text{occ},\beta} \sum_{p}^{\text{occ},\alpha} \sum_{\bar{q}}^{\text{occ},\beta} (-1)^{\bar{n}+p+\bar{q}-1} \det \mathbf{S}_{i\bar{n},p\bar{q}}$$
$$\times \left(c_\lambda^{(\bar{n})} - \sum_{\bar{u}}^{\text{occ},\beta} c_\lambda^{(\bar{u})} S_{\bar{n}\bar{u}} \right) c_\mu^{(p)} c_\nu^{(\bar{q})} \qquad (4.18)$$

$$B_\sigma = \sum_{r}^{\text{occ},\alpha} \sum_{\rho} c_\sigma^{(r)} c_\rho^{(r)} \langle \mathbf{k}_i | \rho \rangle, \qquad (4.19)$$

where the indices (including their variants with an overbar) p, q, r refer to anion MOs, n, u to neutral MOs, and $\det \mathbf{S}_{in,pq}$ denotes the minor determinant of the overlap matrix between continuum and bound state orbitals where the rows of the free electron orbital $\tilde{\psi}(\mathbf{k}_i)$ and neutral orbital χ_n as well as the columns of anion orbitals ϕ_p and ϕ_q have been deleted. For the full derivation of these equations the reader is referred to Ref.[26].

Nonadiabatic couplings

The nonadiabatic coupling terms given in Eqs. (4.7) and (4.9) could in principle be computed from the scalar product of nuclear velocities and nonadiabatic coupling vector, $D_{nm} = \langle \Phi_n | \dot{\Phi}_m \rangle = \dot{\mathbf{R}} \cdot \langle \Phi_n | \nabla_R | \Phi_m \rangle$. A commonly used and more efficient alternative, which avoids the computation of wavefunction gradients, consists in using the finite-difference approximation for the time derivative[163,186,187], which results in the scalar nonadiabatic coupling to be obtained from wavefunction overlaps at neighboring time steps:

$$D_{i0}(t) = \langle \Phi_i(t) | \frac{d}{dt} \Phi_0(t) \rangle \tag{4.20}$$

$$\approx \frac{1}{2\Delta t} \Big(\langle \Phi_i(t - \Delta t) | \Phi_0(t) \rangle - \langle \Phi_i(t) | \Phi_0(t - \Delta t) \rangle \Big) \tag{4.21}$$

Notice that both approaches rely on the numerical approximation of the time derivative, either by using electronic wavefunctions at consecutive time steps or by the inherent approximative nature of the nuclear velocities obtained from the numerical solution of Newton's equations of motion. However, this accuracy is well controllable by appropriately adjusting the nuclear time step. In the case of two anionic bound states, these terms are evaluated according to Refs.[137,163,188].

One can simplify the arising terms by integrating over all but one electron coordinate. For the first term of equation 4.21 this yields

$$\langle \Phi_i(t') | \Phi_0(t) \rangle = N^{-1/2} \langle \tilde{\psi}(\mathbf{k}_i, t') | \psi^D(t', t) \rangle , \tag{4.22}$$

where we have abbreviated $t' = t - \Delta t$ and have defined the one-electron function $\psi^D(t', t)$, which is an analog to a molecular Dyson orbital with the N- and $N - 1$- wavefunctions taken at different time steps and geometries. Using equations 4.12 and 4.22 the resulting nonadiabatic coupling terms read

$$D_{i0}(\mathbf{k}_i, t) = \frac{(\Delta \mathcal{V}_k)^{\frac{1}{2}} \mathcal{N}_{ortho}}{2\sqrt{N} \Delta t} \Big[\langle \psi(\mathbf{k}_i) | \psi^D(t', t) \rangle - \langle \psi(\mathbf{k}_i) | \psi^D(t, t') \rangle$$

$$- \sum_n \langle \psi(\mathbf{k}_i) | \phi_n(t) \rangle \langle \phi_n(t') | \psi^D(t', t) \rangle$$

$$+ \sum_n \langle \psi(\mathbf{k}_i) | \phi_n(t) \rangle \langle \phi_n(t) | \psi^D(t, t') \rangle \Big]. \tag{4.23}$$

4.2.3   Adiabatic ionization and electronic decay

The main focus of the above presented methodology lies on describing the nonadiabatic process of vibrational autoionization. However, in the course of the molecule's dynamical evolution instances can occur where the occupied anionic state becomes unbound as the result of changes in nuclear geometry. In this case, ionization is possible as an exclusively *adiabatic* electronic process without coupling to the nuclear motion. This process can be included approximately in our method by simulating the temporal spread of the ejected

electron as a wavepacket evolving freely in space. As a quantitative measure, the electronic spatial extent, i.e., the expectation value of $\hat{\mathbf{r}}^2$, is calculated as a function of time.

Specifically, once a time step is reached where the VDE has become negative, the highest-occupied orbital of the last bound geometry, $\phi(\mathbf{r}, t_0)$, is used as the initial free electronic wavepacket. In the case where one only considers the anionic ground state, this corresponds to the HOMO. If also an excited state is involved, natural transition orbitals (NTOs)[189] are calculated and the highest-occupied and lowest-unoccupied NTO (HONTO and LUNTO) are used for the anionic ground and excited state, respectively. Such an electronic wavepacket is then propagated in time and its spatial extent is evaluated according to

$$\langle \hat{\mathbf{r}}^2 \rangle (t) = \langle \phi(\mathbf{r}, t) | \hat{\mathbf{r}}^2 | \phi(\mathbf{r}, t) \rangle$$
$$= \sum_{\mu\nu} c_\mu c_\nu \langle \varphi_\mu(\mathbf{r}, t) | \hat{\mathbf{r}}^2 | \varphi_\nu(\mathbf{r}, t) \rangle . \tag{4.24}$$

Here $\varphi_{\mu,\nu}$ denote the Gaussian atomic basis functions freely propagated in time:

$$\varphi_\mu(\mathbf{r}, t) = \int d^3\mathbf{r}' \, K(\mathbf{r}, \mathbf{r}', t, 0) \varphi_\mu(\mathbf{r}', 0) \tag{4.25}$$

with the free electron propagator

$$K(\mathbf{r}, \mathbf{r}', t, 0) = \left\langle \mathbf{r} \left| e^{-i\hat{\mathbf{p}}^2 t/2m_e \hbar} \right| \mathbf{r}' \right\rangle . \tag{4.26}$$

Using Cartesian Gaussian basis functions of s, p and d type one obtains the following analytic expression for the electronic wavepacket:

$$\varphi_\mu(\mathbf{r}, t) = N_{l_x l_y l_z} e^{-\frac{\alpha}{1+i\beta t} \mathbf{r}^2} \left[-\Lambda \frac{i\beta t}{2\alpha} (1 + i\beta t)^{-\frac{5}{2}} + \right.$$
$$\left. (1 + i\beta t)^{-\frac{3}{2} - \sum_j l_j} \prod_{j=x,y,z} (r_j - A_j)^{l_j} \right], \tag{4.27}$$

where $\mathbf{A}$ is the spatial center of the respective basis function, l_i denotes the angular momentum quantum number for the i'th spatial direction and Λ is a constant that is unity if one of the $l_i = 2$ and zero if all $l_i < 2$. The AO integrals in equation 4.24 are calculated with an implementation of the McMurchie-Davidson scheme[179]. To relate the spatial extent in a simple way to the lifetime of the unbound state, an auxiliary spherically symmetric electron distribution is considered which within the initially determined radius $r_0 = \sqrt{\langle \mathbf{r}^2 \rangle (t_0)}$ contains a probability of 99%. Subsequently, with $\langle \mathbf{r}^2 \rangle$ increasing with time, the probability within r_0 decreases, giving rise to a population decay curve which can be related to a time constant τ. The latter is incorporated into the propagation of the electronic wavefunction given by equation 4.5 by adding an imaginary component to the electronic state energy,

$$E^{(\mathrm{a})} \to E^{(\mathrm{a})} - \frac{i\hbar}{2\tau}, \tag{4.28}$$

which leads to an exponential population decay due to adiabatic ionization in regions where the VDE is negative for the given electronic state. We wish to emphasize that the above described approach represents only a crude approximation of the adiabatic ionization mechanism. Therefore, inclusion of this option should be handled with care in actual simulations and should only be used after thorough benchmarking. In particular, it does not include the possible presence of electronic resonances, for which our code would need to be coupled with specifically designed quantum chemistry methods, e.g., those employing complex absorbing potentials.[190,191] Although at present, this is beyond the scope of our program, it may be possible in the future in view of promising ongoing development of efficient methods for the simulation of electronically metastable states and their inclusion in molecular dynamics simulations.[143]

4.2.4 Surface-hopping procedure

Solution of the set of equations 4.5 along a nuclear trajectory yields the time-dependent electronic state coefficients $c_n(t)$. Within the surface-hopping methodology, a switch from the occupied bound electronic state n to any other state m is determined by the hopping probability depending on the electronic state populations $\rho_{nn} = |c_n|^2$, which is

$$P_{n \to m} = -\frac{\dot{\rho}_{nn}}{\rho_{nn}} \frac{\dot{\rho}_{mm}}{\sum_k \dot{\rho}_{kk}} \Delta t \qquad (4.29)$$

for $\dot{\rho}_{nn} < 0$ and $\dot{\rho}_{mm} > 0$ and zero in any other instance. In the above expression, the sum over k includes all states with $\dot{\rho}_{kk} > 0$. In case a surface hop occurs, to ensure energy conservation the nuclear velocities are rescaled such that for kinetic energies T and electronic potential energies E_n of anion (a) and neutral (n) the following conditions are fulfilled:

$$T'^{(a)} = T^{(a)} + E_n^{(a)} - E_m^{(a)} \qquad (4.30)$$

for a hop between anionic bound states and

$$T'^{(n)} = E_n^{(a)} + T^{(a)} - E_m^{(n)} - E_{el}(\mathbf{k}_i) \qquad (4.31)$$

for a hop into the continuum (i.e. autoionization). For a more detailed description of the hopping procedure the reader is referred to Ref.[164].

4.3 Program implementation

In the following chapter a detailed account of how the theory is actually implemented in the program package will be provided. For an easier understanding, in Figure 4.1 the program flow is displayed schematically, with a color code indicating the module handling the respective task.
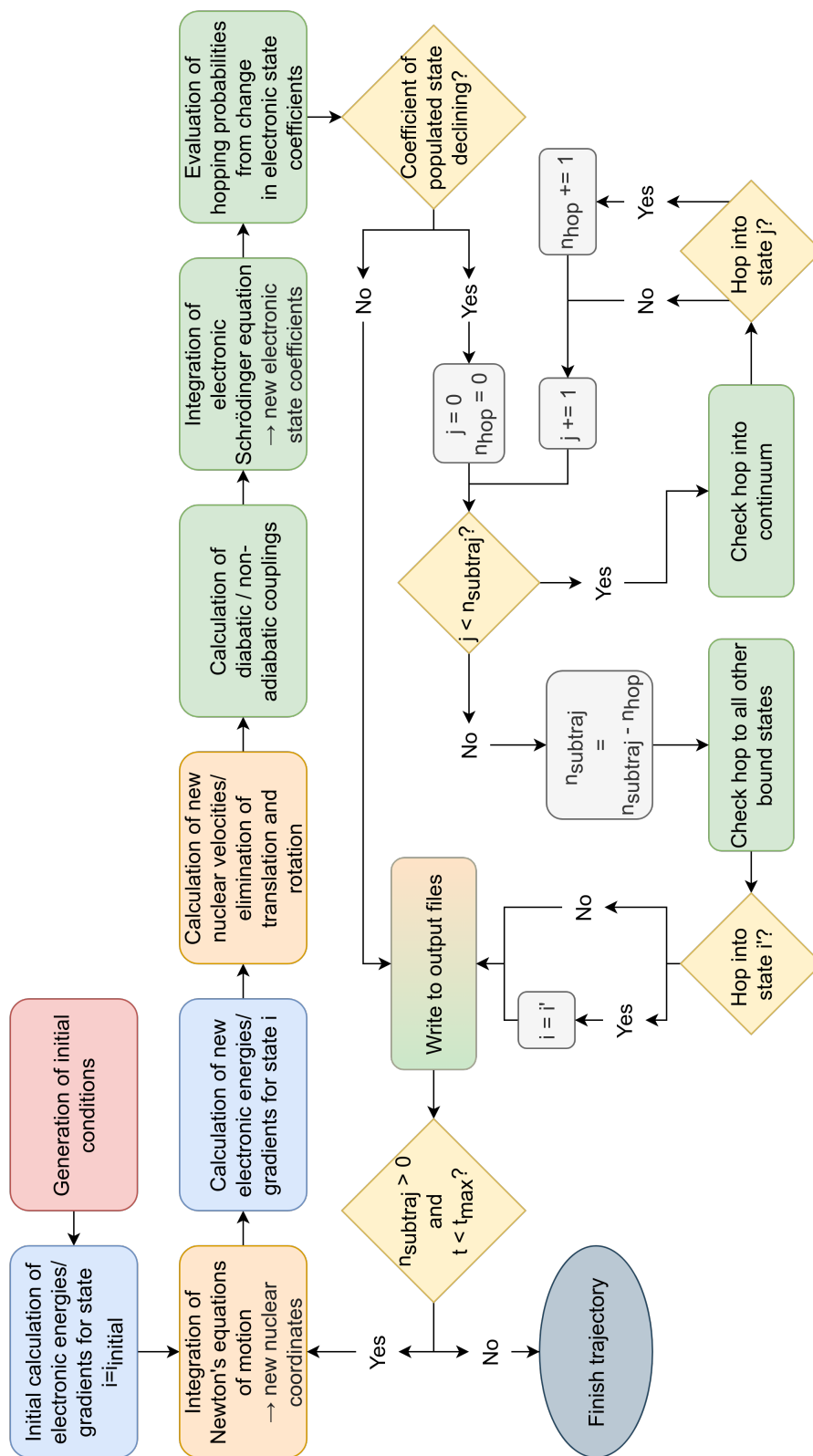
Figure 4.1: Schematic of the dynamics procedure as implemented in the HORTENSIA program package. The box coloration matches the specific tasks to the program modules as follows: red: wigner/wignerEnsemble.py, blue: external quantum-chemistry program, orange: nuclearDynamics.py, green: populationDynamics.py

Starting from the generation of an ensemble of nuclear coordinates $\mathbf{R}(t)$ and velocities $\dot{\mathbf{R}}(t)$ at the time $t = t_{initial}$ using the `wignerEnsemble` module in the `wigner` folder (red), a first quantum-chemical calculation is performed by an external quantum-chemistry program - to date these include Gaussian09/Gaussian16[192] and QChem[193] (blue) - which yields the forces from which the accelerations $\ddot{\mathbf{R}}(t)$ of the nuclei are computed. The nuclei are then propagated by integration of Newton's equations of motion for one nuclear time step using the `nuclearDynamics` module (orange). With the new nuclear coordinates $\mathbf{R}(t+\Delta t)$, a new set of quantum-chemical calculations can be performed, yielding the new energy gradients necessary for the evaluation of the velocities $\dot{\mathbf{R}}(t+\Delta t)$. With the quantum-chemical calculations at t and $t+\Delta t$, one is now able to construct the electronic continuum states (cf. Section 4.2.1) as well as the coupling matrices of the diabatic and nonadiabatic couplings (cf. Section 4.2.2) using the `populationDynamics` module (green). From this point, the electronic state coefficients $\mathbf{c}(t)$ are propagated in parallel to the nuclear dynamics by integrating the electronic Schrödinger equation, yielding $\mathbf{c}(t + \Delta t)$. These are utilized to compute hopping probabilities from the occupied bound state to all other (bound and continuum) states. The switching between the states is induced stochastically according to the respective hopping probabilities given in equation 4.29. After writing the results into the various output files time is shifted to $t = t + \Delta t$, thereby completing one time step.

To make this initial overview more specific, in the following the underlying algorithms are explained in more detail.

4.3.1   Electronic structure calculation

All electronic structure and energy gradient calculations can be performed using the Kohn-Sham (TD)-DFT level of theory as implemented within the Gaussian09, Gaussian16 or QChem program packages. Notice that special care must be taken when choosing appropriate functionals for the description of weakly bound anions. In particular, it is recommended to employ range-separated functionals to ensure the correct long-range behavior of the Kohn-Sham potential, which is crucial given the spatially diffuse electron distributions of anions. In addition, especially when describing multipole-bound systems, an appropriate description of dispersion interactions is needed. For more comprehensive guidance on the proper choice of the adequate DFT model, the reader is referred to Ref.[10] and the literature cited therein. The AO basis set needs to be defined explicitly in a separate input file, thus also allowing for additional augmentation of basis sets, which is of utmost importance when describing molecular anions.[10,112] The `handlerG09` and `handlerQChem` modules provide an interface to the external programs by creating input files and calling the respective programs. The `dysonG09` and `dysonQChem` modules contain classes that parse the external output files and organize the data into the form needed in the program.

4.3.2 Generation of initial conditions

The initial nuclear coordinates and velocities are determined by stochastic sampling of an appropriate probability distribution function for the harmonic normal modes of the system. These can be computed from the electronic Hessian matrix at an optimized geometry of the studied molecule. For molecules in the vibrational ground state as well as for a thermal ensemble of molecules, the Wigner function

$$\rho_W(\{Q_i, P_i\}) = \frac{1}{(\pi\hbar)^N} \prod_{i=1}^{N} \alpha_i(T) \exp\left(-\frac{\alpha_i(T)}{\hbar\omega_i}(P_i^2 + \omega_i^2 Q_i^2)\right) \qquad (4.32)$$

with

$$\alpha_i(T) = \tanh\left(\frac{\hbar\omega_i}{2k_B T}\right) \qquad (4.33)$$

is employed, where $\{Q_i, P_i\}$ denote the normal coordinates and momenta, ω_i is the angular frequency of normal mode ν_i and T the thermodynamic temperature.

Besides these cases, in experiments investigating vibration-induced autoionization another type of initial conditions is often important in which one or more normal vibrations of the system are excited by laser irradiation. In principle, the respective initial conditions could be also generated by using a Wigner function. However, Wigner functions for excited vibrational states can assume negative values and can thus not be directly identified with a probability distribution. This issue might be addressed by sampling the positive and negative parts of the Wigner function separately, propagating the respective ensembles and calculating the final properties of the system by averaging in due consideration of the positive or negative sign associated with each trajectory.

An alternative which gets on with only a single ensemble would be to use a positive definite probability distribution constructed from the product of squared wavefunctions in position and momentum space for the excited vibrational state,

$$\rho_v^{(i)}(Q_i, P_i) = |\chi_v^{(i)}(Q_i)|^2 |\tilde{\chi}_v^{(i)}(P_i)|^2, \qquad (4.34)$$

where $\chi_v^{(i)}(Q_i)$ and $\tilde{\chi}_v^{(i)}(P_i)$ are the harmonic oscillator wavefunctions for the desired excited quantum state v of normal mode ν_i in position and momentum space, respectively. For the specific case of a singly excited normal mode ($v = 1$), this distribution function reads

$$\rho_1^{(i)}(Q_i, P_i) = \frac{4}{\pi\hbar^3} Q_i^2 P_i^2 \exp\left(-\frac{1}{\hbar\omega_i}(P_i^2 + \omega_i^2 Q_i^2)\right). \qquad (4.35)$$

As we have demonstrated in Ref.[185], due to the occurrence of differences in the averaging procedure, employing an excited-state Wigner functions leads to slower convergence of ensemble averages with respect to the number of trajectories compared to using the product of squared wavefunctions, while the ensemble average as such does not differ much. Therefore, we chose to account for vibrational excitation by using equation (4.35).

4.3.3   Nuclear dynamics

Given Newton's equations of motion 4.1, the nuclei are propagated by numerical solution using the velocity Verlet algorithm[49] for a user-defined time step. Within this algorithm, the nuclear coordinates at $t + \Delta t$ are obtained from a Taylor series expansion around the coordinates at t:

$$\mathbf{R}(t + \Delta t) \approx \mathbf{R}(t) + \dot{\mathbf{R}}(t)\Delta t + \frac{1}{2}M^{-1}\mathbf{F}(t)\Delta t^2, \qquad (4.36)$$

where in the last term the acceleration has been formulated using the force $\mathbf{F}$ given by the electronic potential energy gradient (cf. equation 4.1). With the new nuclear coordinates, the force at $t + \Delta t$ can be evaluated, giving rise to the new nuclear velocities

$$\dot{\mathbf{R}}(t + \Delta t) = \dot{\mathbf{R}}(t) + \frac{\Delta t}{2}M^{-1}\left[\mathbf{F}(t) + \mathbf{F}(t + \Delta t)\right]. \qquad (4.37)$$

Due to the approximative nature of the algorithm above and the accuracy of the calculated energy gradients, it is possible that the velocities develop small overall translational or rotational components although the initial conditions were determined with these degrees of freedom set at rest. These numerical inaccuracies are detected, in the case of translational velocity by the shift of the center of mass away from the origin of the coordinate system, in the case of rotation by the calculation of the angular velocity according to

$$\boldsymbol{\omega}_{rot} = I^{-1}\mathbf{L} \qquad (4.38)$$

with the moment of inertia I and the angular momentum $\mathbf{L}$. The translational and rotational portions of the nuclear velocities are then subtracted from the total velocity and the remaining vibrational part is rescaled to ensure energy conservation.

   After each nuclear dynamics step, the new nuclear coordinates and velocities are written into separate output files, the coordinates in a format of consecutive xyz files which can be visualized easily by external software (for example with the VMD program package[194], which is warmly recommended).

4.3.4   Electronic dynamics

Since the evaluation of electronic coupling terms in equation 4.5 is, apart from the external quantum-chemistry calculations, the computationally most expensive step in the dynamics, several approximations need to be implemented, which will be discussed in the following

Calculation of coupling terms

Before calculating the coupling terms, the discretization procedure for the generation of wave vectors needed to construct the continuum state wavefunctions will be discussed. To uniformly discretize angular orientation and kinetic

energy of ejected electrons, it is natural to discretize angular and energetic distribution separately. Since the kinetic energy of a plane wave is

$$E_{kin}(\mathbf{k}_i) = \frac{\hbar^2 |\mathbf{k}_i|^2}{2m_e} \tag{4.39}$$

and therefore proportional to the length of the wave vector squared, this length is discretized such that the desired energy range is covered evenly. For a given energy, the vector orientations are approximately evenly distributed according to the Fibonacci sphere algorithm[155]. The volume elements $\Delta \mathcal{V}_k$ needed for calculating the bound-continuum couplings in equations 4.8 and 4.9 are constructed as the difference of spherical caps around the corresponding wave vectors with the base diameter as an average over the six nearest points on the sphere surrounding the vector.

In the diabatic coupling terms in the AO basis (equation 4.16) two types of four-center integrals are present: (i) such involving four Gaussian-type atomic orbitals (GTOs), $\langle \sigma \lambda | \mu \nu \rangle$. These are evaluated by using the `libcint` library[160] within the PySCF program package[195,196]. (ii) integrals involving a plane wave of wave vector $\mathbf{k}_i$ and three GTOs, $\langle \mathbf{k}_i \lambda | \mu \nu \rangle$. These terms can in principle be calculated analytically as outlined, e.g., in Ref.[162], but this is computationally unfeasible for the present purpose since an immense number of plane waves has to be included for a proper discretization of the ionization continuum. Instead, the plane waves are approximated by their Taylor expansion around the center of basis function $|\mu\rangle$, $\mathbf{R}_\mu$. As will be discussed in the Performance Section later on, for sufficient accuracy in the approximation it is necessary to include not only the zero'th order term (assuming the plane wave to be constant in the vicinity of the molecule), but also the first-order term, resulting in the approximation

$$\begin{aligned} \mathrm{e}^{i\mathbf{k}\cdot\mathbf{r}} &= \mathrm{e}^{i\mathbf{k}\cdot\mathbf{R}_\mu} \mathrm{e}^{i\mathbf{k}\cdot(\mathbf{r}-\mathbf{R}_\mu)} \\ &\approx \mathrm{e}^{i\mathbf{k}\cdot\mathbf{R}_\mu} \left[1 + i\mathbf{k}\cdot(\mathbf{r}-\mathbf{R}_\mu) \right]. \end{aligned} \tag{4.40}$$

This leads to two terms for the two-electron integrals as follows:

$$\langle \mathbf{k}_i \lambda | \mu \nu \rangle \approx \mathrm{e}^{i\mathbf{k}\cdot\mathbf{R}_\mu} \left[\langle \lambda | \mu \nu \rangle + i\mathbf{k} \langle \lambda | \tilde{\mu} \nu \rangle \right]. \tag{4.41}$$

In the above expression, $|\tilde{\mu}\rangle$ is an AO basis function with an angular momentum quantum number by one higher than $|\mu\rangle$ while having the same Gaussian exponent. This heavily reduces the amount of two-electron integrals to be computed from $n_{AO}^3 n_{PW}$ to $n_{AO}^2 [n_{AO} + n'_{AO}]$, with n_{AO} being the total number of AO basis functions, n'_{AO} the total number of basis functions with increased quantum number and n_{PW} the total number of plane waves. For instance, in the case of vinylidene in Ref.[26], this amounts to a reduction by a factor of ~ 30000. These terms are again evaluated using the PySCF module. The prefactors A, $\bar{A}$ and B present in equation 4.16 are straightforwardly implemented in Python according to equations 4.17, 4.18 and 4.19. Evaluation of the Dyson orbitals needed for the calculation of the nonadiabatic couplings

is implemented as described before in Ref.[140] for arbitrary basis sets for the anion and the neutral molecule. After construction of the Dyson orbitals from all bound anionic states to the neutral ground state the nonadiabatic coupling terms are then calculated according to equation 4.23. To ensure that the wavefunctions of bound states do not switch their arbitrary signs (which can happen, since the external quantum-chemistry calculations are independent of each other), the overlap of electronic wavefunctions of all bound states are tracked throughout the trajectories and accounted for in all formulae involving the respective states.

Calculation of electronic state coefficients

The electronic degrees of freedom are propagated by solving the time-dependent Schrödinger equation 4.5 in the manifold of all considered bound anion and continuum electronic states using Adams' method as implemented in the `ode` class of Python's `scipy.integrate` module[177] with a user-defined integration time step. For increased computational stability the equations are beforehand transformed into the interaction picture, introducing the new electronic state coefficients

$$a_n(t) = c_n(t) \; \mathrm{e}^{\frac{i}{\hbar} H_{nn} t}.$$ (4.42)

Inserting this into equation 4.5 leads to the actually implemented electronic equation of motion

$$\dot{a}_n(t) = \sum_m \left[-\frac{i}{\hbar} \tilde{H}_{nm} - D_{nm} \right] a_m(t) \mathrm{e}^{-\frac{i}{\hbar}(H_{mm} - H_{nn})t}$$ (4.43)

where $\tilde{H}_{nm}$ denotes the Hamiltonian matrix of the system with zeros on the diagonal.

Hopping procedure

Hopping probabilities are directly evaluated according to equation 4.29 from the state coefficients: A random number between 0 and 1 is generated using the `random` function in the `numpy.random` module and hopping is conducted accordingly. Once a trajectory hops into a continuum state, it could in principle be straightforwardly continued on the potential energy surface of the neutral molecule. Although this can be quite insightful if one is interested in the subsequent geometric changes of the ionized system, we follow a different approach and stop the trajectories after electron detachment since our focus is set on the actual autoionization process. This allows us to implement a modification of the surface-hopping procedure that leads to a great improvement of the hopping statistics. The idea is to divide a single trajectory into 'sub-trajectories', i.e. to evaluate if a trajectory hops a number $n_{subtraj}$ of times (see Figure 4.1). Every time a sub-trajectory hops into the continuum, $n_{subtraj}$ is reduced by one and once it reaches zero, the underlying nuclear dynamics is stopped. It has

to be noted that this procedure is only followed for hops into the continuum, while for hops between bound anionic states only a single hopping event per trajectory and time step is possible due to the need to continue the nuclear dynamics on an unambiguously determined potential energy surface.

4.3.5   Graphical user interface

Our program package comes with a graphical user interface (GUI) for the input generation as well as an analysis tool for trajectories. An example of the former is displayed in Figure 4.2. In the input generator, which is started with

```
$ hortensia —gui
```

in addition to all relevant settings for the actual simulation, the user may find options for the generation of a complete folder structure for the trajectories as well as bash submit scripts to be used with the Slurm Workload Manager [197]. Furthermore, the above mentioned Wigner ensemble scripts can be used and initial conditions can be generated. Therefore it is highly recommended to use the GUI feature.

Additionally, through the command

```
$ hortensia —analysis
```

one can open the analysis tool which is able to read output files and visualize them in a sub-window using the `matplotlib` program package[198].

4.3.6   Installation

The most convenient way to install the program package is downloading or cloning the *repository on our Github page* [199]. In the main folder, execute

```
$ python cysetup.py build_ext —inplace
$ pip install .
```

to first compile the Cython modules and then install the program. The program package requires (and will automatically pip install)

- `python >= 3.8`

- `cython` - for faster summation of large arrays, mainly in the calculation of the two-center integrals in equations 4.16 and 4.41

- `scipy` - mainly in the integration of the electronic Schrödinger equation as outlined in subsection 4.3.4

- `pyscf` - for the calculation of the two-electron integrals in equations 4.16 and 4.41

- `joblib` - for the parallelization of diabatic couplings

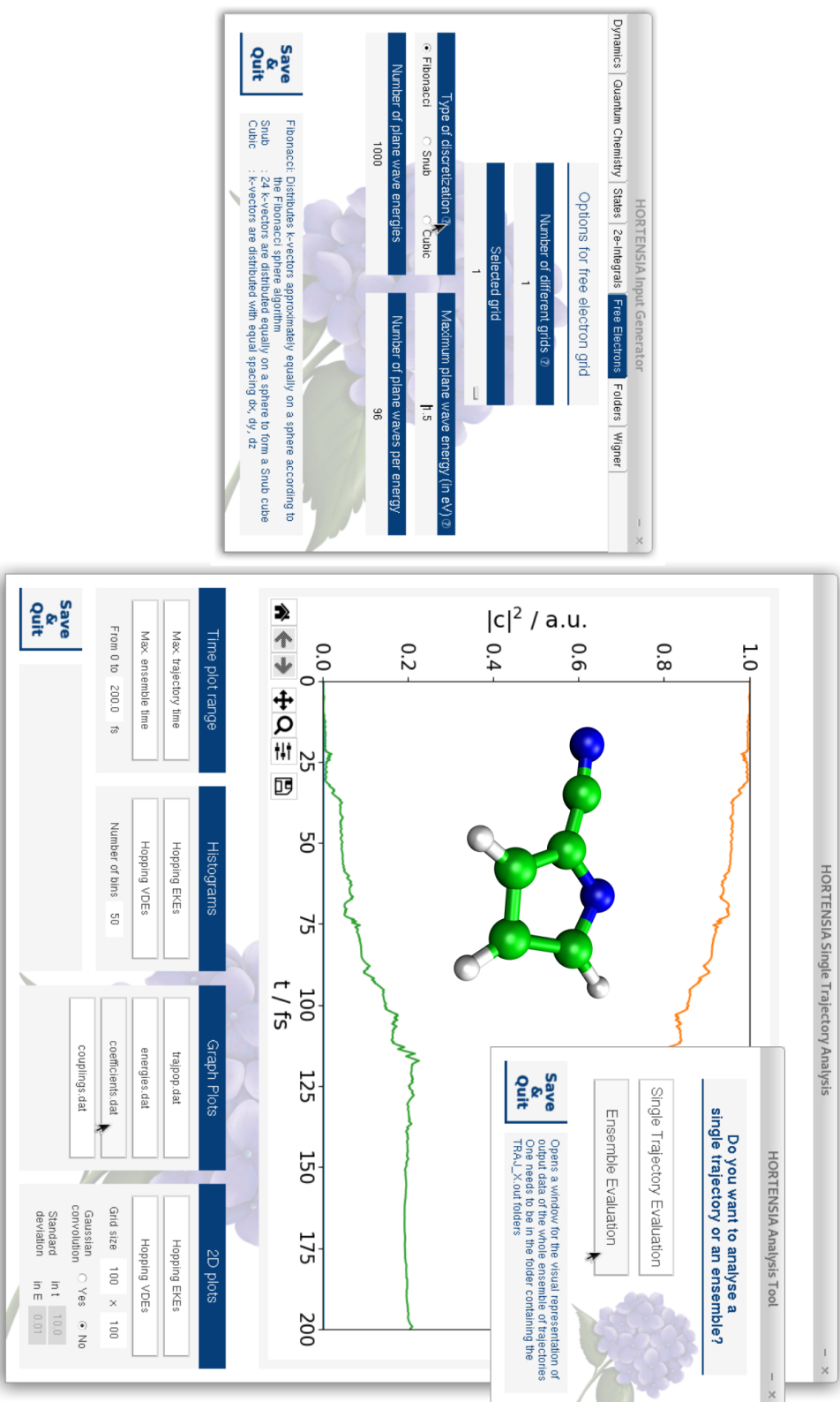- `matplotlib` - for the plots in the sub-window of the analysis tool described before

Figure 4.2: Left: example page of the graphical input generation tool; right: output analysis GUI with the electronic state coefficients of a single, exemplary 2-cyanopyrrolide trajectory. The molecular structure is only an illustrative image, which was created using the VMD program, and its creation is not part of the presented program.
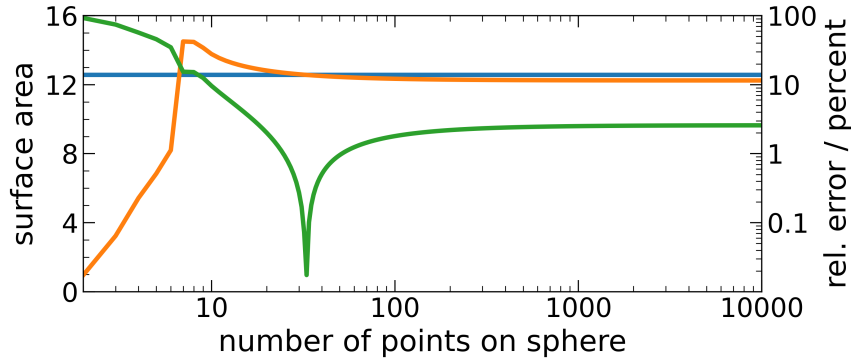
Figure 4.3: Comparison of the actual surface area of a unit sphere ($A_{\mathrm{sphere}} = 4\pi$, blue line) and the approximated surface area as described in subsection 4.3.4 for up to 10^4 vector orientations (orange). The relative error is given in green.

and all dependencies thereof. Using the command

```
$ pip uninstall hortensia_latest
```

will uninstall the program package.

4.4 Discussion

In this section we will quantify aspects of the program related to overall performance. This includes the quality of approximations within the methodology as well as optimization of time consumption and computational resources. Moreover the exemplary autoionization dynamics of the 2-cyanopyrrolide anion is discussed.

4.4.1 Accuracy of k-vector discretization and integral approximations

The accuracy of the Fibonacci sphere algorithm for angular discretization in k-space is illustrated in Figure 4.3 by the covered surface area of a unit sphere using a given number of distributed points. The total surface area (orange graph) is presented with the relative error $|A_{\mathrm{fib}} - A_{\mathrm{sphere}}|/A_{\mathrm{sphere}}$ (green graph) to the exact surface area $4\pi \approx 12.566$ (blue line). The approximated area rapidly converges to a value of ~ 12.243, which corresponds to a relative error of ~ 2.575 %. Since in the coverage of k-vector lengths no additional approximation is introduced and for their respective volume elements the k-space is divided energetically evenly (thus covered exactly with respect to vector length), the error in the surface area for specific vector lengths equates to the overall error of the volume elements. Therefore the sum of these volume elements results in a total volume that deviates by less than 3 % from the actual sphere for arbitrary numbers of vector orientations $n_s \geq 30$ and lengths n_E (giving a total number of wave vectors $n_k = n_E \cdot n_s$).

The approximation of the plane wave by the first terms of its Taylor expansion as introduced in equation 4.41 relies on the assumption that the amplitude
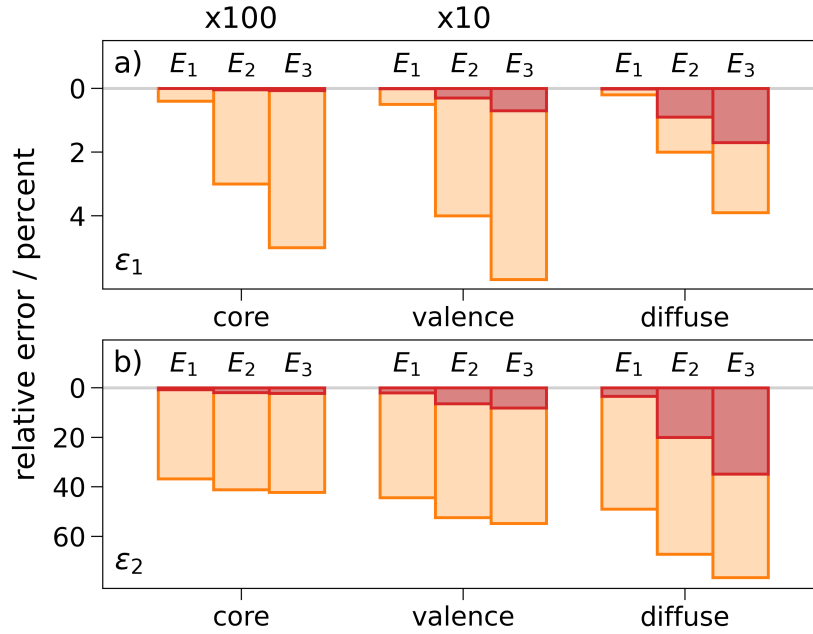
Figure 4.4: Errors (in %) of hybrid Gaussian-plane wave electron repulsion integrals $\langle \mathbf{k}_i \lambda | \mu\nu \rangle$ for 2-cyanopyrrolide employing the 6-311++G** +3s2p basis set. The molecular structure has been optimized in the dipole-bound excited state at the TDDFT/ωB97XD level using the same basis set. Two types of error measures are reported: a) $\epsilon_1^{\mathrm{ap}} = \langle |I_{ex} - I_{ap}| \rangle / \langle |I_{ex}| \rangle$ and b) $\epsilon_2^{\mathrm{ap}} = \langle |I_{ex} - I_{ap}| / |I_{ex}| \rangle^a$, where I_{ex} denotes the exact integral, I_{ap} the approximate value either according to equation 4.41 (linear, red bars) or assuming the plane wave to be constant (orange bars). For ϵ_2^{ap} the average has been computed for all integrals with $|I_{ex}| > 10^{-16} E_H$. To compute the average the integrals are grouped according to the exponent α of basis function μ as core ($\alpha > 10 a_0^{-2}$), valence ($10 a_0^{-2} < \alpha < 0.1 a_0^{-2}$), and diffuse ($\alpha < 0.1 a_0^{-2}$). For each plane wave energy ($E_1 = 0.0015$ eV, $E_2 = 0.1$ eV, $E_3 = 0.2$ eV), the average has been taken over all distinct integrals provided by the basis set as well as over 24 different k-vectors corresponding to the direction vectors of the vertices of a snub cube. In a), the core and valence error bars are multiplied by a factor of 100 and 10, respectively, to enhance visibility.

of the plane wave only changes marginally within the extent of the AOs. Figure 4.4 shows a comparison between the approximation with linear terms, an even simpler constant-wave approximation where $\mathrm{e}^{i\mathbf{kr}} \approx \mathrm{e}^{i\mathbf{kR}_\mu}$ and the exact integrals for selected plane wave vectors for 2-cyanopyrrolide, which serves as an example molecule illustrating the applicability of the program (see section 4.4.3 below). Two error measures are compared: a relative value of average deviations (ϵ_1) in Figure 4.4a) and an average value of relative deviations (ϵ_2) in Figure 4.4b), which differ insofar as in ϵ_1, the deviations between exact and approximate integrals are averaged first and then divided by the overall average value of the exact integrals, while in ϵ_2, first for each individual integral the relative error is computed, followed by averaging the results. The averages are reported for three illustrative plane wave energies and grouped according to the Gaussian exponent of the basis function sharing its electron coordinate with the plane wave as "core", "valence" and "diffuse" with decreasing size of the exponent (for details see Figure 4.4). Overall, it becomes evident that

for both error measures, the linear approximation of the plane wave is clearly superior to the constant approximation. The values of ϵ_1 are always much smaller than those of ϵ_2, which is due to the fact that the relative errors of smaller integrals tend to be larger than those of larger ones, and the definition of ϵ_1 partially compensates for this fact. Errors larger than a few percent only occur for ϵ_2 calculated for diffuse basis functions at larger plane wave energies. Since in the actual computations, the approximate integrals are employed to calculate the diabatic couplings and for this, the sum over the entire basis set is taken (cf. equation 4.16), especially the smallness of error ϵ_1 encourages the use of the linear approximation.

4.4.2 Optimization of program performance

Where computationally advantageous, we separate the time-dependent and -independent parts of the underlying equations and pre-calculate the time-independent terms at the beginning of the simulation. This results in higher overall memory usage, however of only several hundred MB to a few GB (depending on the molecular system), but leads to significant time-saving, which is still a desirable trade-off when calculating on CPU clusters but may limit the use of the program on single desktop computers.

Furthermore, for increased performance the summation over the four-center integrals in terms 2 and 4 on the right side of equation 4.16 is implemented as follows: one first pre-calculates the terms A, $\bar{A}$ and B given in equations 4.17-4.19 for all AOs. Then the calculation of the four-center integrals using the PySCF program package is divided into n_{proc} smaller terms, n_{proc} being the user-defined number of processors, and then evaluated in parallel utilizing the joblib[200] library by explicit summation over all AO combinations implemented in a Cython[201] module, therefore reducing the memory usage by ridding oneself from massive arrays while also improving the runtime performance of this time bottleneck through parallelization.

Together with the calculation of coupling terms, the most time-consuming step of the simulation is the two external quantum-chemical calculations needed in each time step. There are a few options to improve the performance of these calculations, the easiest of which are to increase the number of utilized processors and to reduce convergence time by loading the results of the last time step as an initial guess for the new calculation. Another possibility is in the choice of basis sets. Finding a basis set for anions prone to autoionization can be challenging due to the small ionization energies and the diffusity of the states that comes with it. Therefore one has to consider basis sets augmented with enough diffuse basis functions to reasonably describe the properties of the system[10]. Although popular basis sets such as doubly and triply augmented Dunning-style basis sets (daug-cc-pVDZ, taug-cc-pVDZ) are (generally speaking) a potentially good choice for the description of loosely-bound anions, the size of these basis sets is computationally prohibitive if one aims to run dynamics simulations and therefore thousands of consecutive quantum-chemical calculations. A good alternative can be the usage of smaller basis sets (such

as 6-311++G**[169,170]) augmented with additional diffuse functions generated by geometric progressions of the Gaussian exponents as outlined in Ref.[112].

Considering the overall time consumption, no real performance benchmarks exist with which to compare our program package, since the theory behind it is rather novel. Therefore we will briefly discuss the specific case of vinylidene from our work presented in Ref.[26] and the 2-cyanopyrrolide example discussed in detail in section 4.4.3 below.

The vinylidene dynamics was performed for a total time of 3 ps in 15000 nuclear dynamics time steps at the ωB97XD[166]/d-aug-cc-pVDZ level of theory, which consists of 146 primitive Gaussian basis functions and 96000 plane waves, amounting to ∼460 million 2-electron integrals per time step to be solved (cf. equations 4.16 and (4.41)). Using 6 Intel Xeon E5-2660 (v3) processors per trajectory, the average computation time was around 11 days and 14 hours with a peak memory usage of ∼9 GB. Of the total time, around 5 days (or 43 %) were needed for the external quantum-chemistry calculations with the Gaussian09 program package. It also has to be noted that of the remaining time ∼30 % can be attributed to the calculation of the 2-electron integrals in the diabatic couplings running on a single processor, which has since been parallelized for improved performance.

In the simulation of the 2-cyanopyrrolide dynamics, the 6-311++G**+3s2p basis set consists of 297 primitive Gaussian basis functions which results in ∼7.8 billion 2-electron integrals to be summed over per time step. The average computation time amounted to 13 days and 12 hours on 10 Intel Xeon E5-2660 (v3) processors per trajectory, for a total time of 200 fs in 1000 nuclear time steps. The inclusion of an excited state leads to a massive increase in time consumption in the quantum-chemical calculations (which account for ∼47 %/ 6.4 days of the total computation time) as well as the evaluation of diabatic couplings, where the summation of all integral terms (cf. equation 4.16) is now also conducted on 10 processors using the `joblib` module.

4.4.3   Illustrative example: Autoionization of the 2-cyanopyrrolide anion

To illustrate the scope of our program, we simulated the vibration-induced autoionization dynamics of the example anion 2-cyanopyrrolide. Experimentally, this molecule was measured to have an adiabatic electron affinity of 3.0981 eV and possesses a Rydberg-s type dipole-bound state 29.8 meV below the ionization threshold.[84] As can be seen in Table 4.1, which compares several quantum-chemistry methods and basis sets with the data measured by Wang *et al.*, the experimental data is reproduced quite well using the ωB97XD functional and large, diffuse basis sets such as triply augmented pVDZ/pVTZ. Moreover, although the description of the molecule with standard Pople-type basis sets is fairly inaccurate, further augmentation with extra diffuse basis functions (see Ref.[112]), in this case placed on the nitrogen atoms, also leads to good agreement with the experimental values. At the same time this approach

Table 4.1: Comparison of adiabatic electron affinities (AEA), vertical detachment energies to the anionic ground state (VAE$_{GS}$) and excitation energy to the dipole-bound state (ΔE_{DBS}) for the 2-cyanopyrrolide anion. The superscript indicates at which optimized geometry (a = anion, n = neutral) the respective value is calculated. The method used in the dynamics simulation is indicated in bold font. The added basis functions +Xs etc. are generated according to Ref.[112] (with a factor for the geometric progression of 3.5) and centered on the nitrogen atoms. All energies values are given in eV. In some cases AEA$_{DBS}$ could not be obtained, instead the vertical attachment energy at the neutral equilibrium geometry is given as an approximation (denoted with *). [a] Ref.[171], [b] Ref.[171,172], [c] Ref.[171–173], [d] Ref.[170], [e] Ref.[169,170], [f] Ref.[175,176]

Method	AEA$_{GS}$	AEA$_{DBS}$	VDE$_{GS}^a$	VAE$_{GS}^n$	ΔE_{DBS}^n
ωB97XD / aug-cc-pVDZ[b]	3.075	-0.674	3.225	2.932	3.612
ωB97XD / d-aug-cc-pVDZ[c]	3.071	-0.117*	3.221	2.929	3.046
ωB97XD / t-aug-cc-pVDZ[c]	3.070	0.031*	3.220	2.928	2.897
ωB97XD / t-aug-cc-pVTZ[c]	3.044	0.044*	3.200	2.899	2.855
ωB97XD / 6-31+G**[d]	3.062	-1.374	3.212	2.919	4.302
ωB97XD / 6-31+G** +3s2p	3.064	0.060*	3.217	2.921	2.861
ωB97XD / 6-311++G**[e]	3.095	-0.759	3.249	2.949	3.716
ωB97XD / 6-311++G** +3s	3.095	0.064	3.249	2.949	2.887
ωB97XD / 6-311++G +3s2p**	**3.094**	**0.063**	**3.248**	**2.948**	**2.887**
ωB97XD / 6-311++G** +3s2p2d	3.076	0.055*	3.230	2.930	2.875
EOM-CCSD[f] / t-aug-cc-pVDZ	2.844	-0.102*	3.016	2.686	2.788
EOM-CCSD / 6-31+G** +3s2p	2.679	-0.346*	2.855	2.518	2.864
EOM-CCSD / 6-311++G** +3s2p	2.748	-0.148*	2.929	2.584	2.732
Experiment[84]	3.0981	0.0298			

HONTO   LUNTO
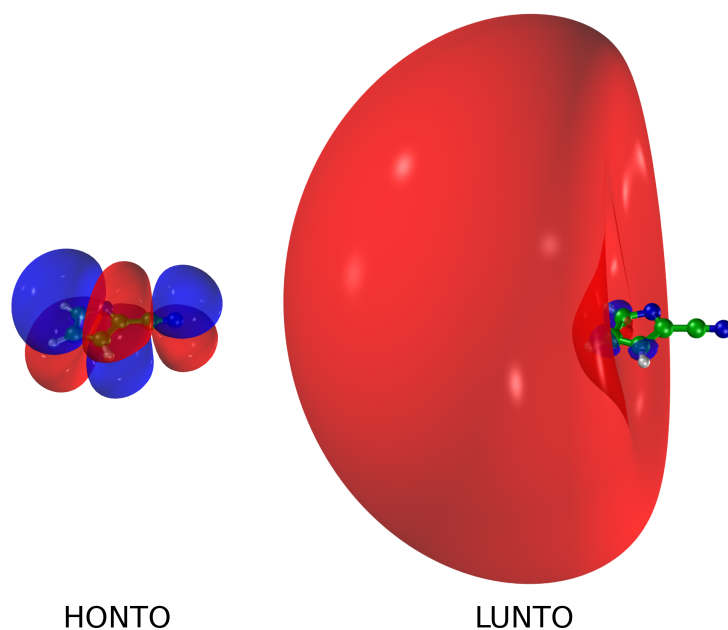
Figure 4.5: HONTO and LUNTO of 2-cyanopyrrolide at the optimized geometry of the dipole-bound first excited state at the ωB97XD/ 6-311++G** + 3s2p level of theory with an isovalue of 0.003
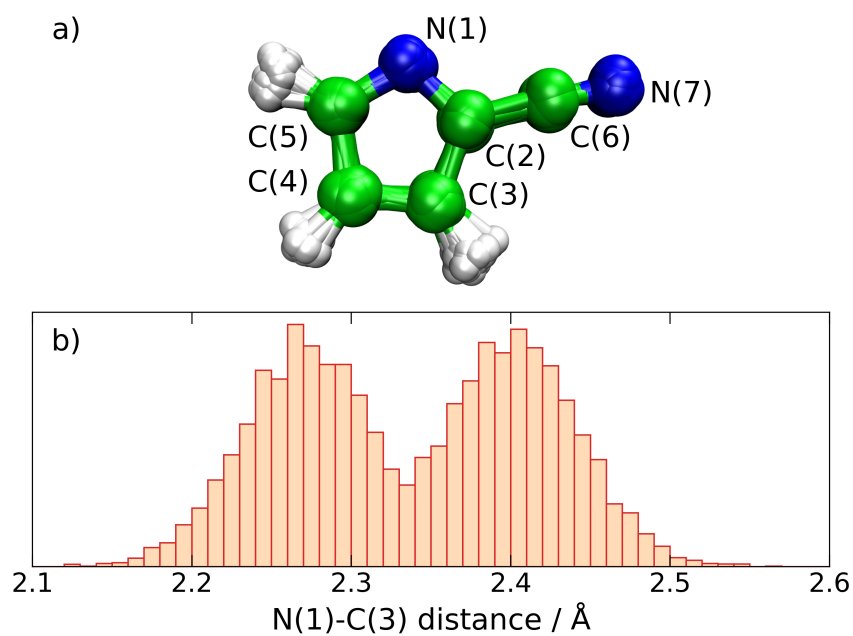
Figure 4.6: a) Overlay of all initial molecular structures used in the dynamics simulation of 2-cyanopyrrolide, b) distribution for 10000 initial conditions as a function of distance (in Å) between the nitrogen (1) and carbon (3) atom as marked in a), showing a bimodal structure.
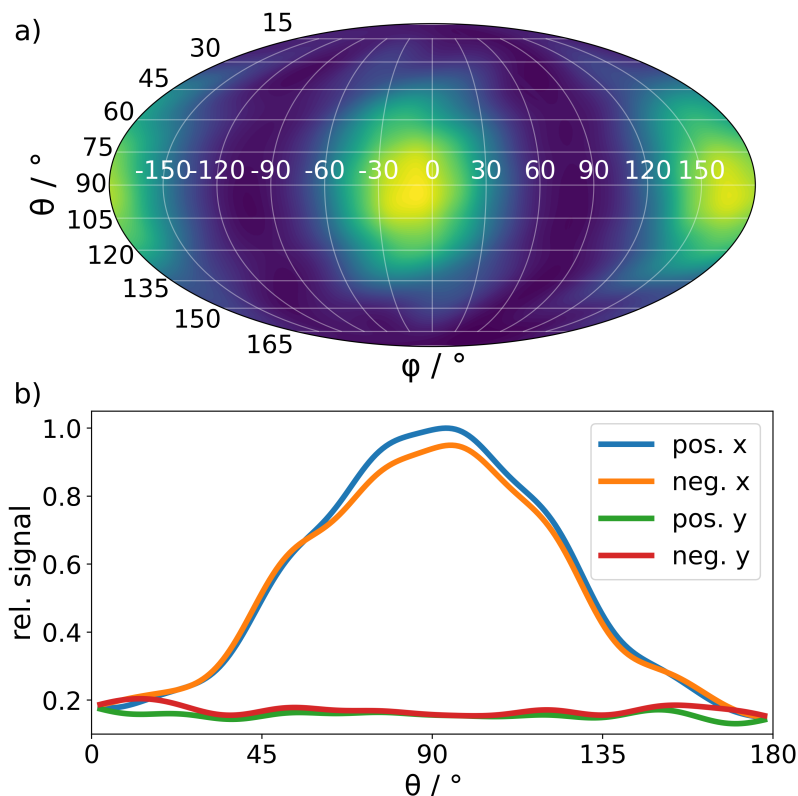
Figure 4.7: a) Mollweide projection of the angular distribution of ejected electrons in the 2-cyanopyrrolide dynamics, summed over all energies. The x-axis ($\varphi = 0$, $\theta = 90$ degrees) is aligned with the cyano group and the molecule lies within the xy-plane ($\theta = 90$ degrees); b) Slices through the Mollweide projection at φ angles of 0 (positive x direction, blue), 180 (negative x direction, orange), 90 (positive y direction, green) and 270 (negative y direction, red) degrees.

retains a significantly smaller total number of basis functions, therefore keeping computational effort manageable. Figure 4.5 shows the HONTO and LUNTO, visualizing the spatial distribution of the excess electron in the ground and excited state at the optimized geometry of the dipole-bound first excited state employing the ωB97XD functional and the 6-311++G** basis set augmented with three diffuse s- and two diffuse p-functions on each nitrogen atom (henceforth abbreviated as 6-311++G** + 3s2p). The shape of the excess electron's probability distribution in the dipole-bound state is of s-type, showing that employing additional higher polarization functions (d-/f-type) would lead to no further improvement in the description of the system. This is in complete agreement with a dipole moment of the neutral species of 5.02 D, well below the second critical dipole moment of $\sim$10 D needed for the binding of an electron in a p-type orbital,[108] consequently resulting in an s-type distribution centered around the positive end of the molecular dipole vector.

Using the 6-311++G** + 3s2p basis set with the ωB97XD functional, we simulated the vibration-induced autoionization dynamics in the first excited state with the normal mode at 946 cm^{-1} of A' symmetry (ν_{11} when sorted by increasing mode energy irrespective of symmetry) excited by one vibrational
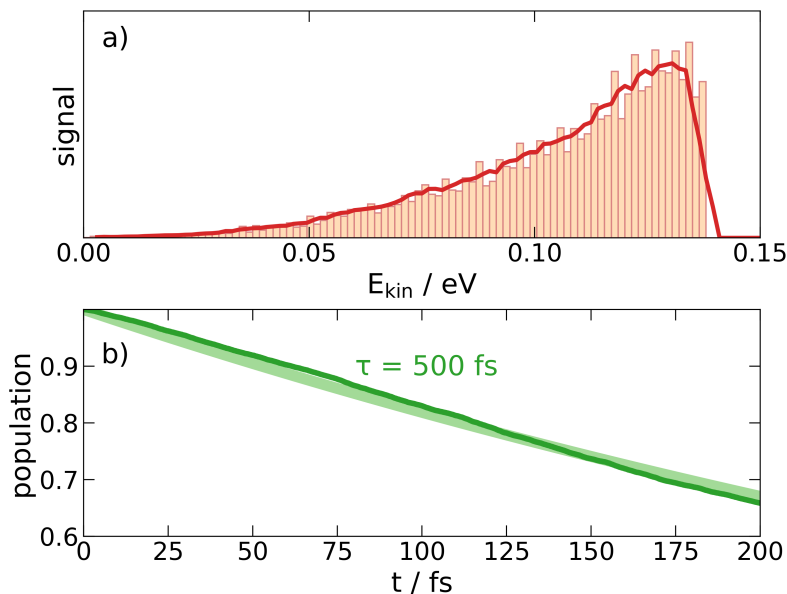
Figure 4.8: a) Simulated electron kinetic energy distribution of all hopping events after excitation of mode ν_{11} and propagation for 200 fs (orange histogram) and running average over 5 points/7.5 meV (red curve), b) time-dependent population of all bound anion states (dark green) and exponential fit with a time constant of $\tau = 500$ fs (light green).

quantum. The initial conditions were generated as described in subsection 4.3.2. Mode ν_{11} involves a symmetric stretching of the C-H bonds at carbon atoms 4 and 5 as well as a ring breathing motion affecting mostly the ring N and carbon 3. The numbering of atoms is provided in Figure 4.6a), which illustrates the resulting set of initial conditions by the superposition of all initial structures. In Figure 4.6b), the distance between the ring nitrogen and the carbon 3 is depicted, which exhibits a bimodal distribution typical for an excited vibrational state. The particular choice of vibrational excitation corresponds to the experimentally observed resonance 7 of the photodetachment spectrum in Ref.[84]. The simulation was carried out propagating an ensemble of 53 trajectories for a total of 200 fs (1000 nuclear time steps) with a discretized continuum of 400 plane wave energies evenly spaced from 0.0 eV to 0.138 eV and 96 orientations per energy. The maximum allowed kinetic energy of the plane wave is the sum of the vibrational excitation energy and the difference in zero-point energies of anion and neutral system, that is, the maximum excess energy available upon ionization.

Notice that due to the very low electron binding energy of the dipole-bound state and the approximative nature of the quantum chemically determined energies, it is challenging to precisely reproduce subtle binding energy differences on the meV scale along the trajectories. Thus, some instances of negative VDE occur in the dynamics. However, the experimental data from Ref.[84] only feature a peak attributed to vibrational autoionization. Therefore, we only include the latter in our simulation and neglect adiabatic ionization.

The nuclear dynamics following the vibrational excitation is characterized by relatively small amplitude motion. This is due to the overall low internal

energy of the molecule and its rigidity as a cyclic system. In the course of the dynamics, the molecular dipole moment associated with the neutral core, which is responsible for electron binding in the excited state, exhibits slight oscillatory behavior while being approximately situated in the molecular plane. This leads to an anisotropic ejection of electrons predominantly in the molecular plane along the axis containing the cyano group, as can be inferred from the Mollweide projection of the angle-dependent distribution of **k**-vectors, summed over all k values shown in Figure 4.7a). The resulting electron distribution is thus p-shaped, with maxima along the x-(cyano group) axis and minima in the yz-plane exhibiting only about 20% of the maximal intensity, as can be seen in Figure 4.7b). This observation is in line with the qualitative considerations of nonadiabatic autoionization from dipole-bound states outlined in Ref.[202]. No transitions to the anionic ground state are observed in our simulation due to a large energy gap regardless of geometry, therefore the angular electron distribution is solely due to ionization from the s-type dipole-bound state.

Regarding the electron kinetic energies, the distribution displayed in Figure 4.8a) is obtained, exhibiting a broad peak near the maximally possible energy of 0.138 eV. This can be attributed to a transition in which the vibrational energy of the excited mode is transferred completely to the outgoing electron, i.e., the vibrational energy of the molecule is reduced by one quantum in line with the propensity rules for vibrational autoionization established by Simons[134]. Further analysis of the peak shape should be taken with care, since for conceptual reasons vibrational resolution is not within the scope of quantum-classical dynamics.

Besides the spatial and energetic distribution of the ejected electrons, our simulation provides access to the timescale in which the ionization process takes place. Figure 4.8b) shows the time-dependent population of the bound anionic states, which exhibits a rapid decay that can be fit to an exponential function with a time constant of 500 fs. This value corresponds to a spectral width of around 70 cm^{-1}, which is of comparable size to the observation made in Ref.[84].

Overall this example calculation shows the applicability and scope of the method in the context of small to medium sized molecular anions, providing a means to gain molecular-level insight into the spatio-temporal dynamics of vibration-induced autoionization processes complementary to experimental measurements.

4.5 Conclusion

We have presented the Python program package HORTENSIA (Hopping real-time trajectories for electron-ejection by nonadiabatic self-ionization in anions) for the simulation of vibration-induced autoionization processes in molecular anions. The program implements our recently introduced extended surface hopping approach for the quantum-classical description of nonadiabatic autoionization dynamics, where the electronic degrees of freedom are treated

quantum-mechanically, while the nuclear motion is represented by classical trajectories. The electronic states included in the dynamics simulation comprise the bound adiabatic anionic states and discretized 'ionized system' states composed of a neutral core and a free electron wave function, between which nonadiabatic transitions are simulated in a stochastical manner from hopping probabilities obtained from changes in electronic state coefficients according to Tully's fewest-switches algorithm. The time-dependent state coefficients are calculated by solution of the electronic Schrödinger equation containing the nonadiabatic as well as diabatic couplings between the considered electronic states according to our presented methodology.

As shown in the example of 2-cyanopyrrolide, time- and angle-resolved electron kinetic energy signals are obtained directly from the surface-hopping trajectories. Since no deactivation to the ground state is observed in our simulation, autoionization with a time constant of 500 fs is identified as the only available deactivation pathway in the dipole-bound state of 2-cyanopyrrolide on the simulated timescale, with an anisotropic, p-like ejection of electrons along the cyano-axis. Moreover, with our program geometric data is yielded which allows for the structural analysis of molecules throughout the autoionization dynamics, providing easy access to geometric characteristics of the considered system, as demonstrated extensively in the example of the vinylidene[26] and 1-nitropropane[185] anions.

Furthermore, the implementation and internal structure of our program package was discussed, which also consists of secondary functionalities such as an input generator and a routine for the creation of initial conditions for nuclear coordinates and velocities within an easy-to-operate graphical user interface (GUI). Moreover, the program package provides the user with an additional GUI for the analysis and graphical representation of the most important dynamics results.

In the future, it may be interesting to study systems for which the autodetachment dynamics has recently been studied experimentally, such as the phenoxide[132] or 4-cyanophenoxide[29] anions. Useful extensions of the methodology could be the implementation of neutral molecules to be ionized, which requires the description of scattering states interacting with a cationic core, as well as the inclusion of laser field coupling (analogous to the FISH method[54]) to describe photoionization beyond the perturbative limit, thereby providing an extension of the approach developed in Ref.[140]. In addition, the treatment of electronically adiabatic autoionization could be combined with an ab inito computation of the electronic resonance lifetimes, e.g., along the lines presented in Ref.[143].

Data availability

The data that support the findings of this study are available from the corresponding author upon reasonable request.

Author declarations

Conflict of Interest

The authors have no conflicts to disclose.

Author Contributions

Kevin Issler: Data curation (lead); Formal analysis (lead); Investigation (lead); Methodology (equal); Software (lead); Visualization (lead); Writing - original draft (equal). Roland Mitrić: Conceptualization (equal); Funding acquisition (lead); Methodology (supporting); Project administration (lead); Resources (lead); Supervision (equal); Writing - review & editing (equal). Jens Petersen: Conceptualization (equal); Formal analysis (supporting); Methodology (lead); Software (supporting); Supervision (equal); Visualization (supporting); Writing - original draft (equal), Writing - review & editing (equal).

Chapter 5

A trajectory surface hopping study of the vibration-induced autodetachment dynamics of the 1-nitropropane anion

Reproduced from

Kevin Issler, Roland Mitrić and Jens Petersen,
"A trajectory surface-hopping study of the vibration-induced
autodetachment dynamics of the 1-nitropropane anion",
Theor. Chem. Acc. 142 (2023) 123.
https://doi.org/10.1007/s00214-023-03063-z

with the permission of Springer Nature.

Abstract

In this study we investigate the autodetachment dynamics of the 1-nitropropane anion after vibrational excitation of the energetically lowest C-H stretching mode using our recently developed extended quantum-classical surface hopping approach including the detachment continuum. Therein the detachment from an electronic bound anion state is treated as a nonadiabatic transition into discretized detachment continuum states for an ensemble of classical nuclear trajectories propagated on quantum-mechanical potential energy surfaces. The initial ensemble is obtained by sampling a phase space distribution accounting for the vibrational excitation of the C-H stretching mode of the molecule to match the experimental conditions.

The simulated kinetic energy distribution of the ejected electrons reproduces characteristic features of the available experimental data. Analysis of the nuclear dynamics points out that the approach to neutral-like geometries with decreased pyramidalization angle of the NO_2 group and reduced the N-O

bond lengths are the crucial factors enhancing the ultrafast autodetachment process in vibrationally excited 1-nitropropane. This is facilitated when the dipole-bound first excited state of the anion is populated, which is structurally similar to the neutral system. Although only a small transient population of this state is observed, it acts as an efficient doorway to the detachment continuum and is responsible for a significant amount of the ejected electrons.

5.1 Introduction

Molecular anions have been of great interest for many years to both theoretical and experimental researchers because of their widespread occurrence in a wide variety of contexts such as, e.g., surface chemistry[203], lower-atmosphere chemical reactions[95,204], nucleophilic substitution reactions[95,205], molecular biology[17,114,206], or acid-base chemistry[207], and simultaneously for the arising difficulties in observing and describing these systems accurately.[9,14] An early spectroscopic method targeting the detection of negative ions for high-resolution data was autodetachment spectroscopy, in which anions were excited into a metastable resonance state high above the detachment threshold, enabling drastically increased signal resolution by measuring the ejected electrons rather than observing the anionic molecules directly.[23] The necessity of this detection method arises from the fact that bound molecular anions, in contrast to neutral molecules, seldom have more than a handful of bound electronic states, if any other than the ground state at all. Therefore, the use of ionizing transitions represents a valuable spectroscopic alternative for these systems.[91]

Nevertheless, molecular anions with bound excited states are known since the discovery of the excited state in C_2^-,[20,123] and the study of such systems has since developed into an active area of modern research. Notable examples include their involvement in the formation of DNA strand breaks[17,114], in a competing deactivation process to E→Z isomerization in biochromophores[206], or the binding of electrons in the field of molecular multipoles[128,208–211], especially in the case of dipole-bound anion states[27,127,209,212,213], which are formed when an electron is bound by the strong permanent dipole moment of a neutral molecular core with very small binding energies usually in the range of only a few up to at most some hundred meV.[108] Possible deactivation paths of such systems include the transition to vibrationally excited states of the electronic ground state, subsequently resulting in autodetachment on time scales as short as hundreds of femtoseconds.[28,131,214]

Some molecular anions feature detachment energies that are small enough that even vibrational excitation of the electronic ground state is sufficient to eject electrons after a finite amount of time, which is a special case of vibration-induced autodetachment.[30,124] There are several examples where the excitation of a vibrational mode induces electron loss[215], as, for instance, recently observed in the isomerization process of the vinylidene anion (whose neutral system is a high-energy isomer of acetylene).[25,82]

The comprehensive theoretical treatment of this phenomenon is challeng-

ing due to a number of reasons: The low binding energies in weakly-bound anions result in very diffuse electron distributions of the extra electron, requiring the inclusion of sufficiently large and diffuse basis sets in the quantum chemical treatment. Furthermore, the wavefunction of the ionized system requires the description of an unbound electron scattered at the molecular core, which poses a computationally very demanding problem that can only be tackled be introducing a number of approximations. Finally, the simulation of time-dependent processes requires an accurate treatment of the detachment continuum to define appropriate occupation probabilities for the continuum states. In an effort to gain more insight into the intricate dynamical processes of weakly-bound anions upon vibrational excitation, we recently presented a novel surface-hopping-based methodology for the quantum-classical description of ultrafast vibration-induced autodetachment dynamics in such systems[26] and illustrated it on the example of the vinylidene anion, allowing us to contribute to the understanding of its autodetachment dynamics. We were able to establish a reasonable connection between the dynamic geometrical deformations ultimately leading to acetylene formation upon excitation of specific vibrational modes of anionic vinylidene and the efficiency of electron ejection, obtaining good agreement with the experimental data.

Our method has been implemented in a software package called HORTENSIA (**Ho**pping **R**eal-time **T**rajectories for **E**lectron-ejection by **N**onadiabatic **S**elf-**I**onization in **A**nions) that has been recently published on the GitHub platform.[85,199]

Opposite to vinylidene, whose anion does not have electronically excited states below the detachment threshold, the group of nitroalkane anions[129,216,217] exhibits a dipole-bound excited state involved in the autodetachment dynamics after vibrational excitation[111,218]. Extensive research, experimental as well as theoretical, is available for the two smallest nitroalkane anions, nitromethane[31,218–226] and nitroethane[219,227–231]. For the next larger homologue 1-nitropropane theoretical data is much scarcer, but there are several experimental studies available, namely by Tsuda *et al.*[219] on the formation of the anion, and by Weber *et al.*, who recorded photoelectron spectra[217] and investigated the characteristics of the autodetachment process induced by infrared excitation of C-H stretching vibrations in comparison to other nitroalkanes.[129] Remarkably, in stark contrast to nitromethane, no vibrational structure was visible in the ejected electron distributions for the higher homologues, which was attributed to fast energy randomization following the population of the metastable vibrational state.[129]

In the present contribution, we aim to deepen the molecular-level understanding of this process by investigating the autodetachment dynamics of 1-nitropropane following vibrational excitation of the energetically lowest-lying C-H stretching mode, employing our above-mentioned quantum-classical surface-hopping approach. The remainder of the paper is structured as follows: In Section 5.2, the theoretical methodology is presented. Computational details are provided in Section 5.3, which is followed by the presentation and discus-

sion of results in Section 5.4. Finally, conclusions are given in Section 5.5.

On the present occasion, we take the liberty to point out that our work in the field of quantum-classical dynamics has over the years been profoundly inspired by seminal works of Maurizio Persico, such as, e.g., Refs.[5,232–235].

5.2   Theoretical Approach

The theoretical methodology employed here for the simulation of the autodetachment dynamics of anionic nitropropane has been presented in detail in Ref.[26] and will here be only sketched briefly. Our approach is based on the trajectory surface-hopping method[52], which describes the nuclear motion classically while maintaining a quantum mechanical treatment of the electronic population dynamics. To account for detachment processes, we augment the manifold of bound electronic states by approximate continuum states and and include the coupling between both manifolds. Specifically, we expand the general time-dependent molecular wavefunction, which is given along the classical trajectory $\mathbf{R}(t)$, into a basis of discrete and continuous states as

$$\Psi\big(\mathbf{r}, \mathbf{R}[t], t\big) = \sum_{m'} c_{m'}(t)\Phi_{m'}\big(\mathbf{r}, \mathbf{R}[t]\big) +$$
$$\sum_{m''} \int d^3\mathbf{k}\ \tilde{c}_{m''}(\mathbf{k}, t)\tilde{\Phi}_{m''}(\mathbf{k}, \mathbf{r}, \mathbf{R}[t]). \qquad (5.1)$$

The continuum part of the wavefunction is subsequently discretized according to

$$\int d^3\mathbf{k}\ \tilde{c}_{m''}(\mathbf{k}, t)\tilde{\Phi}_{m''}(\mathbf{k}, \mathbf{r}, \mathbf{R}[t])$$
$$\approx \sum_i c_{m''}(\mathbf{k}_i, t)\Phi_{m''}(\mathbf{k}_i, \mathbf{r}, \mathbf{R}[t]), \qquad (5.2)$$

and the continuum state wavefunctions $\tilde{\Phi}_{m''}$ are obtained approximately as an antisymmetrized product of the electronic wavefunction of the neutral molecular core (with $N-1$ electrons) and a scattering state of the free electron:

$$\tilde{\Phi}_{n''}(\mathbf{k}_i) = \mathcal{A}\left(\Phi_{n''}^{(\mathrm{n})} \cdot \psi(\mathbf{k}_i)\right), \qquad (5.3)$$

where $\mathcal{A}$ denotes an antisymmetrization operator and the free electron states can be approximated by a plane wave. The discrete bound states are obtained from quantum chemical calculations.

The wavefunction basis constructed in this particular way is not strictly adiabatic: The bound states are only approximations to the adiabatic eigenstates of the anionic system, and this approximation deteriorates with decreasing electron binding energy of the system because of the limited ability of the Gaussian basis sets commonly employed in quantum chemical calculations to mimic the increasingly diffuse electron distribution of a more and more

weakly bound system. Moreover, also the continuum states are not adiabatic since they are constructed from plane waves rather than from true scattering states. Therefore, when inserting the discretized expansion 5.2 into the time-dependent Schrödinger equation, in the arising coupled set of equations for the expansion coefficients c_m,

$$\dot{c}_n(t) = \sum_m \left[-\frac{i}{\hbar} H_{nm}(\mathbf{R}[t]) - D_{nm}(\mathbf{R}[t]) \right] c_m(t), \qquad (5.4)$$

besides the nonadiabatic couplings $D_{nm} = \langle \Phi_n | d/dt | \Phi_m \rangle = \dot{\mathbf{R}} \cdot \langle \Phi_n | \nabla_\mathbf{R} | \Phi_m \rangle$ also nondiagonal matrix elements H_{nm} of the electronic Hamiltonian remain to be present in general. For the sake of compact terminology, we refer to the latter as *diabatic* couplings, although we stress that they are not the result of an adiabatic-to-diabatic transformation of the electronic basis states. We note however that a similar structure of the coupled equations is obtained when constructing a quasi-diabatic basis from adiabatic states, where besides the diabatic couplings also residual nonadiabatic couplings persist, the inclusion of which is necessary to obtain accurate results.[236]

Using the above described basis implies that the electronic states considered as "bound" contain a certain amount of the true continuum states and the continuum states have partial bound character. The extent of this depends on the actual deviation of the states from the strictly adiabatic states and should, at least for the bound states, be the smaller the more strongly the system is bound, i.e., the larger the vertical electron detachment energy. Therefore, we assume that it is justified to take the initial bound state wavefunction obtained from a quantum chemical calculation as a good approximation to the actual adiabatic state, which subsequently, when the energy gap to the detachment continuum closes, gets more mixed with continuum states and thus less adiabatic in character. This effect will be less pronounced the more diffuse the basis sets employed in the bound-state calculation are, and consequently, the importance of the diabatic couplings can be smaller or bigger. To substantiate these general considerations, we include in the Appendix numerical results obtained for an exactly solvable model system, where the exact adiabatic case can be compared with an approximate treatment and conditions can be found under which either the nonadiabatic or the diabatic couplings are dominant. It should be noted that when the approximate states are very similar to the adiabatic ones, the diabatic couplings are found to be small.

Although beyond the scope of the present paper, it might be valuable to further examine the relation between the strictly adiabatic and the approximate treatment also for the molecular case and to investigate if conditions can be identified under which the computationally expensive diabatic couplings could be safely neglected.

While the nonadiabatic couplings are calculated employing a finite-difference approximation for the time derivative following Ref.[163], the diabatic ones can be shown to depend entirely on two-electron integrals involving molecular orbitals of the neutral and anionic species as well as the unbound electron wave-

function. Specifically, if we assume detachment from an anionic wavefunction given by the configuration interaction expansion

$$\Phi_m^{(\mathrm{a})} = \sum_I C_I^{(m)} \Theta_I, \tag{5.5}$$

where Θ_I represents an individual Slater determinant formed from the anion's molecular orbitals (MOs), to an ionized continuum state in which the neutral core is represented by the ground-state Slater determinant $\Phi_0^{(\mathrm{n})}$, the diabatic couplings can be written as

$$H_{0m}(\mathbf{k}_i) = \Delta\mathcal{V}_k \sum_I C_I^m \langle \tilde{\Phi}_0(\mathbf{k}_i) | \hat{H} | \Theta_I \rangle \tag{5.6}$$

$$\equiv \Delta\mathcal{V}_k \sum_I C_I^m V_{im}^{\mathrm{dia}}(\mathbf{k}_i) \tag{5.7}$$

In this expression, $\Delta\mathcal{V}_k$ is a discretized volume element in k-space, and $V_{im}^{\mathrm{dia}}(\mathbf{k}_i)$ denotes the part of the diabatic coupling due to the interaction between the Slater determinants of the neutral ground state and the I'th Slater determinant contributing to the anion state m.

These terms are computed approximately, employing orthogonalized plane waves as the one-electron scattering states and approximating the molecular integrals involving plane waves based on a Taylor series expansion, as outlined in detail in Ref.[26], which results in

$$
\begin{aligned}
V_{im}^{\mathrm{dia}}(\mathbf{k}_i) = \sum_n^{\mathrm{occ}} \sum_u^{\mathrm{virt}} & \langle \chi_n | \phi_u \rangle \langle \mathbf{k}_i \phi_u | \hat{v} | \\
& \times \sum_{q,p<q}^{\mathrm{occ}} (\phi_p \phi_q - \phi_q \phi_p) \rangle \\
& \times (-1)^{n+p+q-1} \det \mathbf{S}_{0n,pq},
\end{aligned} \tag{5.8}
$$

where $\hat{v}$ is the operator for electron-electron interaction, $|\phi_i\rangle$ and $|\chi_i\rangle$ denote the MOs of the anion and neutral molecule, respectively, while $|\mathbf{k}_i\rangle$ is the orthogonalized plane wave describing the free electron and $\det \mathbf{S}_{0n,pq}$ denotes the minor determinant of the overlap matrix between bound and continuum state orbitals obtained by omitting the rows 0 and n (corresponding to the plane wave $\mathbf{k}_i$ and the neutral MO χ_n) as well as the columns p and q (corresponding to the anionic MOs ϕ_p and ϕ_q). Expansion of the above equation into the atomic basis functions (denoted by Greek indices) subsequently leads to

$$
\begin{aligned}
V_{im}^{\mathrm{dia}}(\mathbf{k}_i) = \sum_{\lambda\mu\nu} \Bigg[& A_{\lambda\mu\nu} \Big(\langle \mathbf{k}_i\lambda || \mu\nu \rangle - \sum_\sigma B_\sigma \langle \sigma\lambda || \mu\nu \rangle \Big) \\
& + \bar{A}_{\lambda\mu\nu} \Big(\langle \mathbf{k}_i\lambda | \mu\nu \rangle - \sum_\sigma B_\sigma \langle \sigma\lambda | \mu\nu \rangle \Big) \Bigg],
\end{aligned} \tag{5.9}
$$

where $\langle ab|cd \rangle$ denotes an electron-electron repulsion integral and $\langle ab||cd \rangle$ its antisymmetrized variant. The prefactors $A_{\lambda\mu\nu}$, $\bar{A}_{\lambda\mu\nu}$ and B_σ read (cf. Ref.[26]):

$$A_{\lambda\mu\nu} = \sum_n^{\text{occ},\alpha} \sum_{q,p<q}^{\text{occ},\alpha} (-1)^s \det \mathbf{S}_{0n,pq}$$
$$\times \left(c_\lambda^{(n)} - \sum_u^{\text{occ},\alpha} c_\lambda^{(u)} S_{nu} \right) c_\mu^{(p)} c_\nu^{(q)} \tag{5.10}$$

$$\bar{A}_{\lambda\mu\nu} = \sum_{\bar{n}}^{\text{occ},\beta} \sum_p^{\text{occ},\alpha} \sum_{\bar{q}}^{\text{occ},\beta} (-1)^{\bar{s}} \det \mathbf{S}_{0\bar{n},p\bar{q}}$$
$$\times \left(c_\lambda^{(\bar{n})} - \sum_{\bar{u}}^{\text{occ},\beta} c_\lambda^{(\bar{u})} S_{\bar{n}\bar{u}} \right) c_\mu^{(p)} c_\nu^{(\bar{q})} \tag{5.11}$$

$$B_\sigma = \sum_r^{\text{occ},\alpha} \sum_\rho c_\sigma^{(r)} c_\rho^{(r)} \langle \mathbf{k}_i | \rho \rangle \tag{5.12}$$

where $c_\lambda^{(n)}$ denotes the expansion coefficient of atomic orbital λ in MO n.

During the course of the simulation, vibration-induced autodetachment is described by non-adiabatic transitions (surface hops) into the continuum states in a stochastic manner after obtaining hopping probabilities from the changes of the electronic state coefficients as described in more detail in Refs.[26,53,164].

In addition, during the dynamics situations may arise in which the potential energy of the anionic state increases above that of the neutral state, i.e., the electronic system of the anion becomes unstable with respect to immediate electron loss. This would lead to an evolving free electron wavepacket spreading rapidly in space. We model this *adiabatic* detachment process by including a gradual population loss determined from the 1s-type of a spherical electron distribution having the same electronic spatial extent $\langle \mathbf{r}^2 \rangle$ as the MO from which the electron is ejected. For the free-time propagation of an MO composed of Cartesian Gaussian basis functions of s, p and d type, the following analytic expression is obtained:

$$\varphi_\mu(\mathbf{r}, t) = N_{l_x l_y l_z} e^{-\frac{\alpha}{1+i\beta t}\mathbf{r}^2} \left[-\Lambda \frac{i\beta t}{2\alpha}(1 + i\beta t)^{-\frac{5}{2}} + \right.$$
$$\left. (1 + i\beta t)^{-\frac{3}{2} - \sum_j l_j} \prod_{j=x,y,z} (r_j - A_j)^{l_j} \right]. \tag{5.13}$$

Here l_i denotes the angular momentum quantum number for the ith spatial direction, $\mathbf{A}$ is the center of the basis function and $\beta = \frac{2\hbar\alpha}{m_e}$. The constant Λ is unity if one of the $l_i = 2$ and zero if all $l_i < 2$. The population loss is then monitored within a sphere initially containing a population of 99% for the 1s-type electron distribution dispersing in time according to the evolution of the MO's electronic spatial extent. This rather coarse procedure accounts

for the finite lifetime of the electronically metastable anion state, leading to irreversible population decay and taking also into consideration that the electron ejection rate varies as a function of time within periods during which the anion state is electronically unbound.

More sophisticated approaches based on ab initio calculation of the decay lifetime have been presented recently, but are at the moment only available for the electronic ground state in the frame of the Hartree-Fock method.[143] The electronic decay lifetime is then used within the surface hopping procedure to model the irreversible population decay of the anion states within time periods during which they are electronically unbound.

5.3   Computational

The quantum-chemical calculations on which the dynamics simulations are based are carried out using time-dependent density functional theory (TD-DFT) with the the Gaussian09 program package[174] at the ωB97XD level of theory, employing the 6-31+G** basis set augmented with 2 additional s- and p-functions each, located at the N atom. The exponents of these additional basis functions are generated from the most diffuse s- and p-functions within the underlying basis set with the geometric progression for a factor of 3.5 according to Ref.[112]. Table 5.1 provides a comparison of several quantum-chemical methods for the electronic structure of the molecule carried out using the Gaussian16 program package[192]. Specifically the TD-DFT method employing the ωB97XD[166], CAM-B3LYP[168] and LC-ωPBE[167] functionals, as well as the coupled cluster approach using single and double excitations (CCSD)[175,176] and additional perturbational treatment of triple excitations (CCSD(T))[237], using the 6-31+G**[170], 6-311++G**[169] (with further addition of basis functions) as well as the aug-cc-pVDZ[171,172], d-aug-cc-pVDZ[173] and d-aug-cc-pVTZ[173] basis sets are shown. It is evident that the CAM-B3LYP and LC-ωPBE functionals either provide systematically too high electron affinities or are unable to produce a bound excited state and are therefore not suitable for the simulation. For the ωB97XD functional one can see that the system is described a lot more consistently with experimental data and the chosen combination of a small basis set augmented with diffuse basis functions is a good compromise between the accurate reproduction of experimental observables and the resource efficiency needed to carry out computationally expensive dynamics simulations. Furthermore, this type of basis set augmentation is a popular approach that has yielded good results in the description of weakly-bound anions before.[209,212]

The initial conditions for our dynamics simulations were obtained by sampling a phase space distribution function in terms of harmonic normal modes according to

$$P_v^\nu(Q_\nu, P_\nu) = |\chi_v^\nu(Q_\nu)|^2 |\tilde{\chi}_v^\nu(P_\nu)|^2 \tag{5.14}$$

with the harmonic oscillator wavefunctions of normal coordinate ν in position space, $\chi_v^\nu(Q_\nu)$, and momentum space, $\tilde{\chi}_v^\nu(P_\nu)$. For $v = 0$, this corresponds

Table 5.1: Comparison of adiabatic electron affinities (AEA), vertical detachment energies (VDE), anion vertical excitation energies (ΔE) and anharmonic (harmonic) wavenumbers of the energetically lowest lying CH stretching mode (ν_{27}) of 1-nitropropane in its most stable conformer. Superscripts indicate the anionic (a) and neutral (n) geometry. The added basis functions +XsXp etc. are generated according to Ref. [112] (with a factor for the geometric progression of 3.5) and centered on the nitrogen atom.

	AEA / eV	VDE^a / eV	$\Delta E^a_{1\leftarrow 0}$ / eV	VDE^n / eV	ν_{27} / cm^{-1}
ωB97XD					
6-31+G**	0.282	1.166	2.678	-0.296	2776 (2946)
6-311++G**	0.272	1.146	1.844	-0.273	2755 (2934)
6-31+G** + 2s2p	0.299	1.136	0.973	-0.010	2773 (2940)
6-311++G** + 2s2p	0.281	1.133	0.972	-0.019	2752 (2928)
aug-cc-pVDZ	0.252	1.089	1.695	-0.244	2759 (2930)
d-aug-cc-pVDZ	0.253	1.078	0.974	-0.031	(2929)
d-aug-cc-pVTZ	0.177	1.009	0.880	-0.031	(2921)
CAM-B3LYP					
6-31+G** +2s2p	0.464	1.304	1.077	0.089	2784 (2955)
6-311++G** +2s2p	0.455	1.302	1.068	0.080	2773 (2940)
d-aug-cc-pVDZ	0.431	1.254	1.057	0.070	2772 (2944)
d-aug-cc-pVTZ	0.382	1.215	0.983	0.052	(2932)
LC-ωPBE					
6-31+G** +2s2p	0.376	1.225	1.718	-0.026	2850 (3012)
6-311++G** +2s2p	0.371	1.233	1.721	-0.020	2836 (2996)
d-aug-cc-pVDZ	0.338	1.171	1.719	-0.021	2860 (3000)
d-aug-cc-pVTZ	0.298	1.142	1.666	0.001	(2986)
CCSD					
6-31+G** + 2s2p	0.093	0.940	0.885		(3014)
aug-cc-pVDZ	0.155	1.019	1.479	-0.316	(2953)
d-aug-cc-pVDZ^3	0.165	1.024	0.972	-0.023	-
Experiment					
	0.223[1]	0.92[1]			2753[2]

[1] Ref. [217], [2] Refs. [129,216], [3] at the optimized CCSD/aug-cc-pVDZ geometry
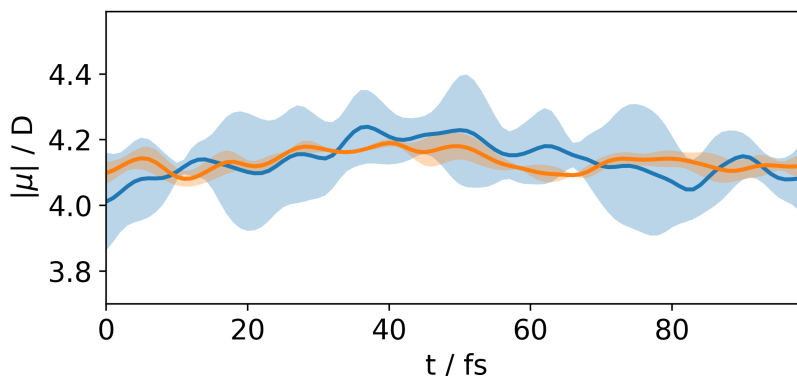
Figure 5.1: Average absolute value of the dipole moment of neutral nitropropane along trajectory ensembles propagated in the anionic ground state. For normal mode ν_{27}, excitation by a single quantum is taken into account by employing either the harmonic Wigner function for the first excited state (blue curve) or the product of squared wavefunctions in position and momentum space (orange curve, cf. equation (5.14)). A total number of 180 initial conditions of the lowest-energy conformer (cf. Fig. 5.2) is propagated at the ωB97XD/6-31+G**+2s2p level of theory, and a standard deviation is computed by calculating the average of four disjoint sub-ensembles of 45 trajectories for each set of initial conditions (areas shaded in light color).

to the common Wigner function. In the example studied here, $v = 1$ for the experimentally excited lowest-energy C-H stretching vibration (mode 27 when enumerating all modes by increasing energy), while $v = 0$ for all remaining normal modes. Notice, that our choice for distribution function for $v = 1$ differs from the Wigner distribution. However, when integrated over positions or momenta, it gives rise to the same marginal distributions and, at the same time, allows for higher computational efficiency since a single ensemble can be used to sample the distribution. For the excited-state Wigner function, by contrast, due to the existence of positive and negative parts, two ensembles would need to be propagated in parallel, and for the calculation of observables the difference of the averages obtained for these two ensembles has to be taken, which means that for a similar quality of the statistics, a higher number of trajectories is necessary. This is illustrated in Fig. 5.1 for the ensemble averages of the dipole moment of the neutral core along sets of anion trajectories propagated over 100 fs with vibrational excitation either incorporated by using the Wigner function for $v = 1$ or the product of squared wavefunctions in position and momentum space, equation (5.14). For both simulations, the averages are very similar (blue and orange curve). However, when calculating the standard deviation of the averages obtained for several smaller sub-ensembles, much larger values result for the Wigner ensemble (blue-shaded area) than for the ensemble generated by equation (5.14) (orange-shaded area).

After the generation of initial conditions, the nuclear trajectories were subsequently obtained by integration of Newton's equations of motion using the velocity Verlet algorithm[49] with an integration time step of 0.2 fs over a total of 1 ps.

Concerning the electronic degrees of freedom, we included the bound anionic ground and first excited state as well as the detachment continuum discretized as outlined in section 5.2 and initiated all trajectories in the anionic ground state. For the detachment continuum, we employed 96000 discretized states, with the k-vectors chosen to account for 1000 evenly spaced kinetic energies between 0.0 and 1.5 eV and 96 different spatial orientations for each energy, generated using the Fibonacci sphere algorithm[155] to evenly cover a spherical surface in k-space. To include the impact of the molecular core on the wavefunction of the extra electron at least approximately, in each nuclear dynamics time step the plane waves were orthogonalized with respect to all occupied anionic molecular orbitals (MOs) using Gram-Schmidt orthogonalization, as has been done successfully in the past.[78–80] 'Occupied' refers here to all MOs included in electronic configurations with significant contribution to the overall wavefunction of an electronic state. For the first excited state, which within TDDFT is described by a CIS-like expansion into excited Kohn-Sham determinants, we considered all determinants, beginning from the highest contribution, which are needed to represent the full CIS wavefunction by 95 % (or until a maximum of 10 configurations was reached). The resulting orthogonalized plane waves were then renormalized.

Within the manifold of the electronic ground and first excited bound anion state as well as 96000 discretized continuum states, the electronic Schrödinger equation 5.4 was solved along the classical trajectories utilizing Adams's method as implemented in the `integrate.ode` class of the `scipy` Python module[177], including the nonadiabatic and diabatic couplings between the considered states. The time-dependent electronic state coefficients obtained this way were subsequently used to evaluate the hopping probabilities at each nuclear time step. In order to prevent an unphysical loss of zero-point energy due to electron ejection, all hops were suppressed in which the free electron's kinetic energy E_{kin} was larger than the vibrational excess energy $\hbar\omega_{27} + E_{\mathrm{ZP}}^{\mathrm{a}} - E_{\mathrm{ZP}}^{\mathrm{n}}$, where $\hbar\omega_{27}$ is the energy of one vibrational quantum of mode 27 and $E_{\mathrm{ZP}}^{\mathrm{a/n}}$ are the zero-point energies of anion (a) and neutral (n).

For the decay of electronically unstable anion states, a gradual population loss modelled from free wavepacket dispersion as described in Sec. 5.2 (cf. equation (5.13)) was taken into account.

Since our interest lies in the dynamics of the anion, the trajectories were not propagated further in the neutral state in the event of a hop into the continuum. This allows us to improve the hopping statistics by assigning to each nuclear trajectory a number of individual "hoppers", for which the stochastic hopping process is performed individually in each time step. For each instance of a successful hop, the actual number of hoppers, $n_{\mathrm{sub}}(t)$, is reduced by one. Starting with $n_{\mathrm{sub}}(t_0) = 1000$, hopping is then checked $n_{\mathrm{sub}}(t)$ times at a given time step, and the hopping procedure is terminated when the number of hoppers has reached zero.

5.4   Results

0 cm^{-1} (0.0 eV)
[78 %]

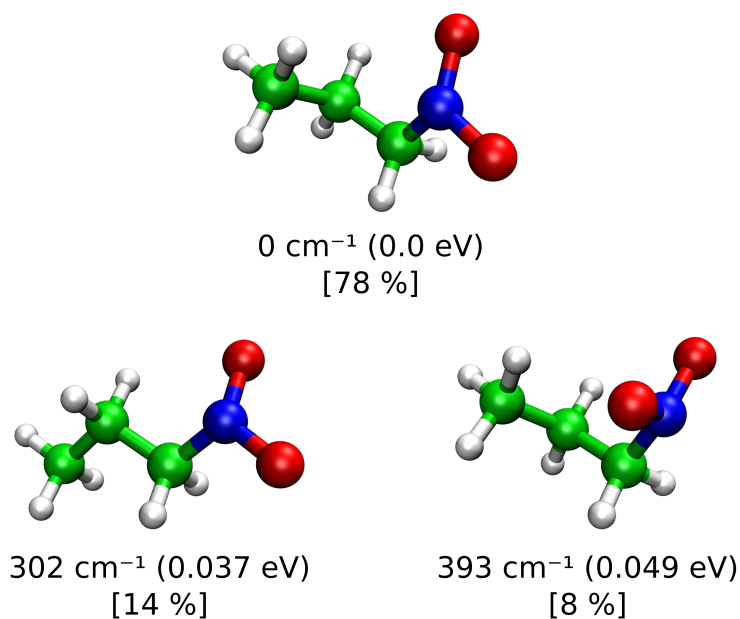302 cm^{-1} (0.037 eV)
[14 %]

393 cm^{-1} (0.049 eV)
[8 %]

Figure 5.2: Optimized geometries of the 1-nitropropane anion (at the ωB97XD/6-31+G**
+ 2s2p level of theory) in its most stable conformers. The relative energies with respect to
the global minimum and the Boltzmann populations at 250 K are given.

In the experiment, electron detachment of the 1-nitropropane anion can be
achieved by vibrational excitation of specific normal modes, in particular, the
infrared-intensive lowest-lying C-H stretching mode (ν_{27}), which involves the
C-H bond closest to the NO_2 group.[129,216] To account for this experimental sit-
uation, we modelled the vibrational excitation by sampling initial coordinates
and velocities from a phase space distribution as outlined in the Computational
Details section. In addition, it has to be taken into account that 1-nitropropane
exhibits several energetically close-lying conformers that can be obtained by
rotation around the C-N and the first C-C axis. We considered the energeti-
cally lowest three of them, which are shown in Figure 5.2 with their respective
state populations according to a Boltzmann distribution at a temperature of
250 K (taken from Ref.[129]) with a partition function only taking into account
these three conformers. In the energetically lowest conformer the dihedral an-
gle $\angle$CCCN amounts to 60°. The second conformer is linear in the sense that
$\angle$CCCN is 180° and the third conformer differs from the first by a NO_2 group
rotated by 60 degrees around the CN axis. The dynamics simulation was per-
formed with a total of 100 trajectories, with the initial conditions sampled from
these three different conformers, amounting to 78 trajectories for the first one,
14 for the second and 8 for the third. Using equation 5.14 and setting $v = 1$
for the C-H stretching mode closest to the NO_2 group (ν_{27} in the case of the
most stable conformer at the ωB97XD/6-31+G** + 2s2p level of theory) and
$v = 0$ for all other modes then results in initial conditions corresponding to
the experimental realization by Weber *et al.*[129].
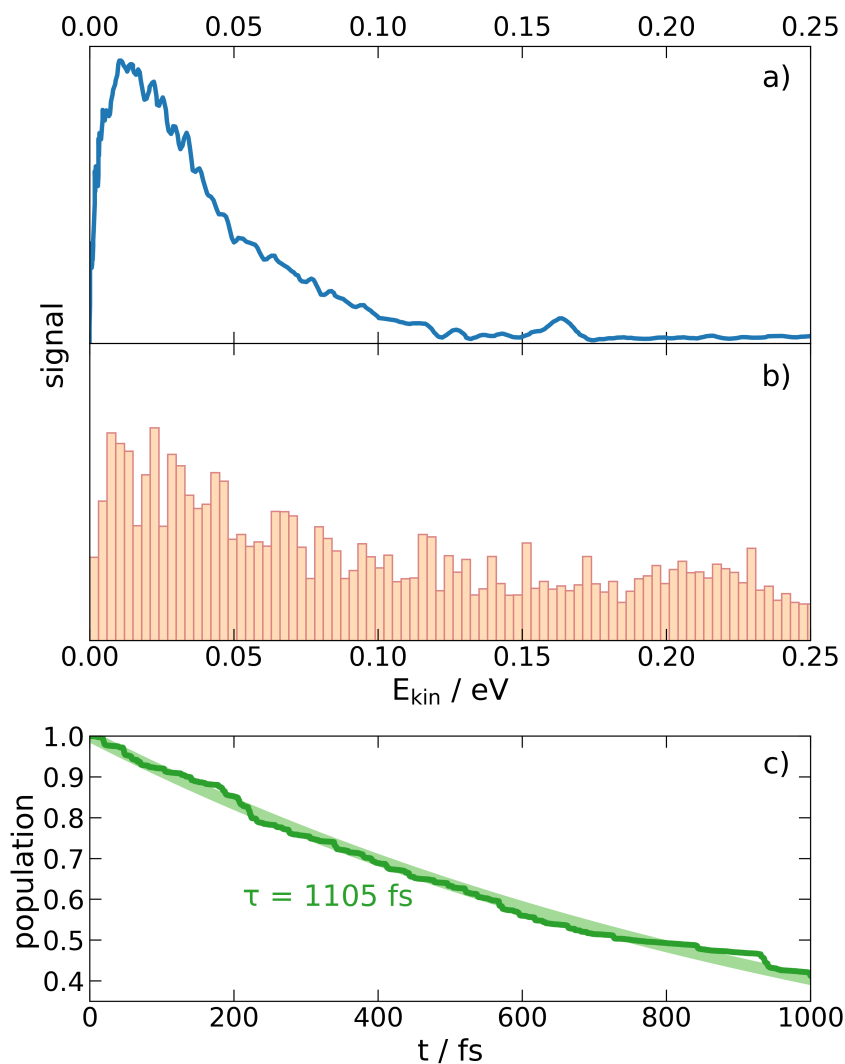
Figure 5.3: a) Experimental electron kinetic energy distribution of the 1-nitropropane anion after excitation of the energetically lowest C-H stretching mode at 2922 cm^{-1} (reproduced from Ref.[129]), b) simulated electron kinetic energy distribution of all hopping events after excitation of the lowest C-H streching mode and propagation for 1 ps (orange histogram) and running average over 5 points/7.5 meV (red curve), c) time-dependent population of all bound anion states (dark green) and exponential fit with a time constant of $\tau = 795$ fs (light green).

In the dynamics simulation autodetachment events are observed, which are analyzed in terms of the kinetic energy of the ejected electrons, which for a nonadiabatic hop is obtained as $E_{\text{kin}} = \frac{\hbar^2 \mathbf{k}_i^2}{2m_e}$ from the k-vectors of the continuum state occupied in the hop, or, in the adiabatic case of an electronically unbound anionic state, from the energy difference between the anionic and the neutral state. The histogram obtained for all hopping events observed during the simulation represents the kinetic energy distribution shown in Figure 5.3b). The signal exhibits its highest values between 0.01 and 0.02 eV, both decaying towards 0 eV as well as towards higher energies. Above 0.25 eV, most hopping events are suppressed by the condition of zero-point energy conservation. These theoretical findings share several important characteristics with the experimentally observed spectrum of Weber *et al.*[129] which is reproduced in Fig. 5.3a), such as the position of the signal maximum and the decreasing signal strength for higher and lower energies. However, the simulated signal is broader than the experimental one, approaching zero only at higher energies.

Furthermore, the ultrafast autodetachment time scale can be estimated from the dynamics simulation. From the population of bound anionic states, a fast exponential decay with a time constant of 1105 fs is revealed, as shown in Figure 5.3c), with approximately 40% of the total population remaining in a bound anion state after the simulation time of 1000 fs.

In addition to revealing the time scale, our simulations offer the possibility to analyze the molecular geometries for characteristic changes connected with detachment transitions. Two distinct parameters can be identified in which the structure differs from the average at all instants of time, as shown in Figure 5.4. In a) the pyramidalization of the NO_2 group, which is quantified as the angle between the O-N-O plane and the C-N axis, at the hopping events and at all time steps is shown in green and blue, respectively. It can be seen that throughout the dynamics, the pyramidalization angle is centered around 30°, which is also found as the equilibrium angle in the anionic ground state. At the instances where surface hops occur this angle is significantly reduced, indicating a planarization of the NO_2 group similar to the case of neutral nitropropane. This is in accordance with the expectation that for very weakly bound anions, the extra electron is so far away from the molecular core that the molecule assumes a geometry more resemblant of the neutral equilibrium geometry. Furthermore, the N-O atomic distances are shifted to smaller values, as shown in Figure 5.4b) and c) for both the larger and smaller of the two bonds. In blue, the distribution for all time steps is provided, exhibiting an average value of 1.33 Å and 1.28 Å. At the hopping events, these values are shortened to ∼1.26 Å and ∼1.23 Å for the longer and shorter of the N-O distances, respectively.

Interestingly, the initially excited C-H stretching mode ν_{27} is not directly responsible for enhancing the detachment efficiency, as can be seen from the histograms in Figure 5.5b) and c) showing the distribution of the associated C-H distance both at the hopping events and at all time steps. The distributions are rather similar, which indicates that the C-H bond distance is no
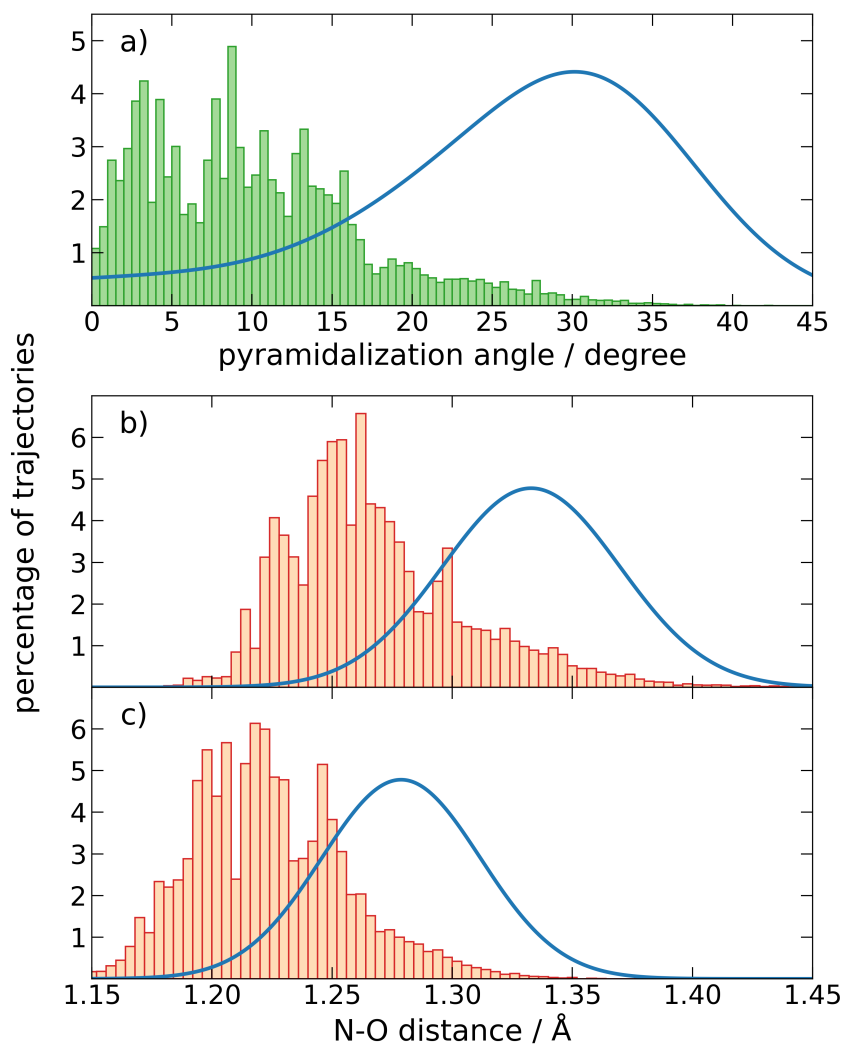
Figure 5.4: a) Pyramidalization angle of the NO$_2$ group at all hopping events into a free electron state for the whole ensemble of trajectories (green histogram) and for the whole ensemble at all time steps (blue curve), b) and c) larger and smaller of the two N-O atomic distances at all hopping events (orange histograms) and at all time steps (blue curves) of the whole ensemble, respectively.
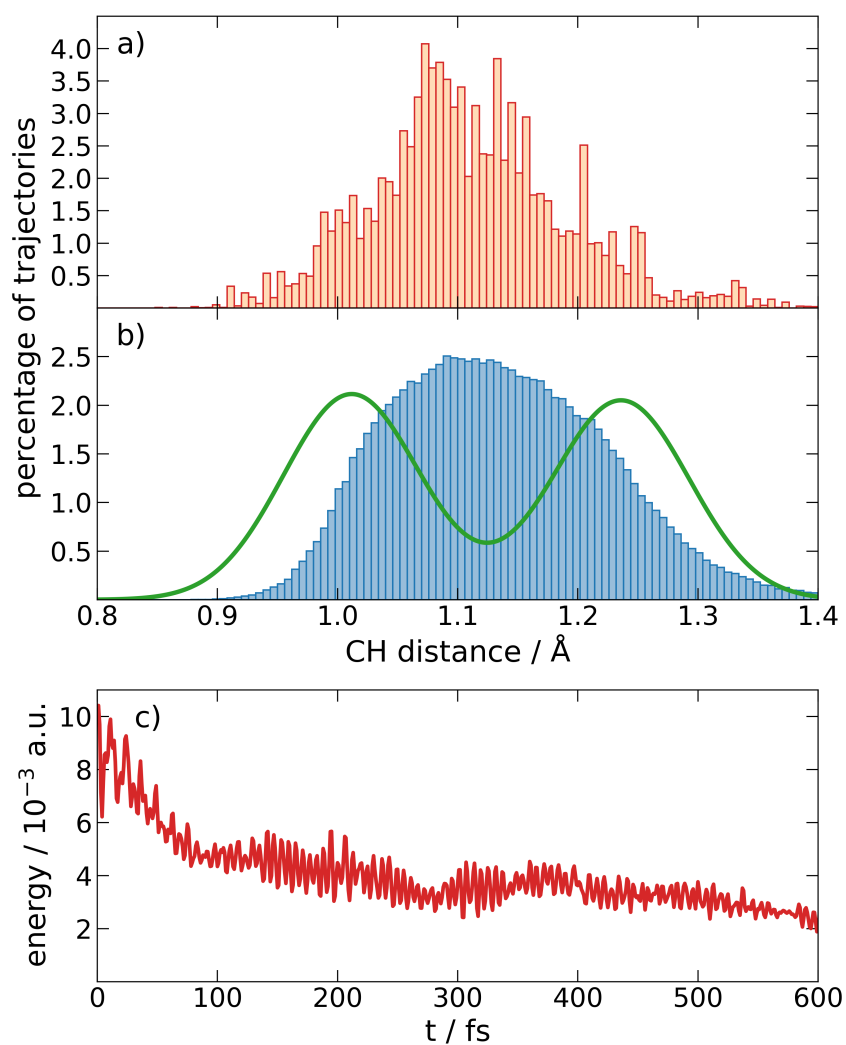
Figure 5.5: C-H distance for the initially excited mode ν_{27} a) at the hopping events, b) for all time steps of the dynamics (blue) as well as the initial distribution at $t = 0$ (green), c) Kinetic energy as a function of time for mode ν_{27} averaged over the ensemble of trajectories.

relevant factor in the detachment process. Instead, the main role of mode ν_{27} is to absorb the energy provided by the infrared irradiation, which is facilitated by its quite large oscillator strength (152 $\frac{\mathrm{km}}{\mathrm{mol}}$ at the DFT/ωB97XD/6-31+G** + 2s2p level of theory). The absorbed energy is rapidly redistributed as can be inferred from the quickly decreasing kinetic energy of the mode, dropping below 50 % of the initial value after less than 100 fs. No single modes were found that were excited particularly strongly in the energy redistribution process, instead the excess energy deposited in the C-H stretching mode is quickly dispersed over all vibrational degrees of freedom in accordance with the interpretation of Weber *et al.*[129] for their experimental findings. This process eventually allows the molecule to assume also geometries with a planar NO_2 moiety. Consequently, since in this way the structure of the neutral species is approached, the electron binding energy of the anion gets strongly reduced, leading to an increased autodetachment rate.

In our simulation, we also included the anion's first excited electronic state, which is of dipole-bound character. Although at a given instant of time, only a small population of this state is reached, which never exceeds $\sim$3% and, on average, amounts to about 0.4% throughout the whole simulation time, it is striking that it is the source of about 56% of the detachment events. This is because the equilibrium structure of the dipole-bound state closely resembles that of the neutral molecule, and the two lie very close in energy, thus increasing the tendency of the system to ionize. In addition, the dipole-bound state gets populated predominantly when the nonadiabatic couplings to the anionic ground state are large, which also is the case in regions of low VDE. Therefore, the dipole-bound state can be regarded as a mediator strongly enhancing autodetachment.

5.5 Conclusion

We have simulated the autodetachment dynamics of the 1-nitropropane anion following vibrational excitation of a CH stretching mode using our recently developed surface hopping approach augmented by the inclusion of discretized continuum states and their coupling to the bound states. Our simulations allow us to infer some general features of the autodetachment dynamics and unravel its mechanism. The additional vibrational energy upon excitation is quickly redistributed throughout the molecule, enabling access to regions on the potential energy surface where the vertical detachment energy (VDE) of the anion is sufficiently small that autodetachment takes place. The geometric structures at which transitions into the detachment continuum mostly occur are characterized mainly by reduced N-O bond lengths and planarization of the NO_2 group, thus bearing similarity to the equilibrium structure of the neutral nitropropane. This is strongly mediated by the dipole-bound first excited state, which is transiently populated in these regions, followed by rapid population decay of the bound anion. The timescale on which these processes take place was found to be $\sim$1 ps. Overall, we were able to gain detailed insight into

the intricate dynamics leading to autodetachment and could therefore not only reproduce the available experimental data very well, but also extend the understanding of the ultrafast deactivation processes after vibrational excitation of the 1-nitropropane anion.

Appendix

In this section we present calculations of bound-to-continuum couplings and detachment probabilities on an exactly solvable one-dimensional model system, namely, the attractive one-dimensional delta potential. The Hamiltonian is given by

$$\hat{H} = -\frac{\hbar^2}{2m}\frac{d^2}{dx^2} + v_0\delta(x). \tag{5.15}$$

For $v_0 < 0$, this system bears a single bound state,

$$\psi_b(x) = \sqrt{\kappa}\,e^{-\kappa|x|}, \tag{5.16}$$

of energy $E_b = -\frac{\hbar^2\kappa^2}{2m}$ ($\kappa = -mv_0/\hbar^2$), and has scattering states of the form

$$\psi_{sc}(x) = \frac{\mathcal{N}(k,\kappa,L)}{\sqrt{\kappa^2+k^2}}\left(k\cos kx - \kappa\sin k|x|\right). \tag{5.17}$$

When the continuum is discretized within a spatial box of length L, the normalization constant $\mathcal{N}$ is determined such that $\int_{-L}^{L}|\psi_{sc}(x)|^2 dx = 1$.

For the approximative solution, we construct the bound state as a linear combination of Gaussian functions,

$$\tilde{\psi}_b(x) = \sum_i C_i\, b_i(x), \tag{5.18}$$

with

$$b_i(x) = \left(\frac{2\alpha_i}{\pi}\right)^{1/4} e^{-\alpha_i x^2}, \tag{5.19}$$

where the C_i and the approximate energy $\tilde{E}_b$ are obtained variationally by constructing the Hamiltonian matrix in the orthogonalized basis of the Gaussian functions and determining eigenvalues and eigenvectors. The approximate scattering states are constructed as

$$\tilde{\psi}_{sc} = \frac{1}{\sqrt{1-S^2}}\left(\tilde{\mathcal{N}}(k,L)\cos kx - S\tilde{\psi}_b(x)\right), \tag{5.20}$$

with $\tilde{\mathcal{N}}$ as the box normalization constant for the cosine function and S as the overlap integral between the normalized cosine and $\tilde{\psi}_b$, resulting in the scattering states being orthogonal to the bound state. The exact bound state energy is shown in Fig. 5.6a) together with two approximate energies obtained employing (i) a basis set of 8 Gaussian functions with exponents of $\alpha_i = 0.005$, 0.01, 0.1, 0.5, 1.0, 5.0, 10.0, and 50.0 (in the following termed
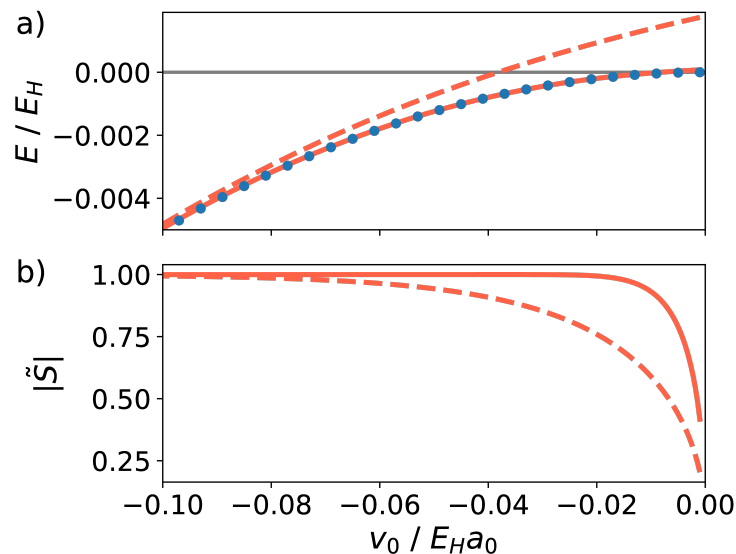
Figure 5.6: a) Bound-state energies for the attractive delta potential as a function of the potential strength v_0. Blue dots: exact energy, red lines: approximate energies (solid: large basis, dashed: small basis, for the basis definition see text). b) Overlap integral between the exact and the approximate wavefunctions (solid line: large basis, dashed line: small basis).

"small basis", all values in a_0^{-2}) and (ii) another one with the same functions plus two additional Gaussians with exponents of 0.0002 and 0.001 a_0^{-2} (henceforth termed "large basis"). Evidently, for the large basis (solid red line) the energy closely follows the exact value (blue dots), while for the small basis (dashed red line), a markedly larger value is obtained which even crosses the line of zero energy. This behavior is due to the inability of the small basis set to properly reproduce the exact wavefunction for small potential strengths (v_0 values approaching zero), since the latter becomes more spatially diffuse than the fixed-width Gaussian functions contained in the basis set allow. This fact is further quantified by the overlap integral $\tilde{S}$ between the exact and the approximate wavefunctions depicted in Fig. 5.6b), which shows that for the large basis set, the overlap is close to unity for almost all values of v_0 except the very smallest ones, while for the small basis set, notable deviations already occur for intermediate potential strengths of about 0.04 $E_H a_0$.

Both for the exact and the approximate wavefunctions, we calculate a nonadiabatic coupling with respect to changes in the parameter v_0:

$$d = \langle \psi_{sc} | \frac{d}{dv_0} | \psi_b \rangle \tag{5.21}$$

$$= \frac{2m}{\hbar^2} \langle \psi_{sc} | \, |x| \, | \psi_b \rangle \tag{5.22}$$

$$\tilde{d} = \langle \tilde{\psi}_{sc} | \frac{d}{dv_0} | \tilde{\psi}_b \rangle \tag{5.23}$$

$$= \sum_i \frac{dC_i}{dv_0} \left(\tilde{\mathcal{N}} \langle \cos kx | b_i \rangle - S \sum_j C_j \langle b_j | b_i \rangle \right). \tag{5.24}$$
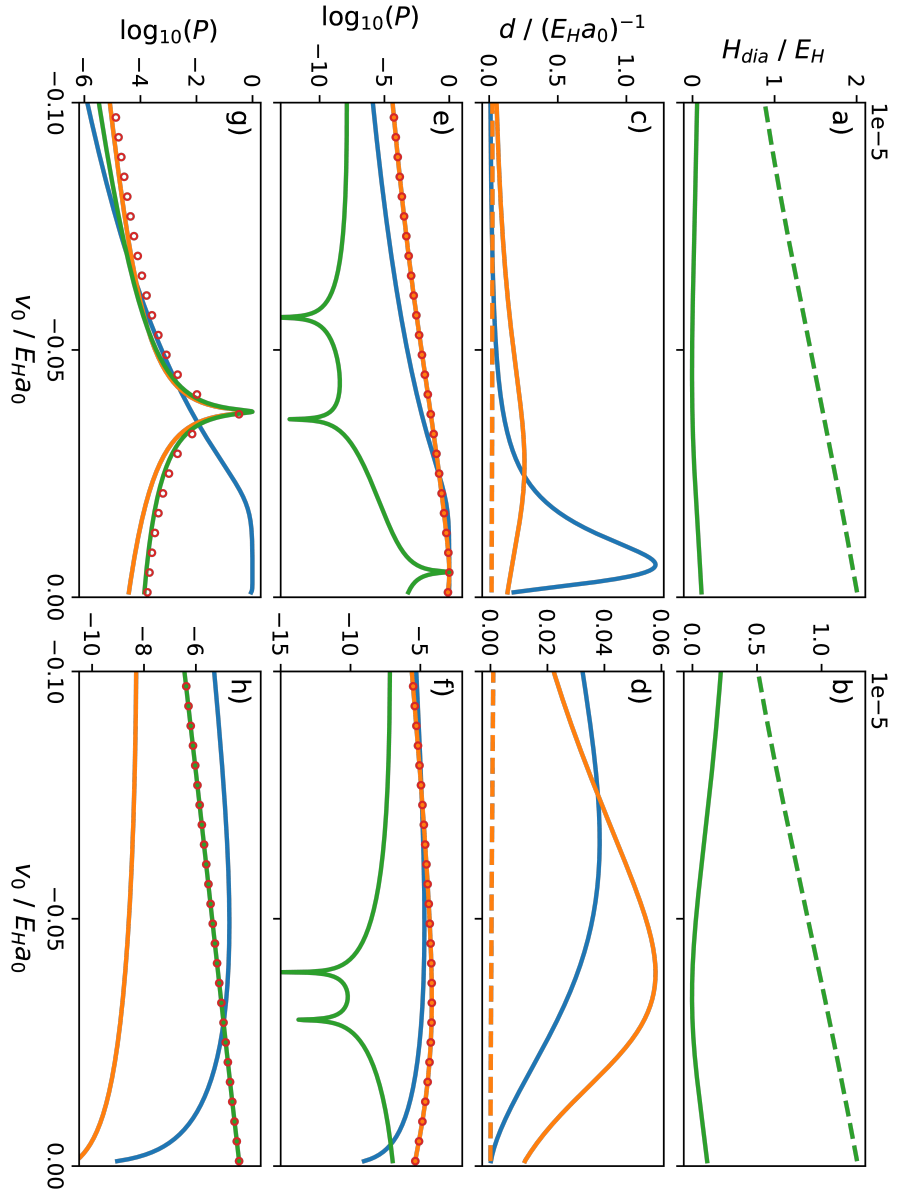
Figure 5.7: Comparison of exact and approximate bound-to-continuum couplings and transition probabilities for the attractive delta potential. Left column: data for a continuum state of $E_{kin} = 1$ meV, right column: data for a continuum state of $E_{kin} = 100$ meV. a)/b): Diabatic couplings H_{dia} for large (solid line) and small (dashed line) basis set. c)/d): Nonadiabatic couplings d for large (solid orange) and small (dashed orange) basis set as well as exact value $\tilde{d}$ (blue). e)/f): Coupling strengths calculated from (blue) the exact nonadiabatic coupling ($V = \hbar\dot{v}_0\tilde{d}$), (orange) approximate nonadiabatic coupling ($V = \hbar\dot{v}_0\tilde{d}$), (green) diabatic coupling $V = H_{dia}$, (red dots) total approximate coupling ($V = i\hbar\dot{v}_0 d + H_{dia}$). The approximate values are computed for the large basis set. g)/h) Same as e)/f) for the small basis set.

In addition, for the approximate solutions also nondiagonal matrix elements of the Hamiltonian (diabatic couplings) are considered:

$$H_{dia} = \langle \tilde{\psi}_{sc} | \hat{H} | \tilde{\psi}_b \rangle \tag{5.25}$$

$$= \left(\frac{\hbar^2 k^2}{2m} - \tilde{E}_b \right) S + v_0 \tilde{\mathcal{N}} \tilde{\psi}_b(0) \tag{5.26}$$

In Fig. 5.7, panels a)-d), the values of these couplings are presented for two different continuum states, one bearing an energy of 0.0085 E_H (1 meV, left column), the other one corresponding to 0.085 E_H (100 meV, right column). In addition, in panels e)-h), the transition probability following from these couplings is exemplified under the assumption that only the bound and a single discretized continuum state of the aforementioned energy are present. For a general coupling V, this probability is calculated as

$$P = \frac{|V|^2}{|V|^2 + (E_b - E_{sc})^2}. \tag{5.27}$$

In the calculation, a discretization parameter of $\Delta k = 10^{-5} a_0^{-1}$ is employed, which determines the normalization constants of the discretized continuum states. The effective nonadiabatic coupling is calculated as $V_{na} = \hbar \dot{v}_0 d$, and for the "velocity" $\dot{v}_0$, a value of $6 \cdot 10^{-4} \frac{E_H^2 a_0}{\hbar}$ is assumed. This corresponds roughly to the maximal change of v_0 when the bound state energy oscillates with a frequency corresponding to a typical molecular vibration of 1000 cm^{-1} around an energy of -0.5 eV with an amplitude of 0.49 eV, i.e., within an energy range of roughly 1 eV.

The following main observations can be made from inspecting Fig. 5.7: The diabatic couplings shown in a) and b) are larger for the approximate wavefunctions obtained with the small basis set (dashed green lines) than for those employing the large basis set (solid green lines), since the former deviate more from the exact solution. Vice versa, the nonadiabatic couplings presented in c) and d) are smaller for the small basis set (dashed orange lines), while for the large basis set (solid orange lines) they are comparable to the exact couplings (blue lines). Consequently, the approximate transition probabilities including both nonadiabatic and diabatic couplings are for the large basis set (e) and f), red dots) dominated by the nonadiabatic contribution (orange) while the diabatic contribution (green) is almost negligible. At the same time, they are close to the exact probabilities (blue) due to the bound states being good approximations to the exact adiabatic states. Still persisting deviations can be attributed to the fact that approximate continuum-state functions are used. Notice that in order to increase visual comparability of the probabilities changing over several orders of magnitude with varying v_0, their decadic logarithm is actually shown in Fig. 5.7.

For the transition probabilities obtained with the small basis set (Fig. 5.7g)/h)), the situation changes. Now the approximate wavefunctions are less adiabatic in character for small potential strengths. Therefore, notable deviations from the nonadiabatic couplings obtained in the exactly adiabatic picture

arise. At the same time, the relevance of the diabatic couplings increases, such that, e.g., for the case depicted in panel h) it is the diabatic coupling (green line) that dominates the total transition probability (red dots). Additionally, for small continuum state energies, the occurence of energy crossings leads to marked maxima in the transition probabilities (cf. the peak in panel g)).

Overall, it can be clearly seen that the different types of couplings are complementary to each other: if one of them is large, the other tends to be smaller and vice versa. The correct quantum mechanical treatment of our system requires both of them to be present, however, cases can be found in which one or the other is dominant.

Author contributions

J.P. and R.M. designed the research, K.I. implemented the method, conducted the simulations and prepared the figures. K.I. and J.P. wrote the manuscript text, R.M. reviewed the manuscript.

Funding

This work received no external funding.

Data availability

The data that support the findings of this study are available from the corresponding author upon reasonable request.

Declarations - Conflict of interest

The authors declare no competing interests.

Chapter 6

Time-resolved photoelectron spectroscopy of 4-(dimethylamino)benzethyne - An experimental and computational study

Abstract

We investigated the excited-state dynamics of 4-(dimethylamino)benzethyne (4-DMABE) in a combined theoretical and experimental study using surface-hopping simulations and time-resolved ionisation experiments. The simulations predict a decay of the initially excited S_2 state into the S_1 state in only a few femtoseconds, inducing a subsequent partial twist of the dimethylamino group within ~ 100 fs. This leads to drastically reduced Franck-Condon factors for the ionisation transition to the cationic ground state, thus inhibiting the effective ionisation of the molecule, which leads to a vanishing photoelectron signal on a similar timescale as observed in our time-resolved photoelectron spectra. From the phototoelectron spectra, an ionisation energy of 7.17 ± 0.02 eV
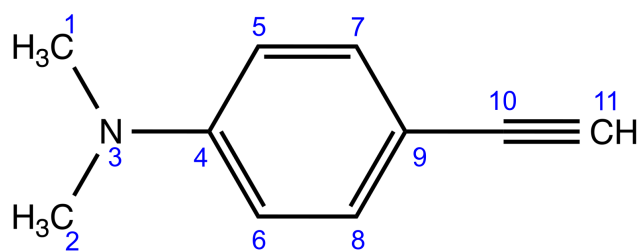
Figure 6.1: Structure of the 4-(dimethylamino)benzethyne (4-DMABE) molecule with labelling of heavy atoms (blue numbers).

was determined. The experimental decays match the theoretical predictions very well and the combination of both reveals the electronic characteristics of the molecule, namely the role of intramolecular charge transfer (ICT) states in the deactivation pathway of electronically excited 4-DMABE.

6.1   Introduction

Intramolecular charge transfer (ICT) is a fundamental process in which electron density is redistributed from a donor to an acceptor site within the same molecule, thus significantly changing the charge distribution with respect to the ground state.[34,42] Therefore, ICT has been a topic of remarkable interest to experimental and computational chemists for many years, considering the possible applications in organic electronics and photovoltaics.[36,238–241] In some organic molecules it is possible to observe a phenomenon in which an excited-state ICT leads to a second fluorescence band, as first observed by Lippert *et al.*[40,41] in the 4-(dimethylamino)benzonitrile (4-DMABN) molecule. This motivated a large amount of work on the electronic structure and character of the relevant excited states in this molecule. Numerous time-resolved experiments, ranging from transient absorption on the pico- and femtosecond time scale[242–245] to time-resolved Raman[246,247] and gas-phase spectroscopy[248,249] have been conducted in 4-DMABN. While Lippert suggested the additional band to be due to emission from the ^1L_a state that is shifted to lower energies in polar solvents, Grabowski and coworkers proposed the TICT (twisted intermolecular charge transfer) model.[42] In this model, the emissive state is stabilised by a 90° twist of the dimethylamino group with respect to the phenyl ring of the molecule in the excited electronic state. Although the charge-transfer character as well as some geometry distortion of the emissive state seem to be established, the TICT model is still debated. As an alternative, a central role of the amino inversion mode was suggested, which couples the S_1 and S_2 states.[250] Sobolewski *et al.* found a $\pi\sigma^*$ state with a bent cyano group as a minimum on the S_1 surface and proposed this state, termed "rehybridised ICT" (RICT) state, as the origin of the CT emission band.[251] Later studies proposed a sequential mechanism in which the RICT state is formed initially, followed by formation of the TICT state on a longer time scale.[243]

In this context, 4-(dimethylamino)benzethyne (4-DMABE), which is depicted in Figure 6.1 and isoelectronic to 4-DMABN, became an interesting reference point. Theory initially proposed a strong tendency for ICT,[251–253] but initial experiments did not observe dual fluorescence.[254,255] Later it was concluded from time-correlated single photon counting experiments that ICT does occur at least in strongly polar solvents, but the ICT state is not fluorescent.[256] More recently, time-resolved transient absorption spectra of both molecules in various solvents have been recorded[243,257] and the photophysics was characterised computationally employing multireference perturbation theory.[258] Based on these investigations, it was proposed that the photodynamics in polar solution is characterised by two parallel paths, in which either a locally excited (LE) state which is structurally similar to the ground state, or, alternatively, the bent $\pi\sigma^*$ state, are populated. In 4-DMABN, formation of the TICT state proceeds as a second step, while the respective pathway is blocked for energetic reasons in 4-DMABE.

For a systematic comparison of experiments with high-level theory it seems necessary to study isolated molecules in order to separate the intrinsic molecular dynamics from solvent motion. Experimentally, 4-DMABN itself in the gas phase has been investigated with high resolution spectroscopy[259,260] as well as femtosecond time-resolved spectroscopy,[249] and the initial steps of the photodynamics have been simulated using the surface-hopping dynamics approach.[261,262] In contrast, no studies have been reported for 4-DMABE that would permit the comparison of computations with gas phase data.

We therefore initiated a combined experimental and computational study of 4-DMABE in the gas phase to better understand the photophysics of the isolated molecule. To this end, we employed surface-hopping dynamics simulations[52] in combination with time-resolved photoelectron spectroscopy (TR-PES).[263] It has been shown that this approach makes it possible to disentangle contributions from different electronic states to the ionisation signal and thus allows one to follow nonradiative intramolecular dynamics in real time.[33,140,163,264–266] TRPES has been also successfully employed to study a few related isolated molecules exhibiting ICT,[267] indicating its applicability.

6.2 Methods

The picosecond time-resolved experiments have been conducted in Würzburg with a setup depicted in Figure S1 in the electronic supporting information (ESI) and described in detail recently.[268,269] It consists of a 10 Hz Nd:YLF laser and an optical parametric amplifier. The laser system has a time-resolution of 4-5 ps and a bandwidth of around 20-25 cm^{-1}.

The femtosecond time-resolved experiments were carried out at the ATTO-lab laser platform at LIDYL,[270] Université Paris-Saclay, using a setup combining velocity map imaging (VMI) and time-of-flight mass spectrometry (TOF-MS) that has been described before[33], and is also given in Figure S2 in the ESI. 4-DMABE, commercially obtained from Sigma-Aldrich, was held at room tem-

Table 6.1: Vertical excitation energies and ionisation energies in eV, oscillator strengths [in brackets] and state characters (in brackets) for 4-DMABE.

	S_1	S_2	S_3	IE_{ad}	IE_{vert}
ADC(2)					
aug-cc-pVDZ	4.31 [0.02] ($\pi\pi^*$)	4.61 [0.39] ($\pi\pi^*$)	4.89 [0.22] (s-Ryd)	8.27	10.02
daug-cc-pVDZ	4.31	4.58	4.83		
EOM-CCSD					
aug-cc-pVDZ	4.50 [0.02]	4.74 [0.17]	5.09 [0.43]	6.97	7.33
CAM-B3LYP					
aug-cc-pVDZ	4.55 [0.04]	4.67 [0.26]	4.81 [0.37]	7.01	7.16
6-311++G**	4.62 [0.04]	4.73 [0.30]	4.88 [0.33]	7.05	7.21
ωB97XD					
aug-cc-pVDZ	4.55 [0.04]	4.78 [0.57]	5.03 [0.07]	7.00	7.15
6-311++G**	4.62 [0.04]	4.82 [0.58]	5.11 [0.07]	7.03	7.20
Experiment (adiabatic)	3.95	4.34		7.17	

perature, seeded in 1.1 bar of helium and expanded into a differentially-pumped vacuum chamber by a 100 μm nozzle. The source chamber was operated at a pressure of 3.5×10^{-4} mbar. The resulting jet then passed a 1 mm skimmer, expanding into the detection chamber held at a pressure of 1.8×10^{-6} mbar. Around 15 cm into the detection chamber, the pump and probe laser beams crossed the molecular beam in the center of the ion optics. The ion and electron spectrometers were oriented perpendicular to the laser/jet plane. By applying different voltage gradients, VMI of the electrons/ions were collected on one detector. The VMI detector consists of two microchannel plates and a phosphor screen, with a sCMOS camera imaging the spatial distribution of the charged particles. In addition, time-of-flight mass spectra were recorded on a dual-stage microchannel plate detector in the opposite direction, but are not discussed in the present manuscript.

The tripled fundamental of a Ti:Sa laser (1 kHz, 23 fs) operated between 265 and 272 nm was used as the pump pulse (43 μJ at most). For the probe pulse, either the fundamental of the Ti:Sa laser (794 nm, 1.18 mJ at most) or its second harmonic (397 nm, $\approx$ 200 μJ at most) was employed. At least two photons at 794 nm or one photon at 397 nm are necessary to ionise 4-DMABE from its excited states. Both laser beams enter the detection chamber from the same side with a small crossing angle and are softly focused (f=750 mm lens) in the interaction region with the molecular beam. The distances to the focal points were chosen to minimise one-colour ionisation. The probe pulse was delayed with respect to the pump pulse using a computer-controlled stepper motor. The time intervals between the points varied between 10 fs close to the pump-probe overlap and up to 167 fs far away from it, the points being measured randomly. Each delay trace consists of at least 4 individual delay

scans. The photoelectron spectra were integrated over 3750 laser shots for each point. The polarisation of the pump laser was rotated for each point between parallel and perpendicular with respect to the probe laser.

For the theoretical description of the vertical electronic excitation energies several computational methods were compared as summarised in Table 6.1. Specifically, the algebraic diagrammatic construction through second order (ADC(2))[62,271,272] method in its spin-component scaling (SCS) variant[59,67] together with the aug-cc-pVDZ[171,172] and d-aug-cc-pVDZ[171–173] basis sets was used in the framework of the Turbomole program package[273]. Furthermore, employing the Gaussian16 program package,[192] time-dependent density functional theory (TDDFT) was employed using the long-range corrected CAM-B3LYP[168] and ωB97XD[166] functionals and the aug-cc-pVDZ and 6-311++G**[169,170] basis sets, as well as the equation-of-motion coupled cluster approach with single and double excitations (EOM-CCSD)[175,176,274,275] with the 6-311++G** basis set. The excited states of 4-DMABE are well described within the ADC(2)/aug-cc-pVDZ level of theory, which therefore was subsequently employed for the surface hopping simulations. It needs to be mentioned, though, that the ground state is treated at the second-order perturbation theory (MP2) level within this approach, which does not provide reasonably accurate ionisation energies. These are adequately described within the (EOM-)CCSD and (TD-)DFT methodologies, which, however, give rise to systematically too high excitation energies.

In addition to the vertical excitation energies, geometry optimizations in the excited state have been performed for several isomers employing the TD-DFT/ωB97XD/aug-cc-pVDZ level of theory in the frame of the QChem program package.[193] The nature of the stationary points has been examined by calculating the vibrational frequencies and normal modes. Vibronic Franck-Condon progressions have been calculated based on the obtained normal modes using the ezFCF program.[276,277]

For the quantum-classical dynamics simulations, the surface-hopping methodology as proposed by Tully[52] was utilised, coupled to quantum-chemical calculations at the ADC(2)/aug-cc-pVDZ level of theory using the Turbomole program package. From those results scalar non-adiabatic couplings and electronic transition dipole moments were evaluated using a procedure explained in detail in Refs.[137,163,188]. The classical nuclear dynamics was simulated by integration of Newton's equations of motion using the velocity Verlet algorithm[49] with an integration time step of 0.2 fs. Considering the ground and the three energetically lowest excited states, the electronic population dynamics was determined along the classical trajectories by solving the time-dependent Schrödinger equation including the non-adiabatic couplings between all electronic states. This yields time-dependent electronic state populations from which surface-hopping probabilities are evaluated. The ensemble of 100 initial conditions was sampled from a harmonic Wigner distribution function for the vibrational ground state and the dynamics was started with the population in the second excited electronic state, simulating the relaxation after initial
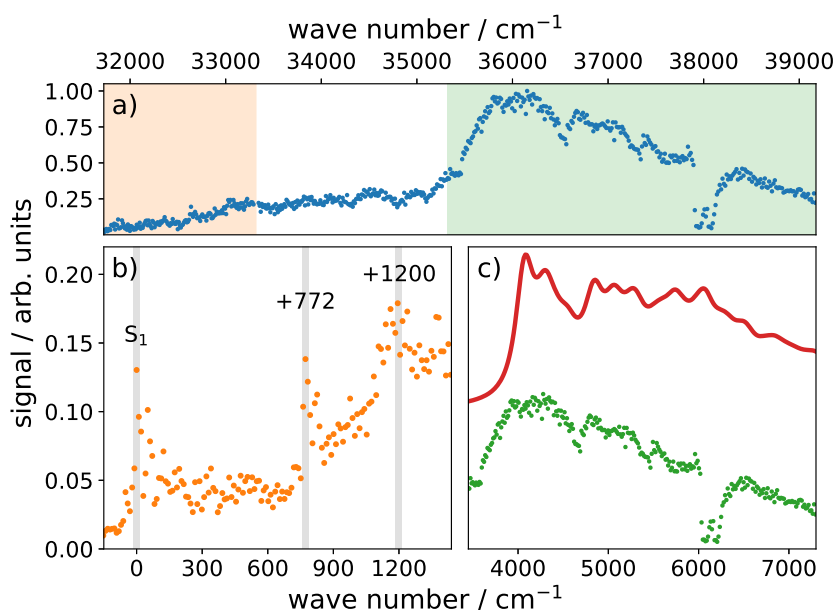
Figure 6.2: a) Experimental one-color REMPI spectrum of 4-DMABE obtained using a ps-laser. The displayed energy ranges of b) and c) are indicated in orange and green, respectively. b) Lower-energy region of the recorded [1+1'] REMPI spectrum with λ_{probe} = 351 nm. Three bands marked in grey represent the S_1 origin at 31854 cm^{-1} and two vibrationally excited states. c) Higher-energy region of the one-color REMPI spectrum (green) and simulated Franck-Condon progression at T=200 K for vibronic transitions from the S_0 to the LE state (red), shifted +930 cm^{-1} to match the experimental progression. The individual transition lines (not shown) have been broadened by a Lorentzian width of 100 cm^{-1}. The spectrum has been obtained at the TDDFT/ωB97XD/aug-cc-pVDZ level of theory. The spectra in b) and c) are shifted so that the S_1 origin is at 0 cm^{-1}.

vertical excitation.

6.3   Results and Discussion

In a first series of experiments one-color REMPI spectra were recorded with a ps-laser in the energy region covering the two lowest electronically excited states, as depicted in Figure 6.2a. Consistent with the theoretical predictions, a lower-lying weak band and a higher-lying strong one are present, which can be identified with the L_b (S_1) and L_a (S_2) states of $\pi\pi^*$ character[251] found at the ground state geometry (cf. Table 6.1). For an interpretation of the vibrational structure, the possible excited state isomers have to be discussed first. Four distinct isomers in the lowest excited state have been described in the literature[258]: the locally excited (LE) state whose geometry only slightly differs from that of the ground state, the fully twisted TICT and the partially twisted pTICT state, as well as the $\pi\sigma^*$ or RICT state characterized by a bent acetylene group. We have optimized these states at the TDDFT/ωB97XD/aug-cc-pVDZ level of theory and illustrate their geometries in the ESI, Figure S3, while the excitation energies and transition dipole moments are summarised in Table 6.2. In our calculations, the specific twisting angles for the TICT and pTICT

structures are 86° or 18°, respectively, while the CCC bending angle of the $\pi\sigma^*$ state amounts to 127°. It should be noted that the stationary points representing the above-mentioned states all lie on the S_1 electronic potential energy surface, although they may correlate with higher-lying states at the ground state geometry. In particular, the LE state correlates with the bright L_a (S_2) state. Based on the theoretical data, we identify the weak experimental band with the pTICT and the strong one with the LE state. The low-energy weak band has been additionally investigated in a [1+1'] experiment, which provides a better signal-to-noise ratio. For ionisation, the 3rd harmonic of Nd:YLF laser at 351 nm has been employed. The data are presented in Figure 6.2b and allow the identification of several vibronic bands. A band with moderate intensity appears at 31854 cm^{-1}, corresponding to 313.9 nm or 3.95 eV and is assigned to the vibronic origin (marked as S_1 in 6.2b). A further band at +772 cm^{-1} could be assigned to a phenyl deformation mode computed at 809 cm^{-1} in the pTICT state. In ps-time-resolved experiments both the origin transition and the band at +772 cm^{-1} exhibit a ns-lifetime (see ESI, Figure S4b and c), confirming that the state giving rise to the weak band is long lived. A further recognizable band appears around +1200 cm^{-1}. Theoretically, there are a lot of different vibrational modes to be found in this energy region, so given the broadness of the peak it is not possible to assign this band to a specific mode.

To further investigate the first excited state, we also recorded photoelectron spectra via the two lower identified bands in Figure 6.2b (S_1 origin, +772 cm^{-1}), presented on the left-hand side of Figure 6.3. Ionisation with a probe wavelength of 351 nm via the S_1 origin leads to electrons with an electron kinetic energy (EKE) of 0.31 eV. When this value is subtracted from the total photon energy of 7.48 eV, we deduce an adiabatic ionisation energy $IE_{ad} = 7.17$ eV. This is in good agreement with the value of 6.97 eV, computed at the CCSD/aug-cc-pVDZ level of theory as well as with the values obtained using DFT (cf. Table 6.1). The two spectra exhibit a similar shape, which indicates that transitions preserving the respective vibrational quantum number are dominant. This indicates a molecular structure that changes only slightly upon ionisation, which is in accordance with the theoretically obtained ground state geometries for the neutral and cationic molecule. The right-hand side of Figure 6.3 shows the spectra as a function of vibrational excess energy in the ion. A band at +900 cm^{-1} is visible, which suggests a vibrational energy increase of $\sim$ 130 cm^{-1} upon ionisation. The spectrum recorded via the excited vibrational state is broadened due to transitions into additional cationic vibrational states.

The strong band seen in the REMPI spectrum is identified with the transition to the LE state. The simulated vibrationally broadened absorption spectrum is presented together with the experimental data in Figure 6.2c . The calculated 0-0 transition at 35004 cm^{-1} (4.34 eV) at the ωB97XD/aug-cc-pVDZ level of theory matches well the first experimental peak around 36000 cm^{-1}. The characteristic bands of the experimental progression are also reproduced reasonably, as can be seen in Figure 6.2c. The observed dip in signal strength

Table 6.2: Adiabatic (ΔE_{ad}) and vibronic 0-0 (ΔE_{00}) transition energies as well as squared transition dipole moments ($|\mu_{01}|^2$) for transitions from the ground state to several stationary points of the S_1 state and the cation, obtained at the TDDFT/ωB97XD/aug-cc-pVDZ level of theory.

Structure	ΔE_{ad}/eV	ΔE_{00}/eV	$|\mu_{01}|^2/e^2 a_0^2$
LE [a]	4.542	4.340	5.606
pTICT	4.366	4.199	0.355
$\pi\sigma^*$	3.734	3.700	0.045
TICT	4.308	4.149	0.009
Cation D_0	7.000	7.014	

[a] the LE structure exhibits 1 imaginary vibrational frequency
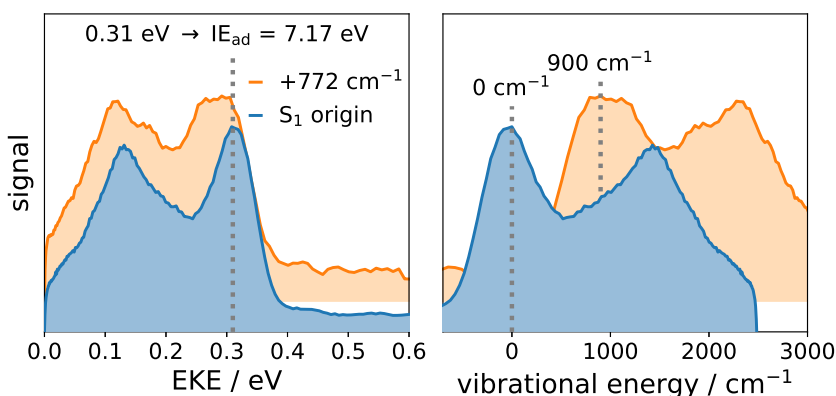
Figure 6.3: [1+1'] photoelectron spectra recorded via the origin and one vibrational band indicated in Figure 6.2. From the EKE an IE of 7.17 eV is derived.

between 37930 cm^{-1} and 38130 cm^{-1} is due to a drop in laser intensity within this small energy region and does not impact the surrounding data. Compared to the situation for the weak band, the time-delay traces recorded after excitation in the bright band change markedly (see ESI Figure S4d and e). They show two components, a fast one that is below the time-resolution of the setup and a second one with a long time constant in the ns region. Hence, contrary to the S_1 state, the dynamics in the S_2 state cannot be fully resolved with the ps-setup. Therefore, in order to unveil the ultrafast processes taking place after excitation into the S_2 state, a combined approach of surface-hopping dynamics and fs-TRPES was employed.

Accordingly, we initiated our nonadiabatic dynamics simulations in the L_a (S_2) state, and also included the next higher state, which is situated at 4.89 eV in the ground state geometry and can be classified as an s-type Rydberg state. With changing molecular geometry, the character of the states may change, though. In particular, it should be noticed that with our choice of the number of excited states also all of the states given in Table 6.2 are covered, as these all belong to the S_1 potential energy surface, albeit at different geometries. From the population dynamics depicted in Figure 6.4a it is clear that very rapidly about 70% of the population flows into the S_1 state, while only a small fraction
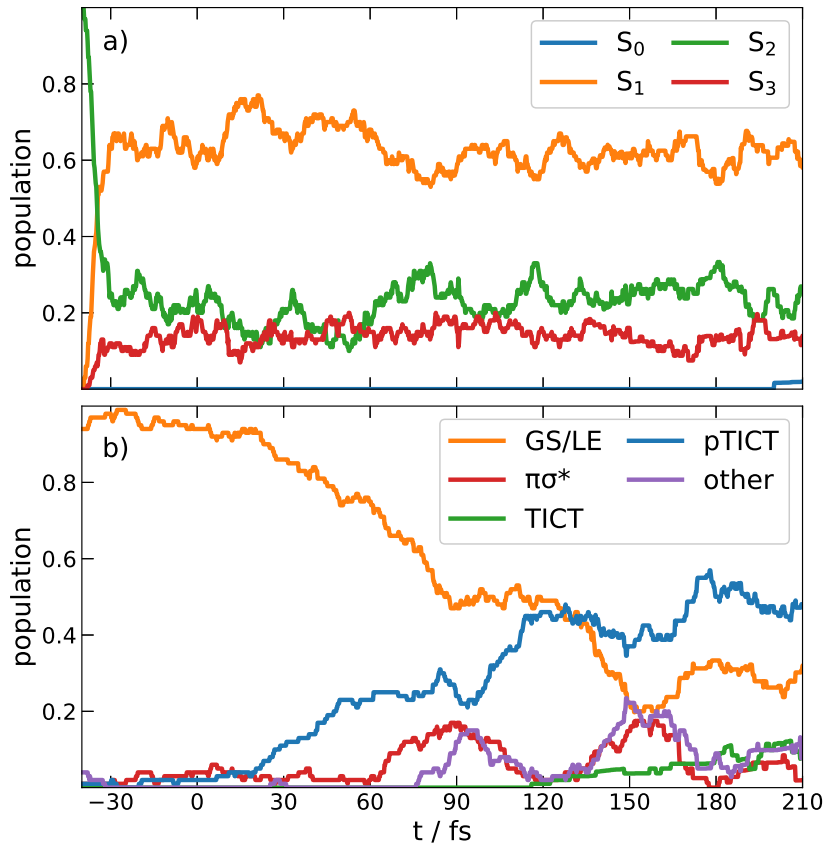
Figure 6.4: a) Time-dependent electronic state populations of 4-DMABE during the ADC(2) surface-hopping simulation initiated in the S_2 state. b) Time-dependent population of characteristic 4-DMABE conformers during the ADC(2) surface-hopping simulation. Both populations are averaged over 100 trajectories. The time axis was shifted to match the experimental pump-probe delay.

resides in the higher states for the simulation time of 250 fs. With regard to the time-dependent ionisation energies, most part of the trajectories should be photo-ionisable by using 397 nm photons in the entire time range. However, as detailed below, in the experiment the time-resolved photoelectron signal quickly disappears within about 100 fs after initial excitation. As a reason, we propose the geometrical deformations of the molecules taking place in the S_1 state.

To this end, we have classified the structures occurring during the dynamics simulations according to their similarity to the excited state isomers discussed before. As a prerequisite, we define the following angles (in the expressions below, $\mathbf{e}_{i,j}$ denotes a unit vector pointing in the direction of the line connecting atoms i and j according to the numbering given in Figure 6.1):

$$\alpha = \arccos(\mathbf{e}_{3,4} \cdot (\mathbf{e}_{1,3} \times \mathbf{e}_{2,3})) - \frac{\pi}{2} \tag{6.1}$$

$$\beta = \arccos(\mathbf{e}_{9,10} \cdot \mathbf{e}_{10,11}) \tag{6.2}$$

$$\gamma = \arccos(\mathbf{e}_{1,2} \cdot \mathbf{e}_{5,6}), \tag{6.3}$$

where α can be interpreted as a measure for pyramidalisation at the amino

Figure 6.5: Vibronic Franck-Condon spectra for the ionisation transitions between the indicated neutral 4-DMABE S_1 state conformations and the cationic ground state. As the horizontal axis, the photoelectron kinetic energy (EKE) for a 3.12 eV (397 nm) probe step has been chosen. The individual transition lines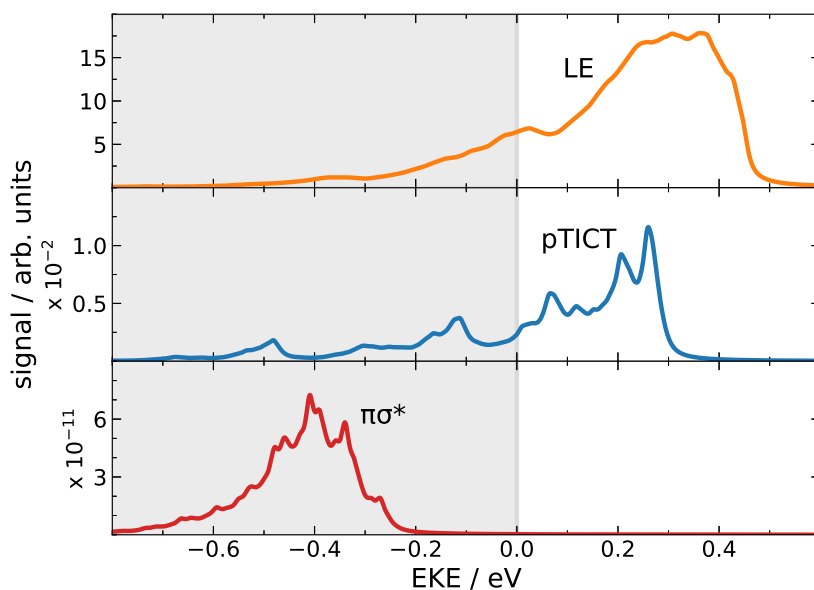 (not shown) have been broadened by a Lorentzian width of 0.01 eV. Areas shaded in grey correspond to formally negative kinetic energies, thus, intensities in these regions are not observable. Notice the drastically different ranges of the y-axis for the three spectra.

group nitrogen atom, β describes the CCC bending at the acetylene group and γ measures the torsion of the dimethylamino moiety with respect to the phenyl ring. For the assignment to any of the 4-DMABE isomers, we require $\alpha < 45°$. Furthermore, for the bent structure of the $\pi\sigma^*$ state, $\beta > 20°$ and $\gamma < 15°$, while for the ground state (GS) and the twisted structures, $\beta < 20°$ must be fulfilled. A GS-like structure is then characterised by $\gamma \leq 15°$, pTICT by $15° < \gamma \leq 45°$ and TICT by $\gamma > 45°$.

The resulting time-dependent structural populations are presented in Figure 6.4b and make clear that although the excited state remains S_1 in most trajectories during the entire simulation time, the geometry deviates from the original ground state structure very quickly, in about 50% of the cases becoming pTICT-like, while other structures also occur to a smaller extent. This has profound implications on the Franck-Condon factors and thus the signal intensities for the ionisation transitions.

To make the point more quantitative, we have computed the Franck-Condon spectra for the photoionisation to the cationic ground state starting from the LE, pTICT and $\pi\sigma^*$ excited state structures, as depicted in Figure 6.5. As the energy axis, the photoelectron kinetic energy obtained when using a single 397 nm probe photon was chosen in order to meet the experimental conditions. In this way, parts of the spectrum appear at negative energies (emphasised by grey background), corresponding to the fact that the ionisation energy in this region is higher than the photon energy, and thus no intensity would be exper-

imentally observed. Two significant observations can be made from the figure:
(i) Only molecules at the LE or pTICT, but not at the $\pi\sigma^*$ geometry can be
ionised with one photon, (ii) the signal intensity for ionisation from the LE
geometry is more than three orders of magnitude higher as compared to the
pTICT geometry. This clearly indicates that a structural change from the LE
(which itself is close to the ground state geometry) to the pTICT geometry
should be accompanied by a drastic decrease of ionisation signal intensity.

In the following, the connection between these theoretical findings with the
results of femtosecond time-resolved experiments will be made. The experiments were conducted using time-resolved photoelectron spectroscopy (TR-
PES). Pump pulses with a central wavelength between 265 nm and 272 nm
were employed, but no differences were observed between them. For ionisation,
probe wavelengths of 397 nm and 794 nm were employed.

A TRPES recorded using 397 nm probe is provided in Figure 6.6. A structureless band is visible, peaking at low EKE. The cutoff at around 0.5 eV is in
excellent agreement with a [1+1'] ionisation process, considering the 7.66 eV
total photon energy and the ionisation energy of 7.17 eV, as determined above.
The signal decays rapidly to zero and exhibits a half-life of about 50 fs. This
confirms a fast dynamics on the excited state potential energy surface. As
discussed above, the theoretical findings suggest that on a time scale of several
hundred fs, the system stays in the S_1 state (cf Figure 6.4a). The decisive
point, however, is the structural dynamics of the molecule. While the ionisation threshold hardly changes upon slight twisting of the initially planar structures (cf. Figure 6.5), the formation of pTICT-like geometries quickly leads
away from the Franck-Condon region, thus reducing the ionisation probability
to the cationic ground state due to smaller Franck-Condon factors. This is
clearly discernible from the comparison of the decaying signal for pump-probe
delays between -30 and 220 fs (Figure 6.6b) with the time-dependent amount of
ground-state-like geometries in the dynamics simulation (Figure 6.6c), which
show a very similar temporal behaviour.

In a second set of experiments, the probe wavelength was shifted to 794 nm.
At least two probe photons are now required to reach the ionisation threshold. Due to the higher laser power available, such multiphoton processes
are straightforward. As visible in Figure 6.7, the appearance of the spectrum changes conspicuously. The 2D map now shows two components, one at
low EKEs between 0 and 0.5 eV, labelled A, with maximal intensity around
t = 0 ps, and a second one, labelled B, that is slightly shifted in time and
maintains considerable intensity at EKE < 1.2 eV at all delay times. The experimental data show a strong rotational anisotropy (cf. ESI, Figure S8) that
was corrected in the Figure 6.7 by taking the appropriate ratio from parallel
and orthogonal polarisation[278] ($I_\parallel + 2I_\perp$). From the photoelectron spectrum
at the left-hand side of the figure we conclude that this component is due to a
three-photon ionisation in the probe step. Component A shows a rapid decay
to about 2/3 of its maximal intensity, again with a half-life of ~ 50 fs similar to
the observations for the 397 nm experiments. In contrast to the experiments
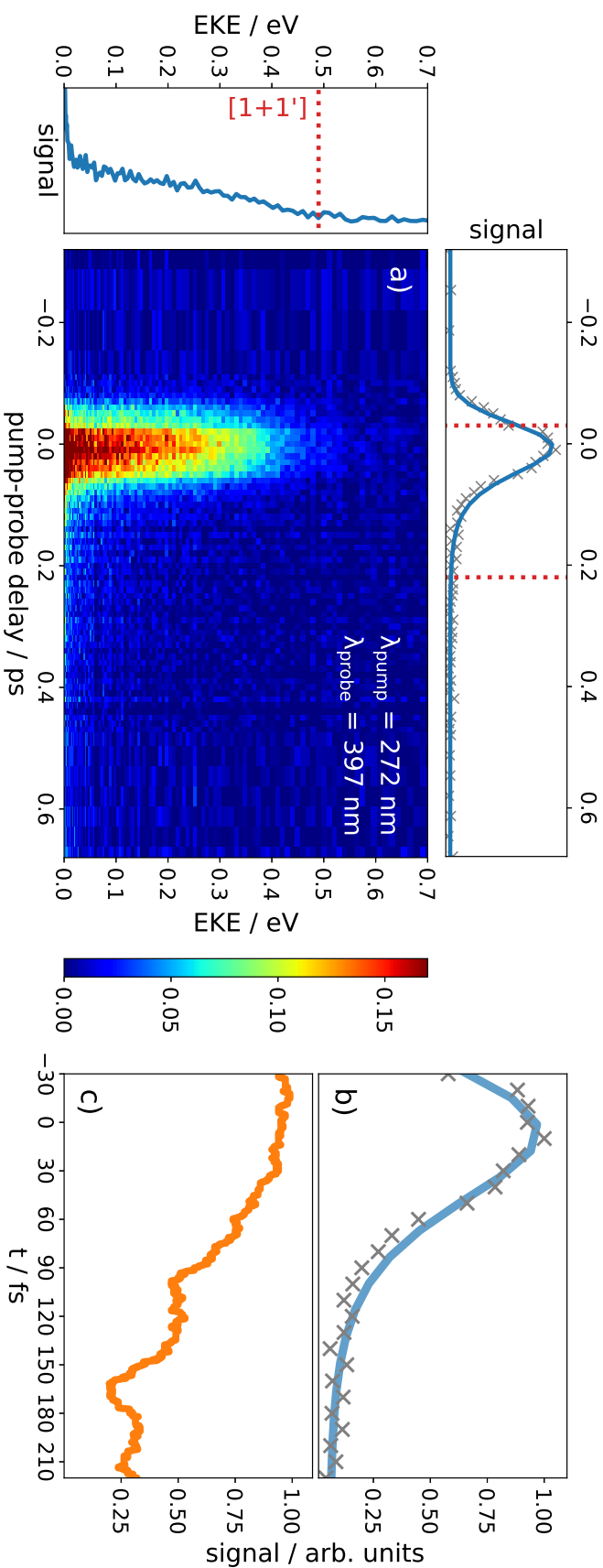
Figure 6.6: a) Time-resolved photoelectron spectrum of 4-DMABE, recorded with 397 nm probe. The data were corrected for rotational anisotropy (cf. ESI, Figure S7). Left panel: Time-integrated photoelectron spectrum. The maximum energy for 1-photon probe ionisation is indicated by the red dotted line. Upper panel: Total energy-integrated signal. A rapid decay is observed with a half-life of about 50 fs. b) Enlarged view of the decaying signal intensity. c) Simulated time-dependent population of molecular structures close to the ground state minimum geometry. Notice that this figure is reprinted as Figure S5 in the ESI employing a perceptually uniform, sequential colormap for the 2D-plot (panel a) in order to ease interpretation in greyscale.
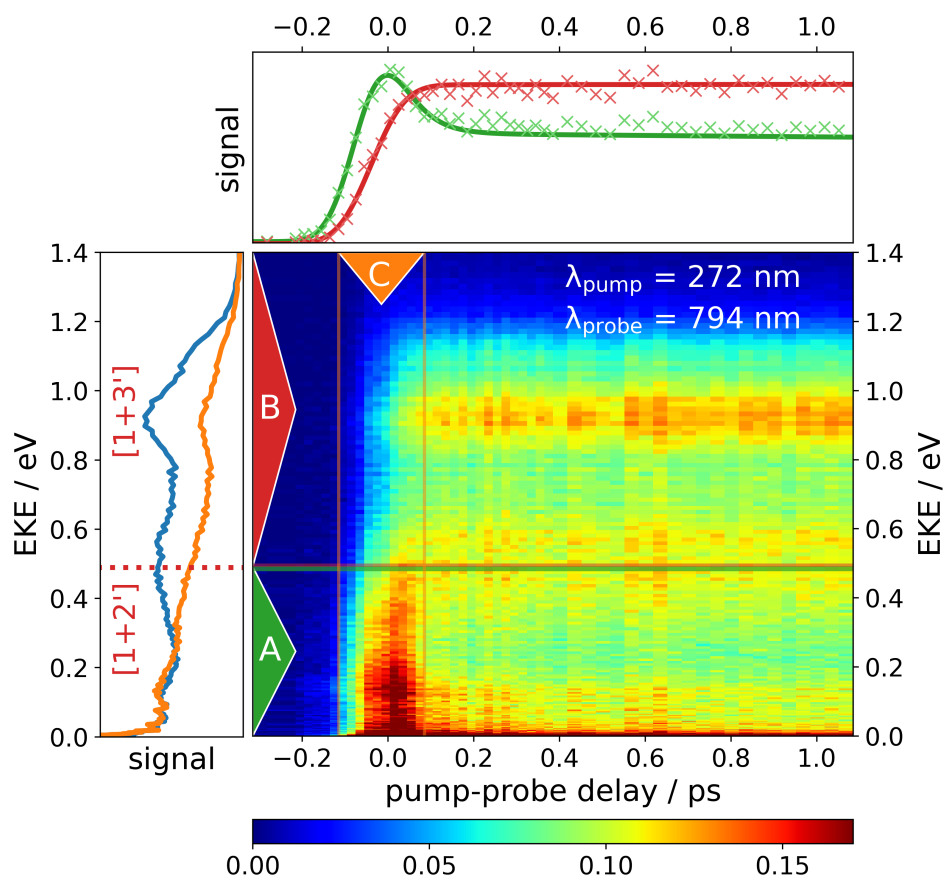
Figure 6.7: Time-resolved photoelectron spectrum of 4-DMABE photoexcited at 272 nm, recorded with 794 nm probe. The rotational anisotropy was removed (see text and ESI, Figure S8). Left panel: Total time-integrated photoelectron spectrum (blue) and short-time spectrum (orange) integrated over the time span indicated by C in the 2D plot. Upper panel: Total signal intensity integrated over the energy regions A (green) and B (red) indicated in the 2D plot. For each set of data points the maximum signal was set to 1. The rapid decay of the initially excited state gives rise to an electronic state that remains excited for > 10 ps. The photoelectron spectrum shows that it is associated with electrons of high kinetic energy that originate from a [1+3'] ionisation. Notice that this figure is reprinted as Figure S6 in the ESI employing a perceptually uniform, sequential colormap for the 2D-plot (middle panel) in order to ease interpretation in greyscale.

at 397 nm probe, it does not decay to zero but retains a considerable, almost time-independent offset that is similar to the observations for component B. The latter increases with a delay also on the order of 50 fs and stays at constant level at least for about a ps. Its appearance can be understood as a stepwise process through intermediate states, enabling an ionisation pathway that was energetically possible but previously not accessible due to the molecule moving out of the Franck-Condon region. Note that the $\pi\sigma^*$ geometry can be ionized by three 794 nm photons, but the computed signal intensity is several orders of magnitude smaller, so we do not expect this process to be relevant.

Therefore, the theoretical and experimental data suggest a sequential model, in which the initially excited S_2 state first decays to the S_1 state on a time scale faster than the experimental time resolution. This state can be ionised by one photon of 397 nm (or two of 794 nm). On a time scale of 50 fs, the corresponding electron signal vanishes completely in the case of 397 nm probe wavelength, while a weak, nearly constant offset remains with 794 nm probe, which is attributed to three-photon ionisation. The presence of two ultra-fast time scales finds its parallels in experimental time-resolved ionisation data of the 4-DMABN molecule where two sub-ps time constants could be identified.[248] This behaviour seems to be caused by the geometrical change of the molecules to a slightly twisted (pTICT) structure on the S_1 potential energy surface, for which the one-photon ionisation probability is strongly diminished. These findings are quite similar to previous ADC(2)-surface-hopping results of Kochman *et al.*[261,262] on the 4-DMABN molecule in the gas phase where a sub-10-fs internal conversion from the initial S_2 to the S_1 state is followed by structural deformation to a slightly twisted geometry. Notice, that the final conclusion of the aforementioned work is the absence of TICT formation in the gas phase, although in Ref.[261] a fair amount of full twisting was observed. This was attributed to the energetic underestimation of the TICT structure within the ADC(2) method, in contrast to its spin-opposite scaled (SOS) variant which was employed in Ref.[262]. In our simulations, we used the more general spin-component scaling (SCS) ADC(2) method which is however very similar to SOS-ADC(2).[59,67] Therefore, also in our simulations no appreciable TICT formation occurred. This is in agreement with experimental data where for 4-DMABE neither dual fluorescence[256] nor transient absorption features that could be attributed to a TICT state[243] were observed. Interestingly, we only find a very small contribution of structures with bent acetylene group (the $\pi\sigma^*$ or "rehybridized" intramolecular CT structure, RICT, of Sobolewski and Domcke[251–253]) which was inferred to play a key role in the photophysics of 4-DMABE by Lee et al.[243] and Segarra-Martí and Coto.[258] One reason for that may be that the $\pi\sigma^*$ structure is strongly polarised and thus much less stable in the gas phase than in polar solvents, similar to the TICT structure. Besides that, for 4-DMABN very recently the assignment of those features in the measured transient absorption (TA) spectra that were previously attributed to the $\pi\sigma^*$ state has been challenged by Kochman et al.,[279] who have simulated the TA spectrum based on surface-hopping dynamics and have found the afore-

mentioned TA signal to be due to excited state absorption of the LE state. A similar situation might also exist in the case of 4-DMABE.

6.4 Conclusions

We conducted a joint theoretical and experimental study on the excited state dynamics of 4-(dimethylamino)benzethyne (4-DMABE). The first excited state (S_1) was observed to be stable with respect to deactivation on a ns-time scale and therefore investigated using photoelectron spectroscopy (PES), pumping various (vibrational) states observed in REMPI experiments conducted beforehand. An adiabatic IE of 7.17 eV was determined for 4-DMABE. The second excited state (S_2) was observed to deactivate on a timescale unresolvable with a picosecond setup. Therefore this ultrafast photorelaxation dynamics of 4-DMABE after optical excitation at 272 nm was investigated using time-resolved photoelectron spectroscopy (TRPES) on a fs-timescale. Theoretically, starting in the second excited state after vertical excitation we simulated the relaxation of the system using the surface-hopping approach, revealing a fast deactivation in less than 10 fs into the first excited state, which is stable with respect to electronic relaxation on the observed timescale. The initial deactivation is followed by a change in geometry to a structure with a partially twisted dimethylamino group out of the molecular plane (pTICT) on the timescale of $\sim$ 100 fs. Twisting of the amino group is accompanied by a drastically decreasing transition dipole moment for the ionisation process due to diminishing Franck-Condon factors. Hence the structural change of the molecule can directly be linked to the photoelectron intensity, which is in perfect agreement with our TRPES experiments showing a matching temporal intensity evolution. In our TRPES using a probe wavelength of 794 nm, a quasi-constant non-zero intensity was also observed. Although the underlying complex multi-photon process is theoretically not accessible, we observed that in our simulations 4-DMABE is energetically ionisable at all times from its excited states. This suggests the involvement of intermediate states in the multiphoton ionisation, making the process more feasible in comparison to single-photon ionisation, where the small Franck-Condon factors inhibit effective ionisation.

Overall we were able to bring to light the deactivation pathway after excitation and resolve the role of twisted structures in the characteristic ionisation properties of 4-DMABE. While a prolonged dispute was found in the literature whether after excitation the molecular structure remains planar or changes to a perpendicularly twisted geometry in 4-DMABE and related molecules, in this case we found that the truth may lie between the two extremes.

Conflicts of interest

There are no conflicts to declare.

Acknowledgements

Chapter 7

Discussion & Conclusion

The work presented in this thesis aimed at the understanding of electron detachment processes and the theoretical description of the underlying coupled electron-nuclear dynamics. This very broad topic was divided into two aspects: firstly the development of a new quantum-classical dynamics methodology for the description of ultrafast autodetachment in molecular anions, amounting to the biggest part of this thesis in the form of three publications describing the method and the implementation of the HORTENSIA program package, validated by three different example molecules. And secondly the investigation of bound-state nonadiabatic dynamics after excitation of neutral molecules and its effect on the experimentally detected photoelectron signal in a case study on the 4-(dimethylamino)benzethyne (4-DMABE) molecule.

The development of a novel methodology for the simulation of autodetachment dynamics was the main achievement of this thesis. Thereby, for the first time, the problem of describing the time- and angle-resolved ejection of electrons induced by vibrational motion was addressed on a molecular level beyond a model-system based approach. By extending the quantum-classical surface-hopping dynamics method to a discretized continuum, electron detachment is described as nonadiabatic transitions to the ionized electronic states. The continuum electronic wavefunctions are approximated by orthogonalized plane waves, from which the ionized molecular system states are constructed as an antisymmetrized product with the bound neutral core wavefunction. Analytical expressions for the arising coupling terms between involved states were derived, thereby introducing sensible approximations to keep computational efforts manageable. These couplings are evaluated from results of quantum-chemical calculations and the electronic degrees of freedom propagated by numerical integration of the electronic Schrödinger equation, while the nuclear degrees of freedom are propagated classically according to Newton's equations of motion. This newly-developed methodology was implemented into the HORTENSIA program package (written in the Python programming language and publicly available in the respective *GitHub repository*).

To validate the developed methodology, the dynamics of several example molecules was simulated and compared with experimental results:

Firstly the vinylidene anion was studied, in which (with an electron detach-

ment energy of only 0.4866 eV) vibrational excitation of the electronic ground state can already be enough to overcome the detachment threshold. Since it is readily ionized, experimentally, the vinylidene anion was found to be a good starting molecule in the investigation of the prototypical 1,2-hydrogen shifting reaction from neutral vinylidene to acetylene.[82] From that the question naturally arises if the autodetachment and isomerization process are connected or facilitated by one another. By including the electronic continuum in theoretical consideration, this was studied in the frame of the presented autodetachment dynamics approach. Starting the simulation in the electronic ground state vibrationally excited with one quantum in the C-C stretching and C-H antisymmetric stretching mode made electron ejection energetically accessible, resulting in nonadiabatic transitions into the continuum via autodetachment. Indeed it was found that isomerization and autodetachment are closely intertwined. The initially excited C-C stretching mode as well as the CH_2 rocking mode, into which vibrational energy is rapidly redistributed, were identified as the main drivers to T-like geometries with elongated C-C bonding distances. At these structures, which can be viewed as transition states in the vinylidene-acetylene isomerization, the vertical detachment energy (VDE) is significantly reduced, leading to a large amount of detachment events in the dynamics simulation. The angular distribution of ejected electrons, which is explicitly yielded as a result of the discretized description of continuum states, showed a characteristic, anisotropic pattern with most electrons ejected in the molecular plane, roughly along the C-H bonds as well as the gap originating from an increasing C-C-H angle during the formation of T-like structures. From these results it could be concluded that already in the anionic species (with energetically high enough vibrational excitation) geometric regions are reached that directly lead to isomerization, accompanied by electron ejection on a timescale of only a few picoseconds.

With such a small detachment energy, no electronically excited, bound state is supported in the vinylidene anion. Contrary to that, the 2-cyanopyrrolide anion supports an s-type dipole-bound state (DBS) 29.8 meV below the electron detachment threshold, which is prone to autodetachment after vibrational excitation. This called for the extension of the autodetachment dynamics simulation methodology to include electronically excited states. Experimentally, photoelectron spectra are found for the resonant excitation into vibrationally excited states of the DBS.[84] The coupled electron-nuclear dynamics was simulated after creation of initial conditions for the excitation of a specific mode in the electronically excited state. Electron ejection was found to occur in a p-shaped pattern along the axis of the molecules dipole moment with a maximum electron signal at the total excess energy of the molecule upon vibrational excitation, in agreement with the propensity rules for vibrational autodetachment with a vibrational quantum reduced by one. An exponential time-constant of $\sim$500 fs is found for this process. The 2-cyanopyrrolide anion showed no population transfer back to the ground state on the simulated timescale, resulting in autodetachment as the only available deactivation pathway of the

dipole-bound state.

However, in the investigation of the last autoionizing system in this thesis, regarding the 2-nitropropane anion, which also supports a dipole-bound state, it was found that the energy separation between the ground and first excited state becomes small when the molecule comes close to the neutral equilibrium geometry, leading to relevant nonadiabatic coupling between both bound anion states. The simulation was carried out after excitation of the energetically lowest-lying C-H stretching mode in the electronic ground state. By redistributing the vibrational excess energy in the initially excited mode rapidly throughout the molecule, geometric changes towards the neutral equilibrium structure were possible. Specifically, this means that shorter N-O distances and a planar NO_2 group were assumed, which correspond to regions on the potential energy surface that are characterized by both small excitation energies and VDEs leading to strong coupling of the anionic ground state to all other electronic states. A rapid decay in the anionic bound population was observed on the timescale of ∼1100 fs, with the detachment efficiency strongly facilitated by the transiently populated dipole-bound state.

Apart from autodetachment, the aim of this thesis was also to extend the understanding of the influence of molecular motion on photoionization signals (that is, the time-dependent decrease in photoelectron signal after electronic excitation). Therefore in the 4-DMABE molecule, surface-hopping dynamics simulations were carried out after vertical excitation into the second excited state in the manifold of the ground and three lowest excited electronic states. Induced by rapid transition into the first excited state in under 10 fs, still in the vicinity of the equilibrium ground state geometry, the vibrational excess energy predominantly lead to partial twisting of the dimethylamino group (pTICT state) on a timescale of ∼100 fs. On a similar timescale as the theoretically predicted conformeric geometry change, a decreasing experimental photoelectron signal could be observed. This correlation could be explained by the diminishing Franck-Condon overlap of the pTICT state with the ionized species, effectively closing the ionization channel to the cationic ground state. In contrast to the isoelectronic 4-(dimethylamino)benzonitrile (4-DMABN) showing dual fluorescence, no geometric change to a structure with the amino group twisted by 90 degrees (TICT state), which was found to be responsible for the second fluorescence band, was observed. The methodology with which the experimental photoelectron spectrum was understood and explained theoretically was based on geometric attribution of the trajectory ensemble to known local minima of the first excited state (termed locally-excited (LE), $\pi\sigma^*$ (with a bent in the C-C triple bond), pTICT and TICT state), validated with static photoelectron spectra.

Overall it was shown in this thesis that the complex dynamic processes in molecules after excitation, be it vibrationally or vibronically, call for an in-depth theoretical description on a molecular level, for which the quantum-classical surface-hopping approach provides a computationally manageable simulation scheme. Utilizing this methodology, it was possible to reveal the in-

fluence of isomerization on electron detachment behavior, in one case through diminishing photoelectron yield upon twisting of an amino group, in the other case through increased autodetachment efficiency by 1,2 hydrogen shifting. Furthermore the role of higher-lying bound states was investigated. It was shown that in the case of the 4-DMABE molecule, excitation into the S_2 state solely lead to rapid transition into the first excited state (with the S_2 and S_3 state not involved in the dynamics after that), by which enough vibrational energy was available to overcome the isomerization barrier. In the nitropropane anion it was revealed how the large coupling of the electronic ground state with the energetically close-lying dipole-bound state (around the neutral equilibrium) can lead to transient population of the excited state, which acts as a mediator in the subsequent autodetachment resulting in an ultrashort lifetime of the nitropropane anion after vibrational excitation. It was therefore shown that the utilized surface-hopping-based approaches are able to provide a molecular view of the dynamic processes upon excitation, and that moreover, the newly-developed autodetachment dynamics methodology is able to provide the time-resolved electron kinetic energy distribution, where the angular distribution of electron ejection is explicitly described.

In addition to photochemical findings, the implementation of the dynamics methodology into the openly available HORTENSIA program package allows for easy conduct of future studies on molecular anion dynamics. It contains the numerical implementation of the theory presented in chapters 3 to 5. To perform quantum-chemical calculations, HORTENSIA provides an interface to the Gaussian09[174], Gaussian16[192] and QChem[193] program packages and calculations can be carried out using arbitrary DFT functionals and basis sets. The user is able to easily generate initial ensemble conditions as described in detail in chapter 4 using the implemented graphical user interface (GUI), and to quickly analyze the results of dynamics simulations with respect to common quantities (such as electron kinetic energies or geometric parameters at hopping instances) using the aforementioned GUI.

In the future, two possible extensions to the methodology are imaginable: firstly, an implementation for the ionization of neutral molecules. This poses significant challenges: Since the molecular core in these cases is a cation, the continuum functions cannot be approximated with plane waves anymore and different approximation scheme need to be developed and implemented. Secondly, laser field coupling could be implemented to better account for experimental conditions and preparations. On the one hand this would include excitation of electronically-excited (bound) states from the ground state (such as done experimentally in the 2-cyanopyrrolide example in chapter 4) and on the other hand direct photodetachment, as compared to only include autodetachment phenomena.

Chapter 8

Summary

In this thesis, theoretical approaches for the simulation of electron detachment processes in molecules following vibrational or electronic excitation are developed and applied. These approaches are based on the quantum-classical surface-hopping methodology, in which nuclear motion is treated classically as an ensemble of trajectories in the potential of quantum-mechanically described electronic degrees of freedom.

The main focus of this thesis lies on the description of autodetachment processes on the femto- to picosecond timescale. The central idea of the newly developed methodology, which is the main achievement of this thesis, is to extend the surface-hopping approach to the anionic detachment continuum, thereby allowing for autodetachment to be described as a nonadiabatic transition. The detachment continuum is handled in a discretized manner and the electronic wavefunctions are constructed as an antisymmetrized product of the neutral "core" wavefunction and plane waves, employing the Fibonacci sphere algorithm to evenly distribute $\mathbf{k}$-vectors in a given energy range. Furthermore, these plane waves are orthogonalized with respect to anionic molecular orbitals. The nonadiabatic coupling between bound anionic and discretized continuum states is evaluated, where it is shown that the arising terms can be converted to essentially yield Fourier transforms of Dyson orbitals between the respective bound anionic and neutral states, which can be solved analytically. Since the resulting wavefunctions are only approximations to the actual eigenfunctions of the anionic Hamiltonian, non-vanishing diabatic coupling terms also arise, for which approximative solutions are derived.

As an example, the autodetachment dynamics of the vinylidene anion (CCH_2^-), the neutral being a high-energy isomer of acetylene, is simulated after vibrational excitation of the C-C stretching and C-H antisymmetric stretching mode. A characteristic geometric deformation to T-like structures resulting in anisotropic electron-ejection can be observed on the timescale of a few picoseconds, enabling the linking between autodetachment and the isomerization from vinylidene to acetylene.

Moreover, the developed methodology has been implemented in a program package called HORTENSIA (*Ho*pping *r*eal-time *t*rajectories for *e*lectron-ejection by *n*onadiabatic *s*elf-*i*onization in *a*nions), developed as a part of this

thesis. This open-source Python program package provides, in addition to the implementation of the described methodology, an interface to commercially available quantum-chemistry programs, with which the bound state wavefunctions as well as two-electron integrals between atomic orbital basis functions are calculated. From this data all coupling terms are evaluated, followed by the numerical integration of the electronic Schrödinger equation to yield the time-dependent electronic state coefficients, from which hopping probabilities are computed.

The methodology is developed further to include electronically excited bound anionic states and applied to the autodetachment dynamics of the 2-cyanopyrrolide anion. The simulation is conducted starting in a vibrationally excited state of the first electronically excited dipole-bound state, resulting in a lifetime of $\sim$410 fs with a characteristic electron kinetic energy distribution around the maximum excess energy of the system. On this timescale it is shown that relaxation into the electronic ground state is not a probable process because of the large energy gap between the states and thus autodetachment is the only feasible deactivation mechanism on the simulated timescale.

As an example for (autodetaching) molecular anions where bound states are strongly coupled, the 1-nitropropane anion is studied. Here the simulation is conducted beginning with vibrational excitation of the energetically lowest-lying C-H stretching mode in the electronic ground state, also including the first excited dipole-bound state in the dynamics. In this molecule the energetic separation between the electronic states is small at geometries close to the neutral equilibrium (reduced N-O distances and planar NO_2 group), resulting in considerable coupling between the two bound states. Consequently, the dipole-bound state is transiently populated and acts as a mediator for autodetachment on the timescale of $\sim$1100 fs.

To extend the understanding of ionization processes even further, the influence of ultrafast dynamics on photoionization signals is studied as well. This is presented in a combined theoretical and experimental time-resolved study on the 4-(dimethylamino)benzethyne molecule using photoelectron spectroscopy. The experimental signal shows an ultrafast decay, which is explained by characteristic geometric changes evident in the theoretical findings. In contrast to the previous studies, only the bound electronic states are considered in a surface-hopping simulation beginning in the vertically excited S_2 state, which readily deactivates into the S_1 state in less than 10 fs. The additional vibrational energy gained upon relaxation suffices to reach structures with a partially twisted dimethylamino group ("partially twisted intramolecular charge transfer" or pTICT state). The assumption of a pTICT state is accompanied by a severe decrease in Franck-Condon factors to the cationic groundstate, explaining the loss of ionization efficiency. Therefore population of the pTICT state is identified as the cause of the experimental decay in photoelectron intensity on the similar timescale of 100 fs.

Overall the presented surface-hopping based methods are shown to be valuable approaches in the understanding of electron detachment processes at a

molecular level, enabling the analysis of ultrafast changes in geometries and electronic configurations. This provides a versatile means to interpret experimental data and guide future experiments based on theoretical predictions.

Chapter 9

Zusammenfassung

Im Rahmen dieser Arbeit werden theoretische Verfahren zur Simulation von molekularen Ionisierungsprozessen nach elektronischer oder Schwingungsanregung entwickelt und angewendet. Diese Verfahren basieren auf der quantenklassischen Surface-Hopping-Methode, in welcher die Kernbewegung durch ein Ensemble klassischer Trajektorien im Potenzial quantenmechanisch beschriebener Elektronen behandelt wird.

Der Schwerpunkt dieser Dissertation liegt auf der Beschreibung von Autoionisationsprozessen auf der Zeitskala von Femto- bis Pikosekunden. Die Hauptleistung der Arbeit besteht in der Neuentwicklung einer Simulationsmethode, deren grundlegende Idee die Erweiterung des Surface-Hopping-Ansatzes um das anionische Ionisationskontinuum ist, was die Beschreibung der Autoionisierung als nicht-adiabatischen Prozess erlaubt. Das Ionisationskontinuum wird diskretisiert und die elektronischen Wellenfunktionen werden als antisymmetrisiertes Produkt aus neutraler Wellenfunktion und ebenen Wellen konstruiert, wobei die $\mathbf{k}$-Vektoren letzterer gleichmäßig mithilfe des Fibonacci-Algorithmus in einem gegebenen Energiebereich, d.h. auf einer Kugeloberfläche gleicher k-Länge, verteilt werden. Darüber hinaus werden diese ebenen Wellen in Bezug auf die anionischen Molekülorbitale orthogonalisiert. Die nicht-adiabatische Kopplung zwischen gebundenen Anionen- und diskretisierten Kontinuumszuständen wird abgeleitet, wobei gezeigt werden kann, dass die auftauchenden Terme dergestalt umformuliert werden können, dass letztlich Fourier-Transformierte der Dyson-Orbitale zwischen den entsprechenden gebundenen Anionen- und neutralen Zuständen bleiben, welche analytisch berechnet werden können. Da die resultierenden Wellenfunktionen nur Näherungen der tatsächlichen Eigenfunktionen des anionischen Hamiltonoperators sind, entstehen diabatische Kopplungsterme, für welche näherungsweise Lösungen hergeleitet werden.

Beispielhaft wurde die Autodetachmentdynamik des Anions des höherenergetischen Isomers von Ethin, des Vinyliden-Anions (CCH_2^-), untersucht, beginnend mit Anfangsbedingungen mit angeregter C-C- und antisymmetischer C-H-Streckschwingung. Eine charakteristische Geometrieänderung zu T-artigen Strukturen mit anisotropem Elektronensignal kann auf der Zeitskala von wenigen Pikosekunden beobachtet werden, was klar die räumliche und zeitliche

Verbindung zwischen Autodetachment und Isomerisierung von Vinyliden zu Ethin ermöglicht.

Des Weiteren wurde diese neuentwickelte Methode in einem Programmpaket mit dem Namen HORTENSIA (*Ho*pping *r*eal-time *t*rajectories for *e*lectron-ejection by *n*onadiabatic *s*elf-*i*onization in *a*nions) implementiert, welches auch als Teil dieser Promotion entwickelt wurde. Dieses Python-Programmpaket, welches quelloffen verfügbar ist, stellt, neben der Implementierung der beschriebenen Methodik, ein Interface zu kommerziell erhältlichen Quantenchemie-Programmen zur Verfügung, welche die Berechnung der Wellenfunktionen gebundener Zustände sowie der Zwei-Elektronen-Integrale zwischen Atomorbital-Basisfunktionen übernehmen. Aus den so erhaltenen Daten werden alle Kopplungsterme berechnet, gefolgt von der numerischen Integration der elektronischen Schrödingergleichung. Die erhaltenen zeitabhängigen Zustandkoeffizienten ergeben letztlich Übergangswahrscheinlichkeiten zu allen anderen elektronischen Zuständen.

Darüber hinaus wird in dieser Arbeit die Methodik auf gebundene, elektronisch angeregte Zustände erweitert und am Beispiel des 2-Cyanopyrrolid-Anions präsentiert. Die Simulation ergibt eine Lebensdauer von ∼410 fs für einen spezifischen angeregten Schwingungszustand des ersten elektronisch angeregten, dipol-gebundenen Zustands, mit einer charakteristischen Verteilung der kinetischen Elektronenenergien um die maximale Überschussenergie des Systems. Es kann gezeigt werden, dass auf dieser Zeitskala keine Relaxation in den elektronischen Grundzustand stattfindet, bedingt durch die große Energiedifferenz zwischen beiden Zuständen, und damit Autodetachment der einzige zugängliche Deaktivierungsmechanismus auf der simulierten Zeitskala ist.

Zusätzlich wird als Beispiel eines (Autodetachment zeigenden) Moleküls mit stark gekoppelten elektronisch gebundenen Zuständen das 1-Nitropropan-Anion untersucht. Hierbei wird, beginnend im elektronischen Grundzustand mit Schwingungsanregung der energetisch niedrigsten C-H-Streckschwingung, die Simulation unter Berücksichtigung des ersten angeregten, dipol-gebundenen Zustands durchgeführt. Bei diesem Molekül ist bei Strukturen nahe der neutralen Gleichgewichtsstruktur (verringerte N-O-Bindungsabstände und planare NO_2-Gruppe) eine stark verringerte Energiedifferenz der elektronischen Zustände zu beobachten. Dies führt zu großen Kopplungen zwischen beiden Zuständen, wodurch der nur transient populierte dipol-gebundene Zustand eine Rolle als Vermittler des Autodetachments auf einer Zeitskala von ∼1100 fs einnimmt.

Um noch weiter zum Verständnis von Ionisationsprozessen beizutragen wird zudem der Einfluss ultraschneller Dynamik auf Photoionisierungssignale untersucht. Dies wird im Rahmen der theoretisch-experimentellen Gemeinschaftsstudie des 4-(Dimethylamino)benzethin-Moleküls auf Basis von Photoelektronenspektroskopie präsentiert. Das experimentelle Signal zeigt einen schnellen Intensitätsabfall, was durch theoretische Simulationen auf charakteristische Geometrieveränderungen des Systems zurückgeführt werden kann. Im Gegensatz zu den vorherigen Molekülen wurden nur die gebundenen elektronischen

Zustände in der Surface-Hopping-Simulation berücksichtigt, die nach vertikaler Anregung in den S_2-Zustand durchgeführt wurde, welcher zunächst in weniger als 10 fs in den S_1-Zustand relaxiert. Die durch diesen Übergang zusätzliche vorhandene Schwingungsenergie ist ausreichend, um zu einer Struktur mit teilverdrehter Dimethylamino-Gruppe (ein sogenannter "partially twisted intramolecular charge transfer oder pTICT-Zustand) zu gelangen. Im Zuge dieser Geometrieveränderung werden die Franck-Condon-Faktoren zum kationischen Grundzustand drastisch verringert, was die Verringerung der Ionisierungseffizienz erklärt. Damit wird die Populierung des pTICT-Zustands klar als Ursache des verschwindenden Photoelektronensignals auf der gleichen Zeitskala von 100 fs identifiziert.

Zusammengefasst konnte in dieser Arbeit gezeigt werden, dass die vorgestellten Surface-Hopping-basierten Methoden wertvolle Ansätze zum Verständnis von Ionisierungs- und Elektronendetachmentprozessen auf molekularer Ebene liefern. Dies erlaubt die Untersuchung von ultraschnellen Änderungen in Geometrie und elektronischer Konfiguration. Hierdurch wird die Möglichkeit eröffnet, experimentelle Daten verlässlich zu interpretieren und Anstöße für zukünftige Experimente auf Basis theoretischer Vorhersagen zu geben.

Declaration of individual contributions

All co-authors of the presented publications are informed about the usage as part of this cumulative dissertation and agree with the specified individual contributions to each publication as stated below. The contributions are divided into categories according to the CRediT system[280] and each individual line is weighted equally in the calculation of the total contribution. All values are given in percent.

Quantum–classical dynamics of vibration-induced autoionization in molecules

Kevin Issler, Roland Mitrić and Jens Petersen,
"Quantum–classical dynamics of vibration-induced
autoionization in molecules",
J. Chem. Phys. 158 (3) (2023) 034107.
`https://doi.org/10.1063/5.0135392`

Author Contributions	Authors			
	KI	RM	JP	Σ
Conceptualization		5	5	10
Methodology	2.5	2	5.5	10
Software	9.5		0.5	10
Investigation	10			10
Data curation	10			10
Formal analysis	5		5	10
Visualization	8		2	10
Writing – original draft	4		6	10
Writing – review and editing		5	5	10
Supervision, Project administration, Resources & Funding acquisition		8	2	10
Total	49	20	31	100

HORTENSIA, a program package for the simulation of nonadiabatic autoionization dynamics in molecules

Kevin Issler, Roland Mitrić and Jens Petersen,
"HORTENSIA, a program package for the simulation of
nonadiabatic autoionization dynamics in molecules",
J. Chem. Phys. 159 (13) (2023) 134801.
`https://doi.org/10.1063/5.0167412`

Author Contributions	Authors			
	KI	RM	JP	Σ
Conceptualization		5	5	10
Methodology	2	1	7	10
Software	9.5		0.5	10
Investigation	10			10
Data curation	10			10
Formal analysis	6.7		3.3	10
Visualization	9		1	10
Writing – original draft	5		5	10
Writing – review and editing		5	5	10
Supervision, Project administration, Resources & Funding acquisition		8	2	10
Total	52.2	19	28.8	100

A theoretical study on the vibration-induced autodetachment dynamics of the 1-nitropropane anion

Author Contributions	Authors			
	KI	RM	JP	Σ
Conceptualization		5	5	10
Methodology	2	1	7	10
Software	9.5		0.5	10
Investigation	10			10
Data curation	10			10
Formal analysis	6.7		3.3	10
Visualization	8		2	10
Writing – original draft	5		5	10
Writing – review and editing		5	5	10
Supervision, Project administration, Resources & Funding acquisition		8	2	10
Total	51.2	19	29.8	100

Time-resolved photoelectron spectroscopy of 4-(dimethylamino)benzethyne - An experimental and computational study

Kevin Issler, Floriane Sturm, Jens Petersen, Marco Flock, Roland Mitrić, Ingo Fischer, Lou Barreau and Lionel Poisson,

Author Contributions				Authors					
	KI	FS	JP	MF	RM	IF	LB	LP	Σ
Formal analysis (Theory)	5		5						10
Formal analysis (Experiment)		7		1			1	1	10
Investigation (Theory)	5		5						10
Investigation (Experiment)		2.5		2.5			2.5	2.5	10
Data curation	5		2.5					2.5	10
Writing – original draft	3.3		3.3			3.3			10
Writing – review and editing			2		2	2	2	2	10
Visualization	9		1						10
Conceptualization Methodology, Supervision & Project administration					5	5			10
Resources & Funding acquisition					3.3	3.3		3.3	10
Total	27.3	9.5	18.8	3.5	10.3	13.7	5.5	11.3	100

Bibliography

[1] P. Atkins, R. Friedman, Molecular Quantum Mechanics, Oxford University Press, New York, 2011.

[2] M. Persico, G. Granucci, Photochemistry: A Modern Theoretical Perspective, Theoretical Chemistry and Computational Modelling, Springer International Publishing, Basel, 2019. `doi:10.1007/978-3-319-89972-5`.

[3] A. Szabo, N. S. Ostlund, Modern Quantum Chemistry: Introduction to Advanced Electronic Structure Theory, Dover Publications, Inc., Mineola, 1996.

[4] A. Dreuw, M. Head-Gordon, Single-reference ab initio methods for the calculation of excited states of large molecules, Chem. Rev. 105 (11) (2005) 4009–4037. `doi:10.1021/cr0505627`.

[5] M. Persico, G. Granucci, An overview of nonadiabatic dynamics simulations methods, with focus on the direct approach versus the fitting of potential energy surfaces, Theor. Chem. Acc. 133 (9) (2014) 1526. `doi:10.1007/s00214-014-1526-1`.

[6] B. F. E. Curchod, T. J. Martinez, Ab initio nonadiabatic quantum molecular dynamics, Chem. Rev. 118 (7) (2018) 3305–3336. `doi:10.1021/acs.chemrev.7b00423`.

[7] R. Crespo-Otero, M. Barbatti, Recent Advances and Perspectives on Nonadiabatic Mixed Quantum–Classical Dynamics, Chem. Rev. 118 (15) (2018) 7026–7068. `doi:10.1021/acs.chemrev.7b00577`.

[8] F. Agostini, B. F. E. Curchod, Different flavors of nonadiabatic molecular dynamics, WIREs Comput. Mol. Sci. 9 (5) (2019) e1417. `doi:10.1002/wcms.1417`.

[9] J. Simons, Molecular anions, J. Phys. Chem. A 112 (29) (2008) 6401–6511. `doi:10.1021/jp711490b`.

[10] J. M. Herbert, The Quantum Chemistry of Loosely-Bound Electrons, John Wiley & Sons, Ltd, 2015, Ch. 8, pp. 391–517. `doi:10.1002/9781118889886.ch8`.

[11] W. T. Naff, C. D. Cooper, R. N. Compton, Transient negative-ion states in alicyclic and aromatic fluorocarbon molecules, J. Chem. Phys. 49 (6) (1968) 2784–2788. `doi:10.1063/1.1670485`.

[12] K. D. Jordan, P. D. Burrow, Temporary anion states of polyatomic hydrocarbons, Chem. Rev. 87 (3) (1987) 557–588. `doi:10.1021/cr00079a005`.

[13] L. Suess, R. Parthasarathy, F. B. Dunning, Nondissociative low-energy electron attachment to SF_6, C_6F_6, $C_{10}F_8$, and c-C_7F_{14}: Negative ion lifetimes, J. Chem. Phys. 117 (24) (2002) 11222–11227. `doi:10.1063/1.1522713`.

[14] E. Illenberger, J. Momigny, Gaseous Molecular Ions: An Introduction to Elementary Processes Induced by Ionization, Steinkopff Verlag, Heidelberg, 1992. `doi:10.1007/978-3-662-07383-4`.

[15] A. M. Scheer, K. Aflatooni, G. A. Gallup, P. D. Burrow, Bond Breaking and Temporary Anion States in Uracil and Halouracils: Implications for the DNA Bases, Phys. Rev. Lett. 92 (2004) 068102. `doi:10.1103/PhysRevLett.92.068102`.

[16] S. Tonzani, C. H. Greene, Low-energy electron scattering from DNA and RNA bases: Shape resonances and radiation damage, J. Chem. Phys. 124 (5) (2006) 054312. `doi:10.1063/1.2148965`.

[17] B. Boudaïffa, P. Cloutier, D. Hunting, M. A. Huels, L. Sanche, Resonant formation of DNA strand breaks by low-energy (3 to 20 eV) electrons, Science 287 (5458) (2000) 1658. `doi:10.1126/science.287.5458.1658`.

[18] F. Martin, P. D. Burrow, Z. Cai, P. Cloutier, D. Hunting, L. Sanche, DNA strand breaks induced by 0 - 4 eV electrons: The role of shape resonances, Phys. Rev. Lett. 93 (2004) 068101. `doi:10.1103/PhysRevLett.93.068101`.

[19] P. H. P. Harbach, M. Schneider, S. Faraji, A. Dreuw, Intermolecular Coulombic Decay in Biology: The Initial Electron Detachment from $FADH^-$ in DNA Photolyases, J. Phys. Chem. Lett. 4 (6) (2013) 943–949. `doi:10.1021/jz400104h`.

[20] G. Herzberg, A. Lagerqvist, A new spectrum associated with diatomic carbon, Can. J. Phys. 46 (21) (1968) 2363–2373. `doi:10.1139/p68-596`.

[21] W. Lineberger, T. Patterson, Two photon photodetachment spectroscopy: The C_2^- $^2\sigma$ states, Chem. Phys. Lett. 13 (1) (1972) 40–44. `doi:10.1016/0009-2614(72)80037-X`.

[22] T. Kvale, G. Alton, R. Compton, J. Thompson, D. Pegg, Autodetachment spectroscopy of metastable negative ions, Nucl. Instrum. Methods Phys. Res. 24-25 (1987) 325–328. `doi:10.1016/0168-583X(87)90653-7`.

[23] K. R. Lykke, K. K. Murray, D. M. Neumark, W. C. Lineberger, A. Carrington, B. A. Thrush, High-resolution studies of autodetachment in negative ions, Philosophical Transactions of the Royal Society of London. Series A, Mathematical and Physical Sciences 324 (1578) (1988) 179–196. `doi:10.1098/rsta.1988.0010`.

[24] K. Yokoyama, G. W. Leach, J. B. Kim, W. C. Lineberger, Autodetachment spectroscopy and dynamics of dipole bound states of negative ions: $^2A_1$-$^2B_1$ transitions of H_2CCC^-, J. Chem. Phys. 105 (24) (1996) 10696–10705. `doi:10.1063/1.472878`.

[25] J. A. DeVine, M. L. Weichman, C. Xie, M. C. Babin, M. A. Johnson, J. Ma, H. Guo, D. M. Neumark, Autodetachment from vibrationally excited vinylidene anions, J. Phys. Chem. Lett. 9 (5) (2018) 1058. `doi:10.1021/acs.jpclett.8b00144`.

[26] K. Issler, R. Mitrić, J. Petersen, Quantum-classical dynamics of vibration-induced autoionization in molecules, J. Chem. Phys. 158 (3) (2023) 034107. `doi:10.1063/5.0135392`.

[27] H.-T. Liu, C.-G. Ning, D.-L. Huang, P. D. Dau, L.-S. Wang, Observation of Mode-Specific Vibrational Autodetachment from Dipole-Bound States of Cold Anions, Angew. Chem. Int. Ed. 52 (34) (2013) 8976–8979. `doi:10.1002/anie.201304695`.

[28] C. S. Anstöter, G. Mensa-Bonsu, P. Nag, M. Ranković, R. Kumar T. P., A. N. Boichenko, A. V. Bochenkova, J. Fedor, J. R. R. Verlet, Mode-specific vibrational autodetachment following excitation of electronic resonances by electrons and photons, Phys. Rev. Lett. 124 (2020) 203401. `doi:10.1103/PhysRevLett.124.203401`.

[29] D. H. Kang, J. Kim, M. Cheng, S. K. Kim, Mode-specific autodetachment dynamics of an excited non-valence quadrupole-bound state, J. Phys. Chem. Lett. 12 (7) (2021) 1947–1954. `doi:10.1021/acs.jpclett.1c00169`.

[30] S. T. Pratt, Vibrational autoionization in polyatomic molecules, Annu. Rev. Phys. Chem. 56 (1) (2005) 281–308. `doi:10.1146/annurev.physchem.56.092503.141204`.

[31] C. L. Adams, H. Schneider, J. M. Weber, Vibrational Autodetachment - Intramolecular Vibrational Relaxation Translated into Electronic Motion, J. Phys. Chem. A 114 (12) (2010) 4017–4030. `doi:10.1021/jp910675n`.

[32] I. Fischer, S. T. Pratt, Photoelectron spectroscopy in molecular physical chemistry, Phys. Chem. Chem. Phys. 24 (2022) 1944–1959. `doi:10.1039/D1CP04984D`.

[33] A. Röder, J. Petersen, K. Issler, I. Fischer, R. Mitrić, L. Poisson, Exploring the Excited-State Dynamics of Hydrocarbon Radicals, Biradicals, and Carbenes Using Time-Resolved Photoelectron Spectroscopy and Field-Induced Surface Hopping Simulations, J. Phys. Chem. A 123 (50) (2019) 10643–10662. `doi:10.1021/acs.jpca.9b06346`.

[34] R. Misra, S. Bhattacharyya, Intramolecular Charge Transfer, John Wiley & Sons, Ltd, 2018, Ch. 1, pp. 1–27. `doi:10.1002/9783527801916.ch1`.

[35] J.-L. Brédas, D. Beljonne, V. Coropceanu, J. Cornil, Charge-Transfer and Energy-Transfer Processes in π-Conjugated Oligomers and Polymers: A Molecular Picture, Chem. Rev. 104 (11) (2004) 4971–5004. `doi:10.1021/cr040084k`.

[36] B. O'Regan, M. Grätzel, A low-cost, high-efficiency solar cell based on dye-sensitized colloidal TiO_2 films, Nature 353 (6346) (1991) 737 – 740. `doi:10.1038/353737a0`.

[37] Z. Zheng, N. R. Tummala, Y.-T. Fu, V. Coropceanu, J.-L. Brédas, Charge-Transfer States in Organic Solar Cells: Understanding the Impact of Polarization, Delocalization, and Disorder, ACS Appl. Mater. Interfaces 9 (21) (2017) 18095–18102. `doi:10.1021/acsami.7b02193`.

[38] Z. Yang, Z. Mao, Z. Xie, Y. Zhang, S. Liu, J. Zhao, J. Xu, Z. Chi, M. P. Aldred, Recent advances in organic thermally activated delayed fluorescence materials, Chem. Soc. Rev. 46 (2017) 915–1016. `doi:10.1039/C6CS00368K`.

[39] Y. Ning, X. Zhao, F. Wu, Y. Wu, J. Chen, F. Wei, H. Wang, X. Chen, Z. Xiong, Charge-transfer dynamics in oleds with coexisting electroplex and exciton states, Phys. Rev. Appl. 19 (2023) 064055. `doi:10.1103/PhysRevApplied.19.064055`.

[40] E. Lippert, W. Lüder, F. Moll, W. Nägele, H. Boos, H. Prigge, I. Seibold-Blankenstein, Umwandlung von Elektronenanregungsenergie, Angew. Chem. 73 (21) (1961) 695–706. `doi:10.1002/ange.19610732103`.

[41] E. Lippert, W. Lüder, H. Boos, Fluoreszenzspektrum und Franck-Condon-Prinzip in Lösungen aromatischer Verbindungen, in: Advances in Molecular Spectroscopy, Pergamon, 1962, pp. 443–457. `doi:10.1016/B978-1-4832-1332-3.50070-6`.

[42] Z. R. Grabowski, K. Rotkiewicz, W. Rettig, Structural Changes Accompanying Intramolecular Electron Transfer: Focus on Twisted Intramolecular Charge-Transfer States and Structures, Chem. Rev. 103 (10) (2003) 3899–4032. `doi:10.1021/cr940745l`.

[43] K. Issler, F. Sturm, J. Petersen, M. Flock, R. Mitrić, I. Fischer, L. Barreau, L. Poisson, Time-resolved photoelectron spectroscopy of 4-(dimethylamino)benzethyne – an experimental and computational study, Phys. Chem. Chem. Phys. 25 (2023) 9837–9845. `doi:10.1039/D3CP00309D`.

[44] E. Schrödinger, Quantisierung als Eigenwertproblem, Ann. Phys. 384 (4) (1926) 361–376. `doi:10.1002/andp.19263840404`.

[45] M. Born, R. Oppenheimer, Zur Quantentheorie der Molekeln, Ann. Phys. 389 (20) (1927) 457–484. `doi:10.1002/andp.19273892002`.

[46] P. Jungwirth, R. B. Gerber, Quantum molecular dynamics of ultrafast processes in large polyatomic systems, Chem. Rev. 99 (6) (1999) 1583–1606. `doi:10.1021/cr9800210`.

[47] M. Feit, J. Fleck, A. Steiger, Solution of the schrödinger equation by a spectral method, J. Comput. Phys. 47 (3) (1982) 412–433. `doi:10.1016/0021-9991(82)90091-2`.

[48] M. D. Feit, J. Fleck, J. A., Solution of the Schrödinger equation by a spectral method II: Vibrational energy levels of triatomic molecules, J. Chem. Phys. 78 (1) (1983) 301–308. `doi:10.1063/1.444501`.

[49] W. C. Swope, H. C. Andersen, P. H. Berens, K. R. Wilson, A computer simu-
lation method for the calculation of equilibrium constants for the formation of
physical clusters of molecules: Application to small water clusters, J. Chem.
Phys. 76 (1) (1982) 637–649. `doi:10.1063/1.442716`.

[50] E. Wigner, On the quantum correction for thermodynamic equilibrium, Phys.
Rev. 40 (1932) 749–759. `doi:10.1103/PhysRev.40.749`.

[51] M. Hillery, R. O'Connell, M. Scully, E. Wigner, Distribution functions in
physics: Fundamentals, Physics Reports 106 (3) (1984) 121–167. `doi:10.
1016/0370-1573(84)90160-1`.

[52] J. C. Tully, Molecular dynamics with electronic transitions, J. Chem. Phys.
93 (2) (1990) 1061–1071. `doi:10.1063/1.459170`.

[53] P. G. Lisinetskaya, R. Mitrić, Simulation of laser-induced coupled electron-
nuclear dynamics and time-resolved harmonic spectra in complex systems,
Phys. Rev. A 83 (2011) 033408. `doi:10.1103/PhysRevA.83.033408`.

[54] R. Mitrić, J. Petersen, V. Bonačić-Koutecký, Laser-field-induced surface-
hopping method for the simulation and control of ultrafast photodynamics,
Phys. Rev. A 79 (2009) 053416. `doi:10.1103/PhysRevA.79.053416`.

[55] W. Pauli, Über den Zusammenhang des Abschlusses der Elektronengruppen
im Atom mit der Komplexstruktur der Spektren, Z. Physik 31 (1925) 765–783.
`doi:10.1007/BF02980631`.

[56] J. Schirmer, Many-Body Methods for Atoms, Molecules and Clusters, Lecture
Notes in Chemistry, Volume 94, Springer, Cham, 2018.

[57] I. N. Levine, Quantum Chemistry, Pearson Advanced Chemistry Series, Pear-
son Education, New York, 2014.

[58] L. Brillouin, Les problèmes de perturbations et les champs self-consistents,
J. Phys. Radium 3 (9) (1932) 373–389. `doi:10.1051/jphysrad:
0193200309037300`.

[59] S. Grimme, Improved second-order Moller–Plesset perturbation theory by sep-
arate scaling of parallel- and antiparallel-spin pair correlation energies, J.
Chem. Phys. 118 (20) (2003) 9095–9102. `doi:10.1063/1.1569242`.

[60] Y. Jung, R. C. Lochan, A. D. Dutoi, M. Head-Gordon, Scaled opposite-
spin second order Møller–Plesset correlation energy: An economical elec-
tronic structure method, J. Chem. Phys. 121 (20) (2004) 9793–9802. `doi:
10.1063/1.1809602`.

[61] M. Gerenkamp, S. Grimme, Spin-component scaled second-order møller–plesset
perturbation theory for the calculation of molecular geometries and harmonic
vibrational frequencies, Chem. Phys. Lett. 392 (1) (2004) 229–235. `doi:10.
1016/j.cplett.2004.05.063`.

[62] J. Schirmer, Beyond the random-phase approximation: A new approximation scheme for the polarization propagator, Phys. Rev. A 26 (1982) 2395–2416. `doi:10.1103/PhysRevA.26.2395`.

[63] J. Schirmer, A. B. Trofimov, Intermediate state representation approach to physical properties of electronically excited molecules, J. Chem. Phys. 120 (24) (2004) 11449–11464. `doi:10.1063/1.1752875`.

[64] F. Mertins, J. Schirmer, Algebraic propagator approaches and intermediate-state representations. I. the biorthogonal and unitary coupled-cluster methods, Phys. Rev. A 53 (1996) 2140–2152. `doi:10.1103/PhysRevA.53.2140`.

[65] A. Dreuw, M. Wormit, The algebraic diagrammatic construction scheme for the polarization propagator for the calculation of excited states, WIREs Comput. Mol. Sci. 5 (1) (2015) 82–95. `doi:https://doi.org/10.1002/wcms.1206`.

[66] C. M. Krauter, M. Pernpointner, A. Dreuw, Application of the scaled-opposite-spin approximation to algebraic diagrammatic construction schemes of second order, J. Chem. Phys. 138 (4) (2013). `doi:10.1063/1.4776675`.

[67] A. Hellweg, S. Grün, C. Hättig, Benchmarking the performance of spin–component scaled CC2 in ground and electronically excited states, Phys. Chem. Chem. Phys. 10 (2008) 1159–1169. `doi:10.1039/B803727B`.

[68] R. G. Parr, W. Yang, Density-Functional Theory of Atoms and Molecules, Oxford University Press, New York, 1994.

[69] P. Hohenberg, W. Kohn, Inhomogeneous electron gas, Phys. Rev. 136 (1964) B864–B871. `doi:10.1103/PhysRev.136.B864`.

[70] W. Kohn, L. J. Sham, Self-consistent equations including exchange and correlation effects, Phys. Rev. 140 (1965) A1133–A1138. `doi:10.1103/PhysRev.140.A1133`.

[71] E. J. Baerends, O. V. Gritsenko, A quantum chemical view of density functional theory, J. Phys. Chem. A 101 (30) (1997) 5383–5403. `doi:10.1021/jp9703768`.

[72] R. Stowasser, R. Hoffmann, What Do the Kohn-Sham Orbitals and Eigenvalues Mean?, J. Am. Chem. Soc. 121 (14) (1999) 3414–3420. `doi:10.1021/ja9826892`.

[73] E. Runge, E. K. U. Gross, Density-functional theory for time-dependent systems, Phys. Rev. Lett. 52 (1984) 997–1000. `doi:10.1103/PhysRevLett.52.997`.

[74] M. E. Casida, Time-Dependent Density Functional Response Theory for Molecules, Recent Advances in Computational Chemistry: Volume 1, World Scientific, Singapore, 1995, p. 155. `doi:10.1142/9789812830586_0005`.

[75] S. Hirata, M. Head-Gordon, Time-dependent density functional theory within the Tamm–Dancoff approximation, Chem. Phys. Lett. 314 (3) (1999) 291–299. `doi:10.1016/S0009-2614(99)01149-5`.

[76] D. J. Griffiths, Introduction to Quantum Mechanics, Pearson Prentice Hall, Upper Saddle River, 2005.

[77] E. Merzbacher, Quantum Mechanics, John Wiley & Sons, New York, 1998.

[78] L. L. Lohr, M. B. Robin, Theoretical study of photoionization cross sections for π-electron systems, J. Am. Chem. Soc. 92 (25) (1970) 7241–7247. `doi: 10.1021/ja00728a001`.

[79] J. W. Rabalais, T. P. Debies, J. L. Berkosky, J. J. Huang, F. O. Ellison, Calculated photoionization cross sections and relative experimental photoionization intensities for a selection of small molecules, J. Chem. Phys. 61 (2) (1974) 516–528. `doi:10.1063/1.1681926`.

[80] K. J. Reed, A. H. Zimmerman, H. C. Andersen, J. I. Brauman, Cross sections for photodetachment of electrons from negative ions near threshold, J. Chem. Phys. 64 (4) (1976) 1368–1375. `doi:10.1063/1.432404`.

[81] J. Simons, Theoretical study of negative molecular ions, Annu. Rev. Phys. Chem. 62 (1) (2011) 107–128. `doi:10.1146/ annurev-physchem-032210-103547`.

[82] J. A. DeVine, M. L. Weichman, B. Laws, J. Chang, M. C. Babin, G. Balerdi, C. Xie, C. L. Malbon, W. C. Lineberger, D. R. Yarkony, R. W. Field, S. T. Gibson, J. Ma, H. Guo, D. M. Neumark, Encoding of vinylidene isomerization in its anion photoelectron spectrum, Science 358 (6361) (2017) 336. `doi: 10.1126/science.aao1905`.

[83] H. S. Taylor, G. V. Nazaroff, A. Golebiewski, Qualitative aspects of resonances in electron—atom and electron—molecule scattering, excitation, and reactions, J. Chem. Phys. 45 (8) (1966) 2872–2888. `doi:10.1063/1.1728041`.

[84] D.-F. Yuan, Y.-R. Zhang, L.-S. Wang, Dipole-Bound State, Photodetachment Spectroscopy, and Resonant Photoelectron Imaging of Cryogenically-Cooled 2-Cyanopyrrolide, J. Phys. Chem. A 126 (37) (2022) 6416–6428. `doi:10.1021/ acs.jpca.2c04405`.

[85] K. Issler, R. Mitrić, J. Petersen, HORTENSIA, a program package for the calculation of nonadiabatic autoionization dynamics in molecules, J. Chem. Phys 159 (13) (2023) 134801. `doi:10.1063/5.0167412`.

[86] J. Simons, Roles Played by Metastable States in Chemistry, 1984, Ch. 1, pp. 3–16. `doi:10.1021/bk-1984-0263.ch001`.

[87] R. Balog, J. Langer, S. Gohlke, M. Stano, H. Abdoul-Carime, E. Illenberger, Low energy electron driven reactions in free and bound molecules: from unimolecular processes in the gas phase to complex reactions in a condensed environment, Int. J. Mass Spectrom. 233 (1) (2004) 267–291. `doi: 10.1016/j.ijms.2003.12.030`.

[88] L.-S. Wang, C.-F. Ding, X.-B. Wang, S. E. Barlow, Photodetachment photoelectron spectroscopy of multiply charged anions using electrospray ionization, Rev. Sci. Instrum. 70 (4) (1999) 1957–1966. `doi:10.1063/1.1149694`.

[89] D. M. Wetzel, J. I. Brauman, Electron photodetachment spectroscopy of trapped negative ions, Chem. Rev. 87 (3) (1987) 607–622. `doi:10.1021/cr00079a007`.

[90] J. C. Rienstra-Kiracofe, G. S. Tschumper, H. F. Schaefer, S. Nandi, G. B. Ellison, Atomic and molecular electron affinities: Photoelectron experiments and theoretical computations, Chem. Rev. 102 (1) (2002) 231–282. `doi:10.1021/cr990044u`.

[91] R. R. Corderman, W. C. Lineberger, Negative ion spectroscopy, Annu. Rev. Phys. Chem. 30 (1) (1979) 347–378. `doi:10.1146/annurev.pc.30.100179.002023`.

[92] K. Müller-Dethlefs, M. Sander, E. W. Schlag, A Novel Method Capable of Resolving Rotational Ionic States by the Detection of Threshold Photoelectrons with a Resolution of 1.2 cm^{-1}, Z. Naturforsch. A 39 (11) (1984) 1089–1091. `doi:doi:10.1515/zna-1984-1112`.

[93] C. C. Arnold, D. M. Neumark, Study of Si$_4$ and Si$_4^-$ using threshold photodetachment (ZEKE) spectroscopy, J. Chem. Phys. 99 (5) (1993) 3353–3362. `doi:10.1063/1.465145`.

[94] J. M. Hollas, Modern Spectroscopy, John Wiley and Sons, West Sussex, 2003.

[95] K. D. Jordan, Negative ion states of polar molecules, Acc. Chem. Res. 12 (1) (1979) 36–42. `doi:10.1021/ar50133a006`.

[96] J. H. Hendricks, S. A. Lyapustina, H. L. de Clercq, K. H. Bowen, The dipole bound-to-covalent anion transformation in uracil, J. Chem. Phys. 108 (1) (1998) 8–11. `doi:10.1063/1.475360`.

[97] R. A. Bachorz, W. Klopper, M. Gutowski, X. Li, K. H. Bowen, Photoelectron spectrum of valence anions of uracil and first-principles calculations of excess electron binding energies, J. Chem. Phys. 129 (5) (2008). `doi:10.1063/1.2965128`.

[98] W. C. Lineberger, Once upon anion: A tale of photodetachment, Annu. Rev. Phys. Chem. 64 (1) (2013) 21–36. `doi:10.1146/annurev-physchem-032511-143753`.

[99] H. Hotop, T. A. Patterson, W. C. Lineberger, High resolution photodetachment study of OH− and OD$^-$ in the threshold region 7000–6450 Å, J. Chem. Phys. 60 (5) (1974) 1806–1812. `doi:10.1063/1.1681279`.

[100] R. J. Celotta, R. A. Bennett, J. L. Hall, M. W. Siegel, J. Levine, Molecular photodetachment spectrometry. ii. the electron affinity of O$_2$ and the structure of O$_2^-$, Phys. Rev. A 6 (1972) 631–642. `doi:10.1103/PhysRevA.6.631`.

[101] A. Kasdan, E. Herbst, W. Lineberger, Laser photoelectron spectrometry of CH$^-$, Chem. Phys. Lett. 31 (1) (1975) 78–82. `doi:10.1016/0009-2614(75)80062-5`.

[102] D. G. Leopold, K. K. Murray, W. C. Lineberger, Laser photoelectron spectroscopy of vibrationally relaxed CH_2^-: A reinvestigation of the singlet–triplet splitting in methylene, J. Chem. Phys. 81 (2) (1984) 1048–1050. `doi:10.1063/1.447741`.

[103] S. M. Burnett, A. E. Stevens, C. Feigerle, W. Lineberger, Observation of X^1A_1 vinylidene by photoelectron spectroscopy of the $C_2H_2^-$ ion, Chem. Phys. Lett. 100 (2) (1983) 124–128. `doi:10.1016/0009-2614(83)80698-8`.

[104] H. K. Gerardi, K. J. Breen, T. L. Guasco, G. H. Weddle, G. H. Gardenier, J. E. Laaser, M. A. Johnson, Survey of Ar-tagged predissociation and vibrationally mediated photodetachment spectroscopies of the vinylidene anion, $C_2H_2^-$, J. Phys. Chem. A 114 (3) (2010) 1592. `doi:10.1021/jp9095419`.

[105] W. Nolting, Elektrodynamik, Springer Spektrum Berlin, Heidelberg, 2013.

[106] R. F. Wallis, R. Herman, H. W. Milnes, Energy levels of an electron in the field of a finite dipole, J. Mol. Spectrosc. 4 (1) (1960) 51–74. `doi:10.1016/0022-2852(60)90065-5`.

[107] O. H. Crawford, Bound states of a charged particle in a dipole field, Proceedings of the Physical Society 91 (2) (1967) 279. `doi:10.1088/0370-1328/91/2/303`.

[108] K. D. Jordan, F. Wang, Theory of dipole-bound anions, Annu. Rev. Phys. Chem. 54 (1) (2003) 367–396. `doi:10.1146/annurev.physchem.54.011002.103851`.

[109] W. Garrett, Critical binding of an electron to a non-stationary electric dipole, Chem. Phys. Lett. 5 (7) (1970) 393–397. `doi:10.1016/0009-2614(70)80045-8`.

[110] M. Gutowski, P. Skurski, Theoretical study of the quadrupole-bound anion $(BeO)_2^-$, Chem. Phys. Lett. 303 (1) (1999) 65–75. `doi:10.1016/S0009-2614(99)00172-4`.

[111] R. N. Compton, J. Carman, H. S., C. Desfrançois, H. Abdoul-Carime, J. P. Schermann, J. H. Hendricks, S. A. Lyapustina, K. H. Bowen, On the binding of electrons to nitromethane: Dipole and valence bound anions, J. Chem. Phys. 105 (9) (1996) 3472–3478. `doi:10.1063/1.472993`.

[112] P. Skurski, M. Gutowski, J. Simons, How to choose a one-electron basis set to reliably describe a dipole-bound anion, Int. J. Quantum Chem. 80 (4-5) (2000) 1024–1038. `doi:10.1002/1097-461X(2000)80:4/5<1024::AID-QUA51>3.0.CO;2-P`.

[113] W. J. Morgan, R. C. Fortenberry, Additional diffuse functions in basis sets for dipole-bound excited states of anions, Theor. Chem. Acc 134 (2015) 47. `doi:10.1007/s00214-015-1647-1`.

[114] P. D. Burrow, G. A. Gallup, A. M. Scheer, S. Denifl, S. Ptasinska, T. Märk, P. Scheier, Vibrational Feshbach resonances in uracil and thymine, J. Chem. Phys. 124 (12) (2006) 124310. `doi:10.1063/1.2181570`.

[115] J. Gu, J. Leszczynski, H. F. Schaefer, Interactions of Electrons with Bare and Hydrated Biomolecules: From Nucleic Acid Bases to DNA Segments, Chem. Rev. 112 (11) (2012) 5603. `doi:10.1021/cr3000219`.

[116] S. Marburger, O. Kugeler, U. Hergenhahn, T. Möller, Experimental evidence for interatomic coulombic decay in Ne clusters, Phys. Rev. Lett. 90 (2003) 203401. `doi:10.1103/PhysRevLett.90.203401`.

[117] M. Mucke, M. Braune, S. Barth, M. Förstel, T. Lischke, V. Ulrich, T. Arion, U. Becker, A. Bradshaw, U. Hergenhahn, A hitherto unrecognized source of low-energy electrons in water, Nat. Phys. 6 (2010) 143–146. `doi:10.1038/nphys1500`.

[118] T. A. A. Oliver, Y. Zhang, A. Roy, M. N. R. Ashfold, S. E. Bradforth, Exploring autoionization and photoinduced proton-coupled electron transfer pathways of phenol in aqueous solution, J. Phys. Chem. Lett. 6 (20) (2015) 4159–4164. `doi:10.1021/acs.jpclett.5b01861`.

[119] R. M. Young, D. M. Neumark, Dynamics of solvated electrons in clusters, Chem. Rev. 112 (11) (2012) 5553. `doi:10.1021/cr300042h`.

[120] F. Arnold, Solvated electrons in the upper atmosphere, Nature 294 (1981) 732–733. `doi:10.1038/294732a0`.

[121] N. Getoff, S. Solar, D. B. McCormick, Photoejection of electrons from flavins in polar media, Science 201 (4356) (1978) 616–618. `doi:10.1126/science.675244`.

[122] A. Dalgarno, R. A. McCray, The formation of interstellar molecules from negative ions, Astrophys. J. 181 (1973) 95–100. `doi:10.1086/152032`.

[123] U. Hefter, R. D. Mead, P. A. Schulz, W. C. Lineberger, Ultrahigh-resolution study of autodetachment in C_2^-, Phys. Rev. A 28 (1983) 1429–1439. `doi:10.1103/PhysRevA.28.1429`.

[124] D. M. Neumark, K. R. Lykke, T. Andersen, W. C. Lineberger, Infrared-spectrum and autodetachment dynamics of NH^-, J. Chem. Phys. 83 (9) (1985) 4364–4373. `doi:10.1063/1.449052`.

[125] C. E. H. Dessent, J. Kim, M. A. Johnson, Spectroscopic observation of vibrational Feshbach resonances in near-threshold photoexcitation of $X^- \cdot CH_3NO_2$ ($X^- = I^-$ and Br^-), Faraday Discuss. 115 (2000) 395–406. `doi:10.1039/a909550k`.

[126] H.-T. Liu, C.-G. Ning, D.-L. Huang, L.-S. Wang, Vibrational Spectroscopy of the Dehydrogenated Uracil Radical by Autodetachment of Dipole-Bound Excited States of Cold Anions, Angew. Chem., Int. Ed. 53 (9) (2014) 2464–2468. `doi:10.1002/anie.201310323`.

[127] J. N. Bull, C. W. West, J. R. R. Verlet, Ultrafast dynamics of formation and autodetachment of a dipole-bound state in an open-shell π-stacked dimer anion, Chem. Sci. 7 (8) (2016) 5352–5361. `doi:10.1039/c6sc01062h`.

[128] G.-Z. Zhu, Y. Liu, L.-S. Wang, Observation of Excited Quadrupole-Bound States in Cold Anions, Phys. Rev. Lett. 119 (2017) 023002. `doi:10.1103/PhysRevLett.119.023002`.

[129] C. L. Adams, K. Hansen, J. M. Weber, Vibrational autodetachment from anionic nitroalkane chains: From molecular signatures to thermionic emission, J. Phys. Chem. A 123 (40) (2019) 8562–8570. `doi:10.1021/acs.jpca.9b07780`.

[130] J. N. Bull, C. S. Anstöter, M. H. Stockett, C. J. Clarke, J. A. Gibbard, E. J. Bieske, J. R. R. Verlet, Nonadiabatic dynamics between valence, nonvalence, and continuum electronic states in a heteropolycyclic aromatic hydrocarbon, J. Phys. Chem. Lett. 12 (49) (2021) 11811–11816. `doi:10.1021/acs.jpclett.1c03532`.

[131] J. N. Bull, C. S. Anstöter, J. R. R. Verlet, Ultrafast valence to non-valence excited state dynamics in a common anionic chromophore, Nat. Commun. 10 (2019) 5820. `doi:10.1038/s41467-019-13819-6`.

[132] D. H. Kang, S. An, S. K. Kim, Real-Time Autodetachment Dynamics of Vibrational Feshbach Resonances in a Dipole-Bound State, Phys. Rev. Lett. 125 (9) (2020) 093001. `doi:10.1103/PhysRevLett.125.093001`.

[133] R. S. Berry, Ionization of molecules at low energies, J. Chem. Phys. 45 (4) (1966) 1228–1245. `doi:10.1063/1.1727742`.

[134] J. Simons, Propensity rules for vibration-induced electron detachment of anions, J. Am. Chem. Soc. 103 (14) (1981) 3971–3976. `doi:10.1021/ja00404a002`.

[135] P. K. Acharya, R. A. Kendall, J. Simons, Vibration-induced electron detachment in molecular anions, J. Am. Chem. Soc. 106 (12) (1984) 3402–3407. `doi:10.1021/ja00324a003`.

[136] J. Simons, Time-domain and tunneling pictures of nonadiabatic induced electron ejection in molecular anions, J. Phys. Chem. A 103 (47) (1999) 9408–9416. `doi:10.1021/jp9917603`.

[137] U. Werner, R. Mitrić, T. Suzuki, V. Bonačić-Koutecký, Nonadiabatic dynamics within the time dependent density functional theory: Ultrafast photodynamics in pyrazine, Chem. Phys. 349 (1-3) (2008) 319–324. `doi:10.1016/j.chemphys.2008.02.061`.

[138] Z. Lan, E. Fabiano, W. Thiel, Photoinduced Nonadiabatic Dynamics of Pyrimidine Nucleobases: On-the-Fly Surface-Hopping Study with Semiempirical Methods, J. Phys. Chem. B 113 (11) (2009) 3548–3555. `doi:10.1021/jp809085h`.

[139] G. Richings, I. Polyak, K. Spinlove, G. Worth, I. Burghardt, B. Lasorne, Quantum dynamics simulations using Gaussian wavepackets: the vMCG method, Int. Rev. Phys. Chem. 34 (2) (2015) 269–308. `doi:10.1080/0144235X.2015.1051354`.

[140] A. Humeniuk, M. Wohlgemuth, T. Suzuki, R. Mitrić, Time-resolved photoelectron imaging spectra from non-adiabatic molecular dynamics simulations, J. Chem. Phys. 139 (13) (2013) 134104. `doi:10.1063/1.4820238`.

[141] A. Röder, K. Issler, L. Poisson, A. Humeniuk, M. Wohlgemuth, M. Comte, F. Lepetit, I. Fischer, R. Mitrić, J. Petersen, Femtosecond dynamics of the 2-methylallyl radical: A computational and experimental study, J. Chem. Phys. 147 (1) (2017) 013902. `doi:10.1063/1.4974150`.

[142] F. Kossoski, M. T. d. N. Varella, M. Barbatti, On-the-fly dynamics simulations of transient anions, J. Chem. Phys. 151 (22) (2019) 224104. `doi:10.1063/1.5130547`.

[143] J. A. Gyamfi, T.-C. Jagau, Ab initio molecular dynamics of temporary anions using complex absorbing potentials, J. Phys. Chem. Lett. 13 (36) (2022) 8477–8483. `doi:10.1021/acs.jpclett.2c01969`.

[144] P. S. Skell, J. H. Plonka, Chemistry of the singlet and triplet C_2 molecules. mechanism of acetylene formation from reaction with acetone and acetaldehyde, J. Am. Chem. Soc. 92 (19) (1970) 5620. `doi:10.1021/ja00722a014`.

[145] H. F. Schaefer, The 1,2 hydrogen shift: A common vehicle for the disappearance of evanescent molecular species, Acc. Chem. Res. 12 (8) (1979) 288. `doi:10.1021/ar50140a004`.

[146] K. M. Ervin, J. Ho, W. C. Lineberger, A study of the singlet and triplet states of vinylidene by photoelectron spectroscopy of $H_2C=C^-$, $D_2C=C^-$, and $HDC=C^-$. vinylidene–acetylene isomerization, J. Chem. Phys. 91 (10) (1989) 5974. `doi:10.1063/1.457415`.

[147] M. J. Jensen, U. V. Pedersen, L. H. Andersen, Stability of the Ground State Vinylidene Anion H_2CC^-, Phys. Rev. Lett. 84 (2000) 1128–1131. `doi:10.1103/PhysRevLett.84.1128`.

[148] R. Dressler, M. Allan, A dissociative electron attachment, electron transmission, and electron energy-loss study of the temporary negative ion of acetylene, J. Chem. Phys. 87 (8) (1987) 4510. `doi:10.1063/1.452864`.

[149] J. A. DeVine, M. L. Weichman, X. Zhou, J. Ma, B. Jiang, H. Guo, D. M. Neumark, Non-adiabatic effects on excited states of vinylidene observed with slow photoelectron velocity-map imaging, J. Am. Chem. Soc. 138 (50) (2016) 16417–16425. `doi:10.1021/jacs.6b10233`.

[150] R. Schork, H. Köppel, Barrier recrossing in the vinylidene–acetylene isomerization reaction: A five-dimensional ab initio quantum dynamical investigation, J. Chem. Phys. 115 (17) (2001) 7907. `doi:10.1063/1.1405120`.

[151] S. Zou, J. M. Bowman, Full dimensionality quantum calculations of acetylene/vinylidene isomerization, J. Chem. Phys. 117 (12) (2002) 5507–5510. `doi:10.1063/1.1507118`.

[152] L. Guo, H. Han, J. Ma, H. Guo, Quantum dynamics of vinylidene photode-tachment on an accurate global acetylene-vinylidene potential energy surface, J. Phys. Chem. A 119 (2015) 8488. `doi:10.1021/acs.jpca.5b05061`.

[153] J. Levin, H. Feldman, A. Baer, D. Ben-Hamu, O. Heber, D. Zajfman, Z. Vager, Study of unimolecular reactions by coulomb explosion imaging: The non-decaying vinylidene, Phys. Rev. Lett. 81 (1998) 3347–3350. `doi:10.1103/PhysRevLett.81.3347`.

[154] R. L. Hayes, E. Fattal, N. Govind, E. A. Carter, Long live vinylidene! a new view of the $H_2CC:\rightarrow HC\equiv CH$ rearrangement from ab initio molecular dynamics, J. Am. Chem. Soc. 123 (2001) 641. `doi:10.1021/ja000907x`.

[155] R. Swinbank, R. J. Purser, Fibonacci grids: A novel approach to global mod-elling, Q. J. R. Meteorol. Soc. 132 (619) (2006) 1769. `doi:10.1256/qj.05.227`.

[156] P.-O. Löwdin, Quantum Theory of Many-Particle Systems. I. Physical Interpre-tations by Means of Density Matrices, Natural Spin-Orbitals, and Convergence Problems in the Method of Configurational Interaction, Phys. Rev. 97 (1955) 1474–1489. `doi:10.1103/PhysRev.97.1474`.

[157] H. Taketa, S. Huzinaga, K. O-ohata, Gaussian-Expansion Methods for Molec-ular Integrals, J. Phys. Soc. Jpn. 21 (11) (1966) 2313–2324. `doi:10.1143/JPSJ.21.2313`.

[158] M. Dupuis, J. Rys, H. F. King, Evaluation of molecular integrals over Gaussian basis functions, J. Chem. Phys. 65 (1) (1976) 111–116. `doi:10.1063/1.432807`.

[159] J. Rys, M. Dupuis, H. F. King, Computation of Electron Repulsion Integrals Using the Rys Quadrature Method, J. Comput. Chem. 4 (2) (1983) 154–157. `doi:10.1002/jcc.540040206`.

[160] Q. Sun, Libcint: An efficient general integral library for Gaussian basis func-tions, J. Comput. Chem. 36 (2015) 1664–1671. `doi:10.1002/jcc.23981`.

[161] D. K. Watson, V. McKoy, Discrete-basis-function approach to electron-molecule scattering, Phys. Rev. A 20 (1979) 1474–1483. `doi:10.1103/PhysRevA.20.1474`.

[162] R. Colle, A. Fortunelli, S. Simonucci, A Mixed Basis Set of Plane Waves and Hermite Gaussian Functions. Analytical Expressions of Prototype Integrals, Il Nuovo Cimento D 9 (1987) 969–977. `doi:10.1007/BF02464849`.

[163] R. Mitrić, U. Werner, V. Bonačić-Koutecký, Nonadiabatic dynamics and sim-ulation of time resolved photoelectron spectra within time-dependent density functional theory: Ultrafast photoswitching in benzylideneaniline, J. Chem. Phys. 129 (16) (2008) 164118. `doi:10.1063/1.3000012`.

[164] R. Mitrić, J. Petersen, V. Bonačić-Koutecký, Multistate Nonadiabatic Dynam-ics "on the Fly" in Complex Systems and Its Control by Laser Fields, Vol. 17 of Advanced Series in Physical Chemistry, World Scientific, Singapore, 2011, p. 497–568. `doi:10.1142/9789814313452_0013`.

[165] J. F. Stanton, J. Gauss, Vibrational structure in the vinylidene anion photoelectron spectrum: Closing the gap between theory and experiment, J. Chem. Phys. 110 (12) (1999) 6079–6080. `doi:10.1063/1.478511`.

[166] J.-D. Chai, M. Head-Gordon, Long-range corrected hybrid density functionals with damped atom–atom dispersion corrections, Phys. Chem. Chem. Phys. 10 (2008) 6615. `doi:10.1039/B810189B`.

[167] O. A. Vydrov, G. E. Scuseria, Assessment of a long-range corrected hybrid functional, J. Chem. Phys. 125 (23) (2006) 234109. `doi:10.1063/1.2409292`.

[168] T. Yanai, D. P. Tew, N. C. Handy, A new hybrid exchange–correlation functional using the Coulomb-attenuating method (CAM-B3LYP), Chem. Phys. Lett. 393 (2004) 51. `doi:10.1016/j.cplett.2004.06.011`.

[169] R. Krishnan, J. S. Binkley, R. Seeger, J. A. Pople, Self-consistent molecular orbital methods. XX. A basis set for correlated wave functions, J. Chem. Phys. 72 (1) (1980) 650. `doi:10.1063/1.438955`.

[170] T. Clark, J. Chandrasekhar, G. W. Spitznagel, P. V. R. Schleyer, Efficient diffuse function-augmented basis sets for anion calculations. III. The 3-21+G basis set for first-row elements, Li–F, J. Comput. Chem. 4 (3) (1983) 294. `doi:10.1002/jcc.540040303`.

[171] T. H. Dunning, Gaussian basis sets for use in correlated molecular calculations. I. The atoms boron through neon and hydrogen, J. Chem. Phys. 90 (2) (1989) 1007. `doi:10.1063/1.456153`.

[172] R. A. Kendall, T. H. Dunning, R. J. Harrison, Electron affinities of the first-row atoms revisited. Systematic basis sets and wave functions, J. Chem. Phys. 96 (1992) 6796. `doi:10.1063/1.462569`.

[173] D. E. Woon, T. H. Dunning, Gaussian basis sets for use in correlated molecular calculations. IV. Calculation of static electrical response properties, J. Chem. Phys. 100 (4) (1994) 2975. `doi:10.1063/1.466439`.

[174] M. J. Frisch, et al., Gaussian 09 Revision D.01, Gaussian Inc. Wallingford CT (2009).

[175] G. D. Purvis, R. J. Bartlett, A full coupled-cluster singles and doubles model: The inclusion of disconnected triples, J. Chem. Phys. 76 (4) (1982) 1910. `doi:10.1063/1.443164`.

[176] G. E. Scuseria, C. L. Janssen, H. F. Schaefer, An efficient reformulation of the closed-shell coupled cluster single and double excitation (CCSD) equations, J. Chem. Phys. 89 (12) (1988) 7382. `doi:10.1063/1.455269`.

[177] P. Virtanen, R. Gommers, T. E. Oliphant, M. Haberland, T. Reddy, D. Cournapeau, E. Burovski, P. Peterson, W. Weckesser, J. Bright, S. J. van der Walt, M. Brett, J. Wilson, K. J. Millman, N. Mayorov, A. R. J. Nelson, E. Jones, R. Kern, E. Larson, C. J. Carey, İ. Polat, Y. Feng, E. W. Moore, J. VanderPlas, D. Laxalde, J. Perktold, R. Cimrman, I. Henriksen, E. A. Quintero, C. R. Harris, A. M. Archibald, A. H. Ribeiro, F. Pedregosa, P. van

Mulbregt, SciPy 1.0 Contributors, SciPy 1.0: Fundamental Algorithms for Scientific Computing in Python, Nature Methods 17 (2020) 261–272. `doi: 10.1038/s41592-019-0686-2`.

[178] J. P. Snyder, Map projections: A working manual, U.S. Government Printing Office, 1987. `doi:10.3133/pp1395`.

[179] L. E. McMurchie, E. R. Davidson, One- and two-electron integrals over Cartesian Gaussian functions, J. Comput. Phys. 26 (2) (1978) 218–231. `doi: 10.1016/0021-9991(78)90092-X`.

[180] C. R. Arumainayagam, H.-L. Lee, R. B. Nelson, D. R. Haines, R. P. Gunawardane, Low-energy electron-induced reactions in condensed matter, Surf. Sci. Rep. 65 (1) (2010) 1–44. `doi:10.1016/j.surfrep.2009.09.001`.

[181] J. R. R. Verlet, C. S. Anstöter, J. N. Bull, J. P. Rogers, Role of Nonvalence States in the Ultrafast Dynamics of Isolated Anions, J. Phys. Chem. A 124 (18) (2020) 3507–3519. `doi:10.1021/acs.jpca.0c01260`.

[182] M. Barbatti, M. Ruckenbauer, F. Plasser, J. Pittner, G. Granucci, M. Persico, H. Lischka, Newton-X: a surface-hopping program for nonadiabatic molecular dynamics, WIREs Comput. Mol. Sci. 4 (1) (2014) 26–33. `doi:10.1002/wcms. 1158`.

[183] S. Mai, P. Marquetand, L. González, Nonadiabatic dynamics: The sharc approach, WIREs Comp. Mol. Sci. 8 (6) (2018) e1370. `doi:10.1002/wcms.1370`.

[184] L. Du, Z. Lan, An on-the-fly surface-hopping program jade for nonadiabatic molecular dynamics of polyatomic systems: Implementation and applications, J. Chem. Theory Comput. 11 (4) (2015) 1360–1374. `doi:10.1021/ct501106d`.

[185] K. Issler, R. Mitrić, J. Petersen, A trajectory surface hopping study of the vibration-induced autodetachment dynamics of the 1-nitropropane anion, Theo. Chem. Acc 142 (2023) 123. `doi:10.1007/s00214-023-03063-z`.

[186] S. Hammes-Schiffer, J. C. Tully, Proton transfer in solution: Molecular dynamics with quantum transitions, J. Chem. Phys. 101 (6) (1994) 4657–4667.

[187] J. Pittner, H. Lischka, M. Barbatti, Optimization of mixed quantum-classical dynamics: Time-derivative coupling terms and selected couplings, Chem. Phys. 356 (1) (2009) 147–152. `doi:https://doi.org/10.1016/j.chemphys. 2008.10.013`.
URL `https://www.sciencedirect.com/science/article/pii/ S0301010408004783`

[188] U. Werner, R. Mitrić, V. Bonačić-Koutecký, Simulation of time resolved photoelectron spectra with Stieltjes imaging illustrated on ultrafast internal conversion in pyrazine, J. Chem. Phys. 132 (17) (2010) 174301. `doi: 10.1063/1.3395160`.

[189] R. L. Martin, Natural transition orbitals, J. Chem. Phys. 118 (2003) 4775–4777. `doi:10.1063/1.1558471`.

[190] T. Sommerfeld, H.-D. Meyer, Computing the energy-dependent width of temporary anions from $\mathcal{L}^2$ ab initio methods, J. Phys. B: At. Mol. Opt. Phys. 35 (2002) 1841–1863.

[191] T.-C. Jagau, K. B. Bravaya, A. I. Krylov, Extending quantum chemistry of bound states to electronic resonances, Annu. Rev. Phys. Chem. 68 (2017) 525–553.

[192] M. J. Frisch, et al., Gaussian 16 Revision A.03, Gaussian Inc. Wallingford CT (2016).

[193] Y. Shao, et al., Advances in molecular quantum chemistry contained in the Q-Chem 4 program package, Mol. Phys. 113 (2) (2015) 184–215. `doi:10.1080/00268976.2014.952696`.

[194] W. Humphrey, A. Dalke, K. Schulten, VMD – Visual Molecular Dynamics, J. Mol. Graph. 14 (1996) 33–38. `doi:10.1016/0263-7855(96)00018-5`.

[195] Q. Sun, T. C. Berkelbach, N. S. Blunt, G. H. Booth, S. Guo, Z. Li, J. Liu, J. D. McClain, E. R. Sayfutyarova, S. Sharma, S. Wouters, G. K.-L. Chan, PySCF: the Python-based simulations of chemistry framework, WIREs Comput. Mol. Sci. 8 (1) (2018) e1340. `doi:10.1002/wcms.1340`.

[196] Q. Sun, X. Zhang, S. Banerjee, P. Bao, M. Barbry, N. S. Blunt, N. A. Bogdanov, G. H. Booth, J. Chen, Z.-H. Cui, J. J. Eriksen, Y. Gao, S. Guo, J. Hermann, M. R. Hermes, K. Koh, P. Koval, S. Lehtola, Z. Li, J. Liu, N. Mardirossian, J. D. McClain, M. Motta, B. Mussard, H. Q. Pham, A. Pulkin, W. Purwanto, P. J. Robinson, E. Ronca, E. R. Sayfutyarova, M. Scheurer, H. F. Schurkus, J. E. T. Smith, C. Sun, S.-N. Sun, S. Upadhyay, L. K. Wagner, X. Wang, A. White, J. D. Whitfield, M. J. Williamson, S. Wouters, J. Yang, J. M. Yu, T. Zhu, T. C. Berkelbach, S. Sharma, A. Y. Sokolov, G. K.-L. Chan, Recent developments in the PySCF program package, J. Chem. Phys. 153 (2) (2020) 024109. `doi:10.1063/5.0006074`.

[197] SchedMD, Slurm Workload Manager, `https://slurm.schedmd.com/`.

[198] J. D. Hunter, Matplotlib: A 2D graphics environment, Comput. Sci. Eng. 9 (3) (2007) 90–95. `doi:10.1109/MCSE.2007.55`.

[199] K. Issler, J. Petersen, R. Mitrić, HORTENSIA program package, `https://github.com/mitric-lab/HORTENSIA_LATEST.git`.

[200] Joblib: running Python functions as pipeline jobs. Release 1.1.0 (2021). URL `https://joblib.readthedocs.io/`

[201] S. Behnel, R. Bradshaw, C. Citro, L. Dalcin, D. S. Seljebotn, K. Smith, Cython: The best of both worlds, Comput. Sci. Eng. 13 (2) (2011) 31–39. `doi:10.1109/MCSE.2010.118`.

[202] J. Simons, Ejecting electrons from molecular anions via shine, shake/rattle, and roll, J. Phys. Chem. A 124 (42) (2020) 8778–8797. `doi:10.1021/acs.jpca.0c08016`.

[203] J. Warneke, M. E. McBriarty, S. L. Riechers, S. China, M. H. Engelhard, E. Aprà, R. P. Young, N. M. Washton, C. Jenne, G. E. Johnson, J. Laskin, Self-organizing layers from complex molecular anions, Nat. Commun. 9 (2018) 1889. `doi:10.1038/s41467-018-04228-2`.

[204] F. C. Fehsenfeld, E. E. Ferguson, Laboratory studies of negative ion reactions with atmospheric trace constituents, J. Chem. Phys. 61 (8) (1974) 3181–3193. `doi:10.1063/1.1682474`.

[205] W. N. Olmstead, J. I. Brauman, Gas-phase nucleophilic displacement reactions, J. Am. Chem. Soc. 99 (13) (1977) 4219–4228. `doi:10.1021/ja00455a002`.

[206] E. K. Ashworth, N. J. A. Coughlan, W. S. Hopkins, E. J. Bieske, J. N. Bull, Excited-State Barrier Controls E→Z Photoisomerization in p-Hydroxycinnamate Biochromophores, J. Phys. Chem. Lett. 13 (39) (2022) 9028–9034. `doi:10.1021/acs.jpclett.2c02613`.

[207] S. N. Eustis, D. Radisic, K. H. Bowen, R. A. Bachorz, M. Haranczyk, G. K. Schenter, M. Gutowski, Electron-driven acid-base chemistry: Proton transfer from hydrogen chloride to ammonia, Science 319 (5865) (2008) 936–939. `doi:10.1126/science.1151614`.

[208] K. D. Jordan, J. F. Liebman, Binding of an electron to a molecular quadrupole: $(BeO)_2$, Chem. Phys. Lett. 62 (1) (1979) 143–147. `doi:10.1016/0009-2614(79)80430-3`.

[209] M. Gutowski, P. Skurski, X. Li, L.-S. Wang, $(MgO)_n^-$ ($n = 1 - 5$) clusters: Multipole-bound anions and photodetachment spectroscopy, Phys. Rev. Lett. 85 (2000) 3145–3148. `doi:10.1103/PhysRevLett.85.3145`.

[210] C. Desfrançois, Y. Bouteiller, J. P. Schermann, D. Radisic, S. T. Stokes, K. H. Bowen, N. I. Hammer, R. N. Compton, Long-range electron binding to quadrupolar molecules, Phys. Rev. Lett. 92 (2004) 083003. `doi:10.1103/PhysRevLett.92.083003`.

[211] K. Fossez, X. Mao, W. Nazarewicz, N. Michel, W. R. Garrett, M. Płoszajczak, Resonant spectra of quadrupolar anions, Phys. Rev. A 94 (2016) 032511. `doi:10.1103/PhysRevA.94.032511`.

[212] M. Gutowski, K. D. Jordan, P. Skurski, Electronic structure of dipole-bound anions, J. Phys. Chem. A 102 (15) (1998) 2624–2633. `doi:10.1021/jp980123u`.

[213] C.-H. Qian, G.-Z. Zhu, L.-S. Wang, Probing the critical dipole moment to support excited dipole-bound states in valence-bound anions, J. Phys. Chem. Lett. 10 (21) (2019) 6472–6477. `doi:10.1021/acs.jpclett.9b02679`.

[214] J. N. Bull, J. R. R. Verlet, Observation and ultrafast dynamics of a nonvalence correlation-bound state of an anion, Sci. Adv. 3 (5) (2017) e1603106. `doi:10.1126/sciadv.1603106`.

[215] A. S. Mullin, K. K. Murray, C. Schulz, D. M. Szaflarski, W. Lineberger, Autodetachment spectroscopy of vibrationally excited acetaldehyde enolate anion, CH_2CHO^-, Chem. Phys. 166 (1) (1992) 207–213. doi:10.1016/0301-0104(92)87019-6.

[216] H. Schneider, K. M. Vogelhuber, F. Schinle, J. F. Stanton, J. M. Weber, Vibrational Spectroscopy of Nitroalkane Chains Using Electron Autodetachment and Ar Predissociation, J. Phys. Chem. A 112 (33) (2008) 7498–7506. doi:10.1021/jp800124s.

[217] C. L. Adams, B. J. Knurr, J. M. Weber, Photoelectron spectroscopy of 1-nitropropane and 1-nitrobutane anions, J. Chem. Phys. 136 (6) (2012) 064307. doi:10.1063/1.3683250.

[218] G. L. Gutsev, R. J. Bartlett, A theoretical study of the valence- and dipole-bound states of the nitromethane anion, J. Chem. Phys. 105 (19) (1996) 8785–8792. doi:10.1063/1.472657.

[219] S. Tsuda, A. Yokohata, M. Kawai, Measurement of Negative Ions Formed by Electron Impact. I. Negative Ion Mass Spectra of Nitroalkanes, Bull. Chem. Soc. Jpn. 42 (3) (1969) 607–614. doi:10.1246/bcsj.42.607.

[220] J. A. Stockdale, F. J. Davis, R. N. Compton, C. E. Klots, Production of negative ions from CH3X molecules (CH_3NO_2, CH_3CN, CH_3I, CH_3Br) by electron impact and by collisions with atoms in excited Rydberg states, J. Chem. Phys. 60 (11) (1974) 4279–4285. doi:10.1063/1.1680900.

[221] L. Adamowicz, Dipole-bound anionic state of nitromethane. Ab initio coupled cluster study with first-order correlation orbitals, J. Chem. Phys. 91 (12) (1989) 7787–7790. doi:10.1063/1.457246.

[222] J. F. Arenas, J. C. Otero, D. Peláez, J. Soto, L. Serrano-Andrés, Multi-configurational second-order perturbation study of the decomposition of the radical anion of nitromethane, J. Chem. Phys. 121 (9) (2004) 4127–4132. doi:10.1063/1.1772357.

[223] C. L. Adams, H. Schneider, K. M. Ervin, J. M. Weber, Low-energy photoelectron imaging spectroscopy of nitromethane anions: Electron affinity, vibrational features, anisotropies, and the dipole-bound state, J. Chem. Phys. 130 (7) (2009) 074307. doi:10.1063/1.3076892.

[224] D. J. Goebbert, K. Pichugin, A. Sanov, Low-lying electronic states of CH_3NO_2 via photoelectron imaging of the nitromethane anion, J. Chem. Phys. 131 (16) (2009) 164308. doi:10.1063/1.3256233.

[225] C. J. M. Pruitt, R. M. Albury, D. J. Goebbert, Photoelectron spectroscopy of nitromethane anion clusters, Chem. Phys. Lett. 659 (2016) 142–147. doi:10.1016/j.cplett.2016.07.022.

[226] G. Liu, S. M. Ciborowski, J. D. Graham, A. M. Buytendyk, K. H. Bowen, Photoelectron spectroscopic study of dipole-bound and valence-bound nitromethane anions formed by rydberg electron transfer, J. Chem. Phys. 153 (4) (2020) 044307. doi:10.1063/5.0018346.

[227] K. Jäger, A. Henglein, Negative Ionen durch Elektronenstoß aus organischen Nitroverbindungen, Äthylnitrit und Äthylnitrat, Z. Naturforsch. A 22 (5) (1967) 700–704. `doi:doi:10.1515/zna-1967-0516`.

[228] S. Lunt, D. Field, J.-P. Ziesel, N. Jones, R. Gulleye, Very low energy electron scattering in nitromethane, nitroethane, and nitrobenzene, Int. J. Mass Spectrom. 205 (1) (2001) 197–208. `doi:10.1016/S1387-3806(00)00376-6`.

[229] A. Pelc, W. Sailer, S. Matejcik, P. Scheier, T. D. Märk, Dissociative electron attachment to nitroethane: C2h5no2, J. Chem. Phys. 119 (15) (2003) 7887–7892. `doi:10.1063/1.1607314`.

[230] S. T. Stokes, K. H. Bowen, T. Sommerfeld, S. Ard, N. Mirsaleh-Kohan, J. D. Steill, R. N. Compton, Negative ions of nitroethane and its clusters, J. Chem. Phys. 129 (6) (2008) 064308. `doi:10.1063/1.2965534`.

[231] C. L. Adams, J. M. Weber, Photoelectron imaging spectroscopy of nitroethane anions, J. Chem. Phys. 134 (24) (2011) 244301. `doi:10.1063/1.3602467`.

[232] A. Ferretti, G. Granucci, A. Lami, M. Persico, G. Villani, Quantum mechanical and semiclassical dynamics at a conical intersection, J. Chem. Phys. 104 (14) (1996) 5517–5527. `doi:10.1063/1.471791`.

[233] G. Granucci, M. Persico, A. Toniolo, Direct semiclassical simulation of photochemical processes with semiempirical wave functions, J. Chem. Phys. 114 (24) (2001) 10608–10615. `doi:10.1063/1.1376633`.

[234] G. Granucci, M. Persico, Critical appraisal of the fewest switches algorithm for surface hopping, J. Chem. Phys. 126 (13) (2007) 134114. `doi:10.1063/1.2715585`.

[235] J. Fregoni, S. Corni, M. Persico, G. Granucci, Photochemistry in the strong coupling regime: A trajectory surface hopping scheme, J. Comput. Chem. 41 (23) (2020) 2033–2044. `doi:10.1002/jcc.26369`.

[236] S. Choia, J. Vaníček, How important are the residual nonadiabatic couplings for an accurate simulation of nonadiabatic quantum dynamics in a quasidiabatic representation?, J. Chem. Phys. 154 (2021) 124119. `doi:10.1063/5.0046067`.

[237] J. A. Pople, M. Head-Gordon, K. Raghavachari, Quadratic configuration interaction. a general technique for determining electron correlation energies, J. Chem. Phys. 87 (10) (1987) 5968–5975. `doi:10.1063/1.453520`.

[238] W. Rettig, Charge Separation in Excited States of Decoupled Systems—TICT Compounds and Implications Regarding the Development of New Laser Dyes and the Primary Process of Vision and Photosynthesis, Angew. Chem. Int. Ed. 25 (11) (1986) 971–988. `doi:10.1002/anie.198609711`.

[239] J. M. Szarko, B. S. Rolczynski, S. J. Lou, T. Xu, J. Strzalka, T. J. Marks, L. Yu, L. X. Chen, Photovoltaic Function and Exciton/Charge Transfer Dynamics in a Highly Efficient Semiconducting Copolymer, Adv. Funct. Mater. 24 (1) (2014) 10–26. `doi:10.1002/adfm.201301820`.

[240] W. Li, Y. Pan, L. Yao, H. Liu, S. Zhang, C. Wang, F. Shen, P. Lu, B. Yang, Y. Ma, A Hybridized Local and Charge-Transfer Excited State for Highly Efficient Fluorescent OLEDs: Molecular Design, Spectral Character, and Full Exciton Utilization, Adv. Opt. Mater. 2 (9) (2014) 892–901. `doi:10.1002/adom.201400154`.

[241] S. Sasaki, G. P. C. Drummen, G. Konishi, Recent advances in twisted intramolecular charge transfer (tict) fluorescence and related phenomena in materials chemistry, J. Mater. Chem. C 4 (2016) 2731–2743. `doi:10.1039/C5TC03933A`.

[242] C. Chudoba, A. Kummrow, J. Dreyer, J. Stenger, E. Nibbering, T. Elsaesser, K. Zachariasse, Excited state structure of 4-(dimethylamino)benzonitrile studied by femtosecond mid-infrared spectroscopy and ab initio calculations, Chem. Phys. Lett. 309 (5-6) (1999) 357–363. `doi:10.1016/S0009-2614(99)00711-3`.

[243] J.-K. Lee, T. Fujiwara, W. G. Kofron, M. Z. Zgierski, E. C. Lim, The low-lying $\pi\sigma*$ state and its role in the intramolecular charge transfer of aminobenzonitriles and aminobenzethyne, J. Chem. Phys. 128 (16) (2008) 164512. `doi:10.1063/1.2901976`.

[244] S. Druzhinin, N. Ernsting, S. Kovalenko, L. Lustres, T. Senyushkina, K. Zachariasse, Dynamics of ultrafast intramolecular charge transfer with 4-(dimethylamino)benzonitrile in acetonitrile, J. Phys. Chem. A 110 (9) (2006) 2955–2969. `doi:10.1021/jp054496o`.

[245] T. Fujiwara, M. Z. Zgierski, E. C. Lim, The role of the $\pi\sigma^*$ state in intramolecular charge transfer of 4-(dimethylamino)benzonitrile, Phys. Chem. Chem. Phys. 13 (15) (2011) 6779–6783. `doi:10.1039/c0cp02706e`.

[246] J. M. Rhinehart, R. D. Mehlenbacher, D. McCamant, Probing the charge transfer reaction coordinate of 4-(dimethylamino)benzonitrile with femtosecond stimulated raman spectroscopy, J. Phys. Chem. B 114 (45) (2010) 14646–14656. `doi:10.1021/jp1023982`.

[247] S. K. Sahoo, S. Umapathy, A. W. Parker, Time-resolved resonance raman spectroscopy: Exploring reactive intermediates, Appl. Spectrosc. 65 (10) (2011) 1087–1115. `doi:10.1366/11-06406`.

[248] W. Fuß, K. K. Pushpa, W. Rettig, W. E. Schmid, S. A. Trushin, Ultrafast charge transfer via a conical intersection in dimethylaminobenzonitrile, Photochem. Photobiol. Sci. 1 (2002) 255–262. `doi:10.1039/B111678A`.

[249] S. Trushin, T. Yatsuhashi, W. Fuß, W. Schmid, Coherent oscillations in the charge-transfer system 4-dimethylamino-benzonitrile, Chem. Phys. Lett. 376 (3-4) (2003) 282–291. `doi:10.1016/S0009-2614(03)00979-5`.

[250] K. Zachariasse, T. Vonderhaar, A. Hebecker, U. Leinhos, W. Kuhnle, Intramolecular charge-transfer in aminobenzonitriles - requirements for dual fluorescence, Pure Appl. Chem. 65 (8) (1993) 1745–1750. `doi:10.1351/pac199365081745`.

[251] A. Sobolewski, W. Domcke, Promotion of intramolecular charge transfer in dimethylamino derivatives: Twisting versus acceptor-group rehybridization, Chem. Phys. Lett. 259 (1-2) (1996) 119–127. `doi:10.1016/0009-2614(96)00724-5`.

[252] A. Sobolewski, W. Domcke, Mechanism of photoinduced intramolecular charge transfer in aminobenzethynes: An ab initio study, J. Photochem. Photobiol. A 105 (2-3) (1997) 325–328. `doi:10.1016/S1010-6030(96)04603-5`.

[253] A. Sobolewski, W. Sudholt, W. Domcke, Ab initio investigation of reaction pathways for intramolecular charge transfer in dimethylanilino derivatives, J. Phys. Chem. A 102 (16) (1998) 2716–2722. `doi:10.1021/jp980435x`.

[254] K. A. Zachariasse, M. Grobys, E. Tauer, Absence of dual fluorescence with 4-(dimethylamino) phenylacetylene. a comparison between experimental results and theoretical predictions, Chem. Phys. Lett. 274 (4) (1997) 372 – 382. `doi:10.1016/S0009-2614(97)00668-4`.

[255] K. A. Zachariasse, T. Yoshihara, S. I. Druzhinin, Picosecond and Nanosecond Fluorescence Decays of 4-(Dimethylamino)phenylacetylene in Comparison with Those of 4-(Dimethylamino)benzonitrile. No Evidence for Intramolecular Charge Transfer and a Nonfluorescing Intramolecular Charge-Transfer State, J. Phys. Chem. A 106 (26) (2002) 6325–6333. `doi:10.1021/jp025814b`.

[256] N. Chattopadhyay, C. Serpa, M. Pereira, J. de Melo, L. Arnaut, S. Formosinho, Intramolecular charge transfer of p-(dimethylamino) benzethyne: A case of nonfluorescent ict state, J. Phys. Chem. A 105 (44) (2001) 10025–10030. `doi:10.1021/jp012390x`.

[257] T. Fujiwara, J.-K. Lee, M. Z. Zgierski, E. C. Lim, Photophysical and spectroscopic manifestations of the low-lying $\pi\sigma^*$ state of 4-(dimethylamino)benzethyne: solvent-polarity dependence of fluorescence and excited-state absorptions, Phys. Chem. Chem. Phys. 11 (14) (2009) 2475–2479. `doi:10.1039/b820371g`.

[258] J. Segarra-Martí, P. B. Coto, A theoretical study of the intramolecular charge transfer in 4-(dimethylamino)benzethyne, Phys. Chem. Chem. Phys. 16 (2014) 25642–25648. `doi:10.1039/C4CP03436H`.

[259] A. Nikolaev, G. Myszkiewicz, G. Berden, W. Meerts, J. Pfanstiel, D. Pratt, Twisted intramolecular charge transfer states: Rotationally resolved fluorescence excitation spectra of 4,4 '-dimethylaminobenzonitrile in a molecular beam, J. Chem. Phys. 122 (8) (2005) 084309. `doi:10.1063/1.1850092`.

[260] A. J. Fleisher, R. G. Bird, D. P. Zaleski, B. H. Pate, D. W. Pratt, High-resolution electronic spectroscopy of the doorway states to intramolecular charge transfer, J. Phys. Chem. B 117 (16, SI) (2013) 4231–4240. `doi:10.1021/jp3041296`.

[261] M. A. Kochman, A. Tajti, C. A. Morrison, R. J. D. Miller, Early Events in the Nonadiabatic Relaxation Dynamics of 4-(N,N-Dimethylamino)benzonitrile, J. Chem. Theory Comput. 11 (3) (2015) 1118–1128. `doi:10.1021/ct5010609`.

[262] M. A. Kochman, B. Durbeej, Simulating the nonadiabatic relaxation dynamics of 4-(n,n-dimethylamino)benzonitrile (dmabn) in polar solution, J. Phys. Chem. A 124 (11) (2020) 2193–2206. `doi:10.1021/acs.jpca.9b10588`.

[263] M. S. Schuurman, V. Blanchet, Time-resolved photoelectron spectroscopy: the continuing evolution of a mature technique, Phys. Chem. Chem. Phys. 24 (2022) 20012–20024. `doi:10.1039/D1CP05885A`.

[264] K. Issler, A. Röder, F. Hirsch, L. Poisson, I. Fischer, R. Mitrić, J. Petersen, Excited state dynamics and time-resolved photoelectron spectroscopy of para-xylylene, Faraday Discuss. 212 (2018) 83–100. `doi:10.1039/C8FD00083B`.

[265] S. Karashima, A. Humeniuk, R. Uenishi, T. Horio, M. Kanno, T. Ohta, J. Nishitani, R. Mitrić, T. Suzuki, Ultrafast ring-opening reaction of 1,3-cyclohexadiene: Identification of nonadiabatic pathway via doubly excited state, J. Am. Chem. Soc. 143 (21) (2021) 8034–8045. `doi:10.1021/jacs.1c01896`.

[266] S. Karashima, X. Miao, A. Kanayama, Y.-i. Yamamoto, J. Nishitani, N. Kavka, R. Mitrić, T. Suzuki, Ultrafast Ring Closure Reaction of Gaseous cis-Stilbene from $S_1(\pi\pi*)$, J. Am. Chem. Soc. 145 (6) (2023) 3283–3288. `doi:10.1021/jacs.2c12266`.

[267] S. Aloïse, Z. Pawlowska, C. Ruckebusch, M. Sliwa, J. Dubois, O. Poizat, G. Buntinx, A. Perrier, F. Maurel, P. Jacques, J.-P. Malval, L. Poisson, G. Piani, J. Abe, A two-step ICT process for solvatochromic betaine pyridinium revealed by ultrafast spectroscopy, multivariate curve resolution, and TDDFT calculations, Phys. Chem. Chem. Phys. 14 (2012) 1945–1956. `doi:10.1039/C2CP22254J`.

[268] M. Flock, M.-P. Herbert, I. Fischer, The excited-state structure and photophysics of isolated acenaphthylene, Chem. Phys. 515 (2018) 744–749. `doi:10.1016/j.chemphys.2018.05.017`.

[269] M. Flock, L. Bosse, D. Kaiser, B. Engels, I. Fischer, A time-resolved photoelectron imaging study on isolated tolane: observation of the biradicalic ^1a_u state, Phys. Chem. Chem. Phys. 21 (24) (2019) 13157–13164. `doi:10.1039/c9cp02222h`.

[270] A. Golinelli, X. Chen, B. Bussière, E. Gontier, P.-M. Paul, O. Tcherbakoff, P. D'Oliveira, J.-F. Hergott, CEP-stabilized, sub-18 fs, 10 kHz and TW-class 1 kHz dual output Ti:Sa laser with wavelength tunability option, Opt. Express 27 (10) (2019) 13624–13636. `doi:10.1364/OE.27.013624`.

[271] A. B. Trofimov, J. Schirmer, An efficient polarization propagator approach to valence electron excitation spectra, J. Phys. B 28 (12) (1995) 2299–2324. `doi:10.1088/0953-4075/28/12/003`.

[272] C. Hättig, Structure Optimizations for Excited States with Correlated Second-Order Methods: CC2 and ADC(2), in: Response Theory and Molecular Properties (A Tribute to Jan Linderberg and Poul Jørgensen), Vol. 50 of

Advances in Quantum Chemistry, Academic Press, 2005, pp. 37–60. `doi: 10.1016/S0065-3276(05)50003-0`.

[273] TURBOMOLE V7.0 2015, a development of University of Karlsruhe and Forschungszentrum Karlsruhe GmbH, 1989-2007, TURBOMOLE GmbH, since 2007; available from
`http://www.turbomole.com`.

[274] H. Koch, P. Jørgensen, Coupled cluster response functions, J. Chem. Phys. 93 (5) (1990) 3333–3344. `doi:10.1063/1.458814`.

[275] J. F. Stanton, R. J. Bartlett, The equation of motion coupled-cluster method. a systematic biorthogonal approach to molecular excitation energies, transition probabilities, and excited state properties, J. Chem. Phys. 98 (9) (1993) 7029–7039. `doi:10.1063/1.464746`.

[276] S. Gozem, A. I. Krylov, The ezSpectra suite: An easy-to-use toolkit for spectroscopy modeling, WIREs Computational Molecular Science 12 (2) (2022) e1546. `doi:10.1002/wcms.1546`.

[277] P. Wojcik, S. Gozem, V. Mozhayskiy, A. I. Krylov, ezFCF program package. URL `http://iopenshell.usc.edu/downloads`

[278] S. Awali, J.-M. Mestdagh, M.-A. Gaveau, M. Briant, B. Soep, V. Mazet, L. Poisson, Time-Resolved Observation of the Solvation Dynamics of a Rydberg Excited Molecule Deposited on an Argon Cluster. Ii. DABCO at Long Time Delays, J. Phys. Chem. A 125 (2021) 4341–4351. `doi:10.1021/acs.jpca.1c01942`.

[279] M. A. Kochman, B. Durbeej, A. Kubas, Simulation and Analysis of the Transient Absorption Spectrum of 4-(N,N-Dimethylamino)benzonitrile (DMABN) in Acetonitrile, J. Phys. Chem. A 125 (39) (2021) 8635–8648. `doi:10.1021/acs.jpca.1c06166`.

[280] L. Allen, A. O'Connell, V. Kiermer, How can we ensure visibility and diversity in research contributions? How the Contributor Role Taxonomy (CRediT) is helping the shift from authorship to contributorship, Learn. Publ. 32 (1) (2019) 71–74. `doi:10.1002/leap.1210`.